Fundamental investigation of cathode materials upon deep lithiation for advanced battery management system parametrization

Camille Usubelli

To cite this version:

Camille Usubelli. Fundamental investigation of cathode materials upon deep lithiation for advanced battery management system parametrization. Other. Université de Strasbourg, 2021. English. NNT : 2021STRAE019 . tel-03968144

HAL Id: tel-03968144
https://theses.hal.science/tel-03968144
Submitted on 1 Feb 2023

UNIVERSITÉ DE STRASBOURG

École doctorale
Physique, chimie-physique
ED 182
Université de Strasbourg

ÉCOLE DOCTORALE DE PHYSIQUE ET CHIMIE-PHYSIQUE

Institut de Physique et Chimie des Matériaux de Strasbourg

THÈSE présentée par :

Camille USUBELLI

soutenue le : **26 Juillet 2021**

pour obtenir le grade de : **Docteur de l'université de Strasbourg**
Discipline/ Spécialité : Physique Chimie-Physique

Fundamental investigation of cathode materials upon deep lithiation for advanced battery management system parametrization

THÈSE dirigée par :	
Mr. DINIA Aziz	Professeur, Université de Strasbourg
Mme. GORLIN Yelena	PhD, Industrial supervisor - Robert Bosch LLC
Mr. CRAIG. Nathan	PhD, Industrial supervisor - Robert Bosch LLC
RAPPORTEURS :	
Mme TANG Maureen	Associate Professor, Drexel University
Mr. SUNTIVICH Jin	Associate Professor, Cornell University

PRESIDENTE DU JURY :	
Mme SAVINOVA Elena	Professeur, Université de Strasbourg

Abstract

The deep lithiation of $Li_xNi_aMn_bCo_cO_2$, a + b + c = 1 (NMC), was studied from x = 0.2 to x = 2. The electrochemical features of the overlithiated materials were linked to structural changes identified by X-ray diffraction (XRD) and to the variations of the oxidation state of the transition metals (TMs) observed by X-ray absorption spectroscopy (XAS). Detailed electrochemical characterization of $LiNi_{0.33}Mn_{0.33}Co_{0.33}O_2$ (NMC111), $LiNi_{0.4}Mn_{0.4}Co_{0.2}O_2$ (NMC442), $LiNi_{0.5}Mn_{0.3}Co_{0.2}O_2$ (NMC532), $LiNi_{0.6}Mn_{0.2}Co_{0.2}O_2$ (NMC622), and $LiNi_{0.8}Mn_{0.1}Co_{0.1}O_2$ (NMC811) combined with XAS and XRD investigations were used to understand the impact of the TMs ratio and the presence of Ni^{3+} ions on the reversibility of the insertion of extra lithium ions and linked to the superior reversibility of NMC532 and NMC622 upon deep lithiation. The impact of the electrolyte degradation at low potential on the formation of a cathode protective layer was studied by On-line Electrochemical Mass Spectroscopy (OEMS).

A novel method for characterization of the open circuit potential vs. state of lithiation curves (referred to as OCP curves) was established using the understanding gained upon overlithiation of cathode materials. The new method was optimized by combing several cycles to identify the current bias, slow-rate cycles at C/50 and C/25 to identify a trust regime where the OCP can be extracted from the average of the lithiation and delithiation curves, and discharging pulses allowing the material to reach its true relaxation potential in the lithiation states outside of the trust regime. By providing a standardized mapping process from the measured gravimetric capacity to the state of lithiation, and improving characterization in the region of the curve that is close to the lithium content of 1, this novel method ensures increased accuracy of the OCP curves of cathode materials, which is a critical aspect of physics-based battery management systems.

Table of Contents

List of acronyms, constants, and symbols

Abbreviation	Description
NMC	$LiNi_aMn_bCo_cO_2$, with $a+b+c = 1$, $a \geq b$
XRD	X-ray diffraction
TM	Transition metal
XAS	X-ray absorption spectroscopy
OEMS	On-line electrochemical mass spectrometer
OCP	Open circuit potential
OCP curve	Open circuit potential vs Li content
BEV	Battery electric vehicle
EV	Electric vehicle
Li	Lithium
LIB	Lithium ion battery
BMS	Battery management system
ABMS	Advanced battery management system
Ni	Nickel
Mn	Manganese
Co	Cobalt
Al	Aluminum
LCO	$LiCoO_2$
LNO	$LiNiO_2$
LMO	$LiMnO_2$
NCA	$LiNi_aCo_bAl_cO_2$, with $a+b+c = 1$, $a \geq b$
EC	Ethylene carbonate
DEC	Diethyl carbonate
FEC	Fluoroethylene carbonate
DMC	Dimethyl carbonate
EMC	Ethyl methyl carbonate
CE	Coulombic efficiency
CAMP	Cell Analysis, Modeling and Prototyping

OCV	Open circuit voltage
SSRL	Stanford Synchrotron Radiation Lightsource
XANES	X-ray absorption near-edge structure
TEY	Total electron yield
FY	Fluorescence yield
SEM	Secondary electron microscopy
BET	Brunauer-Emmett-Teller
TEM	Transmission electron microscopy
EELS	Electron energy loss spectroscopy
ICP-OES	Inductively coupled plasma optical emission spectroscopy
MLCT	Metal-to-ligand charge transfer
LEDC	Lithium ethylene dicarbonate
LiF	Lithium fluoride
VC	Vinylene carbonate
SEI	Solid electrolyte interphase
CEI	Cathode electrolyte interphase

Acknowledgments

I would like to first thank Professor Aziz Dinia for his kind guidance and continuous support over the past few years. Ever since engineering school, I had the chance to benefit from his advice and perspective on scientific work, and I am very grateful for his help in the realization of this thesis. All that could be seen as complications for this thesis; the distance, the topic, the virtual defense; was made possible with his help and support.

I was lucky enough to have two industrial advisors throughout the course of my thesis. Dr. Yelena Gorlin, who supervised my work with Bosch for about two years, guided me with the initial experimental work. I am immensely grateful for her mentorship and the countless discussions we had about electrochemistry. She greatly improved my understanding of Lithium-ion batteries. I am thankful that she had my best interests at heart and pushed me to set ambitious goals, both for my thesis work and for various work projects. She also had a great influence outside of work, by sharing her passion of ultimate for instance. Even though she took on another opportunity and left Bosch, she was always very generous with her time and provided valuable feedback during the thesis writing process.

I want to thank Dr. Nathan Craig for supervising the last year of my thesis. Nate contributed his time and knowledge to help me put my experimental work in context of fundamental electrochemical behaviors. His input was extremely valuable to my work and I am very grateful for all the discussions. I really appreciated his involvement in the thesis writing and all the feedback he provided helped me see my work from a different perspective.

I also want to thank Jake Christensen for his feedback on my work. His knowledge of the field always raised very interesting questions and I appreciate him taking the time to have motivating discussions with me.

I had amazing colleagues who contributed to a great atmosphere in the lab but also outside. I want to thank Reinhardt Klein for sharing his perspective on batteries and the battery management system. It was a pleasure to contribute to his projects. I also owe him for the great food recommendations! I had the chance to closely collaborate with Saravanan Kuppan, Michael Metzger and Münir Besli. I am immensely grateful for them sharing their knowledge with me. I want to thank them for the great discussions, the mental support during this thesis, the amazing camping trips, the hiking, and the very challenging bike rides! I am happy to consider them, and Sara's family, as friends. I want to thank my friend Maya for her support. Having her pursing a PhD at the same time on a different continent was a great way to share this journey together! I would not have been able to finish this work without the support of Münir, and I am extremely grateful that somehow we ended up starting a PhD at the same time with Bosch.

Je voudrais enfin remercier ma famille pour leur immense soutien pendant toute ma scolarité. J'ai beaucoup de gratitude pour ma grand-mère Colette qui a toujours eu un œil bienveillant sur mon parcours, et qui m'a montré, dès mon plus jeune âge que les femmes sont capable de tout accomplir. Nathalie et les enfants, qui m'ont toujours encouragée et suivi dans mes aventures. Je sais que je peux toujours me ressourcer auprès de vous ! J'aurais aimé partager cet accomplissement avec mes grands-parents Pierre et Ginette. Mon grand-père m'a encouragée par sa ténacité et son courage à vouloir me surpasser, que ce soit à vélo ou dans les études. Enfin le plus grand des remerciements va à mes parents. Ils m'ont donné tous les outils pour que j'arrive où je suis aujourd'hui et je leur en suis éternellement reconnaissante. Ces dernières années à distance n'ont pas été les plus faciles mais leur soutien sans faille m'a permis de mener ce projet à terme. Si cette aventure a été possible, c'est grâce à eux.

Mille fois merci !

A Pierrot et Ginou

Introduction

This year 2021 marks a tipping point in the handling of our planet's energy resources. With the entire world forced to a stop because of a global pandemic, the impact of human activity on greenhouse gas emissions was directly measured.[1] The need for practical renewable energy sources to fuel the global energy requirements is widely acknowledged, with tremendous efforts made in research. The spectrum of renewable energies is vast and unevenly distributed. Solar, wind, and tide have geographical limitations, to which the grid infrastructure's growing problems add. Those drawbacks can nevertheless be overcome, and renewable energy sources can be combined with energy storage solutions to achieve a clean energy supply chain. Intense efforts have been made on devices such as fuel cells, super capacitors and batteries, with rechargeable batteries the leading energy storage technology in terms of safety, cost-effectiveness, portability, high energy and power density, and good cycle life.[2] Because of their remarkable capabilities, lithium ion batteries (LIBs) have allowed battery electric vehicles (BEV) to revolutionize the automotive industry over the past few years, and they have the potential to change the entire mobility sector.

The success story of rechargeable batteries was crowned in 2019 with the Nobel Prize in Chemistry awarded to John B. Goodenough, M. Stanley Whittingham, and Akira Yoshino for their contributions to the development LIBs. LIBs are the most successful rechargeable batteries owing to their small size and high energy density, due to the low reduction potential of lithium (-3.04 V vs standard hydrogen electrode). The research on improving the performances of LIBs focuses on its components: the cathode, the anode, the electrolyte and the separator. The current LIB technology consists of the following: a cathode material made of a Li intercalated transition metal (TM) oxide; an anode material such as graphite, lithium titanium oxide ($Li_4Ti_5O_{12}$), silicon based materials, or ideally Li metal; an electrolyte comprising alkyl carbonate solvents and one or several Li salts. The electrolyte medium, made of separator and electrolyte, is a conductor for ions and an insulator for electrons. As depicted in Figure 1 upon discharging (lithiation), the Li ions diffuse from the anode and intercalate in the cathode via the electrolyte medium, while the electrons reach the cathode via an external circuit. The reversed process occurs upon charge (delithiation). Upon current interruption, the equilibrium potential of the battery is proportional to the difference in chemical potentials of the cathode and the anode. In order to improve the capacity of the battery, the specific capacity of one of its components must be increased. Because the specific capacity of the anode is much lower, focus has been put on improving the chemical potential of the cathode material.

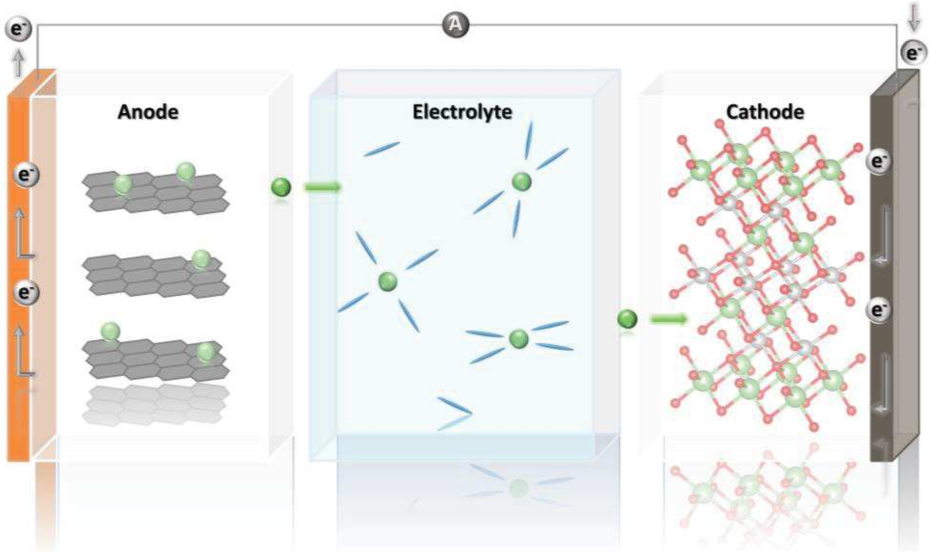

Figure 1: Schematic of a lithium-ion battery with a graphite anode and layered oxide cathode, its components, and the principle of Li ion and electron transport upon lithiation.

The implementation of batteries in portable electronics or electric vehicles (EVs) requires a close control and monitoring of the states of the batteries to ensure safe and reliable operations. This control over the battery is provided by the battery management system (BMS). Additionally, the BMS should optimize the energy delivered by the battery at all times and inform the user of the states of the batteries. A sophisticated advanced battery management system (ABMS) has been developed with a physics-based electrochemical model.[3] This ABMS requires a deep understanding of the fundamental properties of the battery components and the principle operations of the battery. In order to provide accurate estimations of the state of the battery, the parameters of the cathode, the anode, and the electrolyte must be investigated in details. The work of this thesis will focus on a key parameter of the cathode materials: the open-circuit potential as a function of the Li content (OCP curve).

The most common cathode materials have the following structure: layered-structure oxides $LiMO_2$ (M one or several 3d TMs such as Ni, Mn, Co, Al), with a α-$NaFeO_2$-like structure from the $R\bar{3}m$ group; spinel-structure oxide LiM_2O_4 from the space group $Fd\bar{3}m$; and olivine phosphate $LiMPO_4$ from the orthorhombic Pnma structure. Layered materials are the most promising and practical cathode materials and have been extensively studied since the first commercialization of LIBs by Sony in 1991 based on the layered cobalt-oxide cathode developed by Goodenough.[4] Even though $LiCoO_2$ (LCO) cathodes are still used in commercial batteries, Co has been progressively replaced by other TMs such as Ni ($LiNiO_2$ – LNO) or Mn $LiMnO_2$ – LMO) in order to reach more stability, access more capacity, and lower the cost and toxicity of the material. To overcome the drawbacks of the individual layered materials, binary-layered oxides have been studied, and ternary-layered oxides such as $LiNi_aMn_bCo_cO_2$ (with a + b + c = 1, NMC) and $LiNi_aCo_bAl_cO_2$ (with a + b + c = 1, NCA) were introduced as the most promising cathode materials. The high practical capacity of NMC electrodes, ranging from 200-210 $mAh.g^{-1}$ has placed this material at the center of numerous research studies.[5,6] One path to improve the capacity delivered by NMC cathodes is to increase the proportion of Ni in the material, creating a Ni-rich NMC cathode. Those cathodes are the state-of-the-art material in LIBs and current challenges include improving their capacity without sacrificing stability and kinetics.

The stability of NMC materials has been extensively studied at high potential, but little research has been done on the low potential stability of these electrodes. This potential region in the NMC cathodes is of interest for the ABMS, as the physics-based model requires information about the bulk and the surface of the particles, which can reach a higher lithiation degree than the bulk of the material upon lithiation. A detailed study of NMC cathode materials is proposed in this thesis in order to gain fundamental understanding of the states of the cathode materials at high lithiation degree. First, an electrochemical study of various stoichiometry of NMC materials is done in the classic potential window of 3.0 V to 4.3-4.4 V vs Li/Li^+. The potential of the cycling window is lowered to ~ 1.6 V vs Li/Li^+ to regain the initial capacity, and then lowered further to ~ 0.8 V vs Li/Li^+ to reach the theoretical stoichiometry of ~ 2 Li ions per NMC structure. New lithiation and delithiation profiles are observed upon this extended potential window, and linked to theoretical calculations of the valence change of the TMs. In a second part, the structural changes expected from the electrochemical study are investigated with X-ray diffraction and the valence of the TMs is studied with X-ray absorption spectroscopy. An understanding of the TMs' implication upon deep lithiation is proposed for various stoichiometry of NMC materials. In a third part, the influence of the electrolyte on the cycling in this extended potential window is investigated by an electrochemical study of commercially relevant electrolytes, coupled with an X-ray absorption spectroscopy investigation, and analysis of the gases evolving in the cells. After determination of the exceptional stability of the lithiation of NMC materials to the Li content of 1, the fundamental understanding of this deep lithiation is used to develop a new method to determine the open-circuit potential as a function of the Li content (OCP curve). This method allows additional characterization of the material in the tail region, at a Li content that the surface of the material can access upon lithiation in the classic potential window vs graphite, and the setting of the x-axis with the determination of the xLi = 1 position. This OCP curve determination method provides a key electrode parameter for the ABMS, and is proposed as a new standard to compare cathode investigation between research groups.

Experimental techniques

Overview of the experimental techniques

A combination of complementary experimental techniques was used in order to investigate different aspects of cathode materials upon deep lithiation. Due to the use of a slow cycling rate of C/10 in the electrochemical experiments, no electrolyte polarization is expected to occur, and the electrochemical signal is expected to come from the entire thickness of the electrode, as represented in Figure 2. a. Ex-situ techniques were used to diagnose the changes occurring in the material at different stages of lithiation and delithiation, using electrodes harvested from half-cells. X-ray diffraction (XRD) was used to investigate the crystal structure of each electrode after certain cycling conditions, averaging the information throughout the entire thickness of the electrode, as shown in Figure 2. a. To complement the information obtained on the structure of the active material, X-ray absorption spectroscopy (XAS) was used to determine the oxidation state of each transition metal and identify which elements were involved in the structural changes upon deep lithiation. Hard XAS was used to investigate the K-edge of the TMs in the electrodes, giving an overview of the changes occurring in the bulk of the material in similarity to XRD, and soft XAS was used to highlight the differences between the subsurface and the superficial layers of the electrode by probing the L-edge transitions. As represented in Figure 2. a and Figure 2. c, soft XAS measurements provide information on the top 5 nm of the electrode in the total electron yield (TEY) mode, as well as within the first 50 to100 nm with the fluorescence yield (FY) mode, giving, in combination with hard XAS, a depth-resolved picture of the oxidation state variations leading to the structural changes observed via XRD.

Additionally, in order to capture any potential intermediate states and reliably identify the reactions taking place upon deep lithiation, in-situ synchrotron XRD measurements were done on customized coin cells. As represented in Figure 2. b, the in-situ XRD measurements captured the changes occurring in the bulk of the cell upon cycling through a Kapton window. In-situ measurements also allowed to exclude any contamination resulting from the sample preparation as well as side reactions induced by the highly reactive lithiated electrodes.[7] In a custom-design cell, the gases evolving during cycling of the electrode were captured with an on-line electrochemical mass spectrometer (OEMS), giving information on both the electrolyte and the cathode reactions upon deep lithiation, as represented in Figure 2. b.

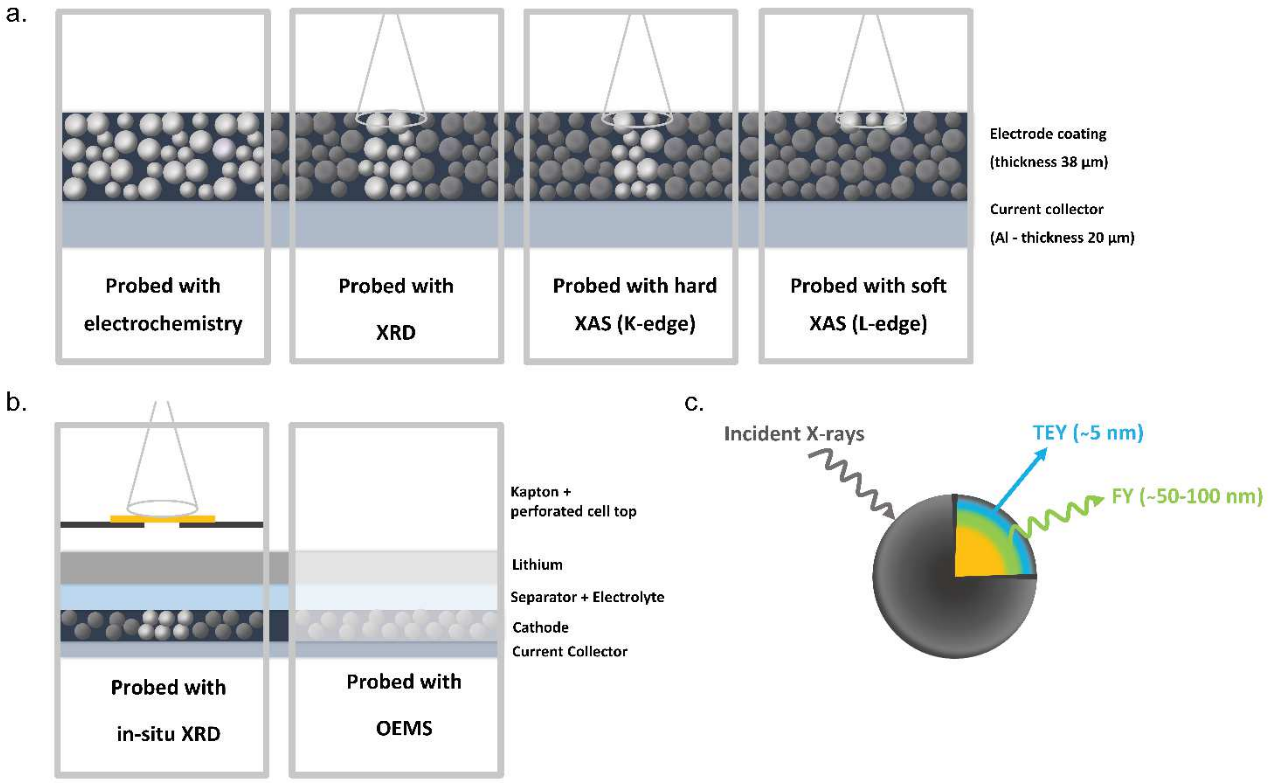

Figure 2: a. Comparison of the different depths probed by the experimental methods used on an electrode with a coating of thickness 38 µm, aluminum sheet of thickness 20 µm and secondary particles of diameter of 7–10 µm; a. Electrochemistry, XRD, hard XAS (K-edge) and soft XAS (L-edge); b. In-situ XRD in an in-situ coin cell with Katpon, operando OEMS measurement; c. Depths probed by incident soft X-ray on a single secondary particle.

Cell preparation

The positive electrodes used in this study were produced at the U.S. Department of Energy's (DOE) CAMP (Cell Analysis, Modeling and Prototyping) Facility, Argonne National Laboratory and their compositions are listed in Table 1.

Table 1: Electrodes composition

	Material	Quantity	Provenance	Coating loading
NMC111	$LiNi_{0.33}Mn_{0.33}Co_{0.33}O_2$	90 wt. %	Toda, USA	11.22 mg.cm^{-2}

	C45	5 wt. %	Timcal/Imerys Graphite & Carbon, Switzerland	
	5130 PVDF	5 wt. %	Solvay, Belgium	
NMC442	$LiNi_{0.4}Mn_{0.4}Co_{0.2}O_2$	90 wt. %	Toda, USA	11.76 mg.cm^{-2}
	C45	5 wt. %	Timcal/Imerys Graphite & Carbon, Switzerland	
	5130 PVDF	5 wt. %	Solvay, Belgium	
NMC532	$LiNi_{0.5}Mn_{0.3}Co_{0.2}O_2$	90 wt. %	Toda, USA	11.40 mg.cm^{-2}
	C45	5 wt. %	Timcal/Imerys Graphite & Carbon, Switzerland	
	5130 PVDF	5 wt. %	Solvay, Belgium	
NMC622	$LiNi_{0.6}Mn_{0.2}Co_{0.2}O_2$	90 wt. %	ECOPRO, Korea	10.03 mg.cm^{-2}
	C45	5 wt. %	Timcal/Imerys Graphite & Carbon, Switzerland	
	5130 PVDF	5 wt. %	Solvay, Belgium	
NMC811	$LiNi_{0.8}Mn_{0.1}Co_{0.1}O_2$	90 wt. %	Targray, Canada	9.12 mg.cm^{-2}
	C45	5 wt. %	Timcal/Imerys Graphite & Carbon, Switzerland	
	5130 PVDF	5 wt. %	Solvay, Belgium	

Electrochemical measurements were performed in four different setups. The setup referred to as half-cell consisted in 2032 coin cell (Hohsen, Japan) as shown in Figure 3. a. The electrodes were prepared using 14 mm diameter punch (Hohsen, Japan) and brought into the glovebox after drying overnight at 120 °C under dynamic vacuum. A 15 mm disk of lithium metal foil (99.9% purity, 500 µm, Rockwood lithium, USA) was used as the anode. Anode and cathode were separated by two layers of Celgard 2325 (Celgard, USA) with a diameter of 18 mm, which were wetted using 30 µL of electrolyte. Two spacers, both with a diameter of 15.5 mm and a respective thickness of 1 mm and 0.5 mm (Hohsen, Japan), were added to the coin cell for compression.

The setup referred to as in-situ coin cell consisted in 2032 coin cell (Hohsen, Japan) with a hole in the top layers as well as the bottom cap to allow for characterization in transmission mode upon cycling, as shown in Figure 3. b. A hole was drilled in the middle of the top and bottom cap (diameter of 2 mm) and sealed with Kapton film and epoxy glue to ensure a seal for the time of the experiments. A hole was also drilled in the middle of the two spacers to allow for measurements using X-rays in transmission mode. The building procedure follows the coin cell building procedure.

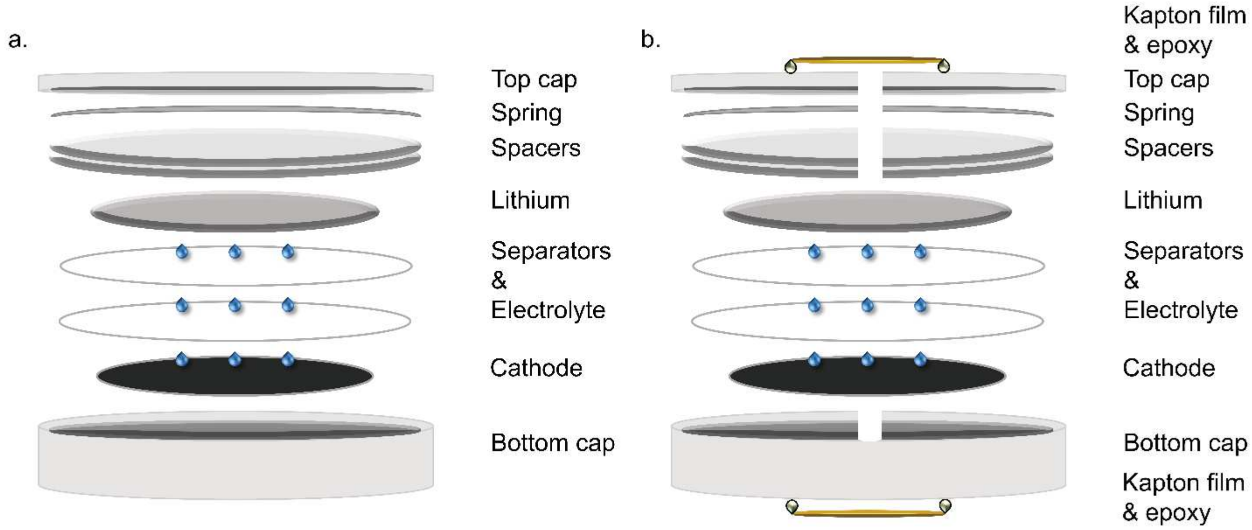

Figure 3: a. Schematic of a coin cell setup; b. Schematic of an in-situ coin cell setup

The setup referred to as El-Cell consisted of an ECC-PAT-Core El-Cell (EL-CELL, Germany) and was used to allow for quick and safe harvesting of the cathode for ex-situ XAS measurements of NMC622, in a first set of experiments. The anode was placed at the bottom of the El-cell and separated from the cathode using one layer of Celgard 2325 and one 260 µm thick glass fiber separator (ECC1- 01-0012-D/L; El-Cell, Germany), with the glass fiber separator coming into contact with the cathode. 100 µl of the electrolyte was used for each El-cell.

The setup referred to as gas analysis cell consisted of a custom design described in the work of Metzger et al.[8–10]. Two cathode materials were used for the gas analysis measurements, carbon nanofoam paper (250 µm thick, Grade II, Marketech, USA) composed of 87 wt% nanoporous carbon and 13 wt% carbon fiber with a reported BET surface area of 600 m^2/g, and a NMC622 electrode prepared in house. The NMC622 electrode was prepared by dispersing 87.99 wt% of $LiNi_{0.6}Mn_{0.2}Co_{0.2}O_2$ active material powder (NMC622, ECOPRO, Korea), 6.0 wt% conductive carbon (Super C65, Timcal, Switzerland), and 6.01 wt% polyvinylidene fluoride binder (PVDF, Sigma-Aldrich, USA) in N-methylpyrrolidone (NMP, anhydrous, 99.5%, Sigma-Aldrich, USA). The slurry was mixed in two sets of 5 min at 2000 rpm in a planetary mixer (Thinky, USA). The ink was spread on Celgard 2325 (Celgard, USA) sheet in order to allow for a better time response of the gas measurement,[10] using a gap bar coater (Elcometer 4340, United Kingdom). The electrode sheet was dried overnight at ambient conditions. The electrodes were prepared using a 17 mm diameter punch (Hohsen, Japan) and brought into the glovebox after drying overnight at 120 °C under dynamic vacuum. The loading of the active material was 15.83 $mg.cm^{-2}$. The cell stack consisted of a lithium metal disk (18 mm diameter, 500 µm thick, Rockwood lithium, USA) placed at the bottom of the cell, separated from the cathode by a Celgard 2325 disk (19 mm diameter, Celgard, USA) soaked with 100 µL of electrolyte. A stainless steel mesh was placed on top of the cathode in place of current collector to allow for gas diffusion in the cell, as represented in Figure 4. a.

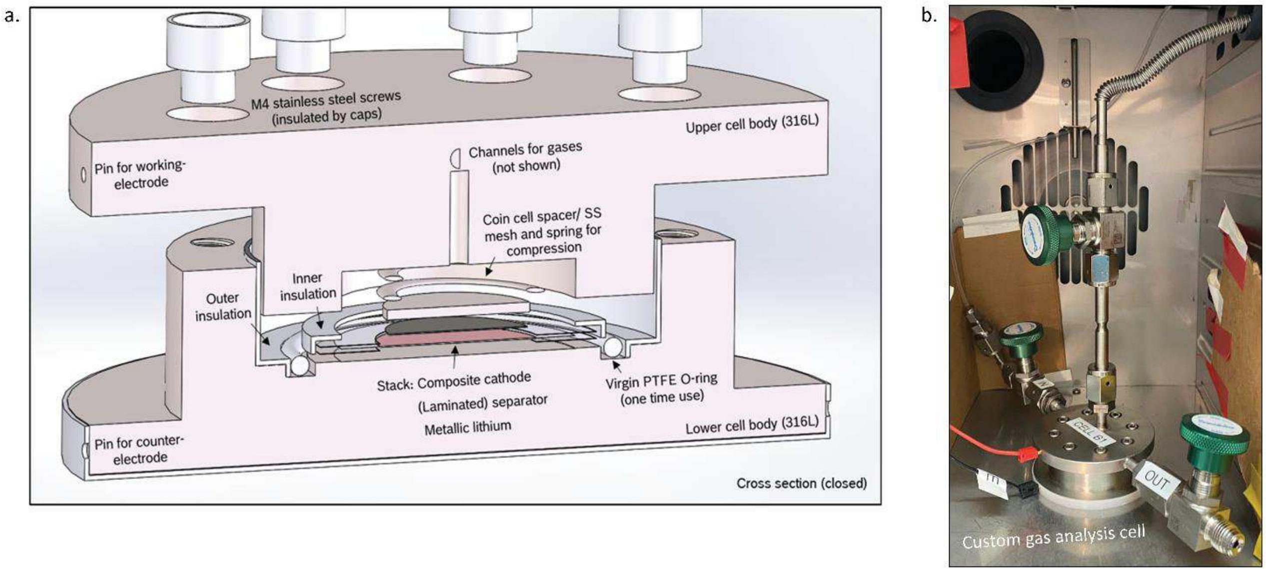

Figure 4: a. Schematic of the cross section of the custom gas analysis cell; b. Picture of the custom gas analysis cell

All the cells built for this study have been assembled inside an argon-filled glovebox (MBraun, Germany; <1 ppm H2O and <1 ppm O2). Unless specified otherwise, the electrolyte consisted of 1 M $LiPF_6$ dissolved in a 50:50 mixture (by weight) of ethylene carbonate (EC) and diethyl carbonate (DEC) (Gotion, USA). The different electrolytes used for the study of the influence of the electrolyte on the deep lithiation in chapter 3 are summarized in Table 2.

Table 2: Electrolytes used and compositions

Salt	Solvent (by weight)	Supplier
1M $LiPF_6$	EC:DEC (50:50)	Gotion, USA
1M $LiPF_6$	EC:DEC:FEC (45:45:10)	Gotion, USA
1M $LiClO_4$	EC:DEC:FEC (45:45:10)	BASF, Germany
1M $LiPF_6$	EC:EMC:DMC (30:40:30)	Gotion, USA

The different ex-situ characterization techniques were performed on harvested cathode materials. A first set of experiments was done on NMC622 cathodes harvested from El-Cells (results presented in Figure 2. 8, Figure 2. 9, Figure 2. 17, Figure 2. 19, and Figure 2. 20) and a second set of experiment was done with all NMC cathode materials harvested from coin cells (results presented in all other figures). After undergoing the desired cycling protocol, the coin cells were brought inside the glovebox and safely opened without shorting by using a coin cell disassembling tool (Hohsen, Japan). The positive electrodes were collected and washed individually in a DMC solution for at least 3 minutes in order to remove potential solid residues. The samples were dried overnight under vacuum inside the glovebox before any characterization.

Electrochemical measurements

The assembled half-cells were connected to a battery tester (Arbin, USA) and cycled in a temperature chamber (TestEquity, USA) at 25°C. The cells were left at OCV for 6-10 hours to allow sufficient wetting. The current for the lithiation and delithiation of the cells was set to a C-rate of C/10 based on about 75% of the theoretical capacity (for NMC622, 1C = 212 $mA.g^{-1}$). The cells were cycled to an upper cut-off potential V_{high} (V_{high} = 4.4 V vs Li/Li^+ for the cells containing $LiNi_aMn_bCo_cO_2$, with a < 0.8, and V_{High} = 4.3 V vs Li/Li^+ for the cells containing $LiNi_aMn_bCo_cO_2$, with a = 0.8) and discharged to different capacity-determined points. Data was collected every 30 seconds or 3 mV. Unless specified otherwise, all cells underwent a formation procedure consisting of a C/10 charge to V_{high} followed by a discharge/charge cycle between 3.0 V and V_{high} to ensure that the behavior of each cell was reproducible. The choice of V_{high} for each material was done in order to limit the side reaction in the active material with the electrolyte of choice based on the current literature understanding.[11–13] The electrochemical results shown in this report represent one set of data for each material. Several cells were prepared and underwent the same cycling protocol (at least 2 for each experiments). The in-situ coin cells and gas analysis cells were cycled on a BioLogic battery tester (BioLogic, France).

- Data processing

The data was processed with MATLAB. In order to report the gravimetric capacity of the active materials, the charge and discharge capacities (mAh) were extracted from the battery cyclers and converted to gravimetric capacity ($mAh.g^{-1}$) using the mass of the active material. Unless the cell did not undergo a formation cycle between 3.0 V and V_{high}, a correction factor was applied to the current in order to correct for the inherent current bias of each Arbin channel. The current bias was extracted by minimizing the difference in capacity at V_{high} for two consecutive cycles. The correction applied on the current was always within the calibration error of the Arbin battery cycler (< 0.05% of full-scale range of current). This current bias correction allowed reliable comparison between cells that underwent the same protocol on different channels or testers as well as comparison to literature data. The lithium content of each pristine electrode was assumed to be 1, corresponding to the theoretical capacity of the material. The gravimetric capacity scale was converted to lithium-content scale by dividing it by the theoretical capacity of the material.

X-ray diffraction (XRD)

The crystal structure of the samples was studied using X-ray diffraction (XRD) with Cu Kα radiation on a Bruker D8 ADVANCE diffractometer (Bruker, USA). The scans were collected from 10° to 70° (2Θ) at a step size of 0.05 and a rate of 3 seconds per step. The scans were interpreted using the TOPAS software.

- ### Synchrotron XRD

The in-situ XRD study was performed at beamline 2-1 at the Stanford Synchrotron Radiation Lightsource (SSRL). The measurements were done at room temperature using an in-situ coin cell previously described, allowing penetration of the incident X-ray beam in transmission mode. The XRD patterns were collected every 15 minutes during galvanostatic discharge at a current density of 21 mA.g^{-1}. To allow for better data comparison with the ex-situ XRD measurements, the 2q scale was converted to angles corresponding to the Cu Kα even though the energy used for the measurements was of 10 keV.

X-ray absorption spectroscopy (XAS)

- ### Hard XAS

The X-ray absorption spectroscopy (XAS) measurements were performed at SSRL. The changes in the oxidation state of TMs in the bulk of the material were measured with a series of hard XAS measurements at the K-edges of the elements of interest (Ni, Co, Mn). The XANES spectra result from the excitation of the metal 1s electron to a valence orbital. The quadrupole-allowed pre-edge transitions correspond to the 1s → 3d excitations, while the dipole-allowed edge transitions consist of 1s → 4p excitations. The shapes of the pre-edge and edge peaks are related to the structural environment of the element, while the position of the edge in a XANES spectrum is known to be sensitive to the oxidation state of the element, where a shift to the higher energies corresponds to an oxidation of the element and a shift to the lower energies corresponds to a reduction of the element.[14,15]

Hard XAS data for the TMs K-edge of Ni and Co were collected in transmission mode at the beam line 2-2 using a Si (220) monochromator detuned by 40% to reject higher harmonics. Mn K-edge data was collected in transmission mode at beam line 4-3 using a Si (111) monochromator with a 10% detune. Energy calibration was carried out by using the first inflection point of the spectrum of the TM foils as a reference (Ni K-edge = 8332.8 eV, Co K-edge = 7708.9 eV, and Mn K-edge = 6539.0 eV). An absolute energy shift was applied to all Mn spectra, so that the Mn^{4+} edge of the pristine material matched the Mn^{4+} edge of MnO_2 in Manceau et al.[16] The step size for measurements was 0.2 eV in the region of interest and a spot size of 1 x 8 mm was used. X-ray absorption near-edge structure (XANES) data were analyzed and normalized using SIXPACK XAS package,[17] with the photoelectron energy origin (E_0) determined by the first inflection point of the absorption edge jump.

- Soft XAS

The surface of the particles was investigated with soft XAS measurements, using both Total Electron Yield (TEY) and Fluorescence Yield (FY) modes. The measurements were executed at the L-edge of Ni, Co, and Mn, probing the electron dipole transition from the 2p core level to the 3d valence states.[18] The TEY mode detects the oxidation state of the elements in the top 5 nm of the film and the FY mode probes deeper into the bulk of the material (~ 50-100 nm).[19] The differences in the spectra obtained in TEY mode (surface) and FY mode (subsurface) or hard XAS (bulk) will provide information on which electrochemical processes are first occurring at the surface of the particles.

Ni, Mn, and Co L-edge were probed at the beamline 8-2 under ultrahigh vacuum (10^{-9} Torr) in a single aluminum sample holder at room temperature using a ring current of 500 mA, a 1100 lines per mm spherical grating monochromator, and a spot size of 1 x 1 mm. The harvested cathode samples were attached to an aluminum sample holder via conductive carbon tape in an argon-filled glovebox (MBraun, Germany; < 1 ppm H_2O and < 1 ppm O_2). The prepared aluminum holder was then packed into pouch bags and double sealed inside the glovebox prior to transport to the experimental beam line station. Transfer of the samples into the ultrahigh vacuum chamber was done with the help of a glove bag filled with argon to minimize their exposure to air. Both total electron yield (TEY) and fluorescence yield (FY) data were acquired in a single load. The baseline of the L-edge data was subtracted and the area normalized with the PyMca software[20] within the range of 633-645 eV for Mn, 771-800 eV for Co and 845-875 eV for Ni.

On-line electrochemical mass spectrometer (OEMS)

The gases evolving inside the custom-made cell hardware were measured operando using an on-line electrochemical mass spectrometer (OEMS) described in details in the work of Metzger et al.[8–10,21–24] The system consisted of the custom gas analysis cell of volume 14 mL, presented in Figure 4. b, placed in a controlled temperature chamber (KB23, Binder, Germany) held at 25°C, connected to the mass spectrometer system (Pfeiffer Vacuum, Germany) heated to 120ºC, under vacuum < 10^{-9} mbar as seen in Figure 5. The gas molecules were transported from the cell through a crimped capillary (Vacuum Technology Inc., USA) to the vacuum chamber where they were ionized by a gas-tight crossbeam ionization source with tungsten filaments. The ionized molecules were separated according to their mass-charge ratio (m/z, in the range of 1-128 amu in a quadrupole mass analyzer with a molybdenum rod system. The ions were then filtered and sent to a secondary electron multiplier detector (SEM).

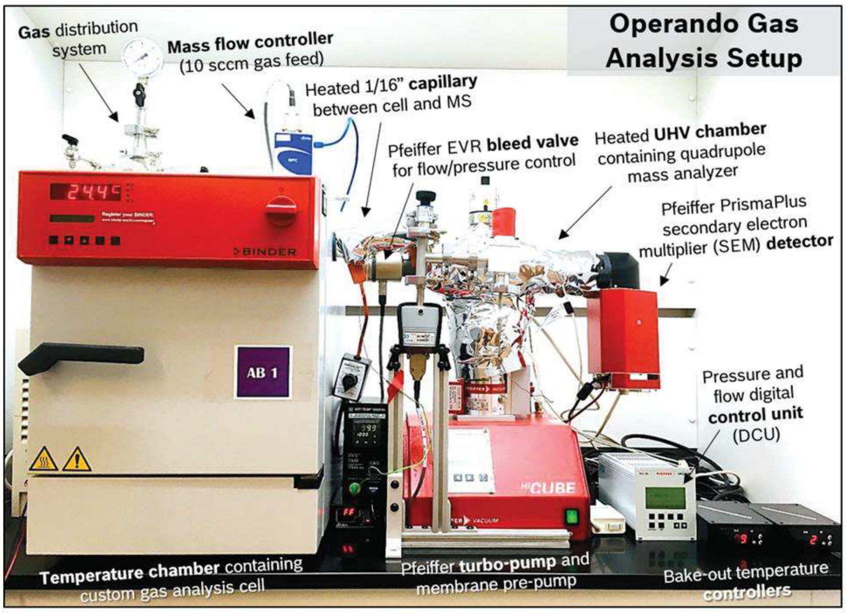

Figure 5: Picture of the OEMS setup

The OEMS system allows for a quantitative analysis of the gases evolving or being consumed inside a tight battery cell over multiple charge/discharge cycles. The gas flow rate was limited by the capillary to ≈ 1 µL/min in order to ensure a short enough response time of the gas measurement in comparison to the processes occurring inside the battery cell (< 1s compared to minutes). The custom setup ensures minor changes in the gas headspace pressure over measurements of ≈ 30 hours.

After assembly under inert atmosphere, the cell was connected to the mass spectrometer system and a potentiostat (SP-150, BioLogic, France). The cell was held at OCV for 6 hours during which the ion current signals reach a stable baseline value. After the equilibration phase, the cyclic voltammetry was done at a scan rate of 0.1 mV/s from OCV (≈ 2.5 V) to 0 V and 1.5 V vs Li/Li^+ in order to identify the potential threshold triggering gas evolution for a specific electrolyte.

- Data processing and analysis

The data is represented with the ion current signal on the y-axis and the measurement time on the x-axis. In order to eliminate the signal fluctuations due to minor pressure changes throughout the measurement, all ion currents (I_Z) are normalized to the ion current of argon (I_{36}) as it is the main gas present upon cell building. The normalized ion currents are denoted I_Z/ I_{36}. The signals measured during the equilibration phase are extrapolated to the measurement time using an exponential fit function in order to create a baseline with respect to which the signals of the gases evolving are monitored during the experiment. The signals are smoothed with a Savitzky-Golay routine. The conversion of the ion currents to concentrations can be done by using calibration gases that are purged in the cell after the measurement. The calibration is done with 2000 ppm of H_2, O_2, C_2H_4, CO, and CO_2 in argon. Additionally the concentrations of the gas evolving can be converted into absolute amounts in units (µmol) using the cell volume and the molar volume of the gases. By normalizing the data to the BET surface area of the electrode, the results can be reported in µmol/m^2.

Chapter 1: Electrochemical overlithiation of NMC cathode materials

Introduction

The omnipresence of lithium-ion batteries (LIBs) in our society has sparked significant research activity on the materials of the cathode, the anode, and the electrolyte. The requirements to improve cathode materials are a high reversible capacity, a high energy density as well as a long lifetime. In addition, the materials must satisfy the high safety and cost standards.[25–27] Layered oxides have been the state-of-the-art choice in cathode materials for many years, with $LiCoO_2$ (LCO) material being the most widely used. LCO has a high theoretical capacity of 274 $mAh.g^{-1}$ and reaches the practical capacity of ~ 140 $mAh.g^{-1}$.[4,28] The high toxicity and high cost of cobalt have driven research towards the use of different transition metals (TMs), and $LiNiO_2$ (LNO) became an attractive alternative due to its high discharge capacity and lower cost.[29] The synthesis difficulties of this material and its instability due to cation mixing between the Ni and Li ions have hindered its use in commercial batteries.[30–32] The use of spinel $LiMn_2O_4$ was motivated by the abundance and low toxicity of Mn. However, the material exhibits a low capacity of ~ 120 $mAh.g^{-1}$ and the reduction of Mn^{4+} ions, leading to Mn dissolution and deposition on the anode, is detrimental to the cycle life of the spinel $LiMn_2O_4$ cathode.[33,34]

The stability of the Ni-based layered oxide was improved by the use of ternary layered oxides with the addition of Mn, Co or Al, permitting their use in LIBs.[35] Consequently, layered cathode materials with high theoretical capacity of ~ 280 $mAh.g^{-1}$, such as $LiNi_{0.8}Co_{0.15}Al_{0.05}O_2$ (NCA) and $LiNi_aMn_bCo_cO_2$ (NMC, $a + b + c = 1$), have been implemented in electric vehicles (EVs).[36–41] Ni-rich NMC materials (with $a > b, c$) have emerged as high capacity materials with reduced cost and toxicity.[13,42–45] Because of their implementation in EVs and their promising performance, the following study is focused on NMC materials.

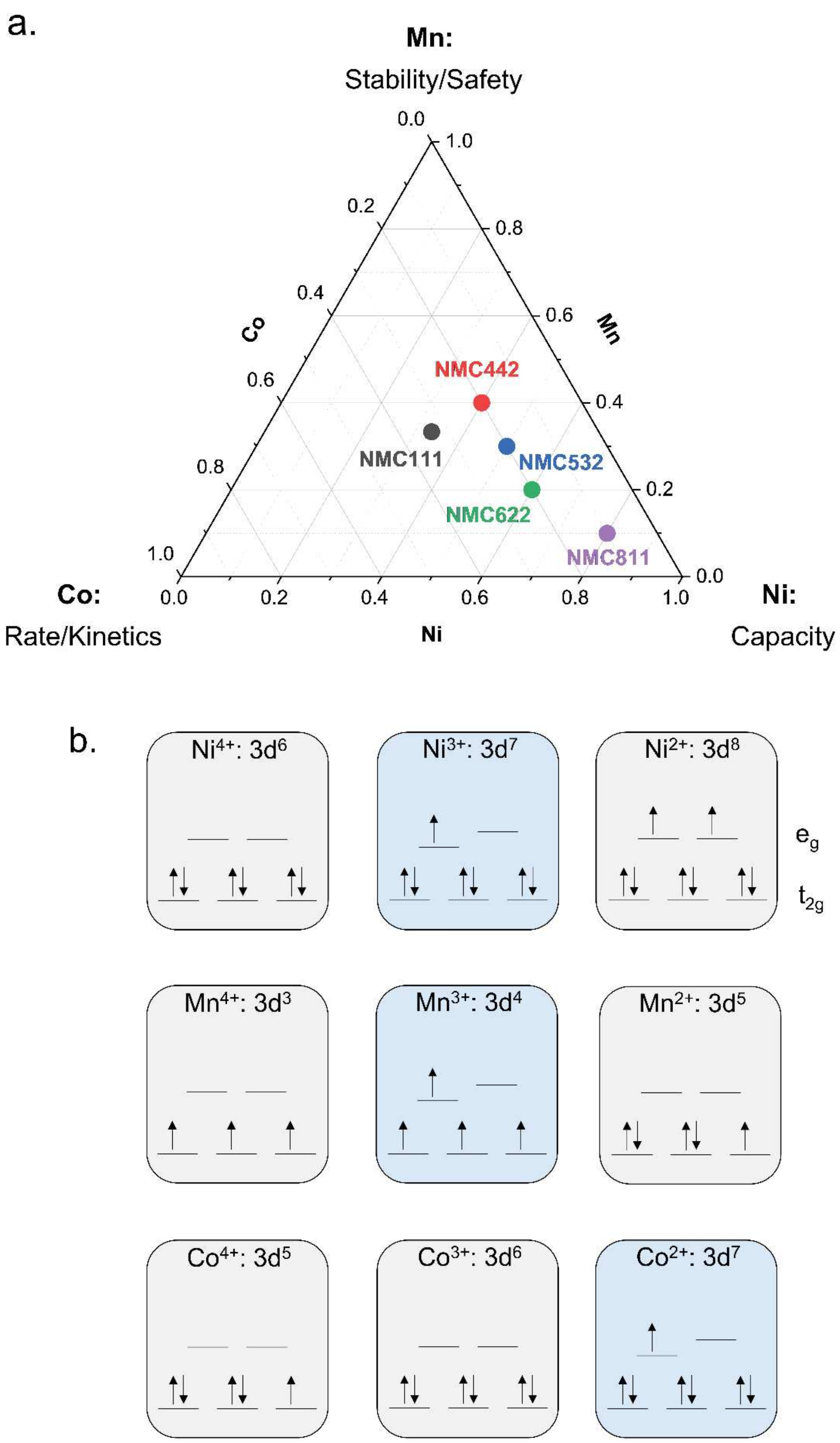

Figure 1. 1: a. Ternary diagram of the NMC materials studied with the main contribution of each transition metal; b. Typical electron configuration in layered oxides, with ions susceptible to Jahn-Teller distortion in blue. The configurations $3d^5$- $3d^6$ - $3d^7$ are shown in low spin.

In the different stoichiometry of NMC materials, each TM contributes to key features, as highlighted in Figure 1. 1. a. Ni contributes to a higher capacity of the material, Co contributes to kinetics, with impact on the cycling rate, and Mn contributes to the structural stability and the safety of the cathode material. The presence of Co was shown to reduce the disordering of the Li and TM layers by limiting the extent of cation mixing.[46] Mn, which remains in the valence state 4^+ upon cycling, also stabilizes the layered structure while Ni is the main redox active transition metal.[38] The electronic configuration of the typical states of Ni, Co and Mn in NMC materials are presented in Figure 1. 1. b. The valence state of Mn and Co in the pristine NMC materials are respectively 4^+ and 3^+.[6,47] The valence of Ni varies with the amount of Ni and Mn present in the materials, with Ni exclusively in a divalent state in pristine NMC111 and NMC442, and Ni in a mix of divalent and trivalent states in pristine Ni-rich NMCs. Upon cycling, a spontaneous symmetry breaking occurs in the presence of a single electron in the doubly degenerate e_g orbitals, as marked in blue in Figure 1. 1. b (corresponding here to the elongation of the bond to the ligand). The Jahn-Teller distortion causes one e_g level to go down in energy and the other one to go up, lowering the overall energy of the system, and inducing detrimental lattice strain.[6,48]

The standard cycling window of NMC materials is imposed by the potential of the graphite anode, resulting in a half-cell equivalent potential for the cathode ranging from 3.0 V to 4.3 – 4.5 V vs Li/Li^+.[27,42,49,50] In this classic potential window were mainly Ni is active, the typical practical capacity delivered in half-cells upon the first charge increases with increasing Ni content, with NMC111 delivering 160 $mAh.g^{-1}$ and NMC811 delivering 200 $mAh.g^{-1}$ at C/10.[42,50] A known feature of NMC materials, the capacity lost between the first charge and the subsequent discharge, varies between 10 and 15% of the practical capacity. This apparent capacity loss has been interpreted in various ways in literature. Delmas et al. justified this capacity loss as an impossibility for Li to intercalate back into the layered oxide material after a first charge because of lattice collapse. This phenomenon is thought to be due to a certain amount of divalent Ni ions being present in the Li layer ($r_{Li^+} = 0.76, r_{Ni^{2+}} = 0.69$Å) as a result of the synthesis of LNO materials.[32] The oxidation of the Ni^{2+} present in the Li layer to Ni^{3+} upon charge leads to a decrease in size ($r_{Ni^{3+}} = 0.56$Å), creating a local collapse of the lattice and hindering the Li intercalation in the cathode material. The re-intercalation of the Li in the neighboring site becomes difficult but is assumed possible at very low rate.[51,52] Arai et al. hypothesized that the observed capacity loss in Ni-based layered oxides is irreversible and due to the creation of inactive amorphous regions at high potential ($x < 0.2$ in Li_xNiO_2) upon first charge.[30] This assumption was invalidated by the demonstration of Delmas et al. that the capacity loss is still present when the first charge of the material is done up to a lower potential.[51] Kang et al, building up on the work of Mueller-Neuhaus et al,[53] attributed this apparent capacity loss to diffusion limitation due to the formation of a Li_2MO_2-like phase on the surface of the particles upon the voltage drop observed during lithiation[26,53–55] but no detailed investigation of the properties of NMC cathodes upon deep lithiation exists.

To gain insight on the structure of the industry-relevant NMC cathodes, we investigate different NMC materials in an extended potential window of 4.4 – 4.3 V to 1.6 V vs Li/Li^+ with galvanostatic cycling and confirm that the so-called irreversible capacity loss can be recovered when discharging to a lower cut-off potential. As will be presented in chapter 4, the understanding of the potential Li_2MO_2-like phase formed at the surface of the particles is critical to the parameterization of the advanced battery management system (ABMS). In order to study this phase in NMC materials, we decrease the potential further down to 0.8 V vs Li/Li^+ in an attempt to extend the formation of this phase to the bulk of the material. We observe that by a deep lithiation of NMC electrodes, we can access more than 500 $mAh.g^{-1}$, suggesting the accommodation of about two Li ions per structure. Finally the reversibility of these deep lithiations is investigated upon delithiation back to 4.4 – 4.3 V vs Li/Li^+ and compared across different cathodes of the NMC family.

1. Electrochemical study of NMC materials in the classic potential window

We begin electrochemical characterization of NMC electrodes by examining a well-recognized feature of Ni-containing cathode materials: the first cycle capacity loss.[27,42,56–58] We do so by characterizing the electrodes at a C-rate of C/10 in a conventional window of 3.0 V to V_{high}. The materials $LiNi_{0.33}Mn_{0.33}Co_{0.33}O_2$ (NMC111), $LiNi_{0.4}Mn_{0.4}Co_{0.2}O_2$ (NMC442), $LiNi_{0.5}Mn_{0.3}Co_{0.2}O_2$ (NMC532), $LiNi_{0.6}Mn_{0.2}Co_{0.2}O_2$ (NMC622), and $LiNi_{0.8}Mn_{0.1}Co_{0.1}O_2$ (NMC811) are presented in Figure 1. 2, with the first charge from open-circuit potential (OCP) to V_{high} in a dotted line, and the following cycle between V_{high} and 3.0 V in a dashed line. The upper voltage cut-off V_{high} is chosen as the potential at which the cathode degradation is minimized, based on the current understanding in literature, with $V_{high} = 4.4$ V vs Li/Li^+ for NMC materials with a Ni content below 0.8 ($a < 0.8$ in $LiNi_aMn_bCo_cO_2$), and $V_{high} = 4.3$ V vs Li/Li^+ for NMC materials with a Ni content of 0.8 ($a = 0.8$ in $LiNi_aMn_bCo_cO_2$).[11–13] The Li content x in $Li_xNi_aMn_bCo_cO_2$ ($a+b+c = 1$, $a \geq b$) is calculated by coulomb counting, assuming that the pristine electrode is fully lithiated. (Table SI. 1)

As seen in Figure 1. 2 and summarized in Table 1. 1, upon the first delithiation from the OCV to V_{high}, the electrodes deliver a capacity ranging from 184 to 227 $mAh.g^{-1}$. The capacity accessed upon the first charge increases with increasing Ni content. During relithiation to 3.0 V vs Li/Li^+, the electrodes recover from 168 to 198 $mAh.g^{-1}$, which corresponds to a first-cycle coulombic efficiency (CE) ranging from 87 to 91 %, in line with the literature reports summarized in Table 1. 2.[54,58,59] As listed in Table 1. 1, the CE tends to decrease with the increase of Ni content, with a high CE for NMC111 of 91.2% and a lower CE of 87.5% for NMC811.

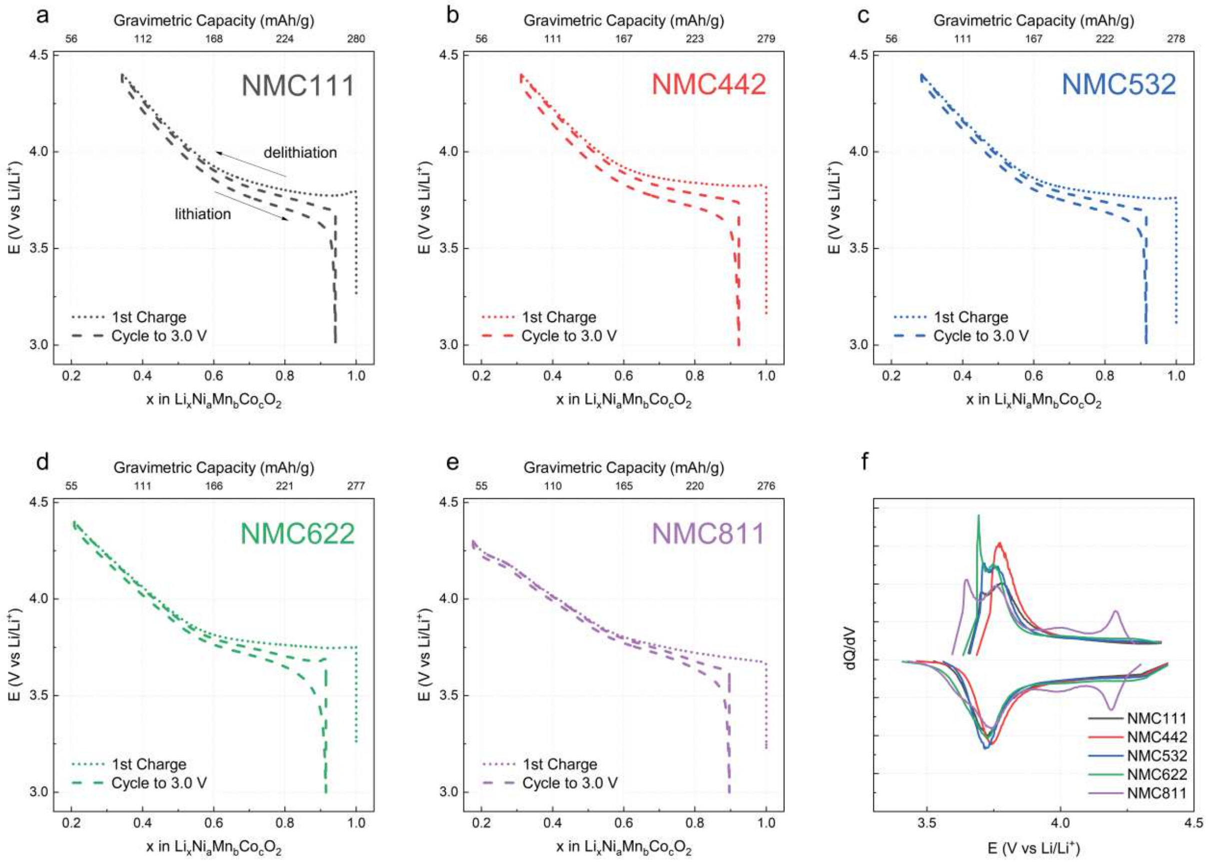

Figure 1. 2: Lithiation/delithiation profile of $LiNi_aMn_bCo_cO_2$, with $a+b+c = 1$, $a \geq b$, 1M $LiPF_6$ in EC:DEC 50:50 half-cells cycled at 0.1C at 25ºC to V_{high} (dotted line) and subsequent cycle between 3.0 V and V_{high} (dashed line) with a 30 min rest between lithiation and delithiation; a. NMC111 (V_{high} = 4.4 V); b. NMC442 (V_{high} = 4.4 V); c. NMC532 (V_{high} = 4.4 V); d. NMC622 (V_{high} = 4.4 V); e. NMC811 (V_{high} = 4.3 V); f. dQ/dV vs V summary of NMC materials - cycle to 3.0 V. A loss of capacity of 10-15% is observed after the first delithiation.

Table 1. 1: Capacity reached upon first delithiation and subsequent lithiation between V_{high} and 3.0 V and corresponding coulombic efficiency

Cathode material	Capacity reached upon the 1st delithiation to V_{high} ($mAh.g^{-1}$)	Capacity reached upon the 1st lithiation to 3.0 V ($mAh.g^{-1}$)	1st Cycle CE (%)
NMC111	183.76	167.51	91.2
NMC442	191.89	170.54	88.9
NMC532	198.58	175.21	88.2
NMC622	210.23	188.95	89.9
NMC811	226.97	198.51	87.5

2. Regain of the first cycle capacity loss

As presented in Figure 1. 3, at a low rate of C/10, lowering the cut-off potential from 3.0 V to 1.8 – 1.1 V vs Li/Li$^+$ allows for a complete recovery of the initial capacity of the first delithiation for each NMC material. The observed necessity to decrease the lower cut-off potential to recover the lost capacity without reducing the applied current is also consistent with a previous study focusing on LNO.[56] Furthermore, several other publications, which have characterized the first cycle capacity loss of Ni-containing electrodes including $LiNi_{1-y}Fe_yO_2$, NMC111, NMC532, and NCA, have shown that the potential needed to recover the first cycle capacity loss is C-rate dependent and can vary from 3.0 V to 1.0 V vs Li/Li$^+$, depending on the magnitude of the applied current and the type of the cathode material.[53,54,61,62] Weber et al. demonstrated the possibility to recover the capacity lost in NMC532 by holding the potential at 3.0 V vs Li/Li$^+$.[62] The potential needed to recover 100% of the initial charge capacity for various materials is summarized in Table 1. 2.

Table 1. 2: First cycle coulombic efficiency and recovery potential of the initial charge capacity of different cathode materials

Cathode type	1st cycle CE (to 3.0 V)	Recovery	References
$LiNiO_2$	92% @ C/40	~2.0 V	Dahn 1990[60]
$LiNi_{1-y}Fe_yO_2$	83% @ C/50	~1.9 V	Mueller-Neuhaus 2000[53]
$LiNi_{0.33}Co_{0.33}Mn_{0.33}O_2$	89% @ 8 mA/g	1.47 V	Kang 2008[54]
$LiNi_{0.33}Co_{0.33}Mn_{0.33}O_2$	91% @ C/10	1.38 V	This work
$LiNi_{0.4}Mn_{0.4}Co_{0.2}O_2$	82% @ C/20	Not studied	Li 2015[63]
$LiNi_{0.4}Mn_{0.4}Co_{0.2}O_2$	89% @ C/10	1.13 V	This work
$LiNi_{0.5}Mn_{0.3}Co_{0.2}O_2$	89% @ C/50	Hold at 3.0 V	Weber 2017[62]
$LiNi_{0.5}Mn_{0.3}Co_{0.2}O_2$	88% @ C/10	1.58 V	This work
$LiNi_{0.6}Mn_{0.2}Co_{0.2}O_2$	90% @ C/20	Not studied	Arumugam 2016[56]
$LiNi_{0.6}Mn_{0.2}Co_{0.2}O_2$	89% @ C/10	1.60 V	This work
$LiNi_{0.8}Mn_{0.1}Co_{0.1}O_2$	91% @C/20	Not studied	Li 2015[64]
$LiNi_{0.8}Co_{0.15}Al_{0.05}O_2$	87% @ 8 mA/g	1.81 V	Kang 2008[54]
$LiNi_{0.8}Co_{0.15}Al_{0.05}O_2$	87% @ C/10	1.79 V	This work
$LiCoO_2$	98% @ 8 mA/g	1.17 V	Kang 2008[54]

Our results are in line with the interpretation of Mueller-Neuhaus et al. that the term "irreversible capacity loss" is a misnomer and that the capacity accessed upon the first charge can be accessed upon different conditions.[53] The possible collapse of the lattice upon the first charge due to the presence of divalent Ni ions in the Li layer is not investigated in details in our experiments.

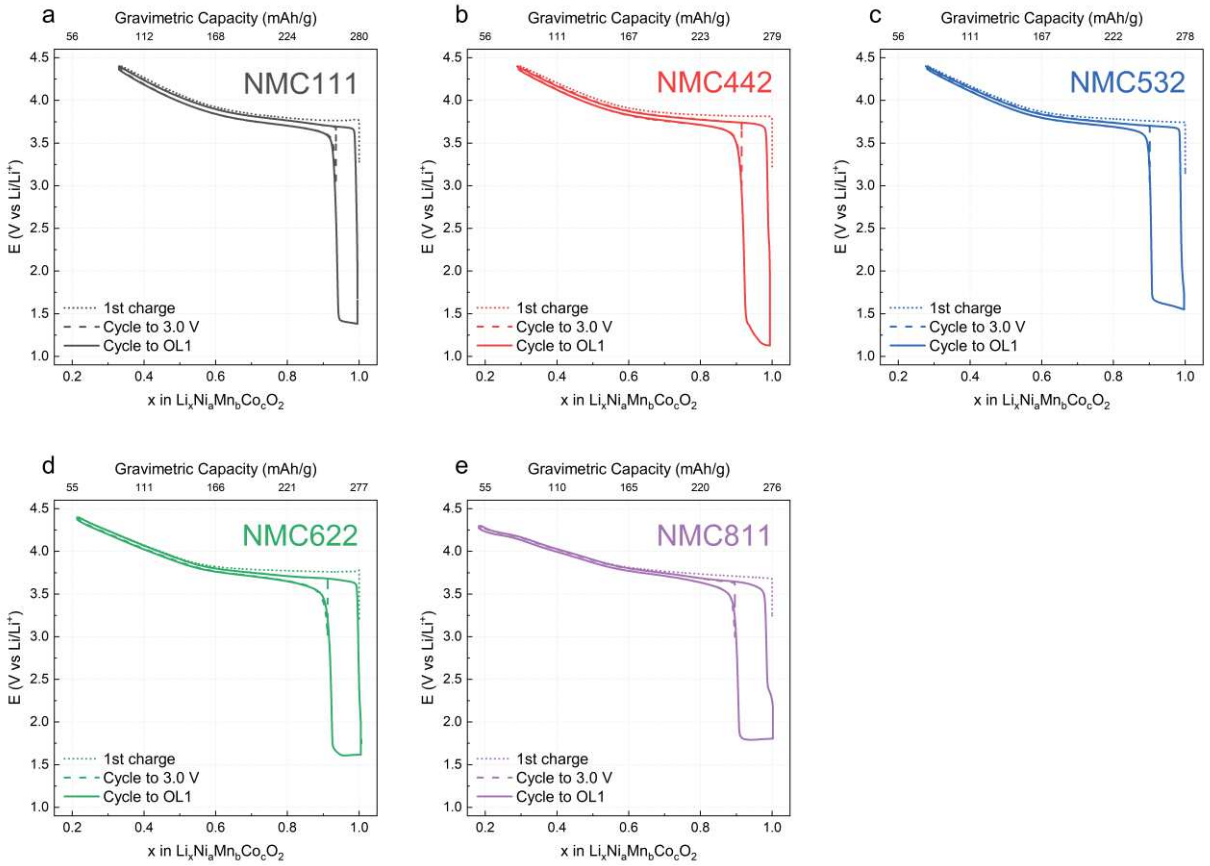

Figure 1. 3: Lithiation/delithiation profile of $LiNi_aMn_bCo_cO_2$, with $a+b+c = 1$, $a \geq b$, 1M $LiPF_6$ in EC:DEC 50:50 half-cells cycled at 0.1C at 25°C to V_{high} (dotted line), cycle to 3.0 V (dashed line), and cycle to xLi = 1 (called OL1) with subsequent delithiation to V_{high} with a 30 min rest between lithiation and delithiation; a. NMC111 (V_{high} = 4.4 V); b. NMC442 (V_{high} = 4.4 V); c. NMC532 (V_{high} = 4.4 V); d. NMC622 (V_{high} = 4.4 V); e. NMC811 (V_{high} = 4.3 V); We observe a regain of the initial capacity by lowering the potential to ~1.4 – 1.8 V vs Li/Li$^+$.

Recovery of the first cycle capacity loss by decreasing the lower cut-off potential below 2.0 V vs Li/Li$^+$, as was done in Figure 1. 3 with NMC electrodes, triggers the apparition of a plateau in the lithiation profile. This plateau is expected to correspond to a two-phase coexistence region.[65,66] The potential of this plateau at C/10 is different for each NMC stoichiometry, ranging from 1.1 V to 1.7 V vs Li/Li$^+$, and is summarized in Table 1. 3. The potential at which this plateau appears for each NMC is clearly visible in the differential capacity plot in Figure 1. 4, where the plateaus appear as sharp horizontal peaks.

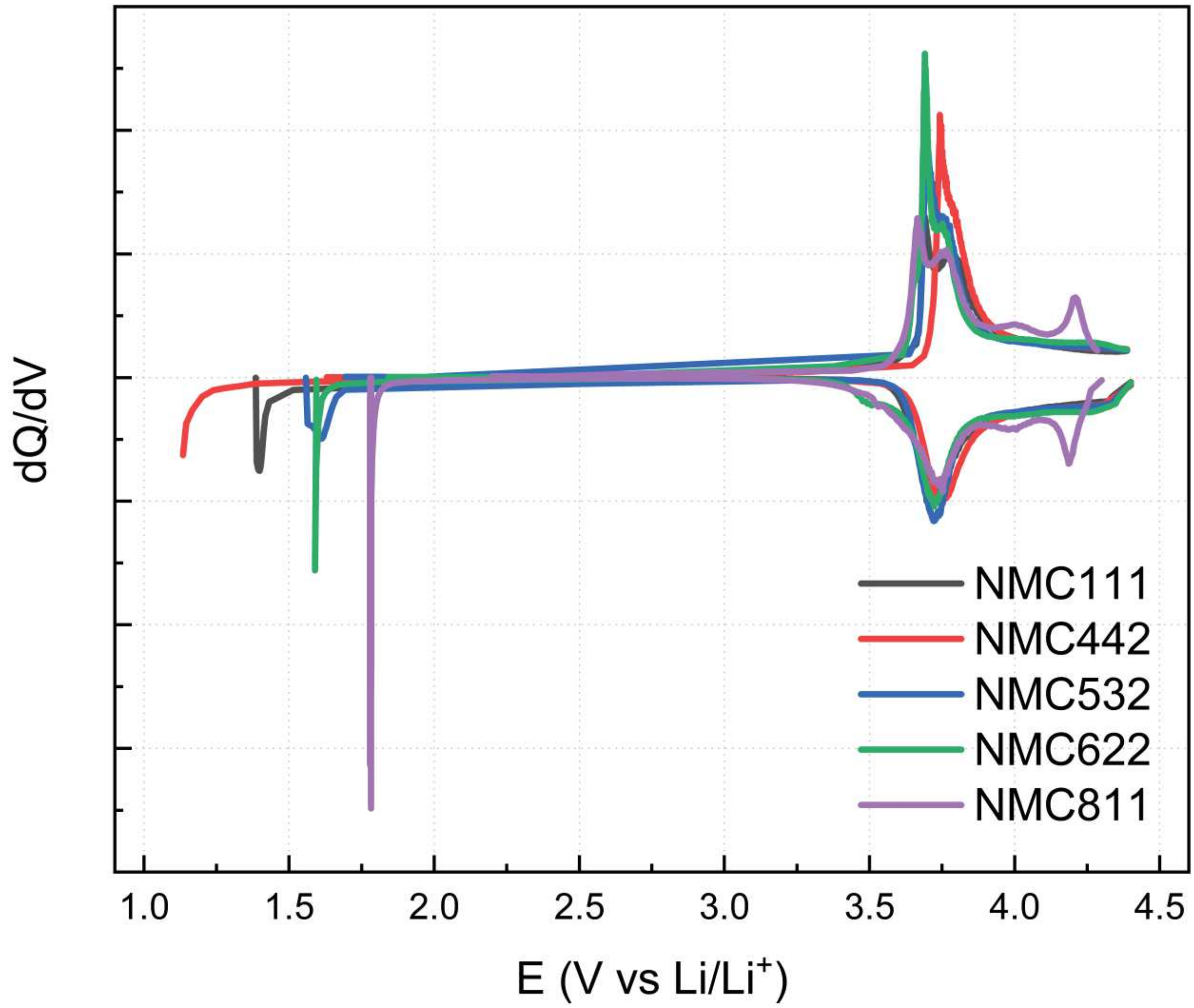

Figure 1. 4: dQdV vs V of lithiation to xLi = 1 and subsequent delithiation to V_{high} for all NMC cathodes

As presented in the work of Dahn et al. on LNO[60] and Johnson et al. on different Ni-based layered oxides,[67,68] the extra capacity accessed upon lithiation of the NMC cathodes to xLi = 1 is assumed to be due to the formation of a Li-rich layer at the surface of the particles. The sharp voltage drop and the transition to a two-phase plateau is understood as a change of mobility of the Li ions in the intercalation host, as described by Van der Ven et al.[69] They proposed a model for the intercalation of Li ions in LCO showing that Li ions can either directly hop through octahedral sites – process called monovacancy hopping, or hop through an adjacent tetrahedral site – process called divacancy hopping. The simulations and calculations of activation barriers suggest that the divacancy hopping path is favored as long as enough vacancies are available. The potential drop observed below ~ 3 V vs Li/Li^+ is triggered by an accumulation of Li at the surface of the particles, filling enough sites to prevent divacancy hopping. Li insertion at the surface of the particle is then done through monovacancy hopping, as depicted in Figure 1. 5, requiring a much bigger activation energy leading to a lower diffusivity of the Li. The transition between the divacancy hopping regime and the monovacancy hopping regime is dependent on kinetics and is expected to occur at xLi = 1 at infinitely slow C-rate, as depicted in Figure 1. 5. After the transition to the monovacancy hopping regime, a Li-rich phase is formed on the surface of the particles leading to a two-phase lithiation plateau.

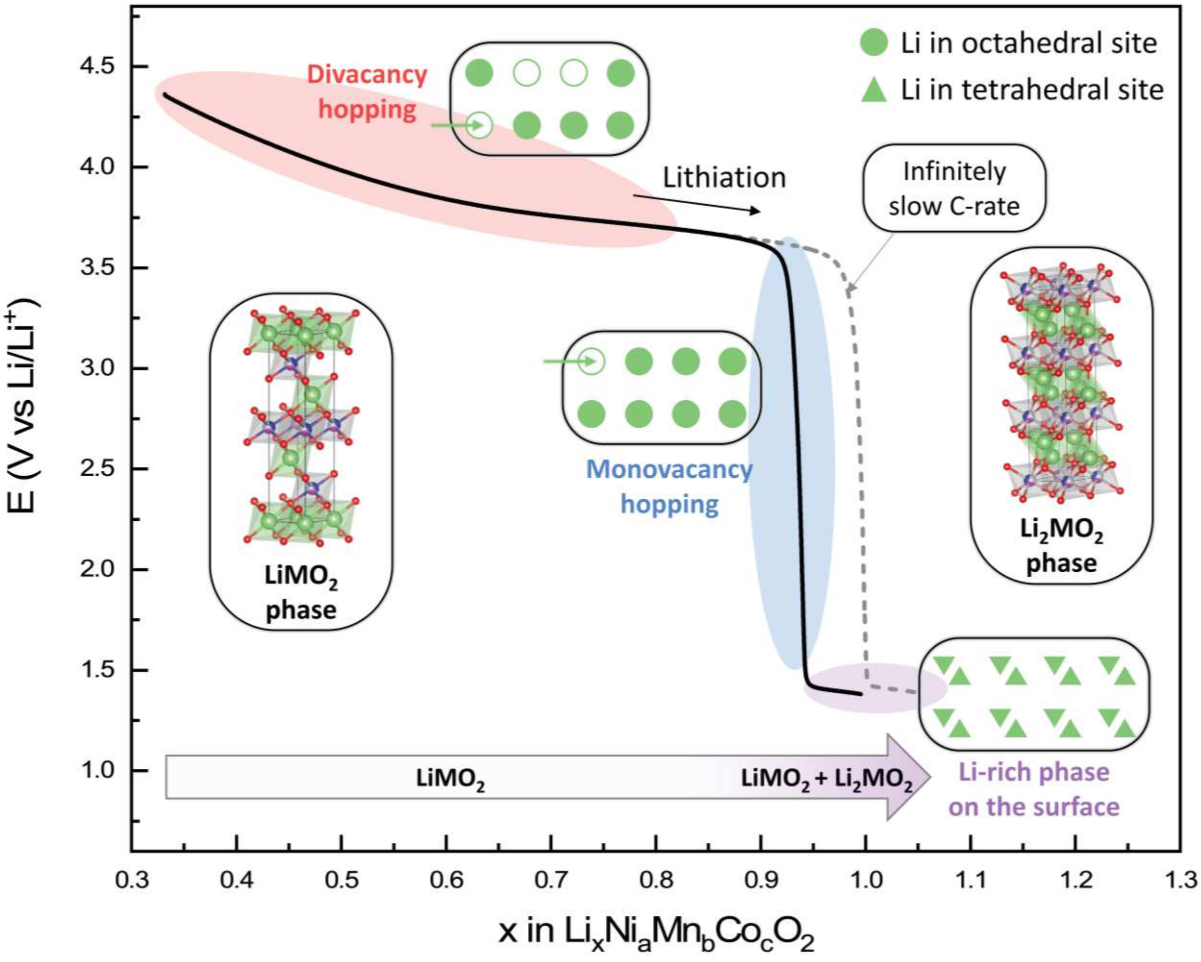

Figure 1. 5: Schematic of the different vacancy hopping regimes upon Li insertion during lithiation in $LiMO_2$ *(M = Ni, Mn, Co, and or Al) materials and formation of a Li-rich* Li_2MO_2*-like surface phase; Li ions in green, TM ions in blue, and O ions in red. The transition from divacancy hopping to monovacancy hopping leads to a voltage drop due to slower Li diffusion. If Li ion are continuously inserted in the material in the monovacancy hopping regime, a Li-rich phase forms on the surface of the particles leading to Li in tetrahedral sites in the Li slab.*

In Figure 1. 4, we observe that higher Ni content leads to higher potential for the lithiation plateau. From the TMs involved in the reduction in the classic potential window, we expect Ni to be reduced at such potentials.[6] This hypothesis is supported by the ~1.8 V vs Li/Li^+ plateau observed by Dahn et al. upon deep lithiation of LNO.[60] The oxidation state of Ni in the pristine electrodes is calculated in Table 1. 3 from a pristine material with Co^{3+} and Mn^{4+}. Two categories can be identified within the NMC electrodes: the NMCs with a Ni:Mn ratio equal to 1 (NMC111 and NMC442), and the Ni-rich NMCs where Ni > Mn, Co. The 'Ni = Mn' NMCs only have divalent Ni in the pristine material. Ni-rich NMCs have a mix of divalent and trivalent Ni, leading to an increase in the valence of Ni with the increase of Ni present in the electrode. The higher potential observed for the plateau of NMC811 indicates that the redox-active energy level of the TM involved along the NMC811 plateau is at a higher energy level than for the other NMC cathodes, which correlates with the abundance of trivalent Ni in the material.[6]

The potential of the plateau observed upon lithiation to xLi = 1 for NMC442 is higher than that of NMC111. Because from the theoretical calculations both pristine cathodes contain only divalent Ni, the potential of the plateau would be expected to be similar. NMC111 is known to have a higher amount of disordering in the structure that could lower the Li diffusion due to Ni atoms in the Li slab, and justify the difference in potential threshold observed for the apparition of the plateau.[61,70,71] The valence of Ni in NMC111 will be investigated with characterization techniques in chapter 2.

Table 1. 3: Oxidation state of Ni in the pristine material based on a pristine material with Co^{3+} and Mn^{4+}, proportion of Ni^{2+}/Ni^{3+}, and potential of apparition of the first plateau upon deep lithiation to xLi = 1.

Cathode material	Ni oxidation state in pristine material	Ratio		Potential of plateau #1
		Ni^{2+}	Ni^{3+}	
NMC111	+2	0.33	0	1.38 V
NMC442	+2	0.4	0	1.13 V
NMC532	+2.4	0.3	0.2	1.58 V
NMC622	+2.66	0.2	0.4	1.60 V
NMC811	+2.875	0.1	0.7	1.79 V

After lithiation to xLi = 1, the subsequent delithiation back to V_{high} presents a sharp transition from the low potential to ~ 2.25 V vs Li/Li^+, where a kink can be observed, followed by a second sharp potential increase to ~ 3.5 V vs Li/Li^+, where the Li deintercalation leads to a rapid voltage change. A third regime above ~ 3.5 V vs Li/Li^+ follows the same profile as the delithiation in the classic potential window, indicating that the NMC structure is intact after lithiation to xLi = 1 (See comparison of delithiation curves in dQ/dV vs V plot in Figure SI. 2 in appendix section).

The delithiation profile of NMC811 presents the particularity of having a more significant kink upon delithiation at ~2.25 V vs Li/Li^+ than the other NMC cathodes. The two-phase equilibrium of a NMC particle lithiated to OL1 is depicted in Figure 1. 6 through a scheme of a cross section of a NMC particle. From the different intercalation regimes presented in Figure 1. 5, we expect a Li gradient in Li_2MO_2 phase at the surface of the particle. We assume that the Li diffusion in the Li_2MO_2 phase (purple) is comparable with the Li diffusion in the divacancy hopping regime of the $LiMO_2$ phase (red), leading to the Li diffusion in the monovacancy hopping regime being the rate-limiting step. From this interpretation, we can exemplify a bigger Li gradient in the Li_2MO_2 phase at the surface of the particle than the Li gradient in the subsurface and bulk of the particle in the $LiMO_2$ phase. Upon current interruption after infinite time, we expect a relaxation of both gradients towards a homogenous, fully lithiated $LiMO_2$ phase. The presence of the kink in the potential profile upon delithiation suggests an incomplete relaxation of the surface gradient in the Li_2MO_2 phase, leading to a two-phase coexistence upon the 30 min relaxation period in this cycling protocol,[54] as depicted for the particle at xLi = 1 after relaxation. To support this hypothesis, a second NMC811 half-cell was cycled with the same protocol with the difference of a 10 hours rest period after lithiation to OL1. The results presented in the appendix section in Figure SI. 3 highlight the diminution of this low voltage kink in the delithiation profile, supporting the hypothesis of the gradual disappearance of a Li gradient in the Li_2MO_2 phase at the surface of the particles upon current interruption, as depicted in blue in Figure 1. 6. The study of the Li diffusion in the Li_2MO_2 phase to validate our assumptions could lead to a detailed investigation in a follow up work, using galvanostatic intermittent titration technique (GITT) measurements. The predominance of this kink in the NMC811 cathode suggests that the Li diffusion in monovacancy hopping regime is dependent on the NMC composition. A higher degree of cation mixing in the NMC811 material could lead to a lower Li diffusion in this regime. No irreversibility is observed for one cycle for the

NMC materials upon delithiation back to V_{high} after deep lithiation to xLi = 1 (OL1), suggesting no apparent side reactions (CE ≥ 99%). The difference in kinetics observed for NMC811 suggests that irreversibility may arise in this Ni-rich material upon several overlithiation cycles.

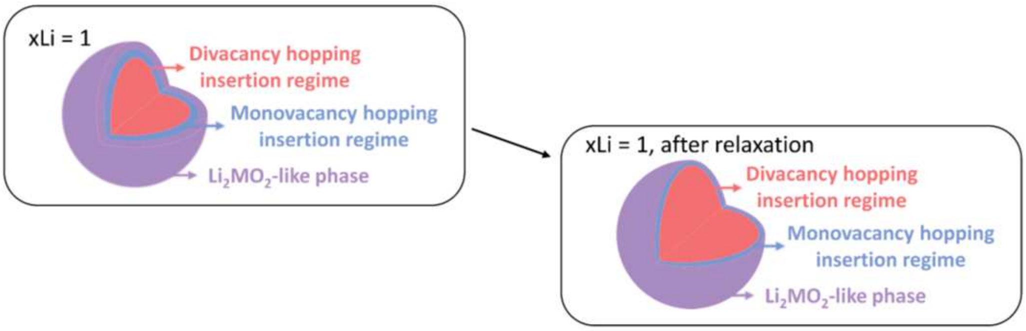

Figure 1. 6: Schematic of a cross section of a NMC particle at different states of lithiation. When xLi = 1, the Li_2 surface phase (purple) presents a gradient that relaxes upon current interruption as Li diffuses towards the bulk, decreasing the proportion of Li_2 phase in the particle. The relaxation gradient of the Li_2 phase is assumed to be limited by the diffusion in the monovacancy hopping regime (blue) in the $LiMO_2$ phase (red), leading to a kink in the potential upon delithiation particularly visible for NMC811

The suspected reversibility of this overlithiation process to xLi = 1 is investigated over several cycles for NMC622, and the cycling profile of the first 5 overlithiation cycles is presented in Figure 1. 7. a. The capacity upon lithiation is based on coulomb counting to match the previous delithiation capacity and the delithiation is voltage controled to V_{high} = 4.4 V vs Li/Li^+. A “walking” of the cycles towards the right can be observed in the cycling, possibly due to some capacity reached upon lithiation not being recovered upon delithiation.[72] The delithiation capacity vs cycle number of the NMC622 half-cell is plotted in Figure 1. 7. b, highlighting the increase in lithiation capacity and the capability of the cell to cycle to OL1 for ~ 40 cycle before deteriorating. The relative reversibility of this overlithiation over an extended amount of cycles will be investigated with characterization techniques.

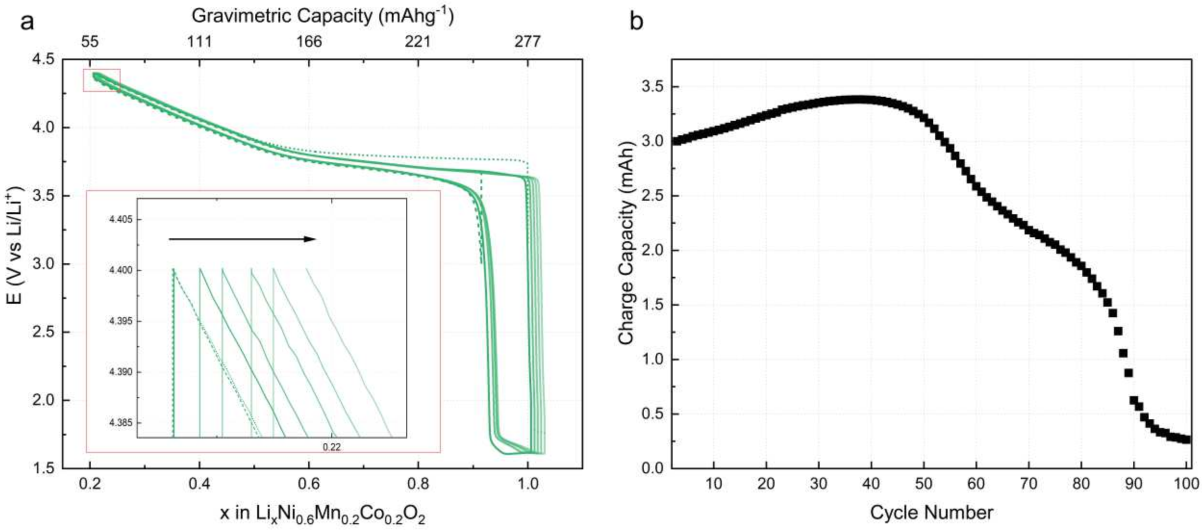

Figure 1. 7: a. Lithiation/delithiation profile of NMC622, 1M $LiPF_6$ in EC:DEC 50:50 half-cell cycled at 25ºC at 0.1C; 1st charge to V_{high} (dotted line), cycle to 3.0 V (dashed line), and cycles to xLi = 1 (called OL1) with subsequent delithiations to V_{high}; b. Charge capacity vs cycle number. The lithiation of NMC622 to xLi = 1 can be sustained for ~ 40 cycles.

In an attempt to characterize and understand the suspected Li_2MO_2 phase formed at the surface of the particles, the lithiation of the NMC cathodes is continued at lower potentials in order to extend the formation of an overlithiated phase into the bulk of the particles.

3. Deep lithiation to lithium content above xLi = 1

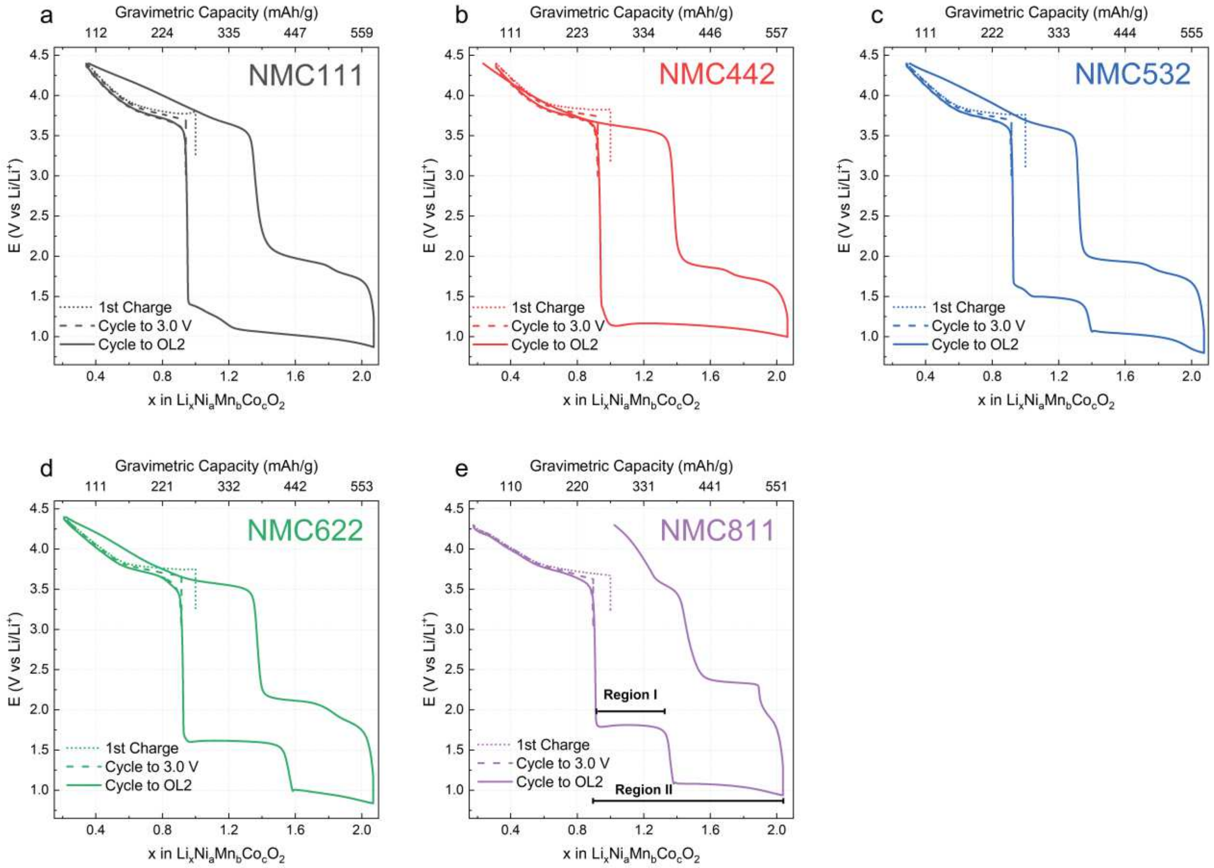

Figure 1. 8: Lithiation/delithiation profile of $LiNi_aMn_bCo_cO_2$, with a+b+c = 1, a ≥ b, 1M $LiPF_6$ in EC:DEC 50:50 half-cells cycled at 0.1C at 25°C to V_{high} (dotted line)), cycle to 3.0 V (dashed line), and cycle to xLi = 2 (called OL2) with subsequent delithiation to V_{high} with a 30 min rest between lithiation and delithiation; a. NMC111 (V_{high} = 4.4 V); b. NMC442 (V_{high} = 4.4 V); c. NMC532 (V_{high} = 4.4 V); d. NMC622 (V_{high} = 4.4 V); e. NMC811 (V_{high} = 4.3 V). The "Ni = Mn" NMCs present one low voltage plateau and the Ni-rich NMCs present two clear plateaus. About 315 mAh.g^{-1} extra capacity is accessed upon lithiation to xLi = 2 with various degrees of reversibility.

For LNO and $LiMn_{0.5}Ni_{0.5}O_2$ cathodes, it has been demonstrated that it is possible to extend the formation of the Li_2MO_2 phase beyond the surface and into the bulk of the particles for at least one cycle.[60,67,68] To determine if cathode materials from the NMC family are also capable of forming bulk Li_2MO_2 phase, we lowered the cut-off potential of different NMC electrodes until enough coulombs could be passed to reach a Li ion stoichiometry of ~2. Figure 1. 8 shows the resulting lithiation/delithiation profiles of NMC electrodes, after they were characterized between V_{high} and ~ 0.8 V vs Li/Li$^+$. The extended cycle allows NMC materials to access an additional ~ 315 mAh.g^{-1} of gravimetric capacity, detailed in Table 1. 4, which corresponds to xLi ~ 2.06 (see assumptions and calculation in appendix section Table SI. 1).

Table 1. 4: Capacity accessed in the classic potential window compared to the capacity accessed along the first plateau, extra capacity accessed upon deep lithiation to OL2 (xLi = 2)

Cathode material	Capacity accessed in the classic potential window ($mAh.g^{-1}$)	Capacity accessed along 1st plateau – region I ($mAh.g^{-1}$)	Capacity accessed up to OL2 ($mAh.g^{-1}$)	Total extra capacity – region 2 ($mAh.g^{-1}$)
NMC111	167.51	-	483.56	316.05
NMC442	170.54	-	488.55	318.02
NMC532	175.21	104.52	496.60	321.39
NMC622	188.95	149.92	505.69	316.74
NMC811	198.51	98.72	512.93	314.42

We note that the decrease in the lower cut-off potential to ~ 0.8 V vs Li/Li^+ introduces interesting features to the lithiation/delithiation curves. In Figure 1. 9 we observe that the "Ni = Mn" cathodes present one low potential lithiation plateau whereas the Ni-rich NMCs present two clear plateaus at approximately 1.6 V and 1.0 V vs Li/Li^+, and a third plateau initiated at approximately 0.8 V vs Li/Li^+. The potentials at which each plateau appear are listed in Table 1. 4. The capacity accessed along the first plateau (Region I) for Ni-rich NMCs is listed in Table 1. 4. In agreement with the observations made on LNO, we hypothesize that the capacity accessed along the first plateau is a result from the reduction of Ni^{3+} to Ni^{2+}.[60]

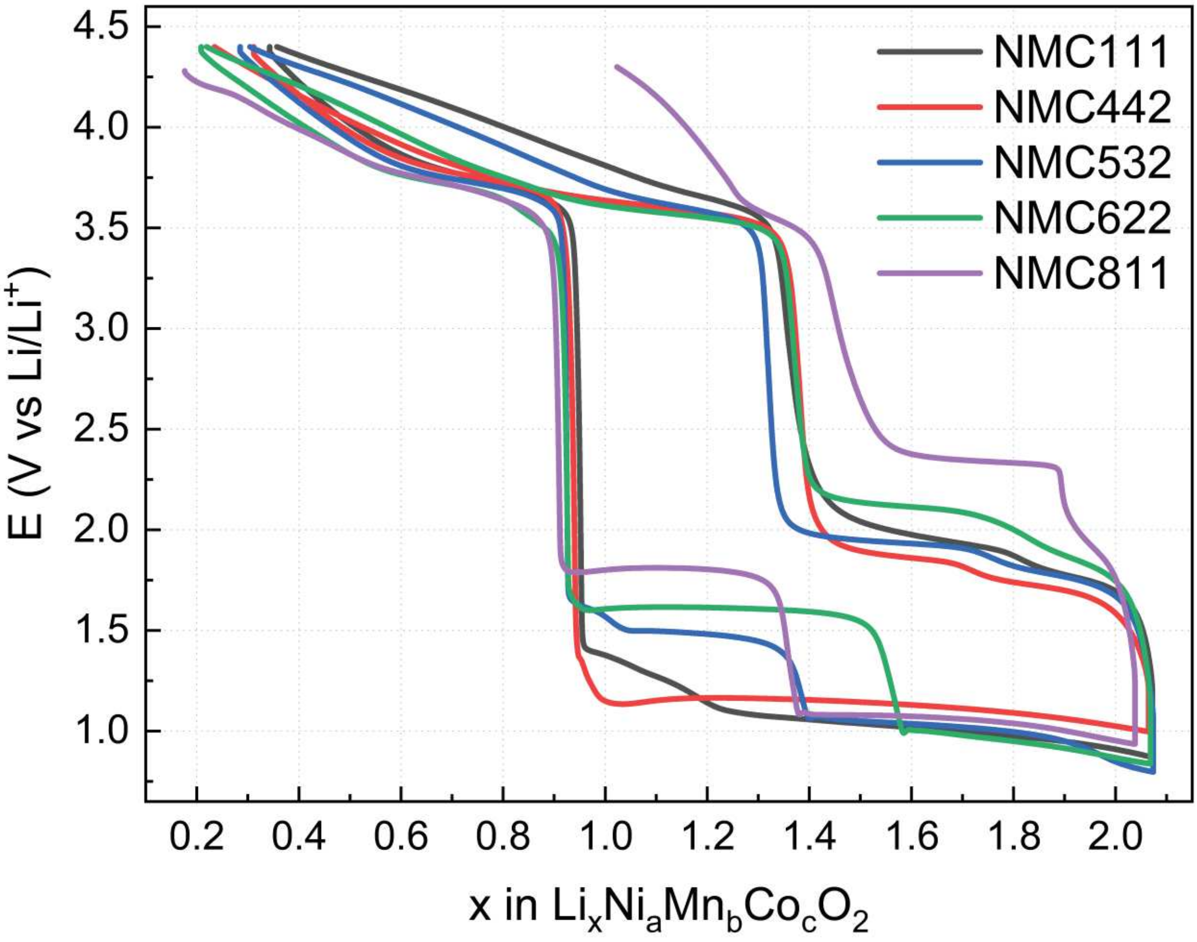

Figure 1. 9: Lithiation/delithiation profile of NMC111, NMC442, NMC532, NMC622, and NMC811 1M $LiPF_6$ *in EC:DEC 50:50 half-cells at 0.1C to xLi = 2 (OL2) and subsequent delithiation to* V_{high}*. The potential of the plateaus is compared, highlighting that the potential of the plateau increases with increasing Ni content for Ni-rich materials.*

To elucidate the origin of the extra capacity observed, we start by calculating the amount of capacity that would result from the reduction of the trivalent Ni ions present in the Ni-rich NMCs. The amount of capacity associated with the valence change of Ni ions to the oxidation state 2^+ is presented in Table 1. 5. The valence change from the pristine to Ni^{2+} is expressed in capacity (coulombs converted to $mAh.g^{-1}$) by dividing the moles of electrons (capacity in coulombs divided by Faraday's constant) by the moles of Ni ions in each cathode. The calculations in Table 1. 5 indicate that the total capacity accessed along the first plateau cannot originate only from the reduction of trivalent Ni ions for NMC532 and NMC622 and must involve the reduction of other transition metals. In a second step, we estimate the capacity associated with the valence change of Mn and Co to the oxidation state 2^+, detailed in the appendix section Table SI. 4 - Table SI. 6. The contribution of any individual TM upon reduction to TM^{2+} is far below the capacity reached upon lithiation to xLi = 2.06, but the sum of the capacity coming from reduction of all TMs approaches the capacity observed via electrochemistry, indicating that all TMs must be involved in the reduction to reach the capacity at xLi = 2.

Table 1. 5: Calculations for estimating the capacity associated with reduction of Ni ions in Ni-rich NMC cathode materials from their pristine oxidation state (valence) to 2⁺

Element	Ni in NMC532	Ni in NMC622	Ni in NMC811	Comment
Initial stoichiometry	0.5	0.6	0.8	$Li_1Ni_aMn_bCo_cO_2$
Initial valence	2.4	2.66	2.875	From Wu et al.[73] Tian et al.[43], Gao et al.[46]
Valence: reduction to 2^+	0.4	0.66	0.875	Difference between initial valence and 2^+
Capacity accessed upon reduction to 2^+	55.52	109.50	192.86	$mAh.g^{-1}$ associated with valence change

The NMC materials from the "Ni = Mn" category do not exhibit a high potential lithiation plateau. This difference may result from the direct reduction of Mn and Co above the Li content of 1, as the overpotential to reduce Mn^{4+} and Co^{3+} to Mn^{3+} and Co^{2+} is smaller than the overpotential to reduce Ni^{2+} to Ni^0.[6,74] The estimated capacities reached from valence reduction of Mn and Co to 2^+ in NMC111 and NMC442 are summarized in Table 1. 6 and Table 1. 7. The total capacity resulting from reduction of the TMs to TM^{2+} is similar to the extra capacity reached after deep lithiation to xLi = 2. The TMs implicated in the capacity accessed upon this second lithiation plateau will be investigated in chapter 2 and potential side reactions will be investigated in chapter 3.

Table 1. 6: Calculations for estimating the capacity associated with reduction of Ni, Co, and Mn ions in NMC111 from their pristine oxidation state (valence) to 2+

Element	Ni in NMC111	Mn in NMC111	Co in NMC111	Comment
Initial stoichiometry	0.33	0.33	0.33	$Li_1Ni_aMn_bCo_cO_2$
Initial valence	2	4	3	From Dixit et al.[47]
Valence: reduction to 2^+	0	2	1	Difference between initial valence and 2^+
Capacity accessed upon reduction to 2^+	0	186.35	93.17	$mAh.g^{-1}$ associated with valence change

Table 1. 7: Calculations for estimating the capacity associated with reduction of Ni, Co, and Mn ions in NMC442 from their pristine oxidation state (valence) to 2+

Element	Ni in NMC442	Mn in NMC442	Co in NMC442	Comment
Initial stoichiometry	0.4	0.4	0.2	$Li_1Ni_aMn_bCo_cO_2$
Initial valence	2	4	3	From Dixit et al.[47]
Valence: reduction to 2^+	0	2	1	Difference between initial valence and 2^+
Capacity accessed upon reduction to 2^+	0	222.94	55.73	$mAh.g^{-1}$ associated with valence change

4. Capacity loss observed after deep lithiation to xLi = 2

A certain amount of capacity is not regained upon the delithiation following the lithiation to xLi = 2, as shown in Figure 1. 9. A clear difference in the capacity lost can be observed within NMC electrodes, as summarized in Table 1. 8. In the Ni-rich NMC category, NMC532 and NMC622 exhibit a very small capacity loss of about 1% of the overlithiation capacity. In contrast, NMC811 exhibits a significant capacity loss of 45.5% of the overlithiation capacity. NMC 811 did not exhibit capacity loss upon lithiation to xLi = 1, indicating that the changes occurring within the material from $1 \leq xLi \leq 2$ are responsible for the observed capacity loss. We hypothesize that the oxidation state changes of the Ni, Mn and Co along the second plateau lead to degradation of the NMC811 structure. This hypothesis will be investigated with characterization techniques in chapter 2.

Focusing on the “Ni = Mn” NMCs, we observe a small capacity loss for NMC111, similar to NMC532 and NMC622, suggesting a good structural integrity for one deep lithiation cycle for these materials. In contrast, NMC442 seems to gain capacity upon delithiation, which appears consistently within duplicate cells. NMC442 is the NMC cathode studied with the highest Mn content. As observed for $LiMn_2O_4$ cathodes, reduced Mn^{4+} tends to dissolve and depose on the anode.[33,34] A significant loss of Mn to the anode side would result in a different NMC stoichiometry, falling in the Ni-rich category. A visual confirmation of Mn deposition on the Li anode has been made for all NMC cells deeply lithiated. The apparent gain of capacity upon delithiation for NMC442 could arise from the formation of a different surface species at the surface of this Mn rich material.

Table 1. 8: Capacity lost upon delithiation after overlithiation to xLi = 2 at 0.1C rate for NMC cathode materials

Cathode material	Capacity loss upon delithiation after 1st overlithiation to xLi = 2	
	in $mAhg^{-1}$	in % of overlithiation capacity
NMC111	4.0	0.8
NMC442	-21.4	-4.4
NMC532	5.3	1.1
NMC622	2.9	0.6
NMC811	233.3	45.5

Summary

Upon electrochemical study of NMC cathodes, a loss of capacity was observed after the first delithiation when the electrodes were cycled between 3.0 V and V_{high}. The coulombic efficiency of NMC materials cycled in this potential window appeared to decrease with increasing Ni content.

The recovery of this capacity lost after this first delithiation was confirmed by lithiating the different NMC cathodes to lower potentials, ranging from 1.8 to 1.4 V vs Li/Li^+. Lithiation plateaus were observed upon recovery of the initial capacity. The potential at which these plateaus appeared was different within the NMC cathodes family. The capacity reached outside of the classic potential window was expected to result from the formation of a Li_2MO_2 phase at the surface of the particles. This phase is formed due to Li diffusion limitations resulting from Li insertion though monovacancy hopping occurring at high lithiation degrees. The formation of this phase lead to a sharp voltage drop below 3.0 V vs Li/Li^+.

Ni^{3+} is expected to be reduced to Ni^{2+} upon lithiation from 3.0 V to xLi = 1. This hypothesis was validated by the potential of the lithiation plateau appearing at a higher potential for the Ni-NMCs with a higher proportion of trivalent Ni in the pristine material. For the NMC materials with a Ni to Mn ratio equal to 1:1, the potential of the lithiation plateau was expected to be the same, and the reasons behind the observed difference will be investigated with the study of the valence of the TMs. No irreversible structural damage was expected to result from one lithiation to xLi = 1 from the comparison of the delithiation profile of a material lithiated to xLi = 1 with that of a material delithiated after lithiation to 3.0 V vs Li/Li^+. This hypothesis was verified by the cycling of NMC622 material between xLi = 1 and V_{high} for 100 cycles, with a relative reversibility of the deep lithiation observed for ~ 40 cycles.

In order to form the suspected surface Li_2MO_2 phase in the bulk of the materials, the potential was lowered to ~ 0.8 V vs Li/Li^+ to reach the stoichiometry of xLi = 2. More than 315 $mAh.g^{-1}$ of extra capacity was accessed in NMC cathodes upon deep lithiation compared to the classic potential window. This lithiation to xLi = 2 lead to new features, Ni-rich NMCs presented a high potential and a low potential lithiation plateaus whereas “Ni = Mn” cathodes presented only a low potential lithiation plateau. The capacity resulting from the valence change of pristine Ni to Ni^{2+} for Ni-rich NMCs was estimated, and it appeared clear that the capacity accessed along the first lithiation plateau cannot result only from the reduction of Ni ions. The capacity estimated from the reduction of all TMs to TM^{2+} was in line with the extra capacity accessed upon lithiation to xLi = 2.

A capacity loss upon delithiation to V_{high} after deep lithiation to xLi = 2 of about 1% was observed for NMC532 and NMC622, whereas the Ni-rich NMC811 material lost ~ 45% of capacity. The structural changes leading to this significant capacity loss are expected to result from the lithiation at $1 \leq x \leq 2$, as no capacity loss was observed upon delithiation after lithiation to xLi = 1. NMC111 exhibited a capacity loss of ~ 1%, however NMC442 appeared to gain capacity upon relithiation to V_{high}. We hypothesized that significant Mn was lost to dissolution upon reduction of Mn^{4+} towards Mn^{2+} for the Mn-rich NMC442, resulting in a different stoichiometry at the end of lithiation. The formation of a different species at the surface of this Mn-rich material is suspected, possibly leading to the extra delithiation capacity observed between xLi = 2 and V_{high}.

In order to confirm the hypotheses made on the structural changes occurring in the NMC materials upon deep lithiation, several characterization techniques are combined. X-ray based techniques are used in chapter 2 to probe the bulk of the materials as well as the surface of the particles in order to elucidate the depth-dependent mechanisms observed via electrochemistry.

Chapter 2: Structural characterization of NMC materials upon deep lithiation

Introduction

Ni-based layered oxide have a close packed oxygen framework with alternative Li layers and TM layers. The TM layers form MO_2 sheets of MO_6 edge-sharing octahedra. A denomination set by Delmas et al. classified the layered crystal structures based on the coordination of the Li ions (O for octahedral, P for prismatic, or T for tetrahedral) and the amount of repeat units.[75] The pristine NMC materials adopt the O3 structure, isostructural with α-$NaFeO_2$ of space group $R\overline{3}m$, where Li ions are in octahedral sites with a repeat unit of three MO_2 sheets.[76] The crystal structure of layered oxides varies upon the intercalation/deintercalation process. Transformations between the primitive O3/O1/P3 stacking sequences and between O2 and P2 can occur by gliding of the MO_2 sheets, while other transformations cost more energy as they require TM-O bond breaking.[77] A transformation from the O3 structure to the spinel structure, which also has a fcc oxygen framework, can occur with minimal energy cost as it requires only ¼ of the TMs to migrate to octahedral sites of the Li layer, and requires Li to either occupy remaining octahedral sites or tetrahedral sites in the Li layer. This transformation is often observed in delithiated states. A transition to a rocksalt phase, a highly disordered phase, can occur upon degradation of the layered structure and is characterized by the Li and TM layers no longer exhibiting periodic order. The transition from layered to rocksalt phase is associated with oxygen release and densification of the structure. The discussed crystal structures are presented in Figure 2. 1.

The Li_2NiO_2 phase observed by Dahn et al.[60] upon deep lithiation of LNO cathodes is characterized by the formation of a "Li-double layer" in the Li slab. Instead of occupying octahedral sites, Li ions insert in tetrahedral sites in the Li slab, accommodating twice as much Li in the material. This insertion of extra Li leads to an increase of the c-lattice parameter. The phase Li_2MO_2 is presented in Figure 2. 1.

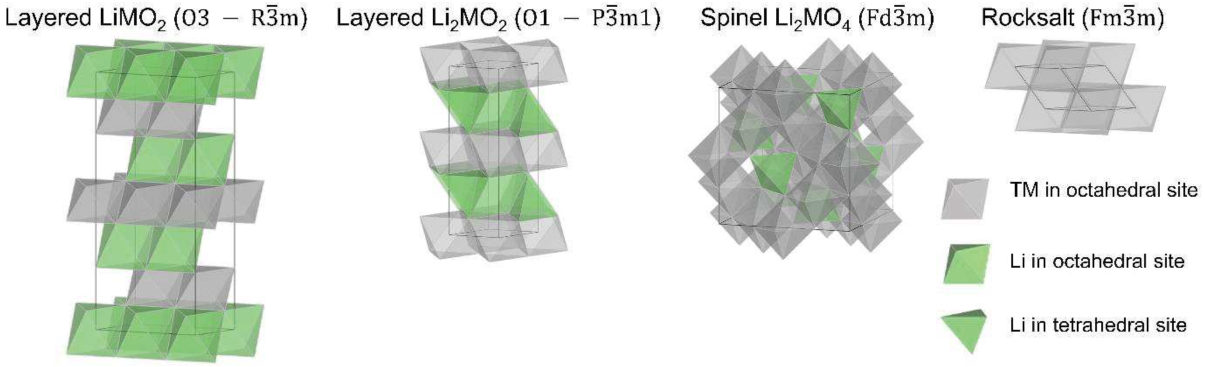

Figure 2. 1: Relevant crystal structures observed in Ni-based layered oxide with M representing one or more transition metals.

Several reversible phase transitions for the O3 structure can occur while preserving the crystal structure. They can be first-order transitions or continuous transitions. First order transitions occur when a (de)intercalation leads to a two-phase coexistence. A plateau appears in the voltage curve, marking the presence of two phases of different compositions, lattice parameters and often symmetry. Continuous transitions do not involve large abrupt changes in the structure and are less likely to result in degradation or kinetic limitations.

Upon cycling of NMC materials in the classic potential window of 3.0 V to 4.3 – 4.4 V vs Li/Li^+, Ni is the main active redox element responsible for the capacity accessed, with a small contribution from Co and negligible contribution of Mn.[43] The plateaus observed in the cycling profiles upon deep lithiation suggest the presence of new phases in the material and the extra capacity accessed suggests the implication of more than just Ni upon Li intercalation. The structural changes upon lithiation are first observed in-situ for NMC622 using synchrotron XRD and then compared to ex-situ XRD samples of all NMC materials studied. After mapping of the structural changes upon deep lithiation, the relevant TM reductions are identified using XAS. A depth-dependent study is done on NMC622 with both surface sensitive and bulk sensitive XAS, followed by a study of the valence of the TMs in the other NMC materials. The same analysis is applied to the samples upon delithiation in order to compare the reversibility of the lithiation to different degrees across different NMC cathodes.

The nomenclature of the capacity at which the cells were cycled in this chapter is presented in Figure 2. 2.

- Pristine refers to the uncycled cathode material
- V_{high} refers to the first delithiation to the high potential cut-off. V_{high} is 4.4 V vs Li/Li^+ for $LiNi_aMn_bCo_cO_2$ with a < 0.8 and 4.3 V vs Li/Li^+ for a = 0.8
- 3.0 V refers to a cathode that underwent a first delithiation to V_{high} and a lithiation to 3.0 V vs Li/Li^+, corresponding to the classic potential window for NMC cathodes
- OL1 refers to a cathode delithiated to V_{high} and lithiated to regain the initial delithiation capacity (CE = 100%, lithiation to return to xLi = 1)
- OL1 – V_{high} refers to a cathode delithiated to V_{high}, lithiated to OL1 and delithiated to V_{high} again, this protocol is designed to evaluate the material after the lithiation to OL1 and compare it to the classic potential window
- OL2 refers to a cathode delithiated to V_{high} and lithiated by coulomb counting to reach twice the theoretical capacity (lithiation to insert 2 Li per NMC structure, to xLi = 2)
- OL2 – V_{high} refers to a cathode delithiated to V_{high}, lithiated to OL2 and delithiated to V_{high} again, this protocol is designed to evaluate the material after the lithiation to OL2 and compare it to the classic potential window

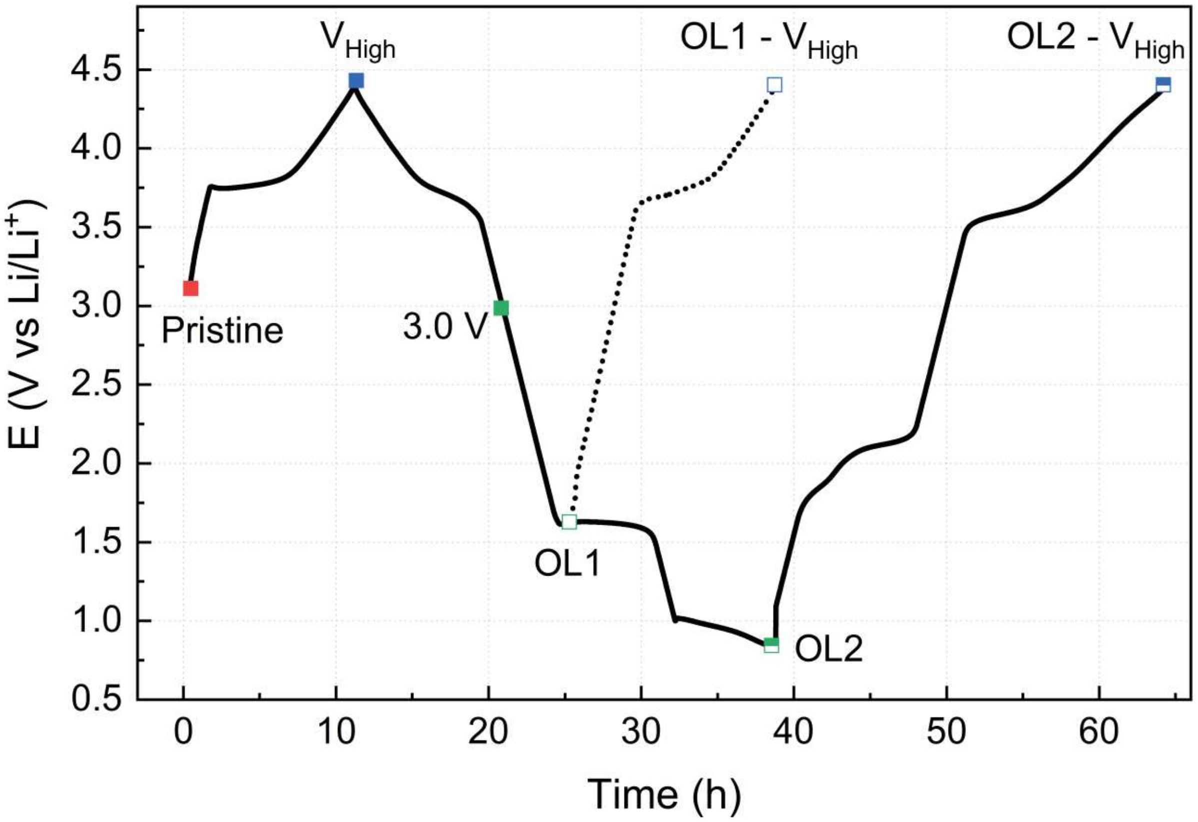

Figure 2. 2: Summary of the different electrochemistry profiles and corresponding designation used. V_{high} *= 4.4 V vs Li/Li*$^+$ *for NMC111, NMC442, NMC532, and NMC622;* V_{high} *= 4.3 V vs Li/Li*$^+$ *for NMC811; OL1 corresponds to the recovery of the initial capacity extracted from the material from OCP to* V_{high} *(xLi = 1), OL2 corresponds to the material reaching twice its theoretical capacity (xLi = 2)*

1. Structural changes investigated with X-ray diffraction upon deep lithiation

- ### Study of NMC622 with in-situ synchrotron XRD and conventional ex-situ XRD

The changes observed via electrochemistry in chapter 1 upon overlithiation suggested the formation of a Li-rich layer at the surface of the particles. Previous reports on overlithiation of layered oxides suspected the formation of a Li_2MO_2 phase but could not identify it with XRD,[54,67,78] as this technique probes the bulk-average of the material. The NMC622 electrode has been selected as a flagship material for a more detailed study, followed by a comparative study of the other NMC cathodes. In order to identify the phases involved in the extra capacity accessed by electrochemistry and map the changes occurring upon deep lithiation, an in-situ coin cell of NMC622 was cycled and probed in a synchrotron XRD set-up. After a first cycle between V_{high} and 3.0 V (Figure 2. 3. b), the cell was lithiated to ~ 0.8 V vs Li/Li^+ at the synchrotron (Figure 2. 3. c), with a round marker on the lithiation profile for each diffractogram acquisition.

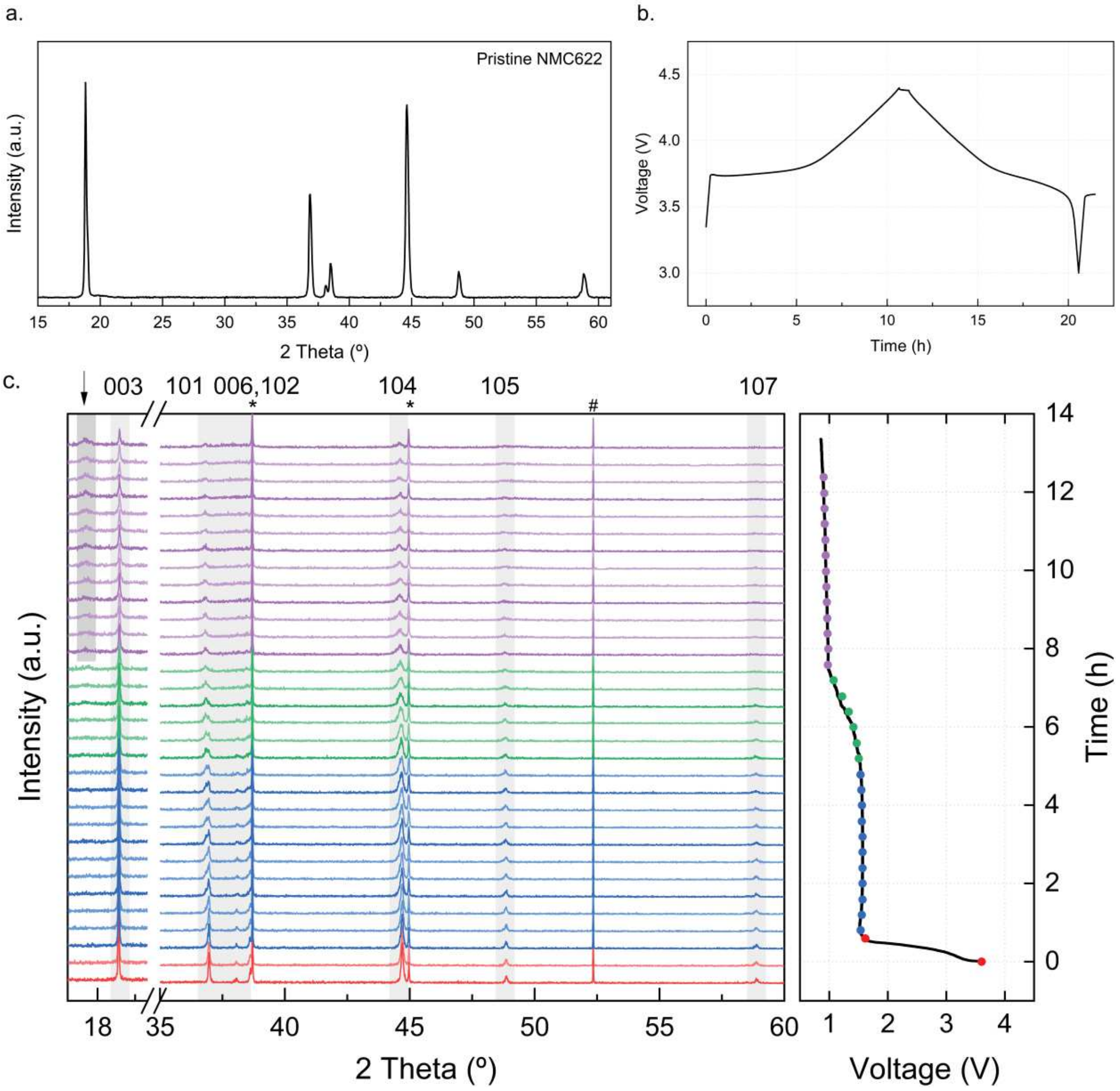

Figure 2. 3: a. Ex-situ X-ray diffraction pattern of pristine NMC622; b. Cycling profile of the in-situ NMC622 cell between OCV - 4.4 V and 3.0 V vs Li/Li^+ prior to the beam cycling c. X-ray diffraction pattern of NMC622 in-situ coin cell upon deep discharge to 0.8 V vs Li/Li^+ at the beamline, where the different markers on the cycling profile on the right indicate the XRD measurement. No peaks are present in the range 20-35°. The peaks of interest are highlighted in grey. The Miller indices of the Bragg peaks are indicated near each peak, referring to the initial layered 3R-$LiMO_2$ phase, the peaks marked by an asterisk indicate the aluminum peaks and the peak marked by the hash sign indicates the stainless steel peak. The arrow indicates the peak (001) of the new 1T-Li_2MO_2 phase

($P\bar{3}m1$). The synchrotron XRD data is plotted on a 2-theta λ_{Cu} scale to allow for comparison with conventional XRD measurements.

The structural evolution of the in-situ cell upon lithiation between the relaxation potential of 3.6 V and ~ 0.8 V vs Li/Li^+ under the beam is shown in Figure 2. 3. c. The energy and wavelength of the X-ray source used for the synchrotron XRD measurements were scaled to the energy of the conventional XRD (Cu Kα with E = 8.04 keV and λ = 1.5406 Å) to allow for data comparison. Compared to the pristine NMC622 (Figure 2. 3. a), no clear change is observed along the first plateau (red and blue markers), indicating that the initial layer structure is maintained in the bulk of the material. Along the second plateau (purple markers), a new peak (001) appears at ~ 17.5°, indicative of the formation of a 1T-Li_2MO_2 phase of the space group $P\bar{3}m1$ (isostructural with lT-TiS_2 or CdI_2),[73] in line with other literature reports.[60,79] This result is consistent with the assumption made in chapter 1 that the Li_2MO_2 phase initiates at the surface of the particles along the first plateau and reaches the bulk of the material in the second plateau. The extra Li in the Li_2MO_2 phase inserts in the tetrahedral sites of the Li layer instead of occupying octahedral sites, allowing for extra Li insertion in the Li slab as it accommodates twice as many Li ions. The peaks (101), (006), (102), (105), and (107) of the initial O3 layered phase appear weaker and wider, indicating a loss of the layered structure, a higher disordering and potentially a particle size reduction.[80] The increase of the disordering can be interpreted as a transition towards a spinel structure, nevertheless the decreasing of the (003)/(104) ratio is not observed for our material and no (511) spinel peak is visible at ~ 59°. The transition to a spinel phase could be initiated at the surface of the material and not be visible with XRD, which is why we recommend the characterization of the surface of the material in a follow up study.

The in-situ XRD allows for a better sensitivity and resolution of diffraction peaks than conventional XRD. Additionally, the detector of the synchrotron XRD is bigger than a conventional XRD, allowing for a faster data acquisition rendering this method better suited for in-situ or operando characterization. A drawback of the in-situ coin cell XRD measurement set-up is a difference in conductivity resulting from the hole in the cell hardware. The hole must be big enough to allow for beam penetration but small enough to maintain the integrity of the cycling, i.e. the exact section probed by the beam does not have the same compression as the rest of the electrode, resulting in local differences in conductivity. Moreover, the data obtained with the synchrotron XRD is only averaged throughout the depth of the area probed, which may not always be representative of the entire electrode. After the mapping of the structural changes upon deep lithiation with synchrotron XRD, we use conventional XRD for ex-situ measurements on harvested cathodes. Because conventional XRD has a bigger beam size, the data is averaged over almost the entire electrode, which allows capturing representative ex-situ information over the entire electrode.

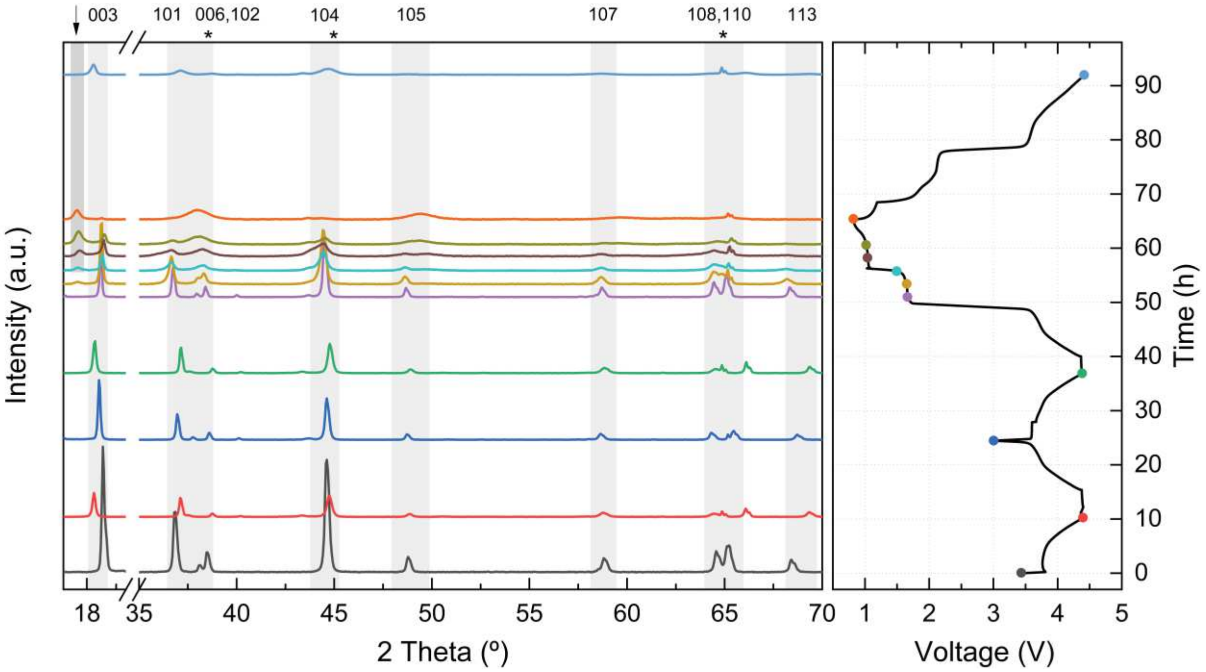

Figure 2. 4: Ex situ X-ray diffraction patterns of NMC622 electrodes measured from cathodes harvested at the potentials marked on the cycling profile. No peaks are present in the range 20-35º. The peaks of interest are highlighted in grey. The Miller indices of the Bragg peaks are indicated near each peak, referring to the initial layered 3R-LiMO$_2$ *phase, the peaks marked by an asterisk indicate the aluminum peaks. The arrow indicates the peak (001) of the new 1T-Li*$_2$*MO*$_2$ *phase (*$P\bar{3}m1$*). The intensity of the (001) peak appears higher than for the in-situ sample due to better conductivity upon cycling. Peaks of the initial layered phase appear weakened and widened by the deep lithiation to xLi = 2, indicative of disordering in the material.*

Ex-situ measurement of harvested NMC622 cathodes are presented in Figure 2. 4. Markers on the right side indicate the potential at which the different electrodes were harvested. The shift in peaks positions in the classic potential window (4.4 V – 3.0 V vs Li/Li$^+$) are consistent with literature reports.[43] The layered structure is maintained in the bulk along the first overpotential plateau were the Li$_2$MO$_2$ phase is thought to be formed at the surface of the particles. As observed with in-situ synchrotron XRD, a (001) peak initiates at ~ 17.5º along the second overlithiation plateau. The intensity of this peak is higher with ex-situ XRD suggesting that this phase was not locally predominant in the in-situ cell, likely due to poor contact at the location of the measurement, as previously discussed. A broadening and decrease in intensity of the peaks of the 3R-LiMO$_2$ phase correlates with the observations made with synchrotron

XRD. The peaks of the initial layered structure are still visible upon lithiation to xLi = 2, suggesting an incomplete phase transformation to the Li_2MO_2 phase. We hypothesize the apparition of cracks in the particles resulting from Li insertion in the layered structure, i.e. the overlithiation along the second plateau may trigger a decomposition of the particles in different clusters, with regions of Li_2MO_2 phase and regions of $LiMO_2$ phase. This cracking of particle could explain the apparition of several domains, leading to the widening of the $LiMO_2$ peaks.

- Ex-situ XRD investigation of NMC cathodes upon deep lithiation

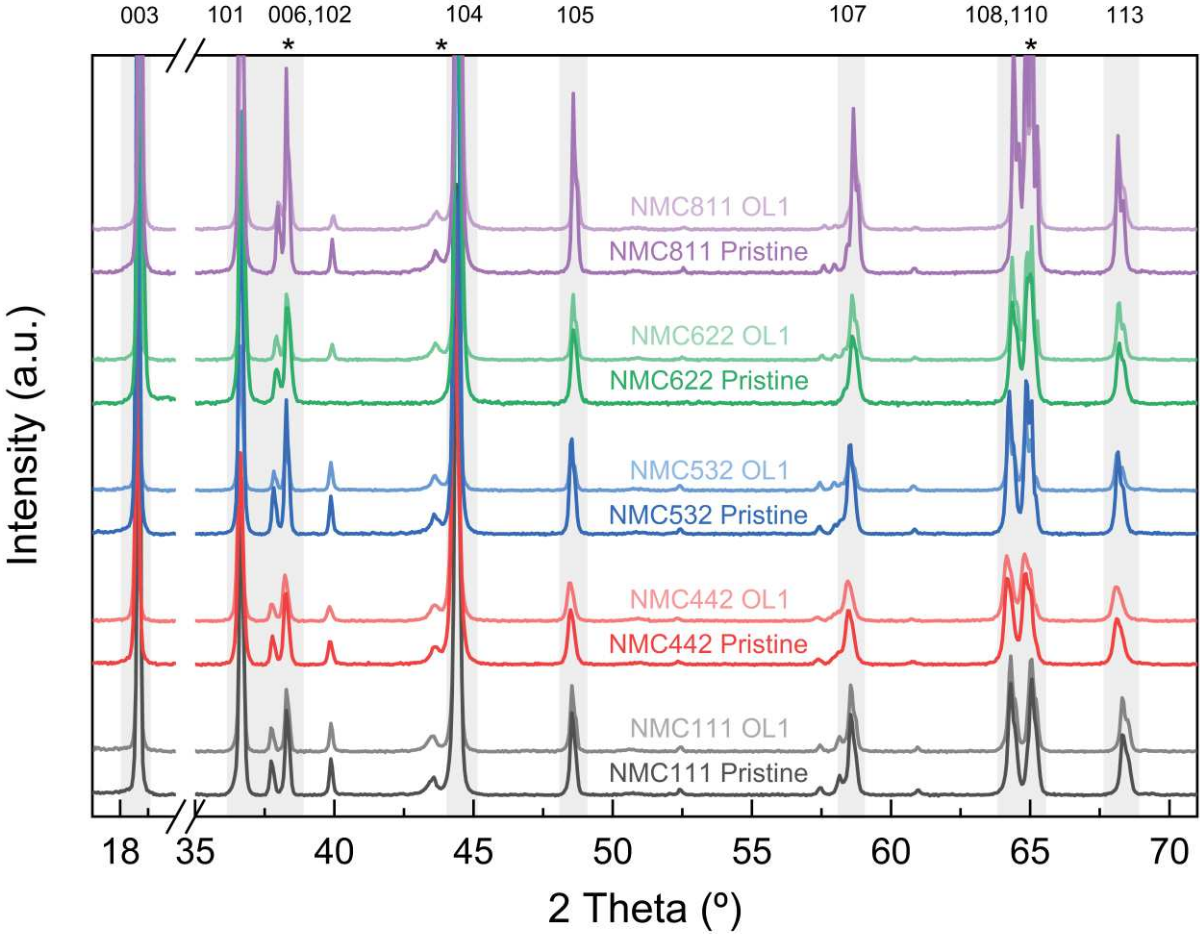

Figure 2. 5: Ex situ X-ray diffraction patterns of NMC electrodes in pristine state and after lithiation to OL1. No peaks are present in the range 20-35º. The peaks of interest are highlighted in grey. The Miller indices of the Bragg peaks are indicated near each peak, referring to the initial layered 3R-$LiMO_2$ phase, the peaks marked by an asterisk indicate the aluminum peaks. The peak at 40º result from the sample holder. No difference is observed in the structure of the bulk of the materials after lithiation to OL1.

To investigate the differences in lithiation profile observed for various NMC cathodes upon lithiation to OL1, the results of ex-situ electrodes of NMC111, NMC442, NMC532, and

NMC811 probed with XRD are presented in Figure 2. 5. No difference is observed between the pristine samples and the samples lithiated to OL1 for each NMC materials. These results confirm that the bulk of the material does not see a structure change upon lithiation to OL1 and retains the initial layered phase ($R\overline{3}m$ space group), as hypothesized with electrochemistry in chapter 1.

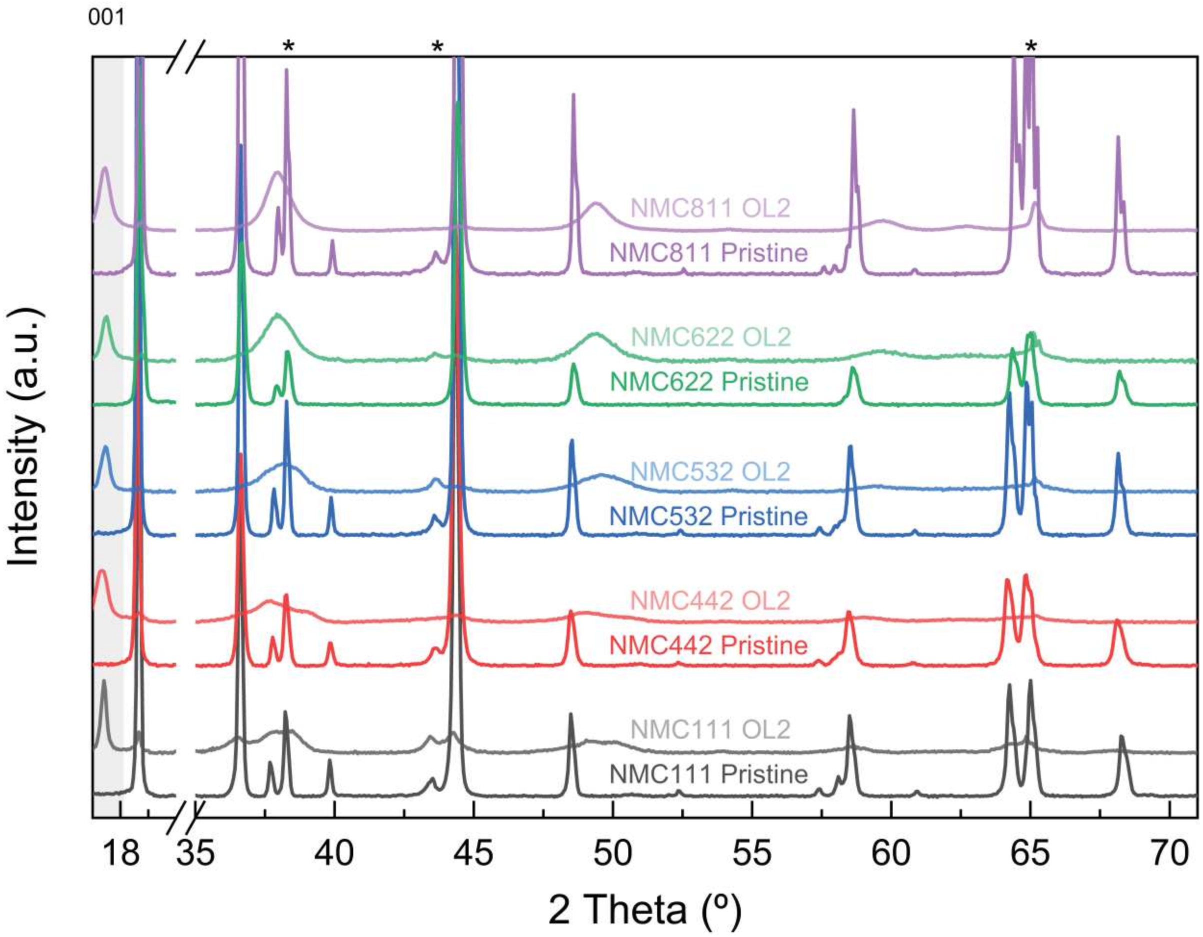

Figure 2. 6: Ex situ X-ray diffraction patterns of NMC electrodes in pristine state and after lithiation to OL2. No peaks are present in the range 20-35°. The peaks marked by an asterisk indicate the aluminum peaks. A clear widening and weakening of the peaks of the initial 3R-$LiMO_2$ structure is observed. A new (001) peak appears at 17.5° marking the partial conversion of the structure to 1T-Li_2MO_2 phase in the bulk and particle size reduction after lithiation to OL2. No significant structural difference is observed upon deep lithiation in the bulk across the different NMC cathodes.

The diffraction patterns of NMC cathodes lithiated to OL2 are compared with the pristine electrodes in Figure 2. 6. Similarly to the changes observed for NMC622 (Figure 2. 3 and Figure 2. 4), all the NMC cathodes present a decrease in intensity and broadening of the characteristic peaks of the initial layered structure, and a new (001) peak indicative of the $P\overline{3}m1$

1T-Li_2MO_2 phase. The deep lithiation to OL2 appears to introduce a destruction of the initial layered phase in all NMC cathodes. No significant difference is observed in the bulk across the different NMC cathodes investigated upon deep lithiation to OL2.

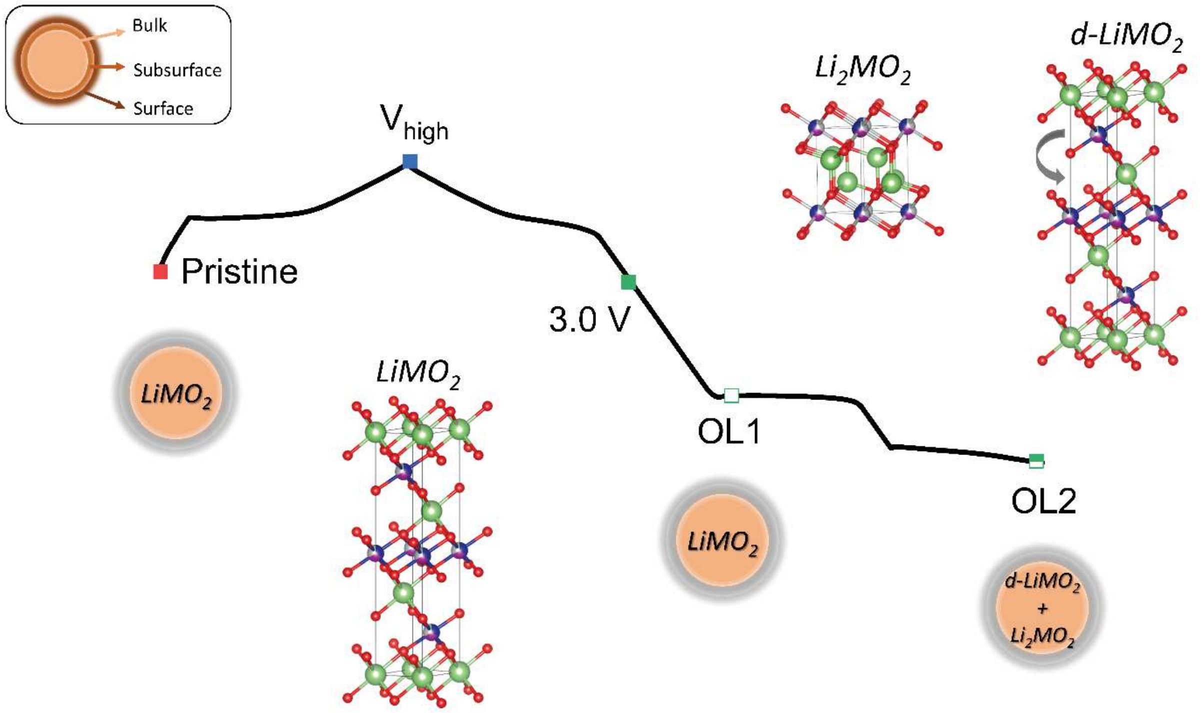

Figure 2. 7: Schematic summary of the structural changes observed in the bulk of the material with XRD upon deep lithiation. $LiMO_2$ *denotes the initial layered* $R\bar{3}m$ *phase,* Li_2MO_2 *the Li-rich phase (*$P\bar{3}m1$*), and d-*$LiMO_2$ *a disordered layered* $R\bar{3}m$ *phase.*

The absence of significant structural change upon lithiation of NMC622 along the first overlithiation plateau was put in evidence with synchrotron XRD analysis. A new (001) peak appeared along the second plateau upon lithiation to OL2, marking the presence of a 1T-Li_2MO_2 phase isostructural with CdI_2 ($P\bar{3}m1$ space group) in the bulk of the material. A widening and weakening of the intensity of the 3R-$LiMO_2$ peaks upon deep lithiation showed an increase of the disordering in the material, and indicated an incomplete phase transformation towards the new 1T-Li_2MO_2 at this lithiation degree. A particle size reduction, potentially due to cracking is suspected. No formation of a spinel phase is observed in the bulk of the material but surface sensitive techniques are recommended to investigate the material in a follow up study. Similar observations are made for NMC622 cathodes from conventional XRD ex-situ measurements, with an increase in intensity of the new (001) peak indicative of a local loss of conductivity in the in-situ cell. The comparison of the diffraction pattern of the pristine

NMC111, NMC442, NMC532, NMC622, and NMC811 to the samples lithiated to OL1 highlighted again the lack of structural change in the bulk upon regain of the initial capacity, supporting the good reversibility observed with electrochemistry upon relithiation after lithiation to OL1 (xLi = 1). All NMC materials studied showed the new (001) peak upon lithiation to OL2 and a widening and weakening of the peaks of the initial layered phase, indicating that the structure of the bulk across all NMCs is similar upon lithiation to OL2 (xLi = 2). A study of the structure of the electrodes with transmission electron microscopy (TEM) or electron energy loss spectroscopy (EELS) could be combined with scanning electron microscopy (SEM) in a follow up study to determine the surface morphology of the electrodes after deep lithiation. The variations of the oxidation state of the TMs across all NMC cathodes are presented in a second part in order to identify differences in the materials upon deep lithiation.

2. Investigation of the oxidation state variations of the transition metals in NMC cathodes upon deep lithiation

To measure changes in the oxidation state of TMs in the bulk of the material upon deep lithiation, we perform a series of hard XAS measurements at the K-edges of the elements of interest (Ni, Co, Mn). To distinguish between electrochemistry occurring at the surface of the particles and the changes throughout their bulk, hard XAS measurements are followed by soft XAS study, using both Total Electron Yield (TEY – top 5 nm) and Fluorescence Yield (FY – 50-100 nm) modes. In similarity to the XRD measurements, a detailed XAS study of NMC622 is first presented followed by investigation of the other NMC electrodes.

- Detailed hard XAS study of NMC622

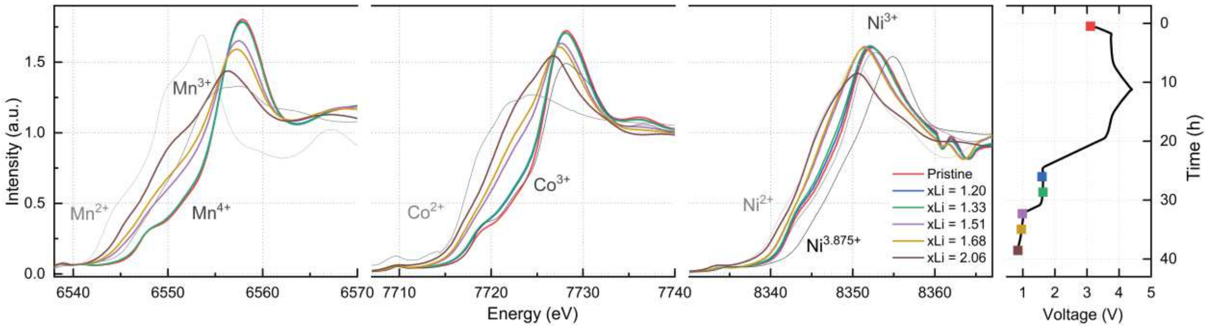

Figure 2. 8: Mn, Co, and Ni K-edge spectra of NMC622 with xLi = 1.20, 1.33, 1.51, 1.68 and 2.06. 70% Chemically delithiated NCA (30% Li, $Ni^{3.875+}$), Pristine NMC622 (Mn^{4+},Co^{3+},$Ni^{2.66+}$), NiO (Ni^{2+}), $CoCl_2$ (Co^{2+}), MnO (Mn^{2+}),[16] Mn_2O_3 (Mn^{3+})[16] used as standards. A clear reduction is observed for all TMs upon deep lithiation.

In a first study, ex-situ hard XAS measurements are carried out on harvested NMC622 cathodes, which were brought to the different lithiation degrees of xLi = 1.20 (1.60 V), xLi = 1.33 (1.52 V), xLi = 1.51 (1.03 V), xLi = 1.68 (1.01 V) and xLi = 2.06 (0.8 V). The measurements are executed at the K-edge of Ni, Co, and Mn, probing the dipole-allowed transition from the 1s level to the 4p valence states. Figure 2. 8 depicts the normalized Mn, Co and Ni K-edge XANES spectra of the NMC622 electrodes harvested at the different lithiation degrees marked on the right on the cycling profile. Since the peak position at the three studied K-edges shifts to the left throughout the overlithiation process, it is clear that all three TMs participate in the reduction. We estimate the oxidation state of Co and Ni from the spectra of the standards by using a linear relationship between the energy of the edge at the normalized intensity of 0.5 and the oxidation state, and by using a linear relationship between the energy of the maximum of the Mn K-edge, as previously reported in literature.[16] The enlarged spectra of Co and Ni at the region of 0.5 intensity are presented in Figure 2. 9. The standards used are MnO (Mn^{2+}),[16] Mn_2O_3 (Mn^{3+}),[16] pristine NMC622 (Mn^{4+},Co^{3+},$Ni^{2.66+}$), $CoCl_2$ (Co^{2+}) and NiO (Ni^{2+}).

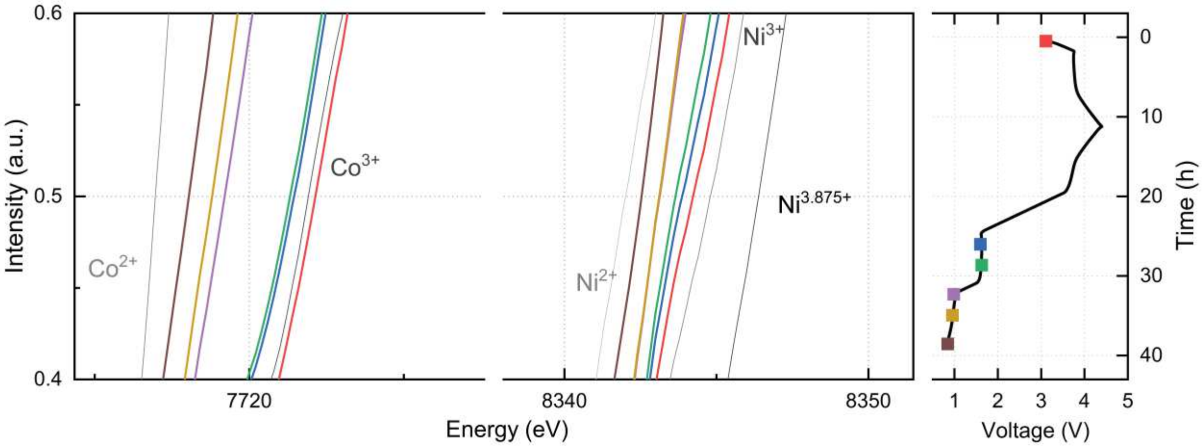

Figure 2. 9: Co, and Ni K-edge spectra of NMC622 with xLi = 1.20, 1.33, 1.51, 1.68 and 2.06. 70% Chemically delithiated NCA (30% Li, $Ni^{3.875+}$), Pristine NMC622 (Co^{3+},$Ni^{2.66+}$), NiO (Ni^{2+}), $CoCl_2$ (Co^{2+}) used as standards enlarged to show the region at 0.5 intensity.

Focusing on Ni, we can see that the first overlithiation plateau (xLi = 1.20 and xLi = 1.33) is associated with a gradual but small shift toward the lower edge energy and therefore a small change from $Ni^{2.66+}$ oxidation state in the pristine electrode to lower values. As the lithiation degree increases from xLi = 1.33 to xLi = 1.51 and the potential drops to ~1.0 V vs Li/Li^+, a significant reduction in Ni oxidation state to about $Ni^{2.30+}$ is observed. Further lithiation along the second overlithiation plateau, however, does not lead to an additional shift in the edge energy, indicating that the change in the chemical state should be occurring in either Co or Mn (it should be highlighted that the spectra for xLi = 1.51 and xLi = 1.68 overlap). As the potential drops below 1.0 V and approaches the 0.8 V plateau, another significant change in the Ni edge position occurs, bringing the bulk oxidation state to $Ni^{1.91+}$. The observations of the oxidation state variations of Ni align with the hypotheses made in chapter 1, confirming the reduction of the bulk Ni along the first high voltage plateau.

For Co, the K-edge shifts slightly to the left as xLi increases from 1.00 in the pristine electrode to 1.20 in the first ex situ sample, and then remains at approximately the same edge position during additional lithiation along the first lithiation plateau (xLi = 1.20 and xLi = 1.33). In similarity to Ni, as the lithiation degree increases further from xLi = 1.33 to xLi = 1.51 and the lithiation plateau drops to ~1.0 V, a significant decrease in Co oxidation state to approximatively $Co^{2.43+}$ is observed. Further lithiation of NMC622, which increases Li stoichiometry first to xLi = 1.68 and then to xLi = 2.06, results in gradual shift in Co edge position to the left and a final lower oxidation state of Co of approximatively $Co^{2.21+}$. The observations of the valence of the bulk Co confirm its minimal implication in the lithiation up to the beginning of the low voltage plateau.

In comparison to Ni and Co K-edges, Mn K-edge shifts only slightly during the first lithiation plateau at 1.6 V, resulting in slightly reduced Mn ($Mn^{3.94+}$). As the stoichiometry of Li increases from xLi = 1.33 to xLi = 1.51, and the potential drops to ~1.0 V vs Li/Li^+, the Mn oxidation decreases significantly going from $Mn^{3.94+}$ to $Mn^{3.02+}$. Further reduction along the second lithiation plateau leads to a small shift in the Mn K-edge to the left, while the transition to second overlithiation plateau results in another significant change in Mn chemical state, bringing Mn to an oxidation state of about $Mn^{2.57+}$. As expected from the electrochemical study presented in chapter 1, the implication of Mn in the lithiation process is negligible until the second lithiation plateau.

The oxidation state variations of the TMs in the bulk NMC622 the material are in line with the hypotheses made in the electrochemical study in chapter 1. Mainly Ni is reduced upon lithiation to xLi = 1 with minimal implication of Co which does not lead to structural changes in the bulk, as observed with XRD. Ni is further reduced along the first lithiation plateau. Co and Mn are significantly reduced along the low voltage plateau, leading to the apparition of a new 1T-Li_2MO_2 phase, and all TMs are reduced to lower valences at ~ 0.8 V vs Li/Li^+. Using the observed oxidation states of all three TM oxides, it is possible to calculate the amount of charge that would need to enter the electrode to result in these measured values and compare the calculated capacity to the capacity, which was obtained electrochemically. The results of these calculations are presented in the appendix section Table SI. 7. Examination of the values reveals that the capacities calculated from the hard XAS data are in reasonable agreement with the capacities reached by the harvested cathodes, suggesting that contributions to gravimetric capacity from side reactions were minor.

- Hard XAS study of NMC cathodes

In order to evaluate the differences in the NMC cathodes observed in the electrochemical study, NMC111, NMC442, NMC532, NCM622 and NMC811 are also studied at different lithiation degrees with hard XAS and the results are presented in Figure 2. 12 - Figure 2. 16. For each NMC material investigated, the lithiation degree at which the cathode has been harvested is marked on the right. Section a marks the study of the NMC cathode upon lithiation to OL1 and delithiation to V_{high}. Section b marks the investigation of the NMC cathode upon deep lithiation to OL2 and delithiation to V_{high}. The K-edge spectra of each sample is plotted alongside the pristine sample and standards (NiO - Ni^{2+}, Pristine NCA - Ni^{3+}, 70% Chemically delithiated NCA - $Ni^{3.875+}$, $CoCl_2$ - Co^{2+}, Pristine LCO - Co^{3+}, MnO - Mn^{2+}, Mn_2O_3 - Mn^{3+}, Pristine NMC111 - Mn^{4+}). The maximum of the energy of the Mn K-edge and the energy at the normalized 0.5 intensity are summarized in Figure 2. 10 and Figure 2. 26.

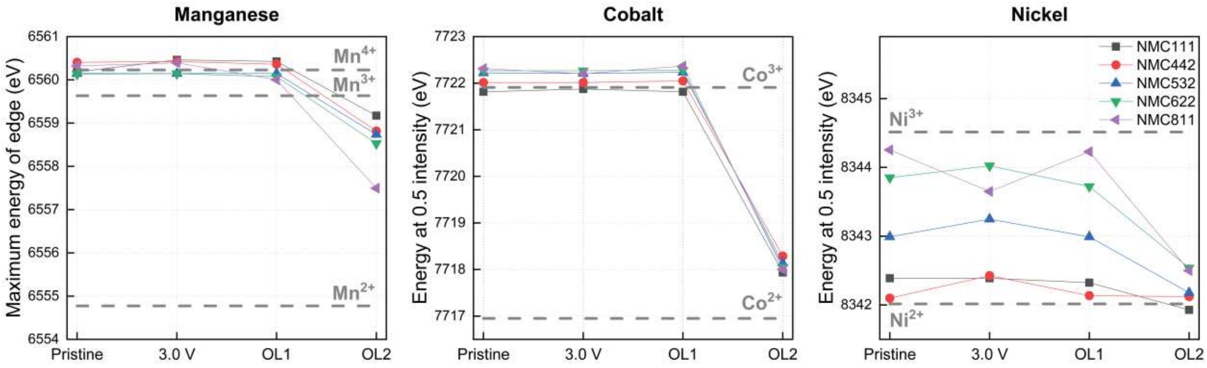

Figure 2. 10: K-edge energy of the cathodes NMC111, NMC442, NMC532, NMC622 and NMC811 in the pristine state, lithiated to 3.0 V vs Li/Li^+, lithiated to OL1, and lithiated to OL2; a. Maximum energy of the Mn K-edge in eV; b. Energy of the Co K-edge at 0.5 intensity in e; c. Energy of the Ni K-edge at 0.5 intensity in eV. The energy of the standards is marked by a dashed line. A clear reduction of all the TMs is observed upon deep lithiation to OL2.

The variations of the edge energy from the cathodes cycled to 3.0 V vs Li/Li^+ are compared to the cathodes lithiated to OL1 and to OL2 in Figure 2. 10. As seen for NMC622, no significant change is observed for Co and Mn between 3.0 V and OL1 for all NMCs. Additionally, no significant change is observed in the Ni bulk oxidation state between a pristine sample and a sample lithiated to OL1, as OL1 is at the beginning of the first lithiation plateau, and the extra Li insertion due to kinetic limitations at this stage is expected to occur only at the surface of the material. A clear reduction of all the TMs is observed upon lithiation to OL2. The reduction of Mn towards the valence 2^+ increases with increasing Ni content, with a significantly larger reduction of Mn in NMC811 upon lithiation to OL2. The bigger valence change of Mn observed in NMC811 may result from the higher structural instability of the NMC structure due to the minimal amount of Mn present. This bigger reduction of Mn could be responsible for a bigger Mn dissolution and linked to the high capacity loss observed for NMC811 upon delithiation. We notice that the valence of Ni in NMC111 is higher than the expected value of 2^+. This observed valence of 2.1^+ may result from a lower quantity of Ni in the material (0.31 instead of 0.33) or a lower quantity of Li in the pristine material $xLi^{Pristine} = 0.95$ instead of $xLi^{Pristine} = 1$). Such a variation is too small to be determined by inductively coupled plasma atomic emission spectroscopy (ICP-OES) measurements. The minimal presence of trivalent Ni in the pristine NMC111 can confirm the difference in lithiation profile observed with the "Ni=Mn" NMC442 material in chapter 1. Due to the difference in the Ni oxidation state in the pristine NMC electrodes, the edge energy is normalized by the pristine edge of each NMC to allow for better comparison of the extent of reduction in Figure 2. 11.

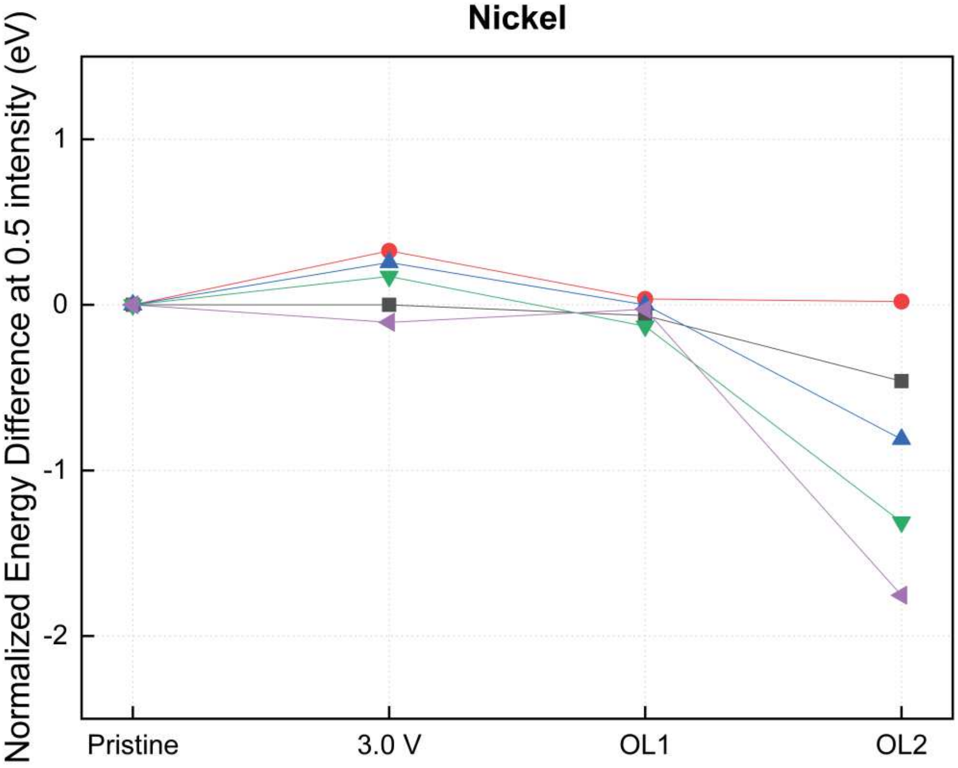

Figure 2. 11: Ni K-edge energy of the cathodes NMC111, NMC442, NMC532, NMC622 and NMC811 in the pristine state, lithiated to 3.0 V, lithiated to OL1, and lithiated to OL2 normalized by the energy of the pristine material to visualize the extent of variation in the Ni valence state for each NMC cathode.

Figure 2. 11 depicts the relative variation of the oxidation state of Ni in NMC cathodes upon deep lithiation. As hypothesized from the electrochemical study in chapter 1, NMC442 that only has divalent Ni in the pristine does not see further reduction of Ni in the bulk. However, the K-edge spectra of Ni in NMC442 upon lithiation to OL2 shows a different

profile, indicative of a different structural environment for the Ni. For the Ni-rich NMCs, a higher Ni content leads to a higher amount of trivalent Ni in the pristine material. The more trivalent Ni is present in the NMC material, the more valence change is observed for Ni upon lithiation to OL2. The extent of variation of the oxidation state of Ni in NMC811 is hypothesized to induce stress in the particles and trigger cracking in the material.

As observed with hard XAS and XRD, no significant difference is observed between a cell cycled to 3.0 V and to OL1 for NMC materials. In similarity to literature reports in the classic potential window, in the regime from pristine to OL1, no changes occur in the valence of Mn in the bulk of the material, minimal changes occur for Co and mainly Ni is responsible for the charge compensation.[81] Upon deep lithiation to OL2, all TMs significantly reduce towards the valence 2^+. As reported from the XRD analysis, more details are needed about the surface of the materials to distinguish between the different NMC materials upon deep lithiation.

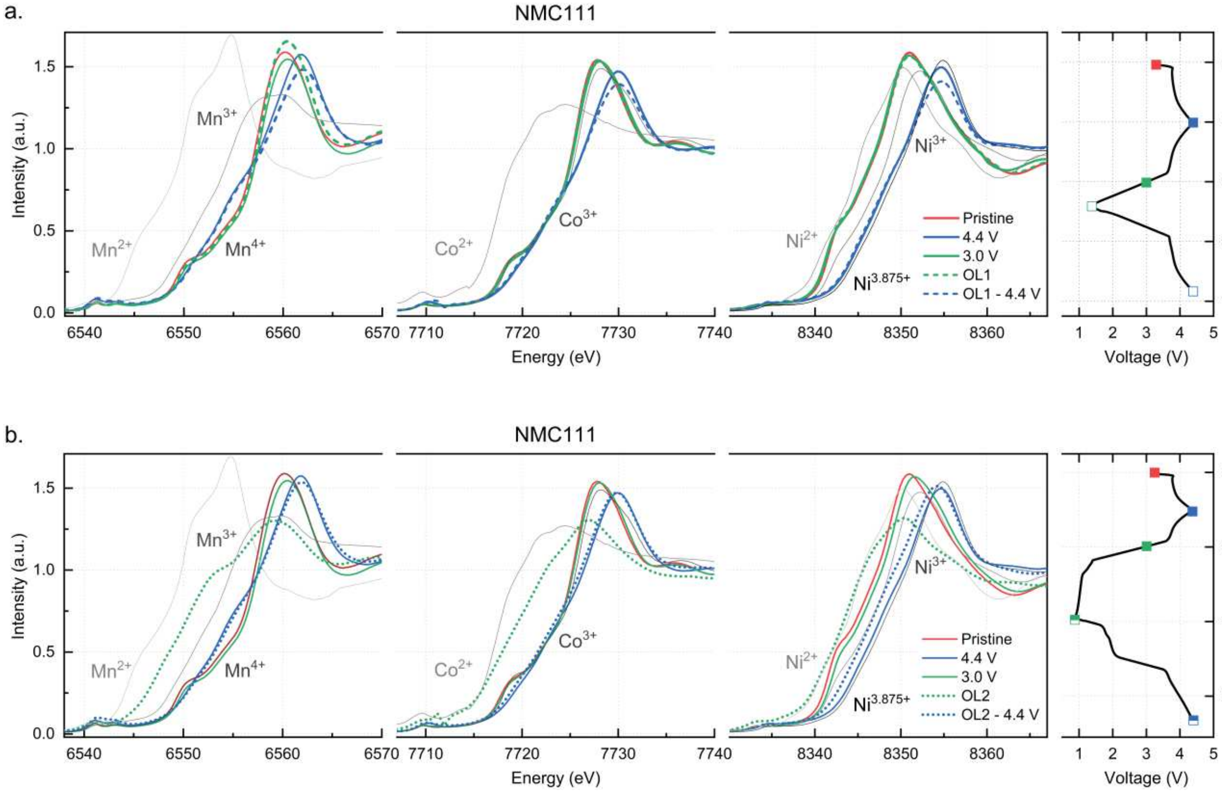

Figure 2. 12: Mn, Co, and Ni K-edge spectra of NMC111 electrodes harvested at various lithiation states with the corresponding voltage profile. NiO (Ni^{2+}), Pristine NCA (Ni^{3+}), 70% Chemically delithiated NCA ($Ni^{3.875+}$), $CoCl_2$ (Co^{2+}), Pristine LCO (Co^{3+}), MnO (Mn^{2+}), Mn_2O_3 (Mn^{3+}), Pristine NMC111 (Mn^{4+}) used as standards. Markers indicate the potential at which the electrode was harvested: full red square for the pristine NMC111, full blue square for the electrode delithiated to 4.4 V, full green square for the electrode lithiated to 3.0 V. a.

Comparison of the K-edge spectra of the transitions metal after a lithiation to the initial capacity of the pristine material (OL1; empty green marker) and the subsequent delithiation (OL1 – 4.4 V; empty blue marker); b. Comparison of the K-edge spectra of the transitions metal after a lithiation to the twice the theoretical capacity of the pristine material (OL2; dashed green marker) and the subsequent delithiation (OL2 – 4.4 V; dashed blue marker).

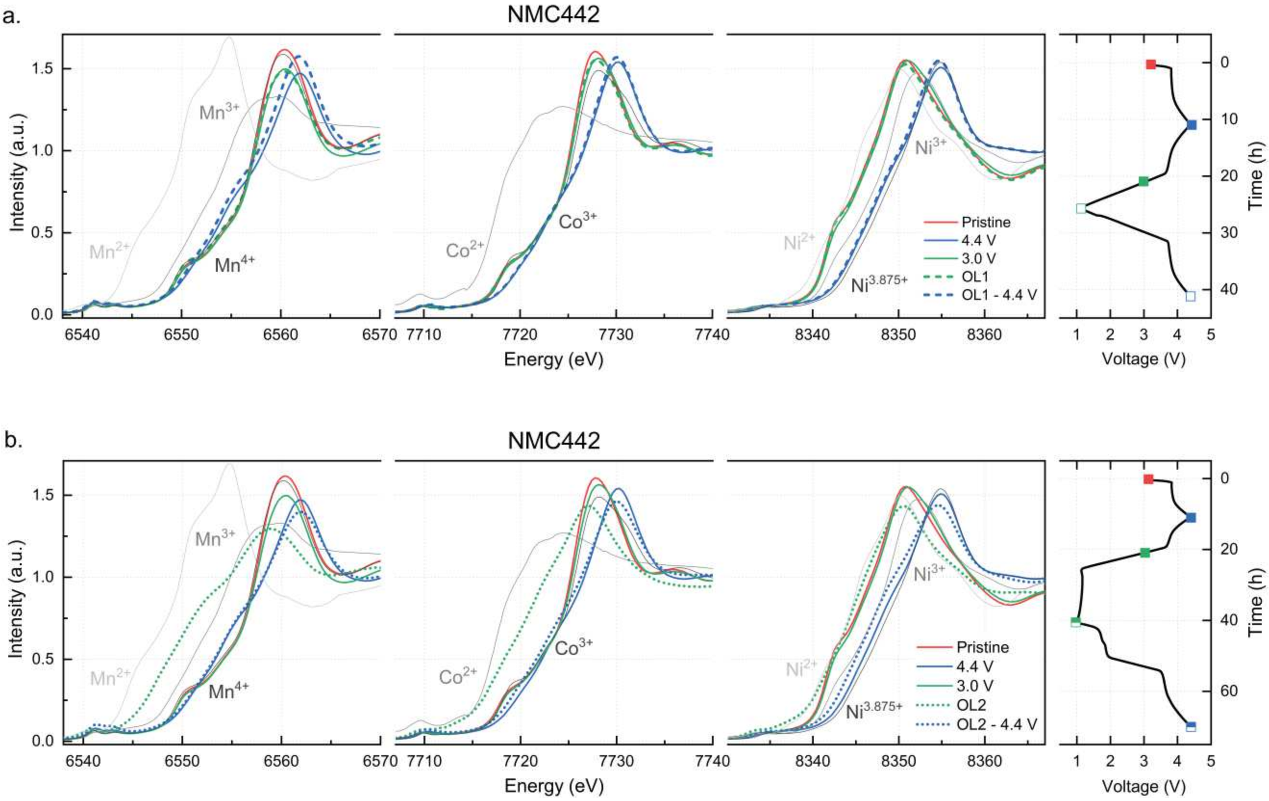

Figure 2. 13: Mn, Co, and Ni K-edge spectra of NMC442 electrodes harvested at various lithiation states with the corresponding voltage profile. NiO (Ni^{2+}), Pristine NCA (Ni^{3+}), 70% Chemically delithiated NCA ($Ni^{3.875+}$), $CoCl_2$ (Co^{2+}), Pristine LCO (Co^{3+}), MnO (Mn^{2+}), Mn_2O_3 (Mn^{3+}), Pristine NMC111 (Mn^{4+}) used as standards. Markers indicate the potential at which the electrode was harvested: full red square for the pristine NMC442, full blue square for the electrode delithiated to 4.4 V, full green square for the electrode lithiated to 3.0 V. a. Comparison of the K-edge spectra of the transitions metal after a lithiation to the initial capacity of the pristine material (OL1; empty green marker) and the subsequent delithiation (OL1 – 4.4 V; empty blue marker); b. Comparison of the K-edge spectra of the transitions metal after a lithiation to the twice the theoretical capacity of the pristine material (OL2; dashed green marker) and the subsequent delithiation (OL2 – 4.4 V; dashed blue marker).

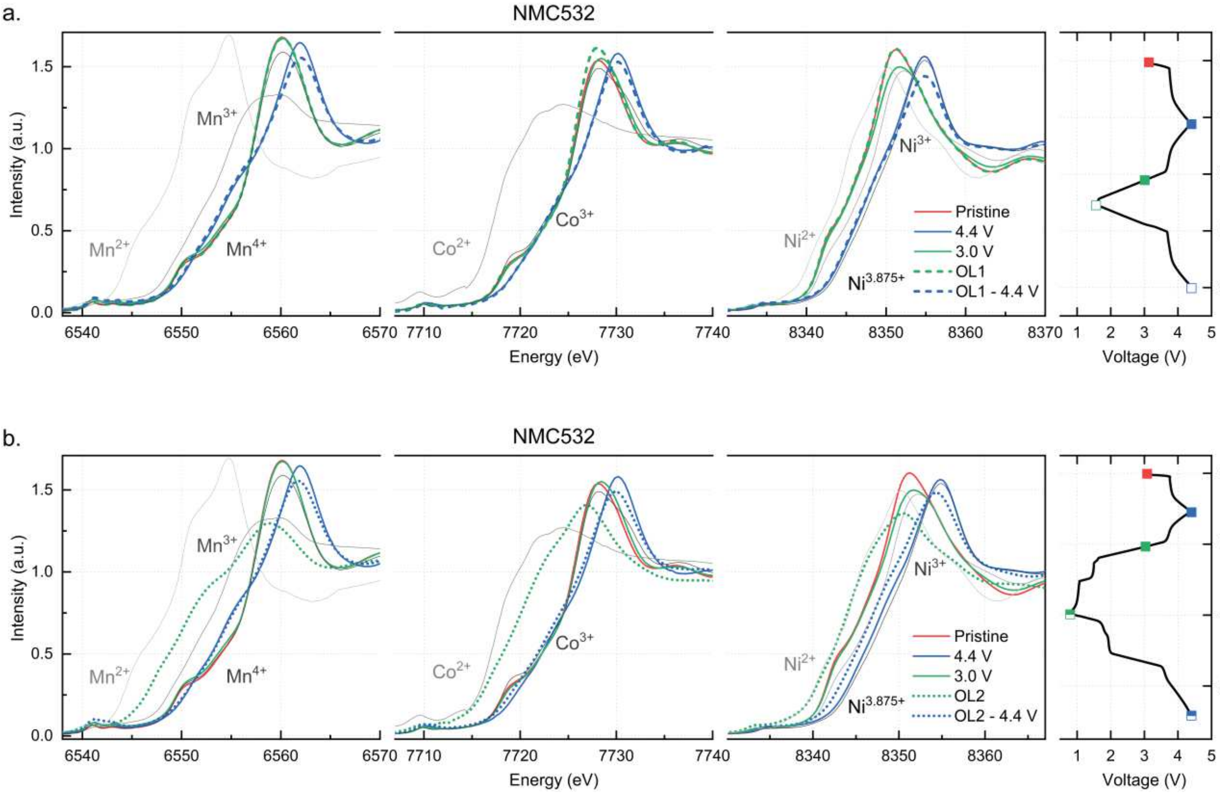

Figure 2. 14: Mn, Co, and Ni K-edge spectra of NMC532 electrodes harvested at various lithiation states with the corresponding voltage profile. NiO (Ni^{2+}), Pristine NCA (Ni^{3+}), 70% Chemically delithiated NCA (Ni$^{3.875+}$), CoCl$_2$ (Co^{2+}), Pristine LCO (Co^{3+}), MnO (Mn^{2+}), Mn$_2$O$_3$ (Mn^{3+}), Pristine NMC111 (Mn^{4+}) used as standards. Markers indicate the potential at which the electrode was harvested: full red square for the pristine NMC532, full blue square for the electrode delithiated to 4.4 V, full green square for the electrode lithiated to 3.0 V. a. Comparison of the K-edge spectra of the transitions metal after a lithiation to the initial capacity of the pristine material (OL1; empty green marker) and the subsequent delithiation (OL1 – 4.4 V; empty blue marker); b. Comparison of the K-edge spectra of the transitions metal after a lithiation to the twice the theoretical capacity of the pristine material (OL2; dashed green marker) and the subsequent delithiation (OL2 – 4.4 V; dashed blue marker).

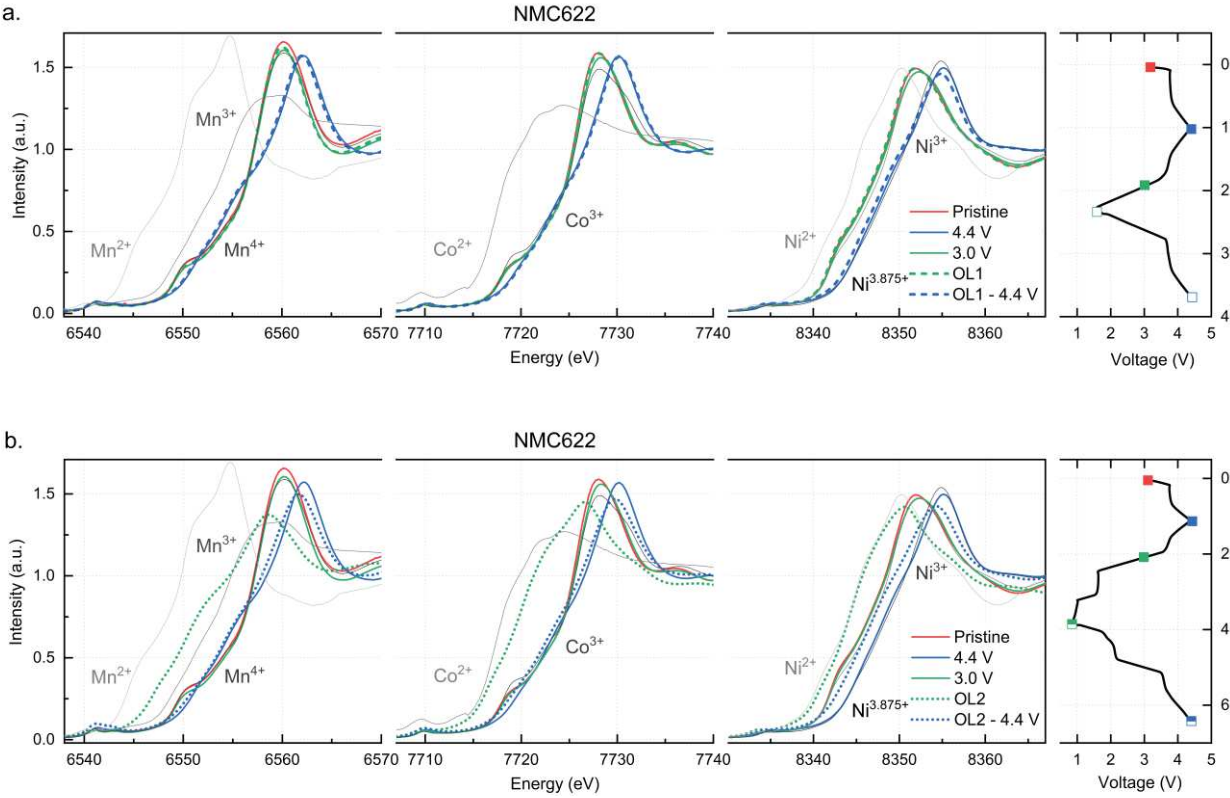

Figure 2. 15: Mn, Co, and Ni K-edge spectra of NMC622 electrodes harvested at various lithiation states with the corresponding voltage profile. NiO (Ni^{2+}), Pristine NCA (Ni^{3+}), 70% Chemically delithiated NCA (Ni$^{3.875+}$), $CoCl_2$ (Co^{2+}), Pristine LCO (Co^{3+}), MnO (Mn^{2+}), Mn_2O_3 (Mn^{3+}), Pristine NMC111 (Mn^{4+}) used as standards. Markers indicate the potential at which the electrode was harvested: full red square for the pristine NMC622, full blue square for the electrode delithiated to 4.4 V, full green square for the electrode lithiated to 3.0 V. a. Comparison of the K-edge spectra of the transitions metal after a lithiation to the initial capacity of the pristine material (OL1; empty green marker) and the subsequent delithiation (OL1 – 4.4 V; empty blue marker); b. Comparison of the K-edge spectra of the transitions metal after a lithiation to the twice the theoretical capacity of the pristine material (OL2; dashed green marker) and the subsequent delithiation (OL2 – 4.4 V; dashed blue marker).

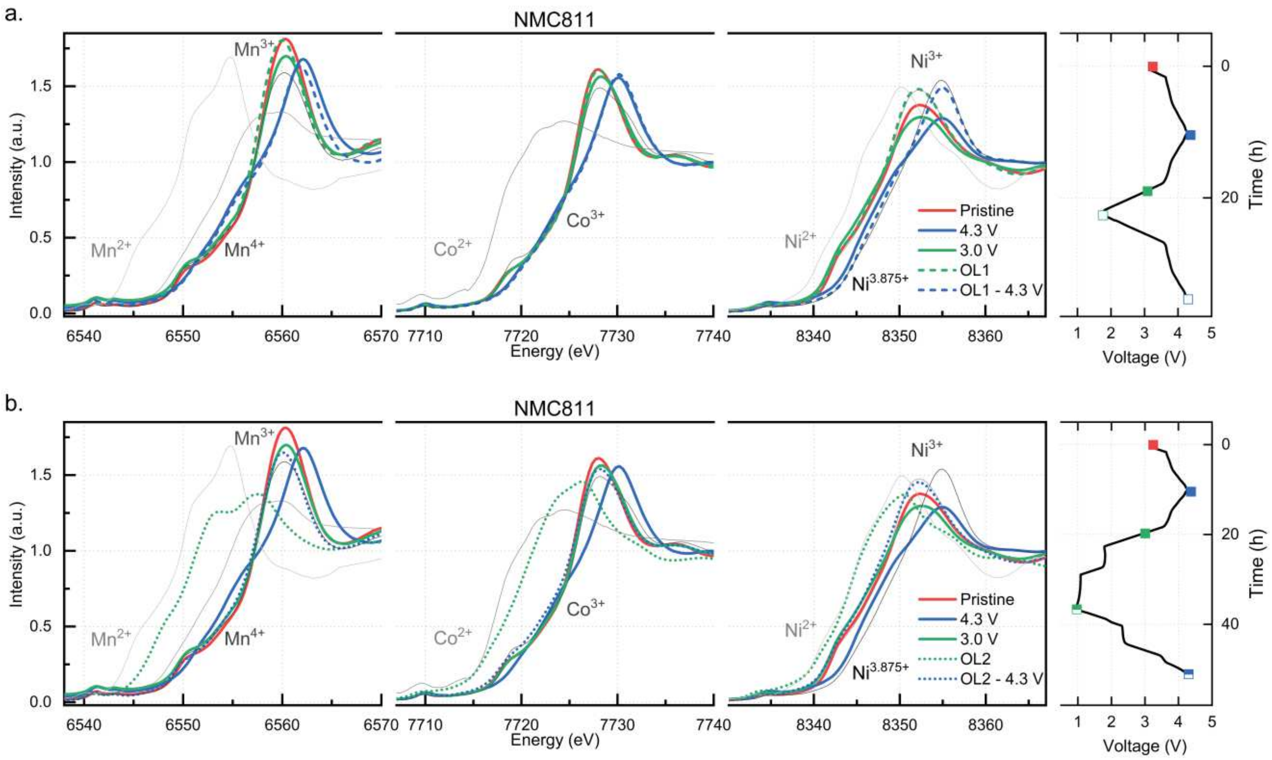

Figure 2. 16: Mn, Co, and Ni K-edge spectra of NMC811 electrodes harvested at various lithiation states with the corresponding voltage profile. NiO (Ni^{2+}), Pristine NCA (Ni^{3+}), 70% Chemically delithiated NCA ($Ni^{3.875+}$), $CoCl_2$ (Co^{2+}), Pristine LCO (Co^{3+}), MnO (Mn^{2+}), Mn_2O_3 (Mn^{3+}), Pristine NMC111 (Mn^{4+}) used as standards. Markers indicate the potential at which the electrode was harvested: full red square for the pristine NMC811, full blue square for the electrode delithiated to 4.3 V, full green square for the electrode lithiated to 3.0 V. a. Comparison of the K-edge spectra of the transitions metal after a lithiation to the initial capacity of the pristine material (OL1; empty green marker) and the subsequent delithiation (OL1 – 4.3 V; empty blue marker); b. Comparison of the K-edge spectra of the transitions metal after a lithiation to the twice the theoretical capacity of the pristine material (OL2; dashed green marker) and the subsequent delithiation (OL2 – 4.3 V; dashed blue marker)

- Detailed soft XAS study of NMC622

To distinguish between electrochemistry occurring at the surface of the particles and the changes throughout their bulk, hard XAS measurements are followed by a soft XAS study, using both Total Electron Yield (TEY) and Fluorescence Yield (FY) modes. The measurements are executed at the L-edge of Ni, Co, and Mn, probing the electron dipole transition from the 2p core level to the 3d valence states.[18] The TEY mode detects the oxidation state of the elements in the top 5 nm of the film and the FY mode probes deeper into the subsurface of the material (~50-100 nm).[19] The differences in the spectra obtained in TEY mode (surface) and FY mode (subsurface) will provide information on which electrochemical processes are first occurring at the surface of the particles. In similarity to the hard XAS study, the material NMC622 has been chosen to be investigated in greater detail.

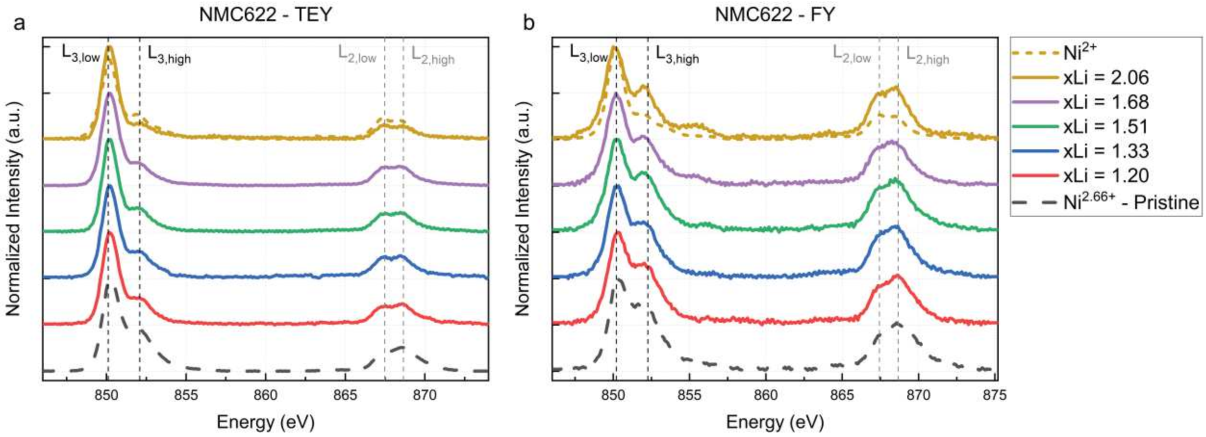

Figure 2. 17: Ni L-edge XAS spectra of NMC622 electrodes with xLi = 1.20, 1.33, 1.51, 1.68 and 2.06 compared to the pristine material and NiO standard; a. TEY; b. FY. The surface Ni appears more reduced than the subsurface Ni for all lithiation degrees.

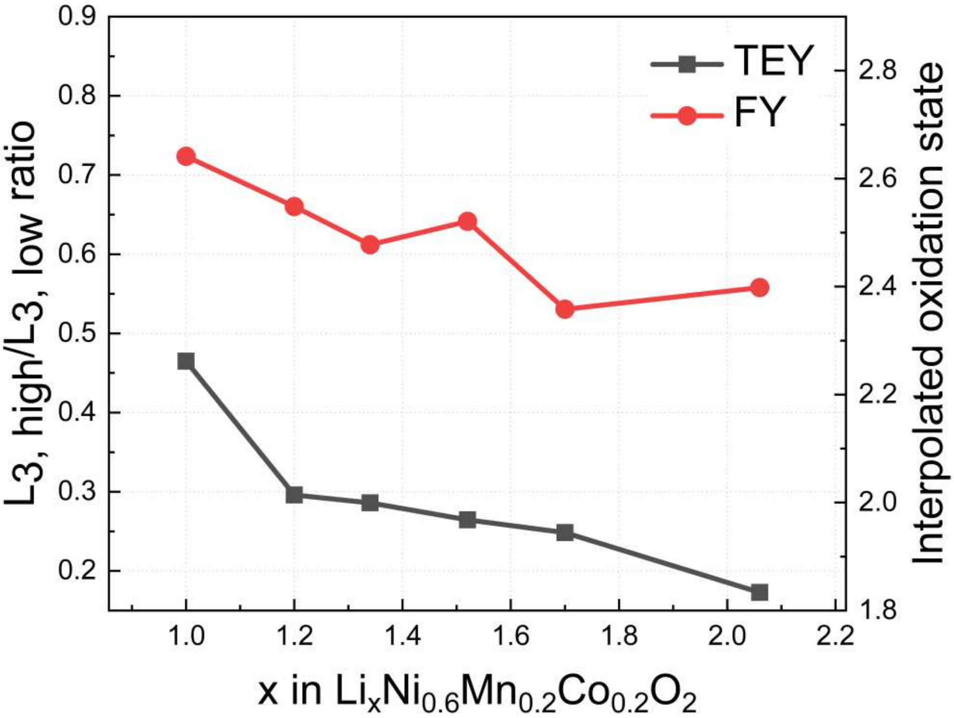

Figure 2. 18: $L_{3,high}/L_{3,low}$ ratio of the Ni L-edge XAS spectra of NMC622 electrodes with xLi = 1.20, 1.33, 1.51, 1.68 and 2.06 and the corresponding interpolated oxidation state of Ni

Ex-situ soft XAS measurements were carried out on harvested NMC622 cathode electrodes brought to the lithiation degrees of xLi = 1.20 (1.60 V), xLi = 1.33 (1.52 V), xLi = 1.51 (1.03 V), xLi = 1.68 (1.01 V) and xLi = 2.06 (0.8 V), as shown in Figure 2. 8. The changes in the Ni L-edge, in Figure 2. 17, can be interpreted by comparison of the $L_{3,high}/L_{3,low}$ ratio of the different spectra with standards,[82,83] as presented in Figure 2. 18. The L-edge of the standards used for the interpolation of the L_3 ratio to the oxidation state of Ni are presented in Figure SI. 8. The surface Ni (TEY, Figure 2. 17. a) is much more reduced than the subsurface Ni (FY, Figure 2. 17. b) for the pristine electrode, as was reported for NMC622 in the potential window of 3.0 V to 4.4 V vs Li/Li^+ by Tian et al.[43] This gradient in the Ni oxidation state within the particle continues upon deep lithiation. The surface Ni is already reduced to approximatively Ni^{2+} along the first lithiation plateau (xLi = 1.20 and 1.33), while both the subsurface and the bulk of the particles (Figure 2. 8) remain at a higher oxidation state. The persistence of the gradient in the Ni oxidation state within the particle indicates that the reduction of the Ni initiates at the surface and then propagates toward the bulk. An increase of valence is observed for the subsurface at the lithiation xLi = 1.51 and xLi = 2.06, however measurement of more samples is needed to properly interpret this result.

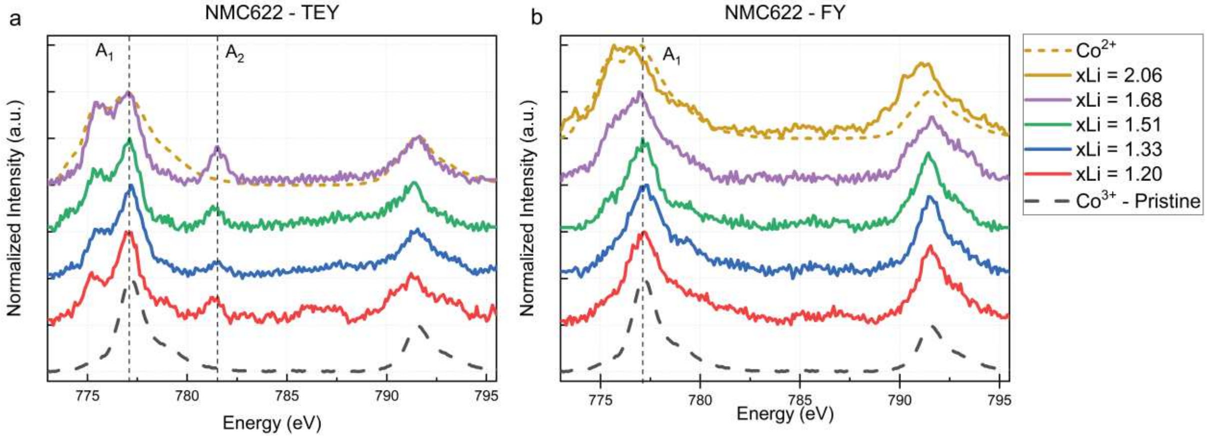

Figure 2. 19: Co L-edge XAS spectra of NMC622 electrodes with xLi = 1.20, 1.33, 1.51, 1.68 and 2.06 compared to the pristine material and CoO standard; a. TEY; b. FY; The characteristic peak position of Co^{3+} is highlighted by the position of A_1, while the peak at the position of A_2 is attributed to a metal-to-ligand charge transfer (MLCT). The TEY absorption spectra for xLi = 2.06 is not shown here, due to insufficient Co signal.

Focusing on the Co TM, the L-edge spectra shown in Figure 2. 19 are qualitatively interpreted by comparison with standards (CoO for Co^{2+} and pristine NMC622 for Co^{3+}).[84] By examining the shapes of the TEY and the FY spectra, we can observe that in similarity to Ni, there is a difference in the Co oxidation state within the particle. More specifically, a clear reduction of the surface Co can be observed upon lithiation as early as xLi = 1.20 (Figure 2. 19. a), whereas the subsurface (Figure 2. 19. b), in agreement with the hard XAS data (Figure 2. 8), shows significant reduction of the Co only along the second plateau.

We note that the Co signal for the TEY mode for the electrode lithiated to xLi = 2.06 was insufficient and is not presented here. Because a similar issue was also observed with the other minor TM component in NMC622 (Mn, Figure 2. 20), it is likely that the insufficient signal for both Co and Mn occurred due to a combination of an ex-situ measurement of a highly lithiated and therefore reactive electrode surface and the low concentration of the element in the sample, as discussed by Johnson et al.[68] In addition, Co has a satellite peak, which we label as A_2 in its TEY spectra. This peak can be attributed to the metal-to-ligand charge transfer (MLCT) transitions to unoccupied ligand orbitals, which could appear due to carbonated degradation by-products on the surface of the particles, as was previously observed for different Ni and Co systems.[85–87]

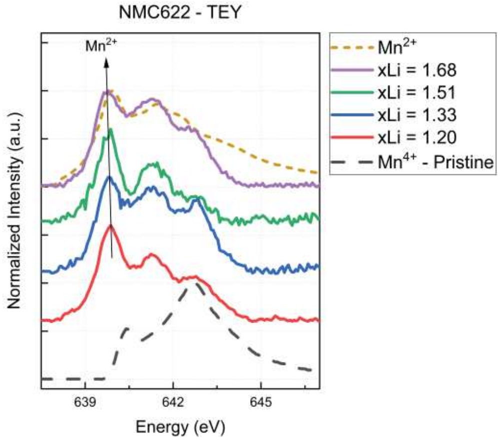

Figure 2. 20: Mn L-edge XAS spectra of NMC622 electrodes with xLi = 1.20, 1.33, 1.51, 1.68, compared to the pristine material and MnO standard; we note that despite of the precautions taken during sample transfer, a minimal exposure of the samples to air is expected and can be seen from the slight oxidation of the MnO standard, which is particularly sensitive to air. The highlighted areas mark the characteristic peaks of Mn^{2+}. The TEY absorption spectra for xLi = 2.06 is not shown here as the Mn signal was insufficient

Only TEY data is shown for the Mn L-edge XAS spectra (Figure 2. 20), as the FY signal of the Mn L-edge appears to be distorted by the O-K emissions.[18,88] The L-edge spectra are qualitatively interpreted by comparison with standards (MnO for Mn^{2+} and pristine NMC622 for Mn^{4+}). A small surface oxidation of the Mn^{2+} standard is observed and results from a minimal contact with air during transfer into the vacuum chamber of the beamline despite the measures taken.[18] Similarly to Co, a clear reduction of Mn^{4+} towards Mn^{2+} is observed for xLi

= 1.20 along the first plateau, while the reduction of the bulk Mn observed with the K-edge spectra initiates along the second plateau. As a result, it is possible to conclude that the reduction of Mn also initiates from the surface of the particles and then proceeds into their bulk.

- Soft XAS study of NMC111, NMC442 and NMC532 cathodes

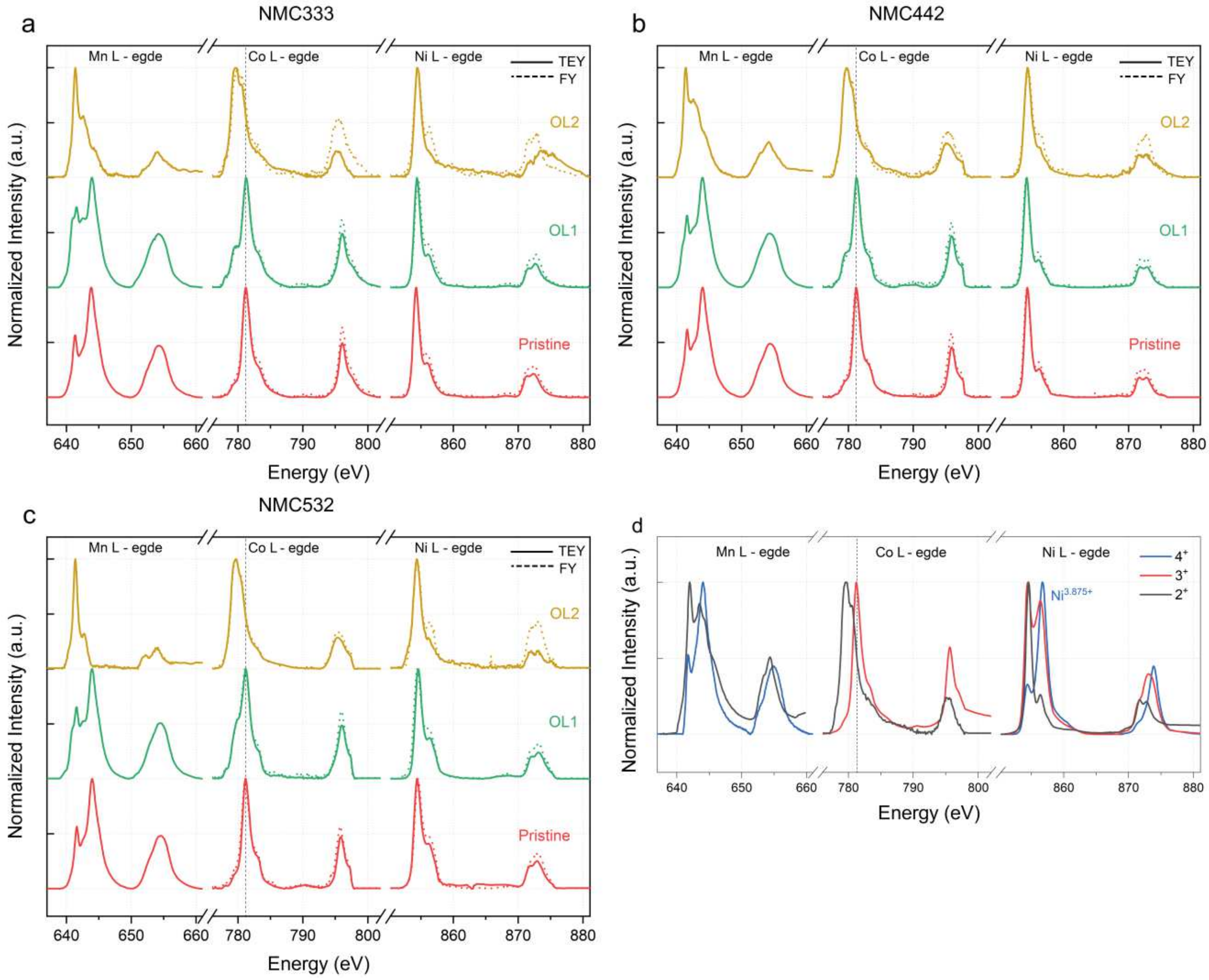

Figure 2. 21: Ni, Co, and Mn L-edge XAS spectra for the pristine material (red), electrodes lithiated to xLi = 1 (OL1 - green), and electrodes lithiated to xLi = 2 (OL2 - yellow) with the TEY spectra in full line and the FY spectra in dotted line; a. NMC111; b. NMC442; c. NMC532; d. Ni, Co, and Mn L-edge XAS spectra of the materials used as standards: NiO for Ni^{2+}, NCA for Ni^{3+}, 70% delithiated NCA for $Ni^{3.875+}$, CoO for Co^{2+},$LiCoO_2$ for Co^{3+}, MnO for Mn^{2+} and, MnO_2 for Mn^{4+}.

In similarity to NMC622 materials, NMC111, NMC442 and NMC532 are investigated with soft XAS. The surface and subsurface of the pristine electrodes was compared with the surface and subsurface of the electrodes lithiated to OL1 and OL2 in Figure 2. 21. The surface L-edge spectra (TEY – full line) is compared with the subsurface spectra (FY – dashed line) for Ni and

Co. No FY spectra was obtained for Mn as discussed in the previous section. The standards used for the interpretation of the spectra are presented in Figure 2. 21. d. The surface Ni in the pristine samples is more reduced than the subsurface, as observed with NMC622. The valence of Mn and Co in the pristine samples are respectively 4^+ and 3^+. As studied in detail with the investigation of NMC622, the beginning of the reduction of the valence of Mn and Co is observed already at OL1 for all NMCs, whereas the K-edge study showed a reduction of the bulk Co and Mn starting at the second lithiation plateau. This observation is consistent with the hypothesis made in chapter 1 of a Li-rich phase at the surface of the particles upon lithiation to OL1, leading to a reduced state for the TMs at the surface of the material. Co and Mn are further reduced towards 2^+ after lithiation to OL2. The oxidation state of the Ni is interpolated from the $L_{3,high}$/ $L_{3,low}$ ratio compared to that of standards, as described for NMC622 (Figure SI. 8). Figure 2. 22 depicts the interpolated oxidation states of NMC111, NMC442 and NMC532 for the surface and subsurface of the pristine samples, the materials lithiated to OL1 and to OL2. The oxidation state of Ni appears more reduced at the surface than in the subsurface for all NMC materials studied, indicating that the reduction of Ni initiates from the surface towards the bulk for NMC111, NMC442 and NMC532. The oxidation state of the surface Ni in NMC111 is higher than 2^+, in agreement with the bulk Ni observed with hard XAS. Very little variation of the oxidation state of Ni is observed from the samples lithiated to OL1. Surprisingly, the oxidation state of the surface and subsurface Ni observed for the samples lithiated to OL2 appears less reduced than the samples lithiated to OL1. This increase in Ni valence supports the hypothesis of charge compensation brought on Ni from a loss of Mn^{2+} ions due to dissolution.

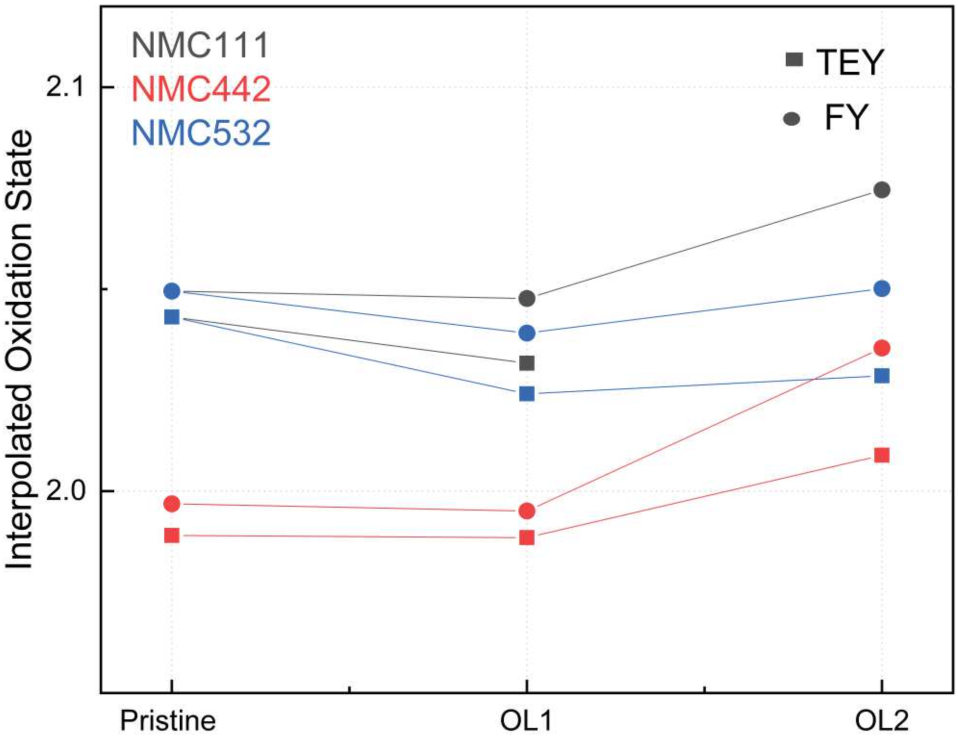

Figure 2. 22: Oxidation state of Ni interpolated from the $L_{3,high}/L_{3,low}$ ratio of the Ni L-edge XAS spectra of NMC111, NMC442, and NMC532 of pristine samples, samples lithiated to OL1 and samples lithiated to OL2. An increase in the Ni valence in the surface and subsurface is observed upon lithiation to OL2, indicative of a charge compensation of the Ni upon Mn^{2+} dissolution.

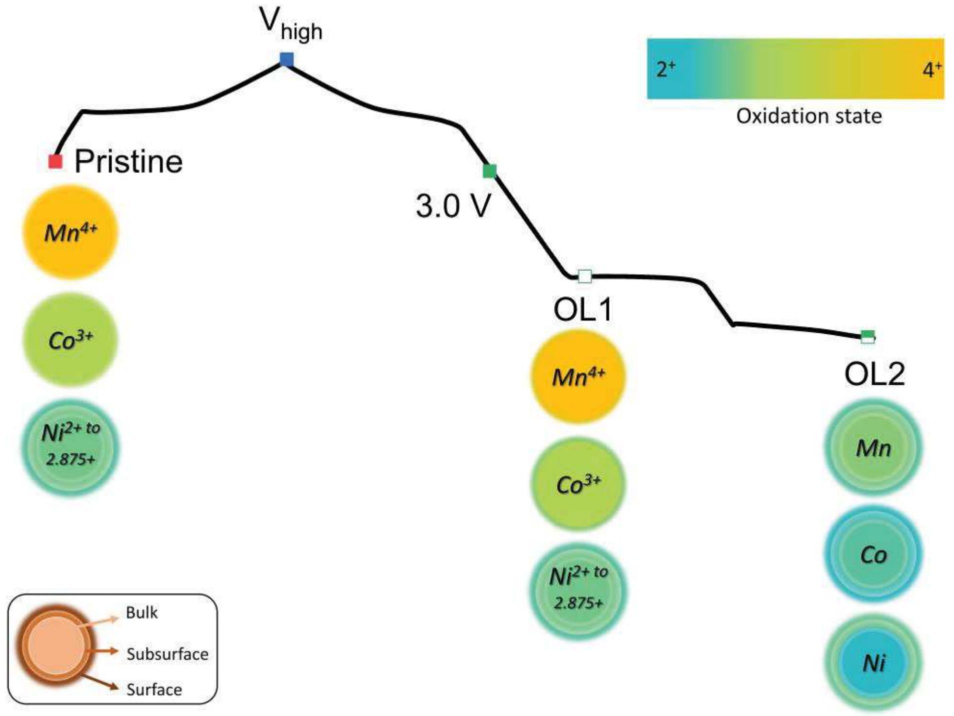

Figure 2. 23: Schematic summary of the valence changes observed in the materials with XAS upon deep lithiation. The oxidation state of the TMs in the bulk of a NMC material is written in the center of the cross-section of a particle. The oxidation state at the surface and subsurface are indicated by the color gradient on the top right. At OL1 the Mn, Co, and Ni at the surface exhibit a small reduction compared to the pristine sample. At OL2, all TMs in the bulk are reduced towards 2^+. The Mn and Co at the surface are more reduced than the subsurface and the bulk, whereas the Ni at the surface and subsurface is less reduced than in the bulk, which is consistent with a charge compensation of the surface Ni due to Mn^{2+} dissolution towards the anode.

The oxidation state of Ni, Mn, and Co in NMC622 in the bulk of the cathode have been investigated by comparison of the K-edge spectra of the TMs with that of standards. A reduction of Ni was observed upon overlithiation along the first lithiation plateau whereas the Co and Mn reduction was minimal, supporting the theoretical calculations done in chapter 1 estimating mainly the reduction of Ni along the first plateau. The transition to the second lithiation plateau marked the reduction of Mn and Co. Mn and Co and significantly reduced towards the valence 2^+ along the second plateau while Ni remained inactive. A clear reduction of all TMs was observed again at 0.8 V vs Li/Li^+. The K-edge study of NMC111, NMC442, NMC532, and NMC811 confirmed the retention of the layered structure in the bulk observed with XRD upon lithiation to OL1 with no difference observed in the oxidation state of the TMs in the bulk. All TMs showed a significant reduction upon lithiation to OL2. An increase in the reduction of Mn was observed with increasing Ni content, with NMC811 exhibiting a higher reduction for Mn and a bigger valence change for Ni. This reduction suggested a significant structure change in NMC811, supporting the higher capacity loss observed upon cycling to OL2 with electrochemistry.

The surface and subsurface of NMC622 cathodes were investigated by comparing the L-edge spectra with that of standards and interpolating the oxidation state of Ni from the $L_{3,high}/L_{3,low}$ ratio. A reduction, initiating at the surface of the material, was observed for Ni, Mn, and Co as early as the first overlithiation plateau, supporting the assumption made in chapter 1 of the formation of a Li_2MO_2 phase at the surface of the material, leading to a higher reduction in the valence of the TMs. The deep lithiation to OL2 showed a strong reduction to ~ 2^+ for all TMs. The surface and subsurface of NMC111, NMC442, and NMC532 were also studied at different lithiation degrees. The same trend was observed, with a small reduction of the surface Ni, Mn, and Co observed for the samples lithiated to OL1. While Mn and Co showed further reduction upon lithiation to OL2, a surprising increase in the valence of Ni was observed both at the surface and the subsurface of the materials. This increase in the oxidation state of Ni was interpreted as a charge compensation on the Ni upon Mn^{2+} dissolution and migration to the anode. The changes in the valence of the TMs upon lithiation confirmed the structural understanding gained with XRD and hard XAS measurements, with a negligible change induced in the valence of the TMs at the surface upon lithiation to OL1 and a significant change in the environment of the TMs upon lithiation to OL2.

3. Investigation of the reversibility of the deep lithiation process on NCM cathodes

- X-ray diffraction

In order to evaluate how the variations observed at the surface and subsurface of the particles upon deep lithiation affect the NMC materials upon delithiation, the diffraction patterns of the electrodes at V_{high}, OL1 – V_{high} and OL2 – V_{high} are plotted in Figure 2. 24.

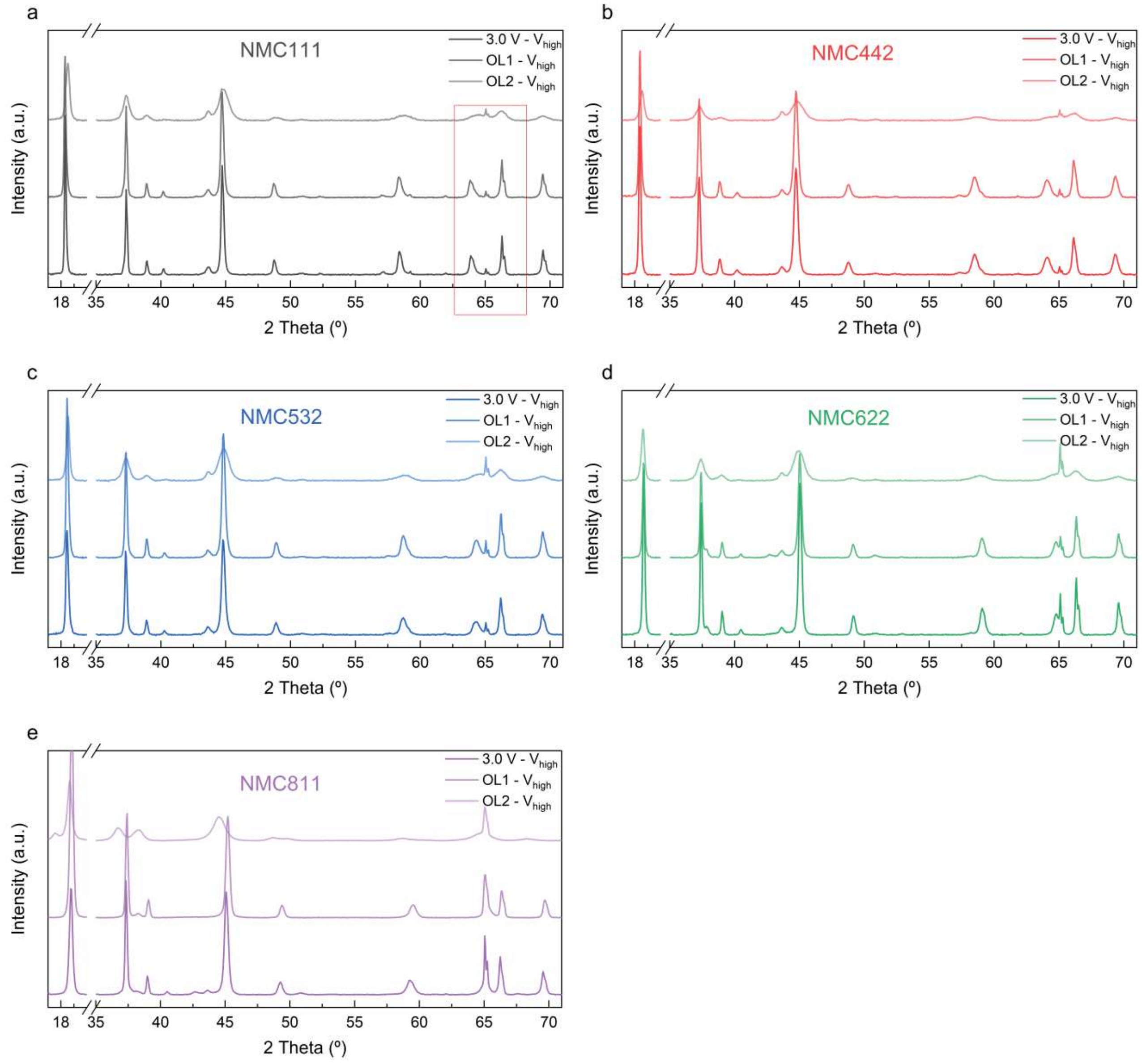

Figure 2. 24: Ex-situ X-ray diffraction patterns of cells cycled to V_{high}, to OL1 – V_{high}, and to OL2 – V_{high}; a. NMC111 (V_{high} = 4.4 V); b. NMC442 V_{high} = 4.4 V; c. NMC532 (V_{high} = 4.4 V); d. NMC622 (V_{high} = 4.4 V); e. NMC811 (V_{high} = 4.3 V); No peaks are present in the range 20-35º. No structural difference is observed upon

delithiation to V_{high} *after lithiation to OL1, whereas the peaks of the initial layered phase appear weaker and wider upon delithiation to* V_{high} *after lithiation to OL2 marking an increase of disordering in the structure.*

In similarity to what is observed upon lithiation to OL1, no significant difference is observed between NMC electrodes cycled to V_{high} and electrodes cycled to OL1 - V_{high}, indicating no structural difference induced by a lithiation to OL1 at the bulk level. This observation is in line with the reported oxidation state in the bulk of the materials upon lithiation to OL1, highlighting that the surface changes observed with the L-edge study do not hinder the regain of the layered phase reached at V_{high}. A broadening of the initial layered phase peaks can be observed upon delithiation to V_{high} after lithiation to OL2. This broadening of the 3R-$LiMO_2$ peak marks an increase in the disordering, already visible upon lithiation to OL2, which could be due to Mn loss. The structural changes observed upon lithiation to OL2 are detrimental to reversible cycling and lead to a partial disappearance of the initial 3R-$LiMO_2$ phase upon delithiation to V_{high}.

The splitting of the peaks (006)/(102) and (108)/(110) is characteristic of the layered structure.[59] It can be used to evaluate the integrity of the layered structure of the material after overlithiation. The highlighted section in Figure 2. 24. a is plotted in Figure 2. 25. We can confirm from the study of this characteristic region that the layered structure in the bulk of the material is retained after lithiation to OL1 and relithiation to V_{high} for all NMC materials. It is clear that no NMC material regains fully the layered structure in the bulk of the material after a deep lithiation to OL2, sign that the deterioration of the layered structure occurs along the low voltage plateau. The high polarization of the delithiation to V_{high} after lithiation to OL2 may result from the decrease in Li diffusivity in the NMC materials due to the loss of part of the layered structure. We suspect that regions of the material are rendered inaccessible by lithiating to OL2. We expect NMC electrodes to degrade rapidly upon continuous cycling between OL2 and V_{high} as the material does not fully maintain the layered structure in the bulk after deep lithiation and could be forming another phase.

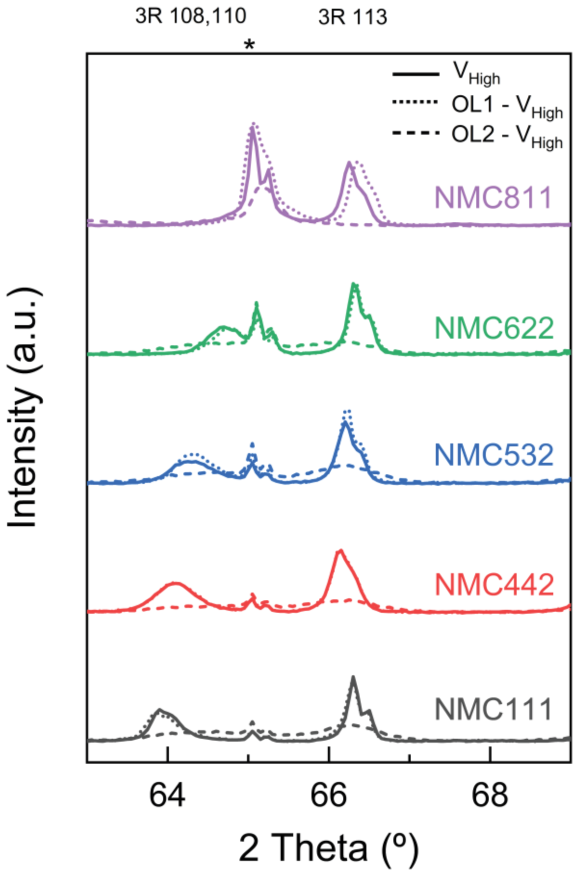

Figure 2. 25: Ex-situ X-ray diffraction patterns of NMC111 (V_{high} = 4.4 V); NMC442 V_{high} = 4.4 V; NMC532 (V_{high} = 4.4 V); NMC622 (V_{high} = 4.4 V); NMC811 (V_{high} = 4.3 V); Cells cycled to V_{high} (full lines), Cells cycled to OL1 – V_{high} (dotted lines), Cells cycled to OL2 – V_{high} (dashed lines) from 63° to 68°, where the loss of the layered structure is marked by the disappearance of the peaks (108)/(110). The Miller indices of the Bragg peaks are indicated near each peak, 3R refers to peaks of the 3RLiMO$_2$ phase, and the peaks marked by an asterisk indicate the aluminum peaks.

- Hard XAS study

The K-edge of the samples delithiated to V_{high} after lithiation to OL1 and OL2 are compared to the samples delithiated to V_{high}. Because all NMC materials but NMC811 accessed a comparable amount of capacity upon delithiation from OL2 – V_{high}, the NMC811 cathode is not included in the following discussion. A secondary set of experiment where the delithiation is controlled by coulomb counting could be designed to include NMC811 in this study, however a significant structural degradation in the material is expected. The energy of the K-edge of Mn, Co, and Ni plotted in Figure 2. 12 - Figure 2. 16 are summarized in Figure 2. 26. The good reversibility of the lithiation to OL1 in the bulk observed by XRD is confirmed by the absence of significant difference in the oxidation state of all TMs between a delithiation in the classic potential window (3.0 V – V_{high}) and a delithiation after lithiation to OL1 (OL1 – V_{high}). For NMC111, NMC442, NMC532, and NMC 622, minimal difference is observed in the oxidation state of Co and Mn upon relithiation from OL2 to V_{high} compared to the materials cycled to V_{high}. A clear reduction of the valence of Ni is observed upon relithiation from OL2 to V_{high} for all samples.

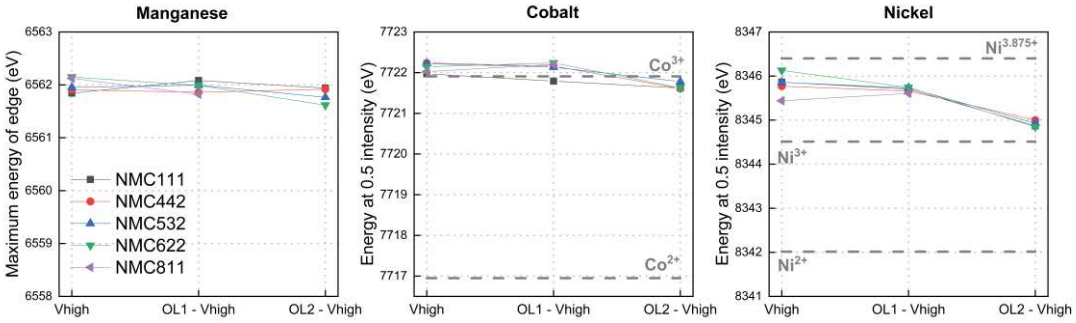

Figure 2. 26: K-edge energy of the cathodes NMC111, NMC442, NMC532, NMC622 and NMC811 in different lithiation states: first delithiation to V_{high}, *OL1 -* V_{high}, *OL2 -* V_{high}; *a. Energy of the Mn K-edge in eV; b. Energy of the Co K-edge at 0.5 intensity in e; c. Energy of the Ni K-edge at 0.5 intensity in eV. A significant Ni reduction is observed for all NMCs at OL2-*V_{high}

- Soft XAS study

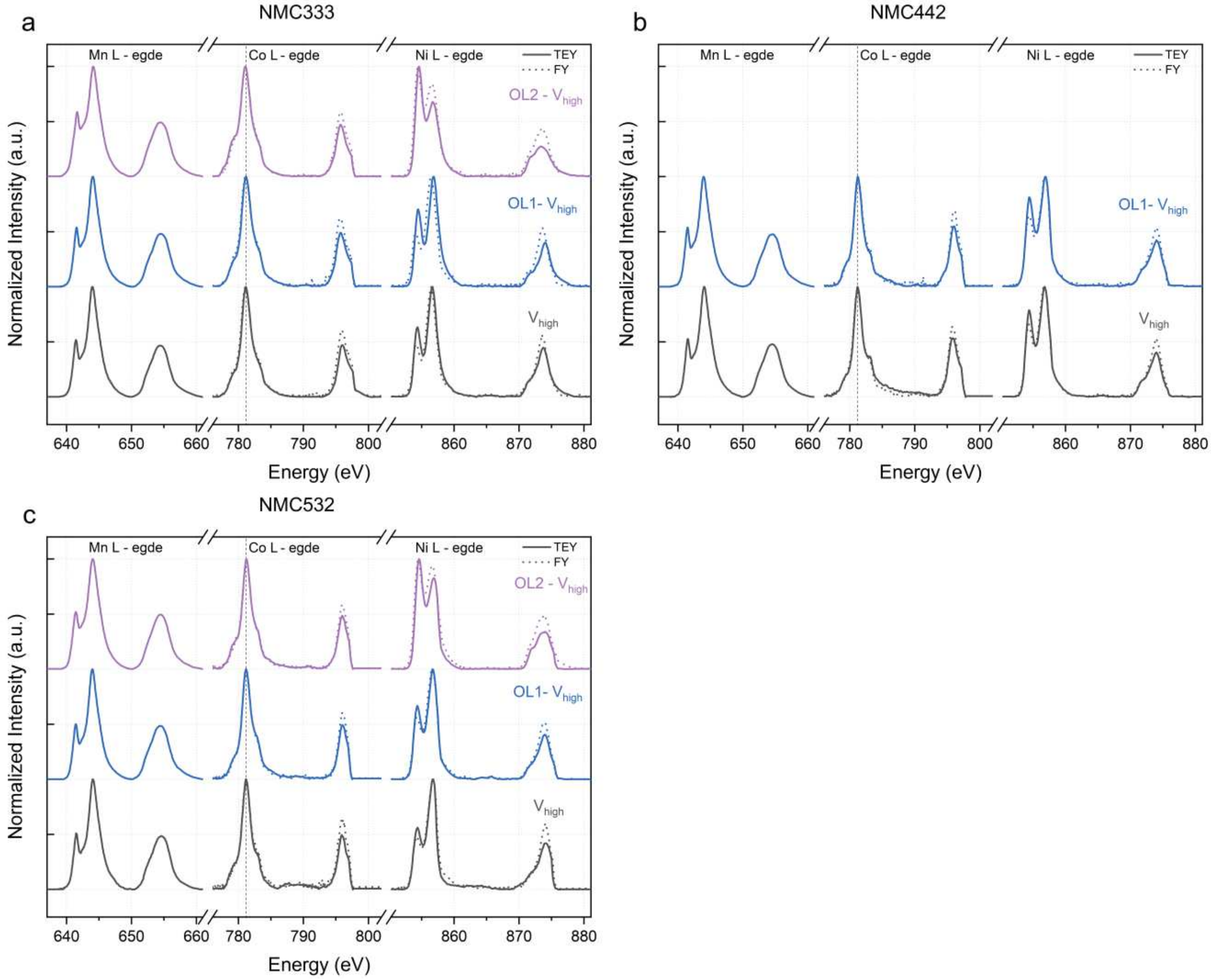

Figure 2. 27: Ni, Co, and Mn L-edge XAS spectra of different cathode material for the electrodes delithiated to V_{High} (blue), and electrodes lithiated to xLi = 1 then delithiated back to V_{High} (OL1 – V_{High} - purple) with the TEY spectra in full line and the FY spectra in dotted line. The spectra are compared to standards (grey), NiO for Ni^{2+}, delithiated NCA for $Ni^{3.7+}$, CoO for Co^{2+}, $LiCoO_2$ for Co^{3+}, MnO for Mn^{2+} and, MnO_2 for Mn^{4+}; a. $LiNi_{0.33}Mn_{0.33}Co_{0.33}O_2$ (NMC111); b. $LiNi_{0.4}Mn_{0.4}Co_{0.2}O_2$ (NMC442); c. $LiNi_{0.5}Mn_{0.3}Co_{0.2}O_2$ (NMC532). No sample was analyzed for OL2 – V_{high} of NMC442

The oxidation state of the TMs at the surface and subsurface of the NMC111, NMC442, and NMC532 materials are investigated in Figure 2. 27. The Mn L-edge and Co L-edge indicate a return to the respective valence state 4^+ and 3^+ for all materials after lithiation to OL1 as well as after lithiation to OL2. For ease of comparison, the interpolated oxidation state of Ni is plotted in Figure 2. 28. We observe a minimal change in valence state upon delithiation after lithiation to OL1. A clear reduction of the surface and subsurface is observed upon relithiation after lithiation to OL2.

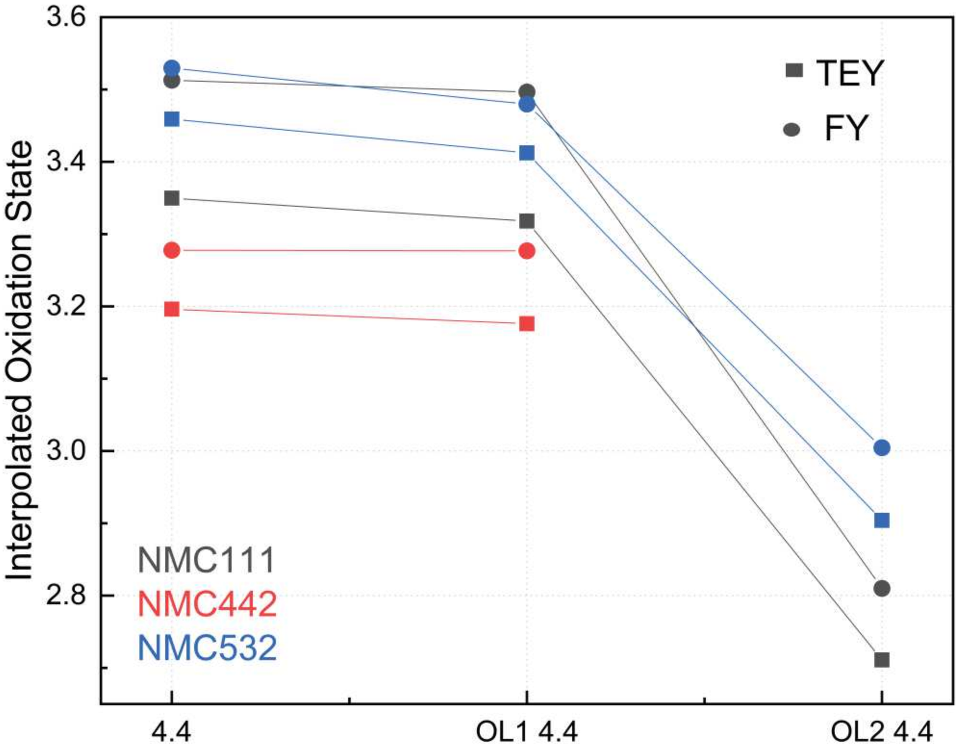

Figure 2. 28: Oxidation state of Ni interpolated from the $L_{3,high}/L_{3,low}$ *ratio of the Ni L-edge XAS spectra of NMC111, NMC442, and NMC532 of samples delithiated to* V_{high}*, samples lithiated to OL1 and delithiated to* V_{high}*, and samples lithiated to OL2 and delithiated to* V_{high}*.*

As expected from the XRD and depth-dependent XAS study at OL2, significant changes can be observed at V_{high} in materials that were lithiated to OL2 compared to materials cycled in the classic potential window. The changes in the valence of Co and Mn, known to provide structural stability in NMC cathodes, upon lithiation to OL2 may lead to a destruction of the layered phase and only partial Li disinsertion remains possible upon delithiation. Only partial samples were measured for NMC442. The study of surface of the sample NMC442 after relithiation from OL2 to V_{high} would allow confirming the creation of a new Ni-rich NMC.

- Reversibility over many overlithiated cycles investigated by electrochemistry

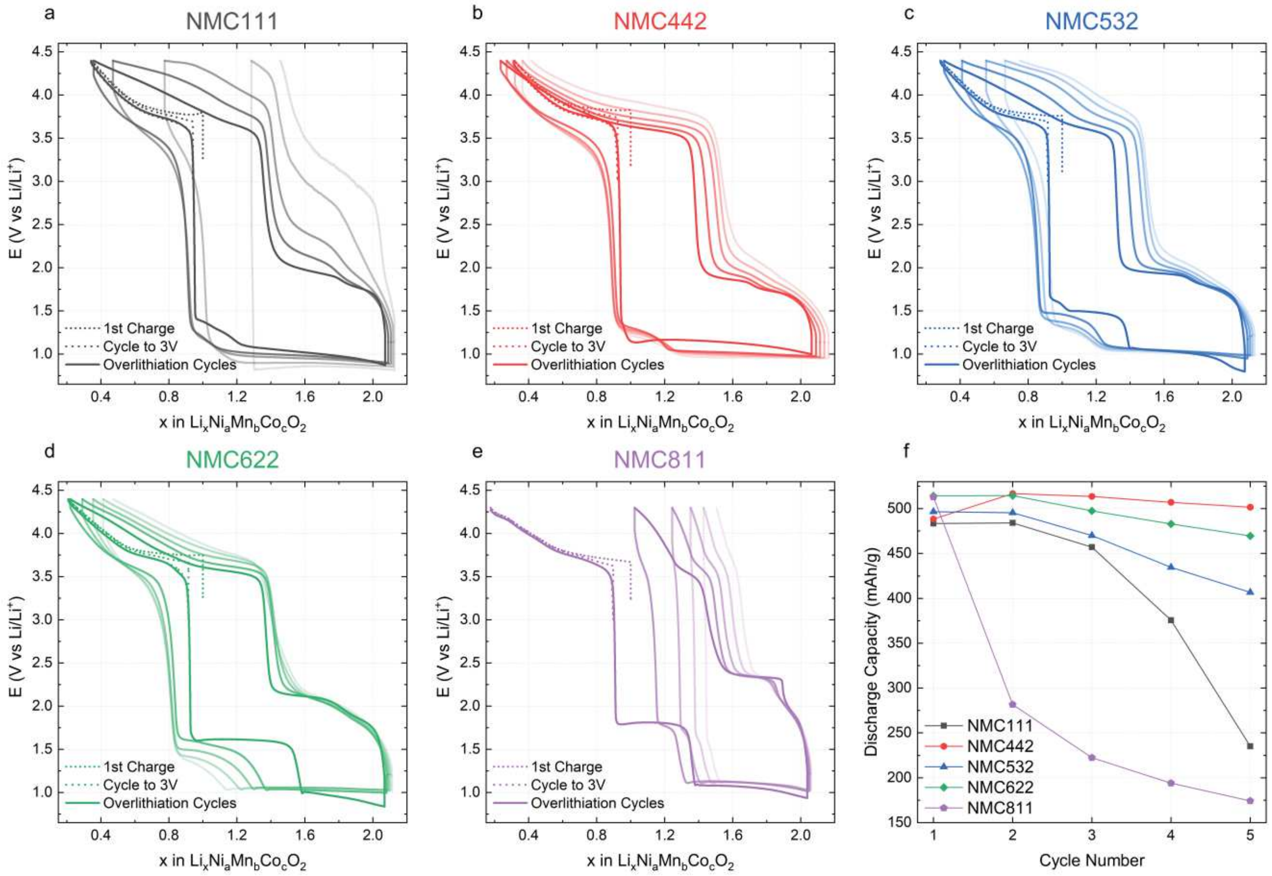

Figure 2. 29: Lithiation/delithiation profile of $LiNi_aMn_bCo_cO_2$, with a+b+c = 1, a ≥ b, 1M $LiPF_6$ in EC:DEC 50:50 half-cells cycled at 0.1C at 25ºC to V_{high} (dotted line), cycle to 3.0 V (dashed line), and cycles to xLi = 2 (called OL2) with subsequent delithiations to V_{high} with a 30 min rest between lithiation and delithiation; a. NMC111 (V_{high} = 4.4 V); b. NMC442 (V_{high} = 4.4 V); c. NMC532 (V_{high} = 4.4 V); d. NMC622 (V_{high} = 4.4 V); e. NMC811 (V_{high} = 4.3 V); f. Discharge capacity upon overlithiation vs cycle number for various cathode materials

In Figure 2. 29 are presented the lithiation profiles of NMC cathodes upon several overlithiation cycles between OL2 and V_{high}. As expected from the results obtained with XRD, partial retention of the layered structure at OL2 – V_{high} does not allow for reversibility of the deep lithiation over many cycles compared to OL1. An increase in polarization upon delithiation is observed in Figure 2. 29. a for NMC111, potentially indicating an increase in impedance at low potential upon the overlithiation cycles. The lithiation capacity to OL2 over 5 cycles is presented in Figure 2. 29. f. We can observe a gradual loss of capacity upon lithiation for NMC532 and NMC622, and a significant drop in capacity for NMC811, as only partial range of the overlithiated regime is cycled due to significant capacity loss upon the first delithiation. The loss of capacity observed is in line with the structural changes observed with

XRD and the oxidation state variation upon delithiation both in the bulk and at the surface. The NMC442 cathode first gains capacity upon delithiation possibly due to a change of NMC stoichiometry upon Mn dissolution to the anode. The subsequent overlithiation cycles reach less capacity, corroborating the hypothesis of the formation of a new Ni-rich NMC structure following the trend of NMC532 and NMC622. The significant loss of capacity of NMC111 is hypothesized as a result of hindered Li diffusion due to cation mixing.

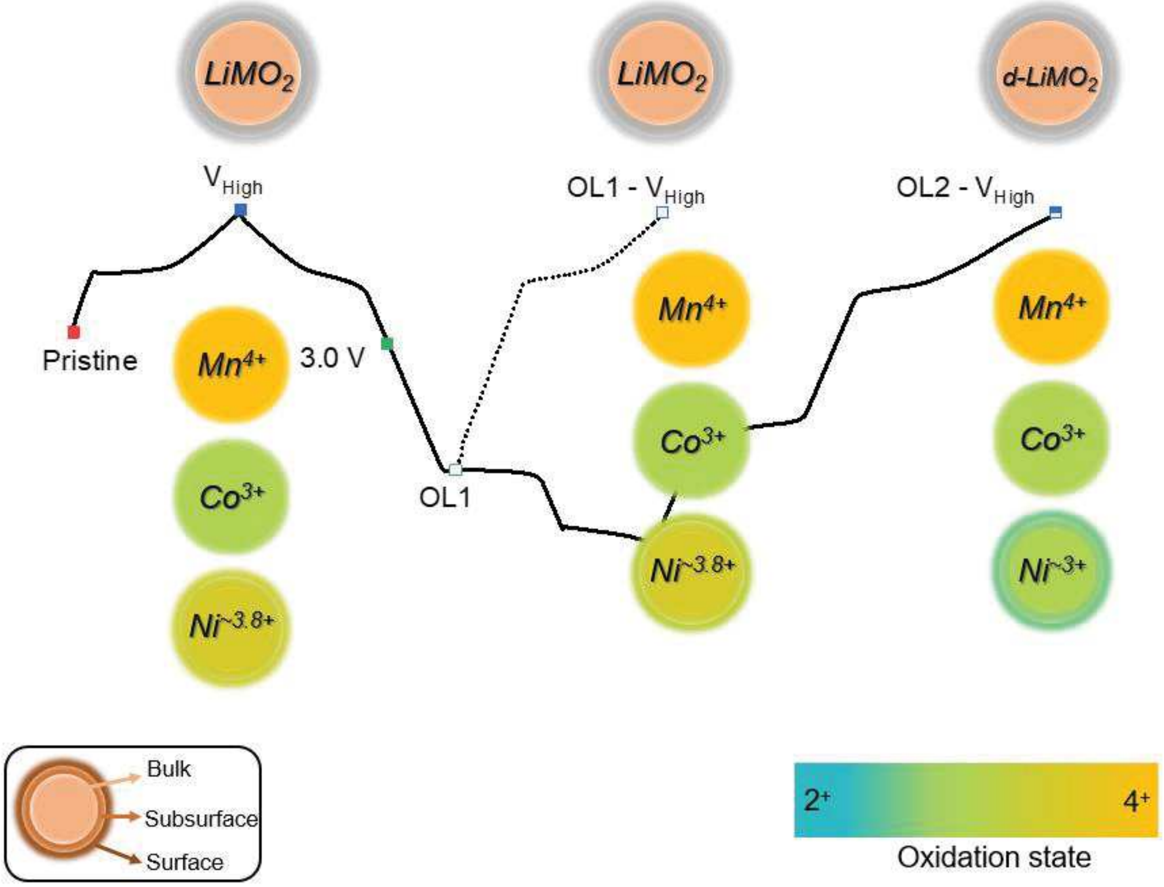

Figure 2. 30: Schematic summary of the structural changes observed in the bulk of the material with XRD and the valence changes observed in the materials with XAS upon relithiation. The oxidation state of the TMs in the bulk of a NMC material is written in the center of the cross-section of a particle. The oxidation state at the surface and subsurface are indicated by the color gradient on the bottom right. $LiMO_2$ denotes the initial layered $R\bar{3}m$ phase, Li_2MO_2 the Li-rich phase ($P\bar{3}m1$), and d-$LiMO_2$ a disordered layered $R\bar{3}m$ phase.

The reversibility of the structure of the NMC cathodes upon relithiation to V_{high} was first investigated with XRD. In similarly to the changes observed upon lithiation to OL1, no structural change was observed in the bulk of the material upon delithiation to V_{high} after lithiation to OL1. This result is in agreement with the CE of > 99% reported in chapter 1. A broadening and decrease of intensity of the 3R-$LiMO_2$ peaks was observed upon delithiation to V_{high} after lithiation to OL2, indicating a partial loss of the layered structure after deep lithiation. The XAS study of the TMs confirmed the good reversibility of the lithiation to OL1 as no difference was observed with a sample delithiated to V_{high} in the oxidation state of the TMs, both in the bulk and at the surface. A significant decrease in the valence of Ni was observed in the NMC cathodes upon delithiation to V_{high} after deep lithiation to OL2, with a lower Ni valence observed at the surface. This lower oxidation state of Ni may indicate a loss of Li to side reactions. The reversibility of NMC811 upon delithiation to V_{high} after lithiation to OL2 was not compared with the other NMC cathodes as the capacity reached was significantly lower. A comparison with the other NMC cathodes would be possible if the delithiation was controlled by coulomb counting, although significant structural degradation are expected to occur above 4.3 V vs Li/Li^+ for the material.

The reversibility of the deep lithiation was investigated for several cycles. As expected from the extensive characterization techniques used, the NMC cathodes do not sustain many overlithiation cycles over this extended potential window. The material NMC442 exhibited first an increase in the discharge capacity, hypothesized as a transformation of the material in a Ni-rich NMC upon Mn^{2+} dissolution. This interpretation is supported by the capacity loss observed over the following overlithiation cycles, following the trend observed for NMC532 and NMC622.

Summary

Through a detailed in-situ and ex-situ XRD investigation of NMC622, we have put in evidence the retention of the initial layered structure for all NMC cathodes lithiated to OL1. The surface, subsurface and bulk valence of the TMs were investigated with XAS, and highlighted the absence of variation in oxidation state of Ni, Mn, and Co in the bulk and subsurface of the material. The surface of the material exhibited a minimal reduction at the lithiation OL1, more significant for Ni. These observations are in line with the hypotheses derived from the electrochemical study of a Li-rich phase initiating at the surface of the material. The good reversibility upon delithiation to V_{high} after a lithiation to OL1 was shown with XRD, as the bulk of the material presented the same structure as the material first delithiated to V_{high}. The TMs in the bulk, subsurface, and surface of the NMC cathodes lithiated to OL1 then delithiated to V_{high} could regain the same valence as the materials initially delithiated to V_{high}, supporting the observations made with electrochemistry that the recovery of the initial layered structure was a reversible process over one cycle.

The structure of the deep lithiation was first reported for NMC622, and compared to that of the other NMC cathodes. The partial formation of a new 1T-Li_2MO_2 phase was highlighted by the appearance of a new (001) peak and the weakening and widening of the peaks of the initial layered phase. The transition to a 1T-Li_2MO_2 phase was not complete as broadened peaks of the 3R-$LiMO_2$ phase remained, suggesting a disordered layer phase and a smaller particle size. No spinel phase was observed in the bulk, nevertheless the use of additional surface sensitive characterization techniques is recommended in a follow-up study. The TMs exhibited a significant reduction towards the valence 2^+ in the bulk of the material, with the Mn and Ni appearing more reduced for the samples with the most Ni as it is the element involved in the redox over the widest potential window. A clear reduction towards the valence 2^+ was also observed for the surface and subsurface Co and Mn. Surprisingly, the oxidation state of the Ni at the surface and subsurface of the materials exhibited a higher oxidation state than the samples lithiated to OL1. This observation was correlated with the Mn^{2+} dissolution towards the anode hypothesized in the electrochemical study, which would require charge compensation for the other TMs or simultaneous oxygen loss. Upon relithiation to V_{high} after lithiation to OL2, the structure of the NMC cathodes appeared to have partially lost the layered structure, indicative of an irreversibility in the deep lithiation process due to the phase change. This observation was correlated with the oxidation state variations in the bulk of the material where Mn, Co, and mainly Ni exhibited a more reduced state at V_{high} after lithiation to OL2. The investigation of the surface and subsurface of NMC111, NMC442, and NMC532 after deep lithiation confirmed the prevalent reduction of the Ni at high potential after deep lithiation to OL2 indicative of a lower Li content, potentially marking side reactions with the electrolyte.

The anticipated lack of reversibility of the deep lithiation, hypothesized from the characterization methods, was confirmed with an electrochemical study of all NMC materials cycled between V_{high} and OL2 for 5 cycles. All NMCs exhibited a gradual loss of capacity achieved in this potential window. As expected from the previous discussions, NMC811 showed the biggest capacity loss as structural degradation lead to poor capacity recovery over one overlithiation cycle. The hypothesis of a transformation of the NMC442 electrode to a Ni-rich system was supported by the capacity loss observed after the initial increase of capacity, in line with the observations made on Ni-NMCs such as NMC532, NMC622, and NMC811.

The fundamental investigation of the deep lithiation confirmed that the surface of the material can exhibit a significantly more reduced state, hence more lithiated, upon lithiation. The reversibility of the lithiation to OL1 was confirmed, allowing the electrochemical characterization of NMC materials in this extended window for the determination of the OCP curve. Although the deep lithiation process is not sustained over mainly cycles for the NMC cathodes studied, an impressive amount of extra capacity is accessed upon one deep lithiation cycle. The implication of the TMs in the extra capacity accessed upon deep lithiation open the door to future studies that could identify a possible combination of NMC materials allowing the reversible intercalation of more than one Li ion per structure.

Chapter 3: Comparison of several electrolytes upon overlithiation of NMC622

Introduction

Electrolytes are a key component of LIBs. They usually consist of a Li salt in an alkyl carbonate solvent. The electrolyte is contained in a porous separator to ensure a physical barrier between anode and cathode, thus preventing electrical contact. The typical electrolyte consists of a $LiPF_6$ salt, with cyclic ethylene carbonate (EC) in combination with a linear carbonate such as diethyl carbonate (DEC), ethyl methyl carbonate (EMC) or dimethyl carbonate (DMC), as summarized in Figure 3. 1.

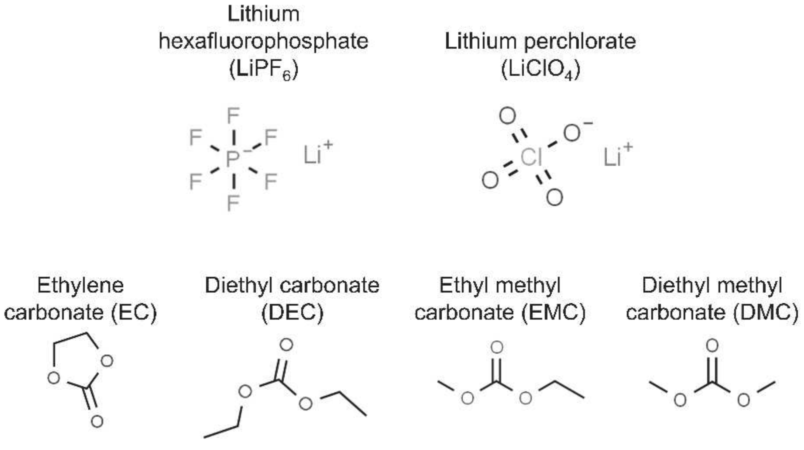

Figure 3. 1: Chemical structures of the relevant Li salts and solvents

The electrolyte in the cells is responsible for the formation of a passivation layer on the anode material called solid-electrolyte interphase (SEI).[89,90] This film of a few nanometer is electrically insulating and inhibits uncontrolled reduction of solvent species while allowing Li ions to (de)intercalate in the electrode. The SEI has been reported to contain various products such as lithium ethylene dicarbonate (LEDC) and lithium fluoride (LiF). The use of additive to design a better passivation layer has been investigated in the past few years. Two of the most popular additives, fluoroethylene carbonate (FEC) and vinylene carbonate (VC) are presented in Figure 3. 2.[91,92]

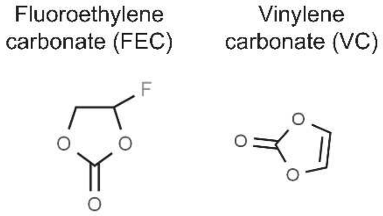

Figure 3. 2: Chemical structures of relevant electrolytes additives

Each electrolyte salt and solvent combination possesses a stability window outside of which it is subjected to reduction or oxidation of its components, leading to formation of byproducts that contaminate the cell, deteriorate the cathode material and can hinder the Li ion diffusion. Because we are cycling the cathode material in an extended potential window, it is important to estimate the impact of the electrolyte on the cathode material and passivation layers in order to understand the mechanism behind (de)intercalation of extra Li in NMC structures.

In this chapter, four electrolytes are used and compared in an electrochemical study of NMC622 upon deep lithiation: 1M $LiPF_6$ in EC:DEC, 1M $LiPF_6$ in EC:EMC:DMC, 1M $LiPF_6$ in EC:DEC:FEC, and 1M $LiClO_4$ in EC:DEC:FEC. Differences are observed upon the first delithiation due to the different passivation layers resulting from the oxidation of the solvents used. Additionally, upon delithiation after lithiation to OL2, a difference in reversibility is observed. The cathodes cycled with the electrolyte 1M $LiPF_6$ in EC:DEC:FEC are investigated with XAS and compared with cathodes cycled with 1M $LiPF_6$ in EC:DEC. A difference in valence of Co and Ni upon deep lithiation is observed and linked to the different capacity accessed, revealing side reactions in presence of FEC in the potential window of 3.0 V to 1.6 V vs Li/Li^+. Finally, the gases evolving in a NMC622 vs Li metal gas analysis cell with 1M $LiPF_6$ in EC:DEC are analyzed and no gas evolution attributed to the cathode material degradation is observed. The different electrolytes are studied in a gas analysis cell to identify potential difference in the passivation layers and electrolyte decomposition at low potential. FEC is shown to trigger CO_2 evolution and smaller amounts of ethylene gas resulting in a different cathode-electrolyte interphase (CEI), leading to a bigger capacity loss upon delithiation.

1. Electrochemical results

In order to elucidate the impact of the electrolyte on the deep lithiation of NMC cathode materials, several cells have been build and cycled in similar conditions with different industry-relevant salts and solvent combinations. The electrolytes used are summarized in Table 3. 1. The cells underwent a 6-hour acclimation step followed by a C/10 charge to 4.4 V, a C/10 cycle between 4.4 V and 3.V, and a C/10 cycle between 4.4 V and xLi = 2 (corresponding to twice the theoretical capacity of NMC622).

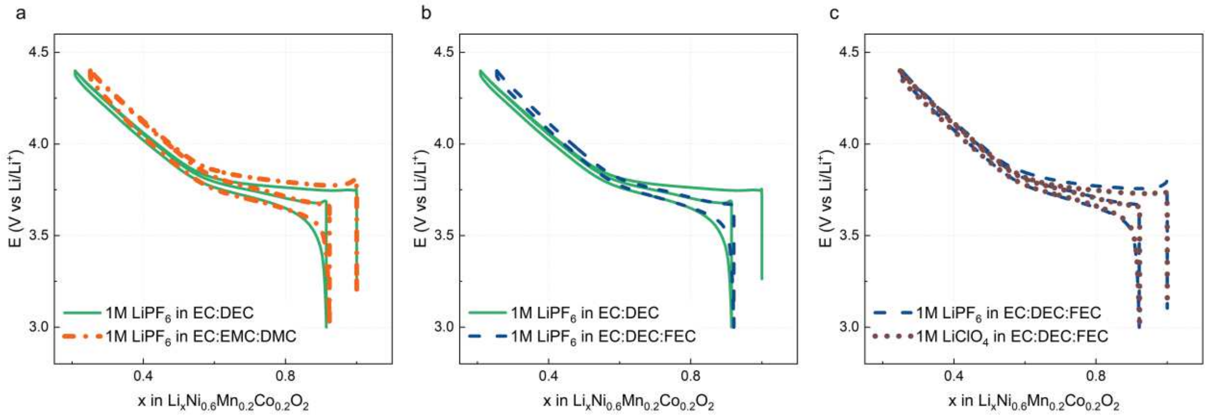

Figure 3. 3: Lithiation/delithiation profile of NMC622, half cells cycled at 0.1C with different electrolytes upon delithiation to 4.4 V vs Li/Li$^+$ and subsequent cycle between 3.0 V and 4.4 V vs Li/Li$^+$; a. 1M $LiPF_6$ in EC:DEC 50:50 and 1M $LiPF_6$ in EC:EMC:DMC 30:40:30; b. 1M $LiPF_6$ in EC:DEC 50:50 and 1M $LiPF_6$ in EC:DEC:FEC 45:45:10; c. 1M $LiPF_6$ in EC:DEC:FEC 45:45:10 and 1M $LiClO_4$ in EC:DEC:FEC 45:45:10

In Figure 3. 3 are presented the cycling profiles of NMC622 half-cells cycled with different electrolytes in the classic potential window. Differences can be observed upon the first delithiation, with the cells cycled with EC:DEC:FEC (dash – blue and dot - brown) or EC:EMC:DMC (dot/dash - orange) accessing less capacity than the cell cycled with EC:DEC (full line - green) as the solvent. Several mechanisms can explain this difference in capacity; on the anode side, a chemical reaction is initiated when the electrolyte is put in contact with Li metal, leading to the formation of a passivation layer. FEC is known to lead to more SEI formation than EC:DEC, leading to a bigger impedance.[93] This chemical reaction can occur during the acclimation step and continue throughout the first cycle, as Li from the cathode is plated on the Li metal anode and more SEI is created on the anode side. A similar rise of impedance can be observed with the EC:EMC:DMC solvent, possibly due to difference in conductivity or charge-transfer resistance leading to a higher impedance in the solvent. On the cathode side, the formation of a CEI on the NMC cathode due to the presence of FEC has been demonstrated by Hekmatfar et al.[94] They observed a CEI formation under similar cycling conditions, resulting from the dehydrofluorination of FEC to form VC and HF, with HF then reacting with Li ions to generate insulating LiF on the surface of the cathode. This increase of impedance is also observed in the CE of the first cycle, with a slightly lower first cycle CE for the electrolytes with EC:DEC:FEC, listed in Table 3. 1. The effect of the different salts and solvents is investigated upon deep lithiation in Figure 3. 4.

Table 3. 1: Capacity accessed upon first delithiation in mAh.g^{-1} and first cycle CE in %

Electrolyte	Capacity accessed upon first delithiation (mAh.g^{-1})	1st cycle CE (%)
1M $LiPF_6$ in EC:DEC	202.81	89.88
1M $LiPF_6$ in EC:EMC:DMC	200.30	89.81
1M $LiPF_6$ in EC:DEC:FEC	199.42	89.19
1M $LiClO_4$ in EC:DEC:FEC	200.93	89.65

Two similar profiles are observed when comparing the electrolytes 1M $LiPF_6$ in EC:DEC (full line - green) and 1M $LiPF_6$ in EC:EMC:DMC (dot/dash - orange), presented in Figure 3. 4. a. Two plateaus are observed, with a difference in capacity along the first plateau of ~ 20 mAh.g^{-1}, as listed in Table 3. 2. The transition from the first to the second plateau has been shown by the XAS study to be the beginning of the reduction of Co and Mn in the bulk of the material whereas Co and Mn are already reduced on the surface of the material along the first plateau. We hypothesize that the difference in capacity accessed along the first plateau is due to a small difference in charge transfer resistance between the solvents EC:EMC:DMC and EC:DEC, leading to an earlier onset for the bulk Co and Mn reduction in presence of EC:EMC:DMC. No significant difference is observed in the delithiation profile of both cells after a deep discharge to xLi = 2, leading to a similar capacity loss of 2-3 mAh.g^{-1} summarized in Table 3. 2. To the exception of a different capacity threshold for the transition of the first plateau to the second plateau, both electrolyte behave in the same fashion upon deep lithiation and subsequent delithiation to 4.4 V vs Li/Li^{+}, suggesting that the species involved in the formation of passivation films are similar between EC:DEC and EC:EMC:DMC based electrolytes.

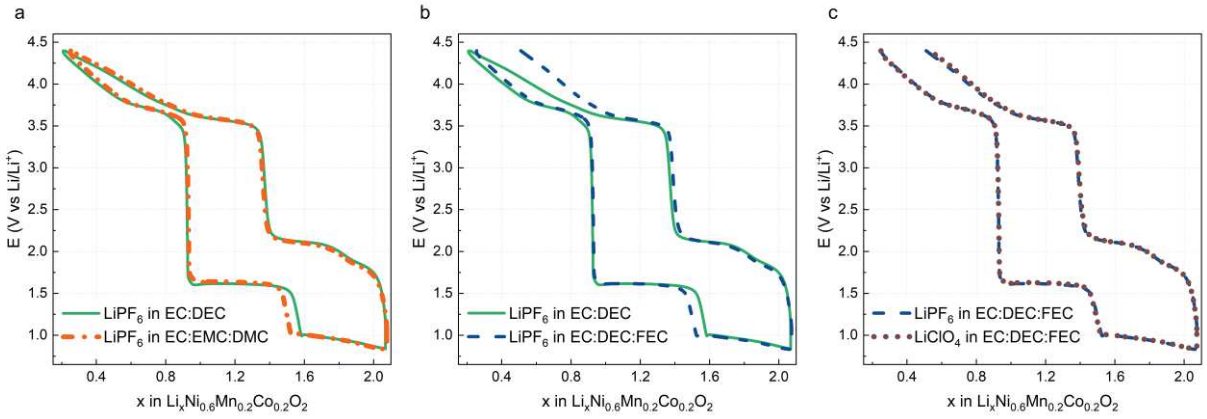

Figure 3. 4: Lithiation/delithiation profile of NMC622, half cells cycled at 0.1C with different electrolytes upon lithiation to xLi = 2 followed by the subsequent delithiation to V_{high} = 4.4 V vs Li/Li$^+$; a. 1M LiPF$_6$ in EC:DEC 50:50 and 1M LiPF$_6$ in EC:EMC:DMC 30:40:30; b. 1M LiPF$_6$ in EC:DEC 50:50 and 1M LiPF$_6$ in EC:DEC:FEC 45:45:10; c. 1M LiPF$_6$ in EC:DEC:FEC 45:45:10 and 1M LiClO$_4$ in EC:DEC:FEC 45:45:10

The addition of solvent FEC is investigated in Figure 3. 4. b by comparing the electrolyte 1 M LiPF$_6$ in EC:DEC (full line - green) with 1M LiPF$_6$ in EC:DEC:FEC (dash - blue). A difference in the capacity threshold leading to the transition from the first to the second plateau is also observed. Additionally, a significant difference is observed in the capacity lost upon delithiation after the deep lithiation. The cell cycled with the electrolyte 1M LiPF$_6$ in EC:DEC lost ~ 3 mAh.g^{-1} upon delithiation while the cell with the electrolyte 1M LiPF$_6$ in EC:DEC:FEC lost ~ 70 mAh.g^{-1}, as summarized in Table 3. 2. This difference suggests a negative effect of the FEC on the deep lithiation at low potential, potentially linked to side reactions in the electrolyte. The hypothesized side reactions may lead to the formation of byproducts at low potential in presence of FEC.

Table 3. 2: Capacity loss upon delithiation after first deep lithiation to xLi = 2 reported for each electrolyte (in mAh.g-1 and in % of capacity reached upon deep lithiation)

Electrolyte	Capacity loss upon delithiation after 1st overlithiation to xLi = 2	
	in mAhg^{-1}	in % of overlithiation capacity
1M LiPF$_6$ in EC:DEC	2.9	0.6
1M LiPF$_6$ in EC:EMC:DMC	2.1	0.8
1M LiPF$_6$ in EC:DEC:FEC	70.6	25.5
1M LiClO$_4$ in EC:DEC:FEC	78.5	28.4

In Figure 3. 4. c are presented the results of different salts tested with the solvent combination EC:DEC:FEC. Two similar profiles are observed upon deep lithiation and subsequent delithiation for the salts $LiPF_6$ (dash - blue) and $LiClO_4$ (dot - brown) in EC:DEC:FEC, supporting the initial assumption that the salt used does not influence the behavior of the NMC electrode at low potential and upon the subsequent delithiation in the potential window of interest.

A clear difference in the cycling profiles was observed depending on the electrolyte used. The capacity accessed upon the first delithiation to V_{high} was smaller for the electrolytes containing EC:EMC:DMC or EC:DEC:FEC than for the electrolyte containing EC:DEC. This small variation can be explained by a difference in conductivity or charge-transfer resistance for the electrolyte. Additionally FEC is known to lead to the formation of a passivation layer from chemical reaction on the anode upon assembly of the cell. A difference in reversibility was observed upon delithiation after lithiation to OL2 in presence of FEC, linked to suspected side reactions at low potential. As the difference in reversibility upon delithiation is expected to be correlated with the oxidation state of the TMs, a XAS study is done on NMC622 half-cells cycled with 1M $LiPF_6$ in EC:DEC:FEC.

2. XAS study of NMC622 cycled with 1M $LiPF_6$ in EC:DEC:FEC electrolyte

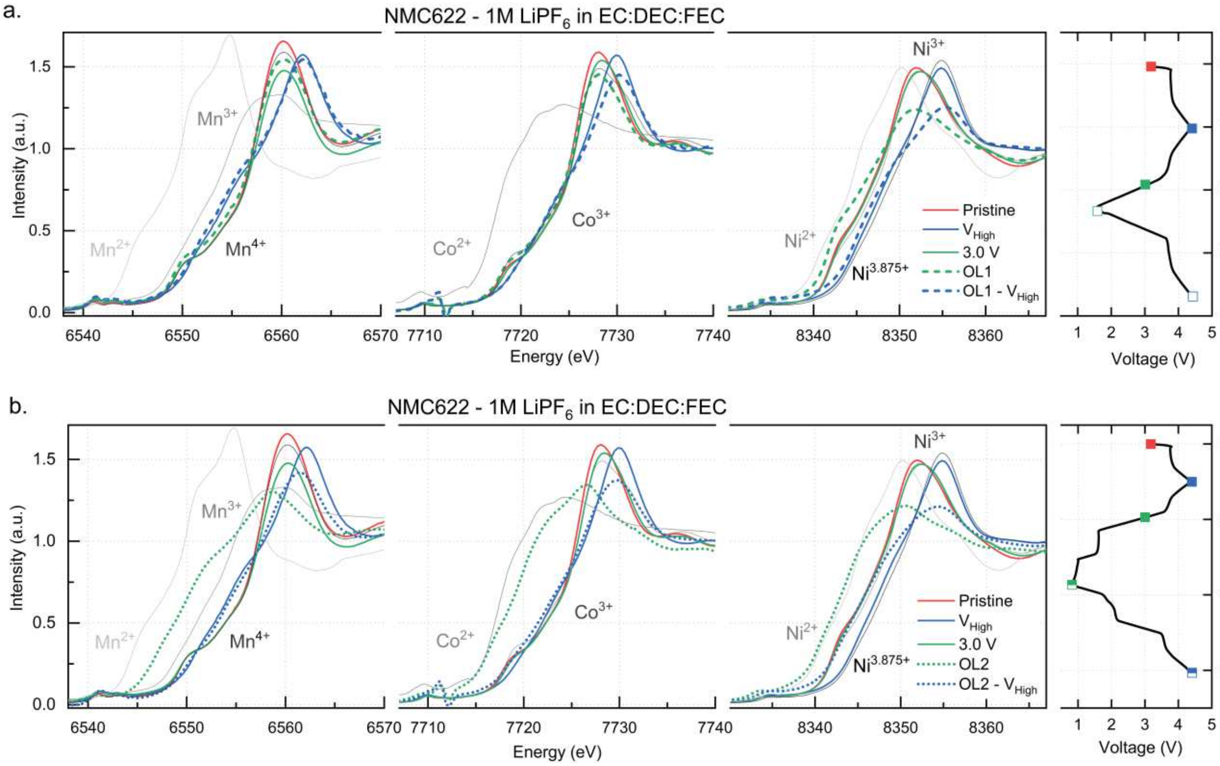

Figure 3. 5: Mn, Co, and Ni K-edge spectra of NMC622 electrodes cycled with 1M $LiPF_6$ in EC:DEC:FEC harvested at various SOCs with the corresponding voltage profile. NiO (Ni^{2+}), Pristine NCA (Ni^{3+}), 70% Chemically delithiated NCA ($Ni^{3.875+}$), $CoCl_2$ (Co^{2+}), Pristine LCO (Co^{3+}), MnO (Mn^{2+}), Mn_2O_3 (Mn^{3+}), Pristine NMC111 (Mn^{4+}) used as standards. Markers indicate the potential at which the electrode was harvested: full red square for the pristine NMC622, full blue square for the electrode charged to 4.4 V, full green square for the electrode discharged to 3.0 V. a. Comparison of the K-edge spectra of the transitions metal after a lithiation to the initial capacity of the pristine material (OL1; empty green marker) and the subsequent delithiation (OL1 – 4.4 V; empty blue marker); b. Comparison of the K-edge spectra of the transitions metal after a lithiation to the twice the theoretical capacity of the pristine material (OL2; dashed green marker) and the subsequent delithiation (OL2 – 4.4 V; dashed blue marker).

In Figure 3. 5 are presented the K-edge spectra of Mn, Co, and Ni for NMC622 cathodes harvested from half-cells cycled with 1M $LiPF_6$ in EC:DEC:FEC at the different lithiation degrees indicated on the right. In similarity to the K-edge study of NMC622 cycled with 1M $LiPF_6$ in EC:DEC presented in Figure 2. 15, a clear shift of energy of the spectra towards the lower energy is observed upon deep lithiation to OL2 in the section b, indicating a reduction of all TMs towards 2^+. In contrast with the previous observations, a significant reduction of Ni is also observed upon lithiation to OL1. In order to compare 1M $LiPF_6$ in EC:DEC and in

EC:DEC:FEC, the energy of the edge at 0.5 normalized intensity for Co and Ni are plotted in Figure 3. 6. b and c, and the maximum energy of the edge of the K-edge spectra is plotted in Figure 3. 6. a for both electrolytes.

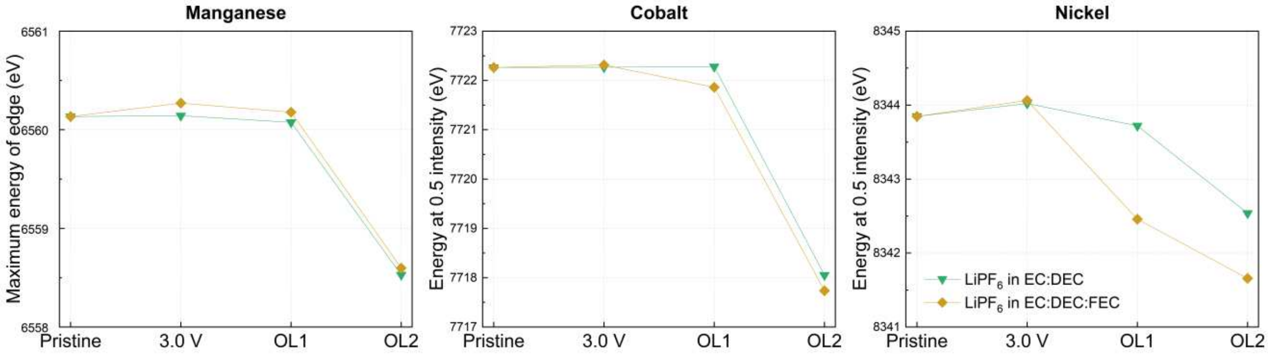

Figure 3. 6: K-edge energy of NMC622 with 1M LiPF$_6$ in EC:DEC and 1M LiPF$_6$ in EC:DEC:FEC in the pristine state, lithiated to 3.0 V, lithiated to OL1, lithiated to OL2; a. Energy of the Mn K-edge in eV; b. Energy of the Co K-edge at 0.5 intensity in e; c. Energy of the Ni K-edge at 0.5 intensity in eV. A clear difference in reduction of Ni can be observed at OL1 and OL2.

The oxidation state of Co and Mn in the cathodes cycled with 1M LiPF$_6$ in EC:DEC:FEC follows the observations made for the electrolyte 1M LiPF$_6$ in EC:DEC. A clear difference is observed for Ni, with a significantly bigger reduction observed in presence of FEC for both cathodes lithiated to OL1 and OL2. The oxidation state variation of Ni in the bulk of the material between the cathodes lithiated to 3.0 V vs Li/Li$^+$ and the cathodes lithiated to OL1 are listed in Table 3. 3. The corresponding capacity accessed by such oxidation state variations is calculated and compared to the actual capacity reached in this window of ~ 22.84 mAh.g^{-1}. The changes in oxidation state of Ni observed for the cathodes cycled with 1M LiPF$_6$ in EC:DEC are in good agreement with the electrochemical data. The changes in oxidation state of Ni for the cathode cycled with 1M LiPF$_6$ in EC:DEC:FEC however correspond to significantly bigger capacity than the capacity accessed, indicating important side reaction in this potential region due to the presence of FEC in the electrolyte. The variations of the oxidation state of Ni from OL1 to OL2 appear to follow the same trend for both electrolytes.

Table 3. 3: Calculation of the capacity corresponding to the observed oxidation state variations of Ni

Element	Ni in NMC622 cycled with 1M $LiPF_6$ in EC:DEC	Ni in NMC622 cycled with 1M $LiPF_6$ in EC:DEC:FEC	Capacity reached with electrochemistry
Valence change from 3.0 V to OL1	$2.80^+ \rightarrow 2.68^+$ ~ 0.12	$2.80^+ \rightarrow 2.17^+$ ~ 0.63	
Corresponding capacity ($mAh.g^{-1}$)	19.90	105.20	22.84

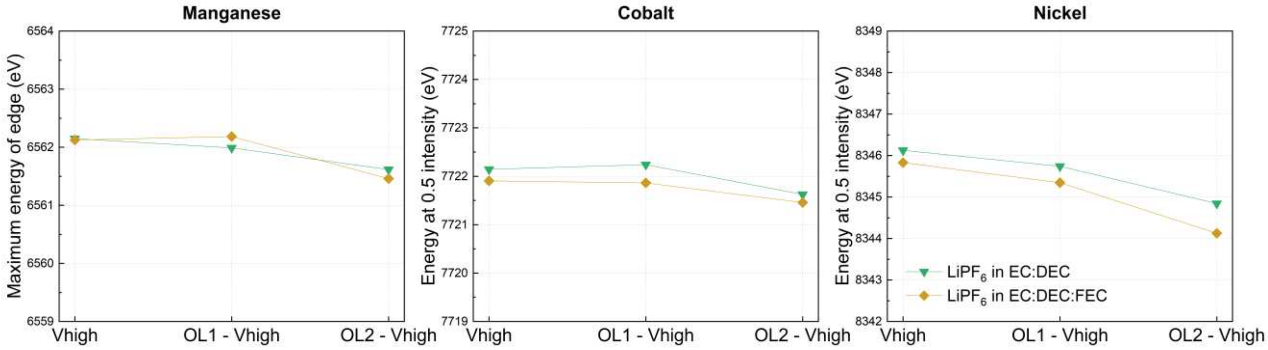

Figure 3. 7: K-edge energy of NMC622 with 1M $LiPF_6$ in EC:DEC and 1M $LiPF_6$ in EC:DEC:FEC in different lithiation states: first delithiation to V_{high}, OL1 - V_{high}, OL2 - V_{high}; a. Energy of the Mn K-edge in eV; b. Energy of the Co K-edge at 0.5 intensity in e; c. Energy of the Ni K-edge at 0.5 intensity in eV.

In Figure 3. 7 are summarized the variations of the K-edge energy of the TMs of NMC622 cathodes cycled with 1M $LiPF_6$ in EC:DEC and with 1M $LiPF_6$ in EC:DEC:FEC. A minimal variation of the oxidation state of all TMs is observed at V_{high} between the two electrolytes tested, reflecting the different capacity reached upon first delithiation observed with electrochemistry. This minimal variation persists after cycling to OL1. In similarity to the previous observations made for NMC622 cycled with $LiPF_6$ in EC:DEC, structural degradation of the NMC cathode does not allow the TMs to regain the same environment upon delithiation to V_{high} after deep lithiation to OL2.

The comparison of the oxidation state of cathodes cycled in 1M $LiPF_6$ in EC:DEC:FEC with that of 1M $LiPF_6$ in EC:DEC highlighted changes in Ni valence upon lithiation to OL1. The capacity corresponding to the valence change in the potential window 3.0 V – OL1 (1.60 V vs Li/Li^+) was calculated and compared to the observed capacity reached with electrochemistry. The changes in Ni valence in presence of FEC represent a much bigger capacity than observed with electrochemistry, highlighting the presence of side reactions in this potential window for this electrolyte. A gas analysis study is performed on cells with different electrolytes in order to elucidate the products of such side reactions as well as investigate potential gases resulting from structural changes in the NMC622 cathode.

3. OEMS experiments in a custom gas analysis cell

To understand the reasons behind the lower reversibility in electrochemistry and associated oxidation state changes, we carry out a series of OEMS gas analysis experiments. Using the custom mass spectrometer setup, we analyze the evolution of gases in an in house cell design with different types of electrodes and different electrolytes. First, NMC622 electrodes coated on polyolefin porous separator (Celgard 2325) were used to perform a series of lithiation/ delithiation in a half- cell with a Li metal foil and 100 µL of 1M LiPF6 in EC:DEC in order to investigate the gases evolving at low potential. In a second set of experiments, a carbon paper electrode was used to perform cyclic voltammetry experiments using Li metal foil as a counter and reference electrode in order to isolate the contribution of the electrolyte in the observed gas evolution.

The electrochemistry of the gas analysis cell was first compared with the coin cell cycling in order to validate the use of the OEMS for operando measurements. Given the difference in loading between our in-house NMC622 electrode and the NMC622 electrode coated by CAMP, it was found that a C/10 C-rate did not exhibit a significant length of the plateaus to observe clear gas evolution with the in-house electrode, and a C/20 C-rate was applied. To be able to compare the gas evolution in the classic potential window (4.4V – 3.0 V vs Li/Li^+) with that of the extended potential window (4.4V – 0.8 V vs Li/Li^+), a first cycle between 4.4 V and 3.0 V vs Li/Li^+ was performed. With the addition of a deep lithiation followed by a delithiation back to 4.4 V vs Li/Li^+, the time scale of the measurement exceeds the time scale usually reported for OEMS measurements (≈ 120 hours for the extended potential window vs ≈ 30 hours for reported OEMS measurements). Therefore, the following OEMS measurements are expected to exhibit some air intrusion and the volume of the cell can slightly fluctuate. The ion currents were converted to ppm and $\mu mol.m^{-2}$ but will be interpreted qualitatively.

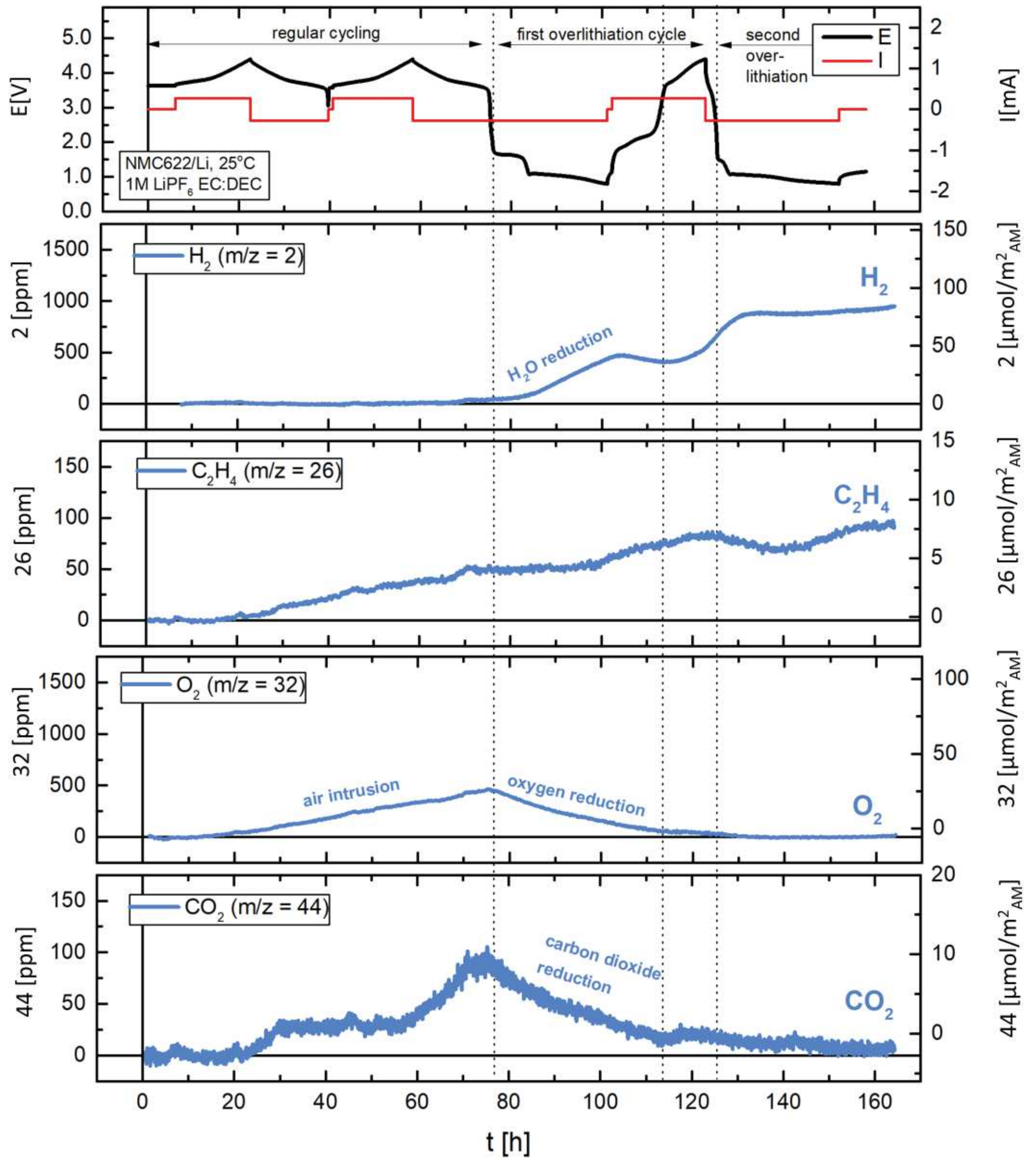

Figure 3. 8: OEMS analysis in a custom-made cell hardware containing a NMC622 electrode coated on Celgard vs. Li/Li$^+$ with 100µL 1M LiPF$_6$ in EC:DEC at 25 ℃; Cell kept at OCV for 6 hours then cycled between 4.4 V and 3.0 V at C/20 followed by two discharge cycles between 4.4 V and 0.8 V

The gas evolution in a cell containing NMC622 electrode and 1M LiPF$_6$ in EC:DEC electrolyte at low potential is presented in Figure 3. 8, with the different ion currents corresponding to H_2 (m/z = 2), C_2H_4 (m/z = 26), O_2 (m/z = 32), and CO_2 (m/z = 44). The evolution of hydrogen (H_2) below 1.5 V vs. Li/Li$^+$ corresponds to reduction of residual water in the electrolyte according to the reaction equation [1], as reported in literature.[22] The presence of residual water in the electrolyte can be due to the storage method in the glovebox and is expected to increase over time. The use of molecular sieve is recommended to limit the residual water in the electrolyte in the future, however battery electrolytes typically contain ~20 ppm H_2O and water can also be introduced through the electrodes even after thorough drying. The continuous evolution of hydrogen is believed to come from reduction of water or HF impurities or reduction of protonic electrolyte oxidation species similar to reaction [2].

$$H_2O + e^- \rightarrow OH^- \text{ to } {}^1\!/_2 H_2 \qquad [1]$$

$$HF + e^- \rightarrow F^- + {}^1\!/_2 H_2 \qquad [2]$$

The evolution of ethylene gas (C_2H_4) is first increasing constantly due to reduction of ethylene carbonate at the metallic Li electrode, where fresh Li surface is created by plating Li initially contained in the cathode. A clear increase of ethylene gas is observed when the potential reaches 0.8 V vs. Li/Li$^+$, which corresponds to the reduction of EC now at the cathode according to reaction [3].[21,95] During the second deep lithiation to 0.8 V vs. Li/Li$^+$, an increase of the ethylene gas can also be observed, confirming the potential dependence of this reaction. The evolution of the oxygen (O_2) in the cell can be linked to air intrusion due to the time scale of the experiment. The residual oxygen is then reduced according to reaction [4].[96] The observed increase of carbon dioxide (CO_2) has been reported in literature as an oxidation of the surface carbonates as well as the electrolyte.[24,97,98] A reduction of the CO_2 is observed below ~1 V vs. Li/Li$^+$ due to the consumption of CO_2 at the cathode surface and incorporation of CO_2 into the CEI formed on the cathode at such low voltage.[95]

$$EC + 2Li^+ + 2e^- \rightarrow LEDC + C_2H_4 \qquad [3]$$

$$O_2 + 2e^- + 2Li^+ \rightarrow Li_2O_2 \qquad [4]$$

No other gas evolution than known low-voltage gassing reactions are observed from the deep lithiation of NMC622 at 25°C. In an attempt to increase the amount of gases produced and identify subtle changes that would have been missed with the experiment at 25°C, a similar cell is built and tested at 50°C.

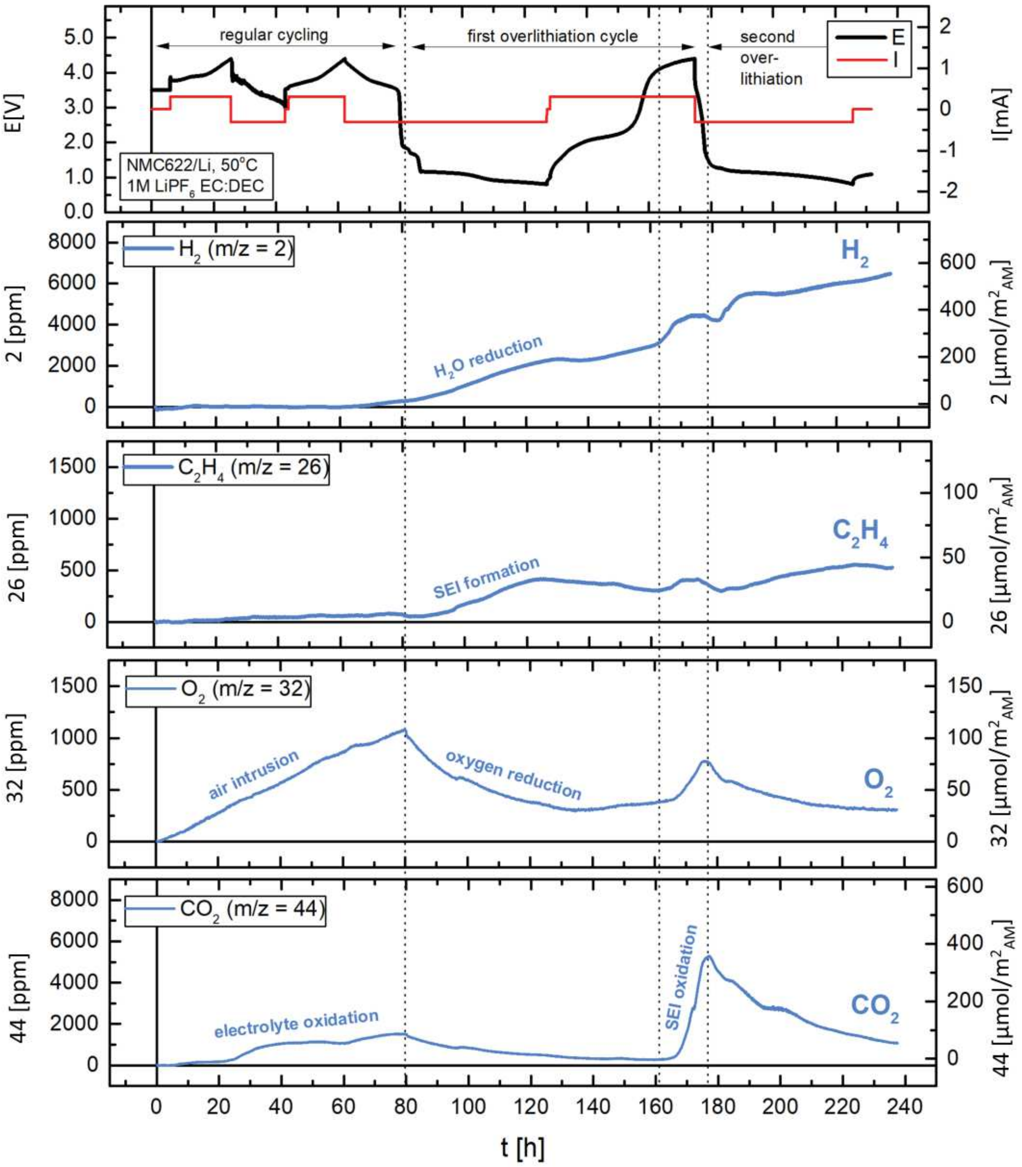

Figure 3. 9: OEMS analysis in a custom-made cell hardware containing a NMC622 electrode coated on Celgard vs. Li/Li$^+$ with 100µL 1M LiPF$_6$ in EC:DEC at 50 °C; Cell kept at OCV for 6 hours then cycled between 4.4 V and 3.0 V at C/20 followed by two discharge cycles between 4.4 V and 0.8 V

As seen in Figure 3. 9, where the data is reported on a different scale, the increase in temperature from 25°C to 50°C intensifies significantly the amount of gases produced in the cell. At higher temperature, both the ionic conductivity of Li salt and the rate of chemical reactions, which follow the Arrhenius equation, are increased.[23] Similarly to the results presented in Figure 3. 8, residual water reduction and protonic electrolyte oxidation lead to hydrogen evolution upon cycling. For this experiment, the ethylene gas evolution is clearly triggered below 0.8 V vs. Li/Li$^+$ and corresponds to the reduction of EC, known to form a SEI layer in full cells.[99] From this analysis, we can conclude that at ~ 0.8 V vs. Li/Li$^+$, a reduced layer is formed on the cathode electrode. In agreement with previous reports, an oxidation of this layer is observed at higher potential, indicated by a significant production of carbon dioxide.[100] This observation confirms the reversibility of this process observed with electrochemistry and that it is still electrically connected. The elevation of temperature has increased the amount of gases produced but similarly to the experiment at 25°C, the gases evolving arise from known low-potential reactions and not triggered by the cathode material degradation.

A second type of cells was built in order to elucidate the influence of the electrolyte on the observed electrochemistry at low potentials. The cathode was replaced by a carbon paper to minimize the structural degradation of the electrode and to be able to quantify the gases evolving in the cell over several low potential cycles. The cells were kept at OCV for 6 hours and cyclic voltammetry was performed from OCV between 0 V and 1.5 V vs Li/Li^+. In contrast with the previous experiments where the batteries were cycled at constant current, similarly to a real application, we now use a voltage-controlled cyclic voltammetry sweep to investigate the potential dependence of the electrolyte reduction processes and clearly resolve the onset potentials. The results presented in Figure 3. 10 show for each cell the potential and current profiles vs. time as well as the normalized ion currents and corresponding concentrations vs. time.

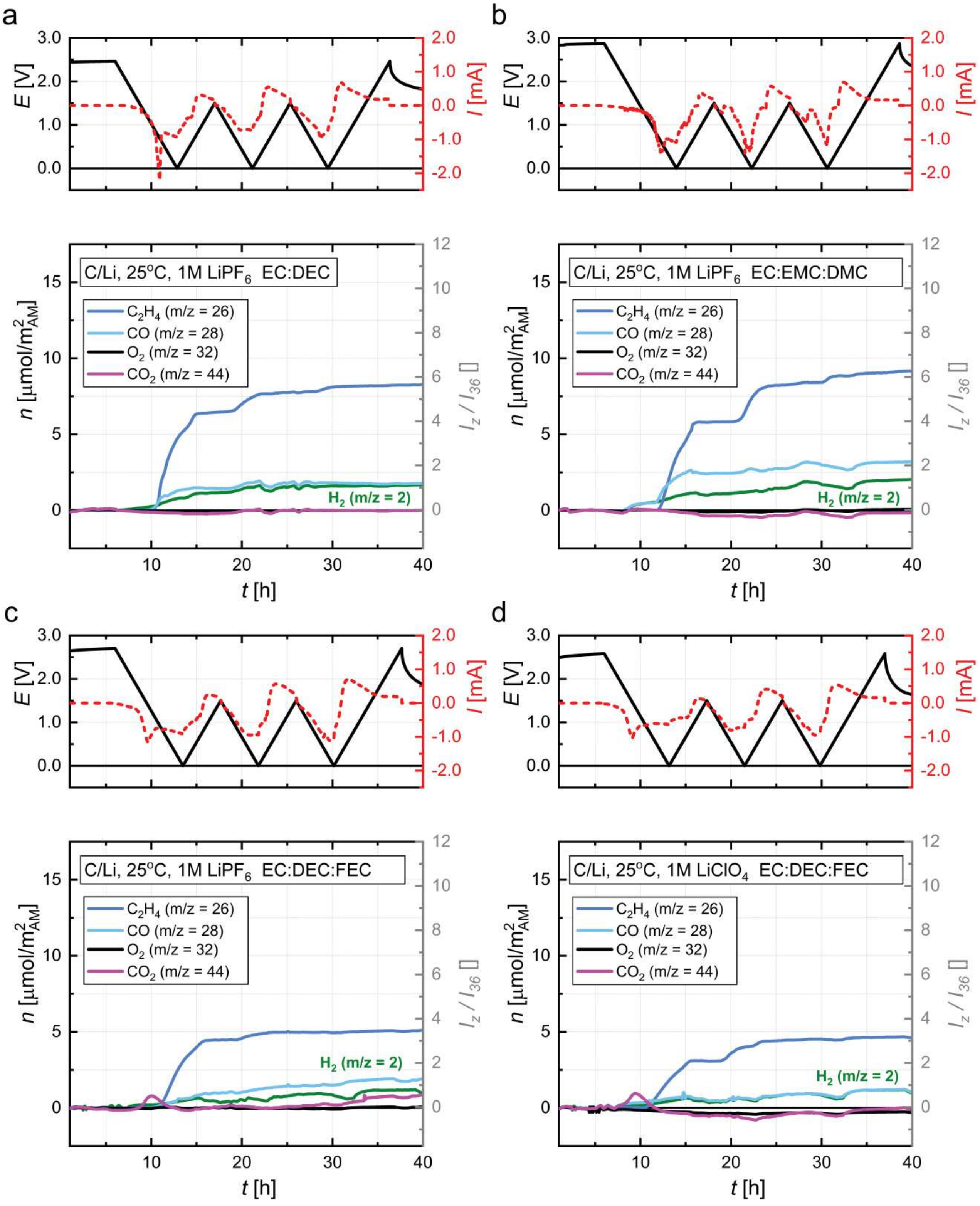

Figure 3. 10: OEMS analysis in a custom-made cell hardware containing a carbon paper electrode vs. Li/Li$^+$ testing different electrolytes (100 µL) with cyclic voltammetry between OCV (≈ 2.5 V – 3.0 V), 0 V and 1.5 V at 0.1 mV/s at 25 ℃; a. 1M LiPF$_6$ in EC:DEC; b. 1M LiPF$_6$ in EC:EMC:DMC; c. 1M LiPF$_6$ in EC:DEC:FEC; d. . 1M LiClO$_4$ in EC:DEC:FEC. The evolution of ethylene gas observed corresponds to EC reduction at potential of

~ 0.8 V vs Li/Li$^+$ *whereas the* CO_2 *evolution observed in presence of FEC corresponds to FEC reduction at ~ 1.5 V vs Li/Li*$^+$*.*

No oxygen evolution is observed over the time of the experiment indicating that there was no air intrusion in the cells. All the electrolytes tested present a similar evolution for the hydrogen and carbon monoxide profiles, due to minimal residual water present in the electrolytes from their storage conditions.[11] A clear evolution of ethylene gas is observed for all electrolytes at the potential of ~0.8 V vs. Li/Li$^+$ during the first charge, as reported in literature and previous experiments, and is due to EC reduction upon the formation of a reduction layer. The amount of ethylene gas produced upon the first discharge is significantly different depending on the electrolyte, with higher quantities produced for the electrolytes 1M $LiPF_6$ in EC:DEC (Figure 3. 10. a) and 1M $LiPF_6$ in EC:EMC:DMC (Figure 3. 10. b). A continuous increase is observed at potentials below 0.8 V vs Li/Li$^+$ for the subsequent cycles, indicating that the layer continues to be formed, with more ethylene gas produced for the second lithiation for the electrolytes 1M $LiPF_6$ in EC:DEC (Figure 3. 10. a) and 1M $LiPF_6$ in EC:EMC:DMC (Figure 3. 10. b). The reduction of EMC has been shown to be similar in terms of gas evolution compared to linear carbonates, which is consistent to the gas evolution observed for the electrolyte 1M $LiPF_6$ in EC:EMC:DMC (Figure 3. 10. b).[95]

The two electrolytes containing EC:DEC:FEC as a solvent present similar gas analysis profiles, supporting the previous assumption of a lack of influence of the salt used on the gases evolving in the cell.[99] A CO_2 evolution is observed at ~ 1.5 V vs. Li/Li$^+$ for the electrolytes containing FEC (1M $LiPF_6$ in EC:DEC:FEC - Figure 3. 10. c and 1M $LiClO_4$ in EC:DEC:FEC - Figure 3. 10. d), corresponding to the potential region in which important side reactions were observed. The CO_2 evolution has been discussed by Jin et al. as a possible product of the reduction of FEC in EC radicals, which then transform in vinoxyl radical leading to CO_2 evolution as depicted in Figure 3. 11. The EC radicals can also be transformed into VC, which then transform in vinoxyl radicals leading to CO_2 evolution as well. Further reduction of vinoxyl radicals can lead to formation of Li_2O that can react with CO_2 to incorporate Li_2CO_3 in the passivation layer.[101] We observe an increase of CO_2 which is immediately consumed, potentially due to the extremely high surface area of the electrode which is not fully passivated, and consumes the CO_2 produced to form Li_2CO_3 species.[24,95] The formation of vinoxyl radicals is not favored in EC-based solvents. It appears from the comparison between the electrolytes 1M $LiPF_6$ in EC:DEC and 1M $LiPF_6$ in EC:DEC:FEC that the spike in carbon dioxide is the trigger for a smaller evolution of ethylene gas, not only for the first low potential cycle but also for the subsequent ones.

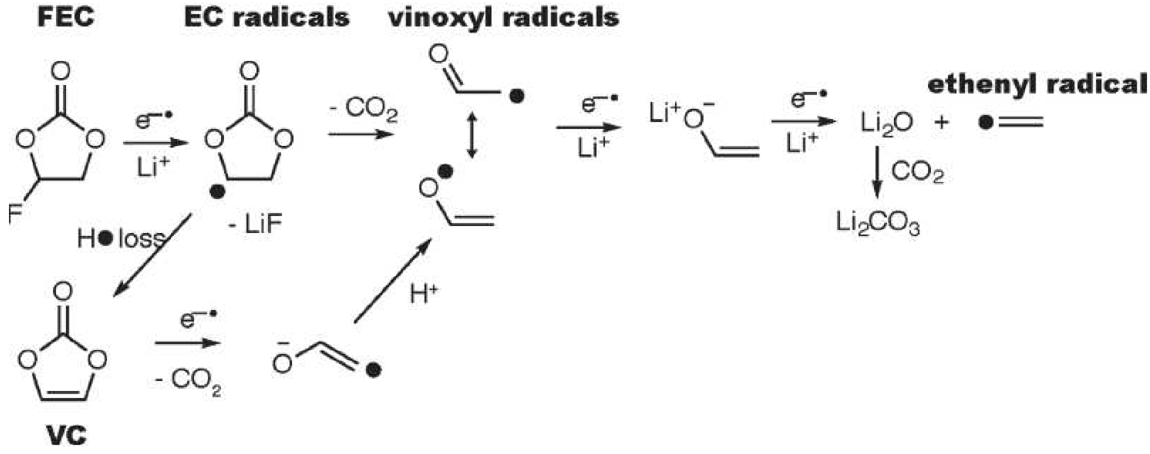

Figure 3. 11: Schematic of possible FEC reduction reproduced with authorization from ref. 101

The comparison of the different electrolytes with the OEMS tool highlights the impact of the formation of a reduction layer on the cathode and the Li consumption used in this process, leading to low cycling reversibility. Indeed the presence of FEC in the electrolyte triggers a CO_2 evolution that potentially creates a Li_2CO_3–rich layer. This CO_2 evolution limits the EC reduction which appears to form a layer reversibly oxidized in EC:DEC electrolytes, but increases the Ni reduction. The presence of FEC may lead to the formation of a layer at low potential that cannot be oxidized at high potentials, unlike what is observed in presence of EC:DEC, leading to higher capacity loss upon delithiation after deep lithiation.

Summary

Different electrolytes have been compared in the classic potential window with NMC622 vs Li metal half-cells. Less capacity was accessed upon the first delithiation for the electrolytes with the solvents EC:DEC:FEC and EC:EMC:DMC in comparison with EC:DEC. This difference was interpreted as a higher impedance in those cells. A SEI is formed with FEC through chemical reaction as soon as the cell is assembled, increasing with the first delithiation as more surface is created upon Li platting on the Li metal. Upon delithiation after deep lithiation to OL2, a significant difference in capacity accessed was observed in presence of FEC, indicative of a negative effect of the FEC on the cathode upon cycling at low potentials. No significant impact of the salt was observed by comparing $LiPF_6$ and $LiClO_4$ in presence of FEC in this potential window.

A XAS study of the cathodes cycled with 1M $LiPF_6$ in EC:DEC:FEC was done at different lithiation degrees and compared to cathodes cycled with 1M $LiPF_6$ in EC:DEC. The corresponding capacity calculated from the reduction of the TMs in presence of FEC between the samples lithiated to 3.0 V vs Li/Li^+ and the samples lithiated to OL1 was far bigger than the observed capacity, indicative a side reactions in this potential window. The oxidation state of Co and Ni at V_{high} appeared lower in presence of FEC, supporting the hypothesis of the formation of a passivation layer limiting the Li deintercalation upon the first delithiation. The differences in capacity observed upon delithiation were linked to differences in formation of passivation layers in presence of FEC.

To evaluate the different gases evolving in the cell, a NMC622 cathode was cycled vs Li metal in a custom gas analysis cell. A significant evolution of ethylene gas was observed upon deep lithiation, sign of EC reduction upon formation of a reduction layer at low potentials. Air intrusion was also observed due to the extended time scale of the measurement but no other gas evolution than known low-potential gassing reaction was observed. The layered formed at low potential was reversibly oxidized at high potential. Because no gas evolution was attributed to structural changes of the cathode material, the contribution of the different electrolytes was studied in a cell with carbon paper vs Li metal upon cyclic voltammetry. All electrolytes triggered an evolution of ethylene gas at potentials ~ 0.8 V vs Li/Li^+ due to EC reduction but in different proportions. EC:DEC and EC:EMC:DMC solvents lead to similar amounts of ethylene gas, supporting the hypothesis of the formation of a similar passivation layers for the two electrolytes, linked to similar reversibility upon deep cycling. The two cells cycled with

FEC triggered a similar evolution regardless of the salt used, supporting the lack of influence of the salt observed with electrochemistry. A first evolution of carbon dioxide was observed, leading to a smaller evolution of ethylene gas, possibly indicating the formation of Li_2CO_3-rich layer on the cathode. The better cycling capabilities of cells with EC:DEC compared to the cells containing EC:DEC:FEC appeared linked to the formation of a reversible layer upon EC reduction, that is hindered in presence of FEC.

Chapter 4: Open-circuit potential curve determination

Introduction: use of overlithiation for OCP determination

For demanding products such as portable electronics, grid electricity storage or electric vehicles (EVs), strict performance requirements are imposed on Li-ion batteries (LIBs). For this reason, the battery system in these products not only consists of the battery packs, but also includes the battery management system (BMS). The BMS is responsible for the control of the charging and discharging of the battery packs and provides information on the state of the batteries. With EVs overtaking the vehicle market, the demand for constant and accurate information on the states of the battery is growing, pushing the requirements on the BMS.

An efficient battery management system (BMS) is composed of hardware and software that control the charging and discharging of the battery while ensuring safe and reliable operations.[102–105] The BMS is also responsible for cell balancing and thermal management of the battery.[106,107] The use of a BMS is essential to ensure the durability and performance of battery packs within the safety limits of operation, as batteries can ignite or explode under abused conditions or when overcharged.[108,109] The constant monitoring of the battery packs is critical as battery behavior changes with aging.[110,111]

The BMS software relies on models to describe the battery. Its key task is to observe the states of the battery and track how the physical parameters evolve as the battery ages. A classic BMS relies on an equivalent circuit model to monitor and control the batteries, but it has limited prediction capabilities.[102] A more innovative type of BMS, incorporating the electrochemical principles governing the reactions within a battery, has been developed. The advanced BMS (ABMS) relies on a physics-based electrochemical model instead of an equivalent circuit model. The physics-based model can predict the essential states of the battery with regard to their spatial distribution, such as the concentration of Li ions and the potential in the electrodes and the electrolyte upon cycling.[102] The knowledge of these parameters is used to determine the different states of the battery (state-of-charge, state-of-health) and the energy it can deliver. The inputs needed to ensure good parameterization of the ABMS are presented in Figure 4. 1.

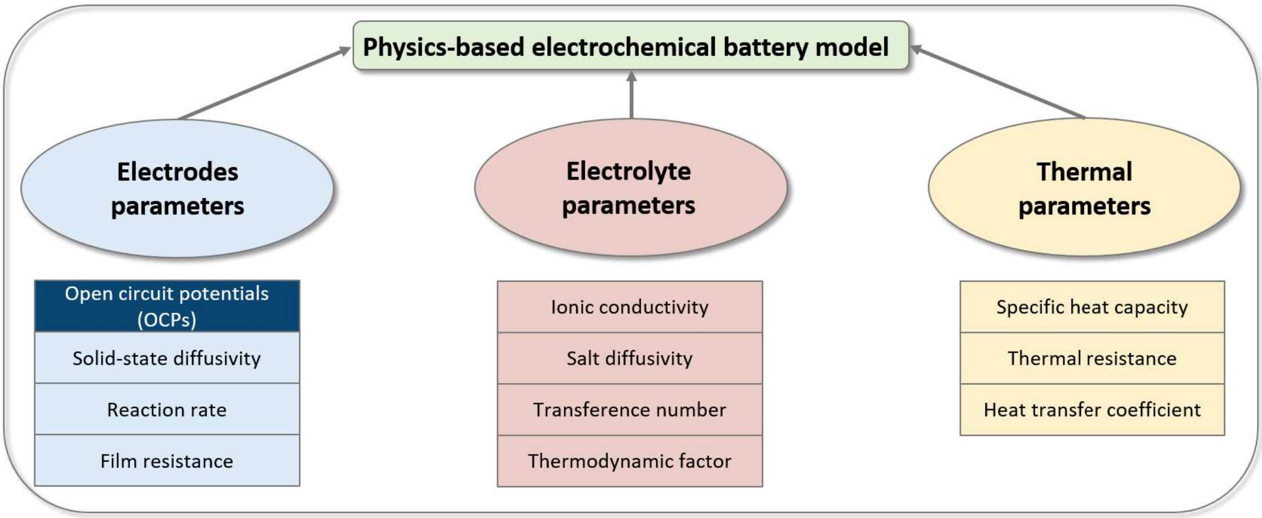

Figure 4. 1: Schematic of the parameters needed to parameterize an advanced battery management system

One of the most important input parameter is the OCP of the electrodes. The electrostatic potential of an electrode can be expressed as a function of how much Li is stored in the electrode. By normalizing the Li content stored in the electrode by the maximum possible concentration, we can quantify the utilization of the electrode. The equilibrium potential of an electrode when no current is applied (OCP), can be expressed as a function of the utilization of the electrode with respect to a Li metal reference, giving the OCP curve of the material. The OCP of an electrode is unique to each material and is different, even within the same family of materials, such as NMCs or NCAs.[112] The OCP of the material does not change over time, as the material (de)intercalates Li near equilibrium in the same way.[66] The OCP curve of the material is used for two main reasons in the ABMS, to determine the OCV of the cell, and to determine the molar flux j_n of the reaction, which is an internal parameter of the ABMS.

- Determination of the OCV of the cell

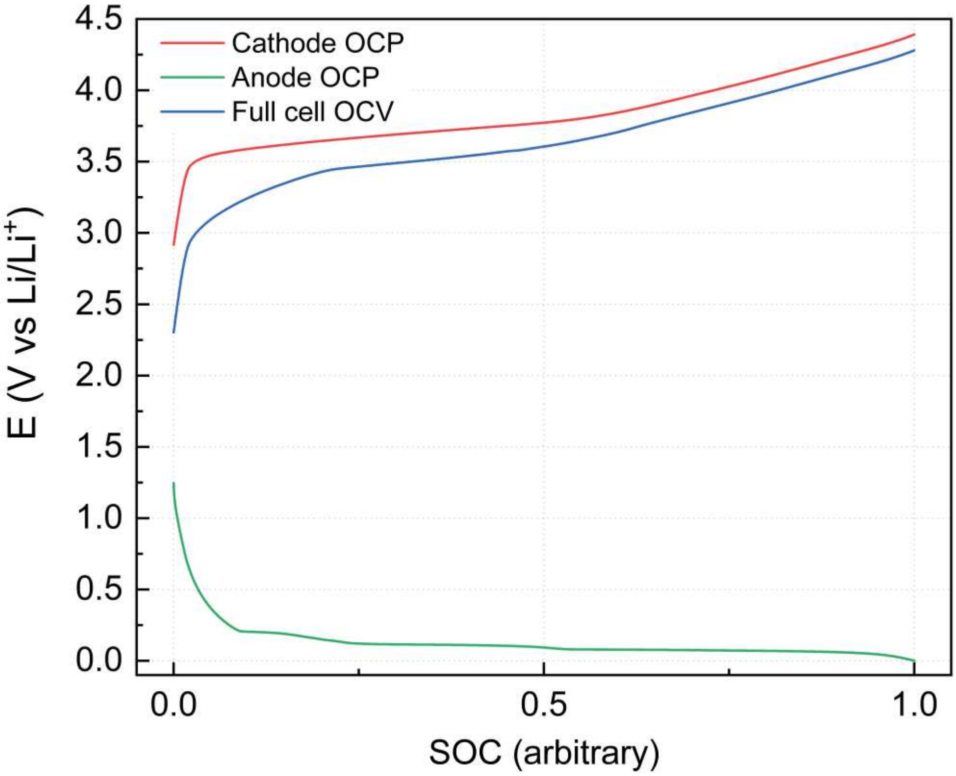

Figure 4. 2: Schematic of the OCV of a fictional cell from the OCP of the electrode materials

Both negative and positive electrodes have an OCP (respectively $\mathcal{U}^-(\xi^-)$ for the negative electrode and $\mathcal{U}^+(\xi^+)$, for the positive electrode, with $\xi = \frac{Li\ concentration}{Li\ concentration_{max}}$ representing the volume-averaged concentration in the electrode). The difference between the OCP of the positive electrode and the negative electrode ($\mathcal{U}^+(\xi^+) - \mathcal{U}^-(\xi^-)$, taking in consideration the electrodes loading and balancing) is referred to as the open-circuit voltage of the cell (OCV), and corresponds to the potential measured between the two electrodes when no current is applied. An exemplary representation of the OCV of a full cell with regards to the OCP of each electrode is presented in Figure 4. 2. The monitoring of the OCV of the cell is essential to ensure safe battery operations.[113]

- Determination of j_n

The molar flux of the reaction is calculated by the Butler-Volmer equation [5]. With

$$j_n(x,t) = \frac{i_0(c_e, c_s, c_m - c_s)}{F} . (e^{\frac{\alpha^{anode}F}{RT}\eta(x,t)} - e^{\frac{\alpha^{cathode}F}{RT}\eta(x,t)}) \qquad [5]$$

$j_n(x,t)$ the molar flux of the reaction, as a function of the position within the cell (x-axis perpendicular to the electrode stack) and time,

$i_0\ (c_e, c_s, c_m\text{-}c_s)$ the exchange current density, as a function of c_e the concentration of Li^+ in the electrolyte, c_s the concentration of Li^+ in the solid, c_m the maximum concentration of Li^+,

α^{anode} the anodic charge transfer coefficient, $\alpha^{cathode}$ the cathodic charge transfer coefficient with $\alpha^{anode} + \alpha^{cathode} = z$, amount of electrons,

R the gas constant,

T the absolute temperature,

F Faraday's constant,

$\eta(x,t)$ the overpotential for the intercalation reaction.

The overpotential represents the deviation between the thermodynamic equilibrium potential and the potential difference a charged species would go through when passing the passivation film (SEI or CEI). It is calculated from equation [6], with

$$\eta(x,t) = U^{solid\ electrode}(x,t) - U^{electrolyte}(x,t) - OCP\left(c_s\left(x, R_p, t\right)\right) - R_f F j_n(x,t) \qquad [6]$$

$U^{solid\ electrode}\ (x,t)$ the potential in the solid electrode as a function of x and time,

$U^{electrolyte}\ (x,t)$ the potential in the electrolyte as a function of x and time,

$OCP\ (c_s(x, R_p, t))$ the equilibrium potential of the reaction in the solid electrode as a function of the solid concentration (c_s) measured at the particle radius (R_p), x, and t,

R_f the film resistance (either SEI or CEI).

The OCP value used for the calculation of the intercalation reaction overpotential is dependent on the concentration of the surface of the particle. Because the Li content at the surface of the material can be different from the Li content in the bulk, the OCP curve used as an input for the ABMS must carry information above and below the classic potential window of a full cell. As depicted in Figure 4. 3, the surface concentration can exceed the bulk content upon lithiation, prompting the need to characterize the materials below the potential range of the full cell. Reciprocally, upon delithiation the surface of the particles can be Li deficient compared to the bulk, hence the need for the OCP of the material above the potential range of the full cell. Nevertheless, the characterization of the OCP of cathode materials in these regions is limited by the stability of the material as well as the stability of the state-of-the-art electrolytes.

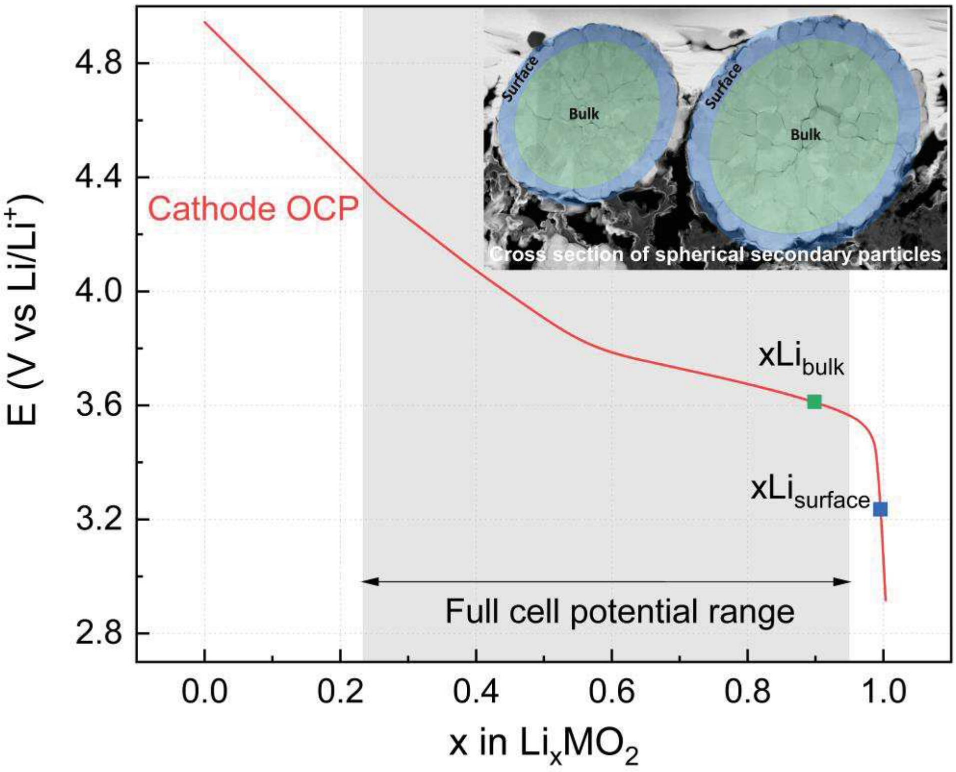

Figure 4. 3: Representation of the bulk and surface Li content in a fictional cathode upon lithiation at a given potential, representing the possible significant difference in Li content from the OCP curve between the surface and the bulk of the particle

Several methods have been developed to characterize the OCP curve of cathode materials. The x-axis commonly used to report the OCP, called SOC, can carry different definitions, as discussed by Barai et al.[66] Confusion can come from the misunderstanding of the SOC definition adopted by each group and careful explanation of the considerations made should be done before reporting of the data. The most common process to reach the equilibrium potential of a material for a given Li content is to use the galvanostatic intermittent titration technique (GITT).[114] In this method, a current is applied for a given period, often 10% of the SOC, and the evolution of the potential upon current interruption is recorded, often over one hour. The variations of the potential upon relaxation are due to the relaxation of concentration gradients in the electrolyte and solid phase as well as the redistribution of Li in the solid phase.[115] The precision of the measurement is dependent on the C-rate used and the length of the relaxation period. The accuracy of this method derive from the fact that it avoids kinetic limitations. Nonetheless, it can be highlighted that depending on the material investigated, a great error can arise from the assumption that the thermodynamic equilibrium of the cell is reached after one hour of current interruption.[116–119]. In order to circumvent the long rest period required to reach potential equilibrium upon relaxation, that could lead to slow side reactions within the cell, a fit of the relaxation profile has been used in literature to approximate the equilibrium potential.[106,108] Barai et al. established that the optimal conditions to determine the OCP curve with the GITT method was to measure the rest potential for 4 hours for every 1% of SOC, leading to a measurement of several weeks,[116] whereas Baccouche et al. recommended steps of 2.5% of SOC.[120] To maximize the GITT investigation, Nikolian et al. recommended not using constant increments but instead increasing the measurements in non-linear regions.[121] The long measurement time of the GITT method has been decried in literature,[66] however the benefits deriving from the increase of accuracy of the OCP curve are vast.

When a lower resolution for the OCP curve is required, the thermodynamic information can be reached by cycling the cell with a constant current upon charge and discharge at a low C-rate, in order to obtain a pseudo-OCP curve. A C-rate of C/25 or lower is considered in literature as a low C-rate. The widely used pseudo-OCP method allows to reduce the kinetic contributions, ensure a low electrode polarization and low ohmic heat generation while significantly shortening the measurement time.[122–129] One drawback of this method is that the curves obtained change with the C-rate applied as the capacity reached is C-rate dependent. Additionally, even though it is considered to be a low C-rate, a C/25 cycle still presents significant polarization on the charge and discharge for many electrodes, including Ni-based cathode materials. To minimize the impact of the polarization, groups have been using the average of the charge and discharge as a pseudo-OCV curve.[124,126,129]

GITT measurements provide extra accuracy to identify the different electrochemical reactions and phases in the electrode compared to the pseudo-OCV method.[130] Yet, the x-axis mapping is done by dividing the equilibrium potential by the Li content of the cycled potential range (usually from 3.0 V to 4.2-4.5 V), which varies between experiments. This lack of standardized methodology can lead to misunderstandings in the interpretation of the data. Development of a standardized method for the characterization of the OCP curve of electrode materials would allow for better comparison between research results from different laboratories. Additionally, because the surface of the particle may exceed the classic potential window of the full cell, the OCP curve of the electrodes needs to be characterized on a broader x-axis. Due to the current limitations rising from the stability of the electrolyte at high potential,[131,132] we focus in this study on the determination of the OCP curve at lower potentials, to the Li content of xLi = 1.

At first, a method was developed in our group to attempt to define the OCP curve at 25ºC below 3.0V vs Li/Li^+ and consisted of a C/50 measurement using the pseudo-OCP method between V_{high} and 3.0 V vs Li/Li^+ followed by a lower C/100 lithiation and a C/200 lithiation to 3.0 V vs Li/Li^+. Similarly to the use of a voltage hold to regain the capacity loss in the first cycle for layered cathode materials discussed in chapter 1, this process allowed to reach more capacity than by using a constant current in the classic potential window, but did not bring more information on the position of xLi = 1. Resulting from the study of the deep lithiation of NMC materials presented in Chapter 1 and the XAS and XRD characterizations discussed in chapter 2, we identified that NMC materials are capable of cycling reversibly one Li ion per NMC structure (xLi = 1, OL1). Additionally, any surface change observed by XAS at this degree of lithiation is reversible and the materials' original layered structure is preserved. Based on these results, the OCP characterization method at 25ºC summarized in Figure 4. 4 was developed:

- Step 1: Initial estimation of the $xLi^{ini} = 1$
- Step 2: Current bias (I_{bias}) determination through processing of two subsequent C/50 cycles
- Step 3: Determination of a trust region where the pseudo-OCP can provide an accurate OCP curve, by comparison of the average of a C/50 cycle with the average of a C/25 cycle
- Step 4: Intermediate step where a C/50 cycle is applied to regain the initial charge capacity
- Step 5: Pseudo-GITT rests to determine the rest potential after the trust region
- Step 6: Correction of the $xLi^{ini} = 1$ estimation from the pseudo-GITT relaxation profiles
- Step 7: Determination of the OCP curve with a newly characterized tail region by combining the results obtained in the trust region and fitting the pseudo-GITT relaxation potentials

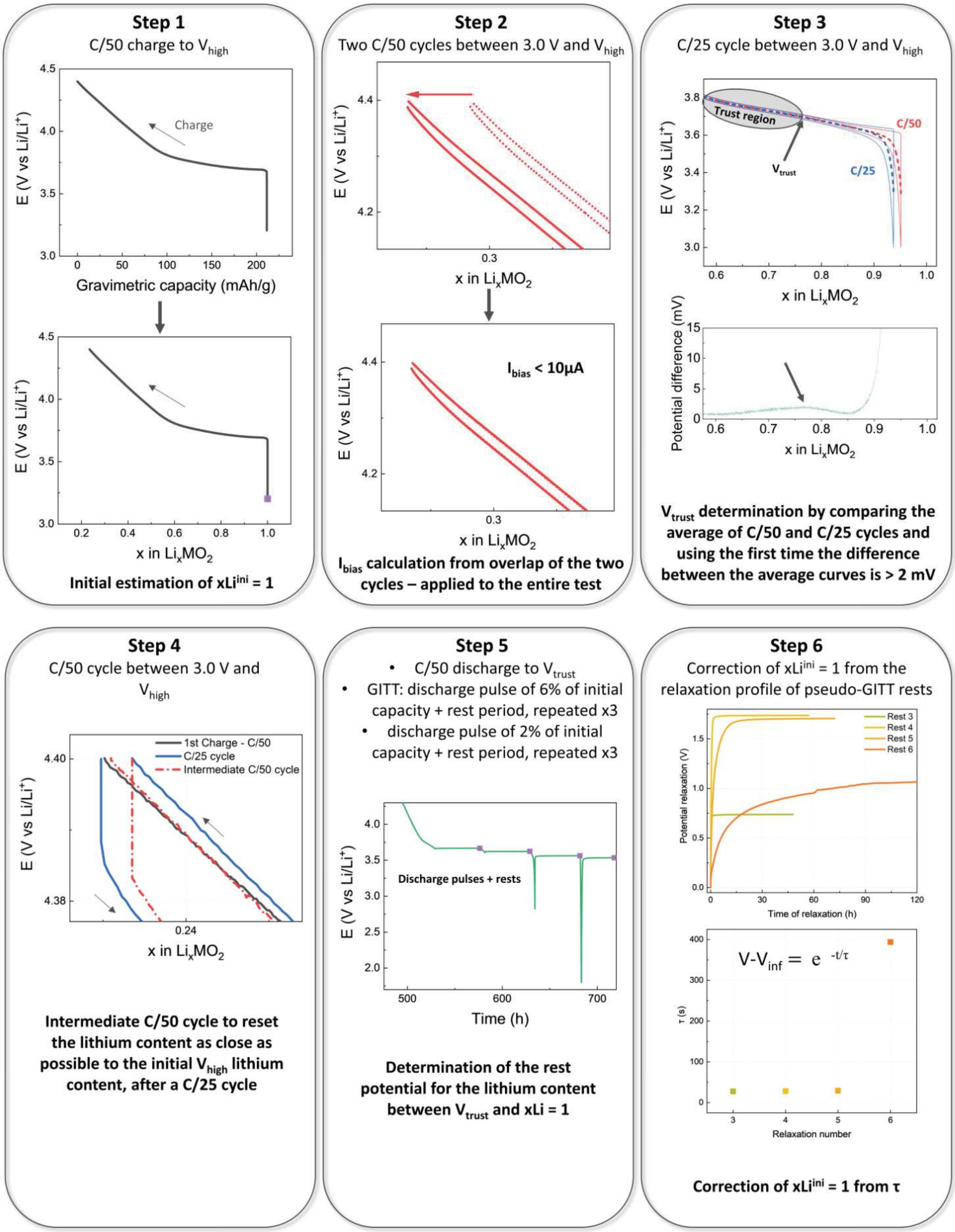

Step 1

C/50 charge to V_{high}

Initial estimation of $xLi^{ini} = 1$

Step 2

Two C/50 cycles between 3.0 V and V_{high}

I_{bias} calculation from overlap of the two cycles – applied to the entire test

Step 3

C/25 cycle between 3.0 V and V_{high}

V_{trust} determination by comparing the average of C/50 and C/25 cycles and using the first time the difference between the average curves is > 2 mV

Step 4

C/50 cycle between 3.0 V and V_{high}

Intermediate C/50 cycle to reset the lithium content as close as possible to the initial V_{high} lithium content, after a C/25 cycle

Step 5

- C/50 discharge to V_{trust}
- GITT: discharge pulse of 6% of initial capacity + rest period, repeated x3
- discharge pulse of 2% of initial capacity + rest period, repeated x3

Determination of the rest potential for the lithium content between V_{trust} and xLi = 1

Step 6

Correction of $xLi^{ini} = 1$ from the relaxation profile of pseudo-GITT rests

$$V\text{-}V_{inf} = e^{-t/\tau}$$

Correction of $xLi^{ini} = 1$ from τ

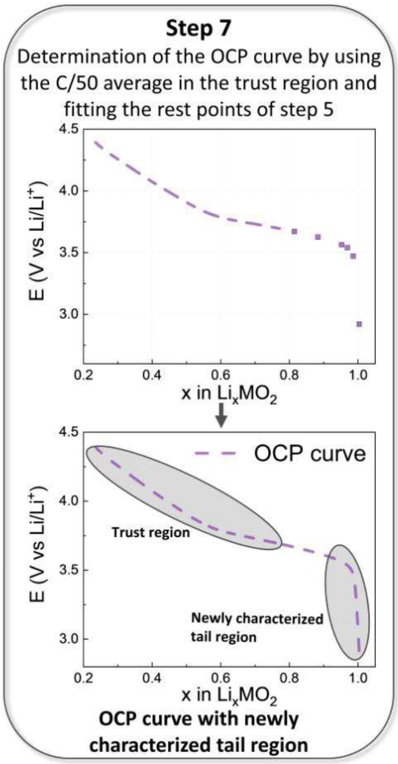

Figure 4. 4: Schematic of the 7 steps developed to determine the OCP curve of Ni-based layered material at 25ºC

1. Proposed OCP curve determination method

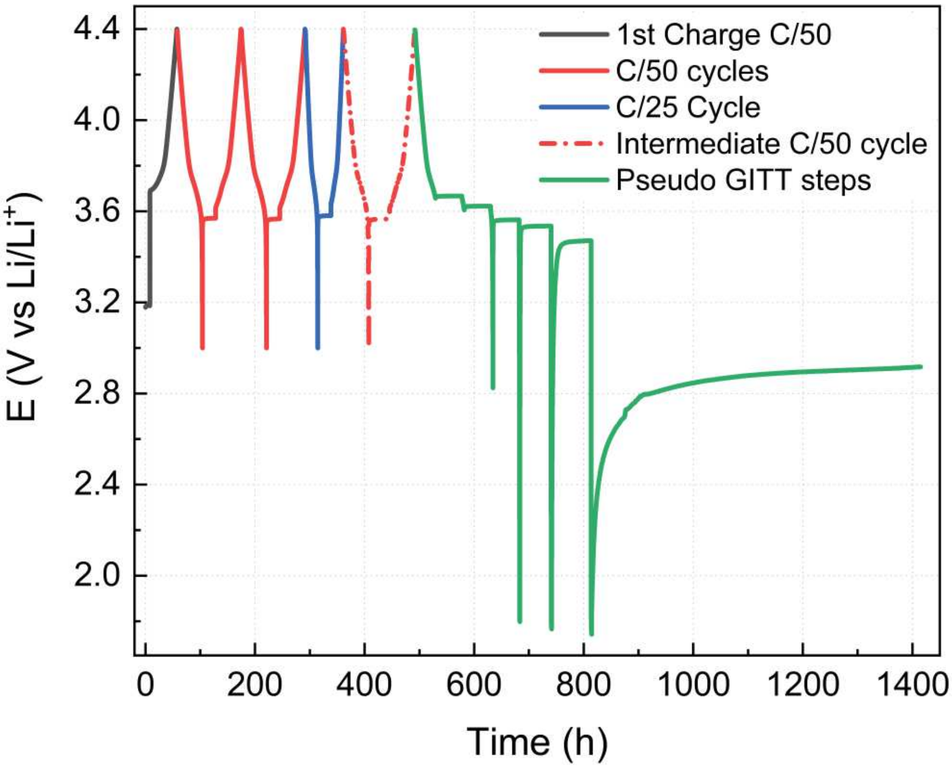

Figure 4. 5: Overview of the cycling profile of the OCP test on NMC622 vs Li/Li^+ half-cell with 1M $LiPF_6$ in EC:DEC at 25°C

The new proposed OCP method consists of 7 steps in order to provide an accurate OCP to Li content curve (called OCP curve) at 25°C. This method has been applied on layered cathode materials with the electrolyte 1M $LiPF_6$ in EC:DEC and is presented in Figure 4. 5. This method requires a significant amount of time (> 1200 hours), hence the importance of identifying an electrolyte without side reactions over the window of interest. The selection of the electrolyte 1M $LiPF_6$ in EC:DEC for the OCP determination of NMC622 relies on the previous experiments presented in Chapter 3.

After an acclimation period of 6 -10 hours to allow for homogenous electrolyte distribution and separator wetting,[12] the cell is cycled from OCV to V_{high} at a slow C-rate of C/50. The first step of this method, represented in grey on Figure 4. 5, is used to determine a preliminary value for $xLi^{ini} = 1$ by assuming that the pristine material is fully lithiated. It is important to obtain this first estimation to assess the initial capacity of the material and this value will be corrected in step 6 depending on the rest profile of the pseudo-GITT steps. Setting the xLi = 1 position in the OCP curve is key to estimating the Li content of the electrode sheet.

Indeed, some electrodes can be designed to contain slightly more than one Li ion per structure, or the material can lose some Li to surface-contaminant species upon storage,[133] leading to a Li deficient electrode. In Figure 4. 6. a, the first charge is represented in the gravimetric scale by dividing the capacity accessed by the weight of the active material (mAh.g^{-1}) and converted to Li content scale in Figure 4. 6. b by assuming the pristine electrode is fully lithiated (xLi = 1 in pristine electrode).

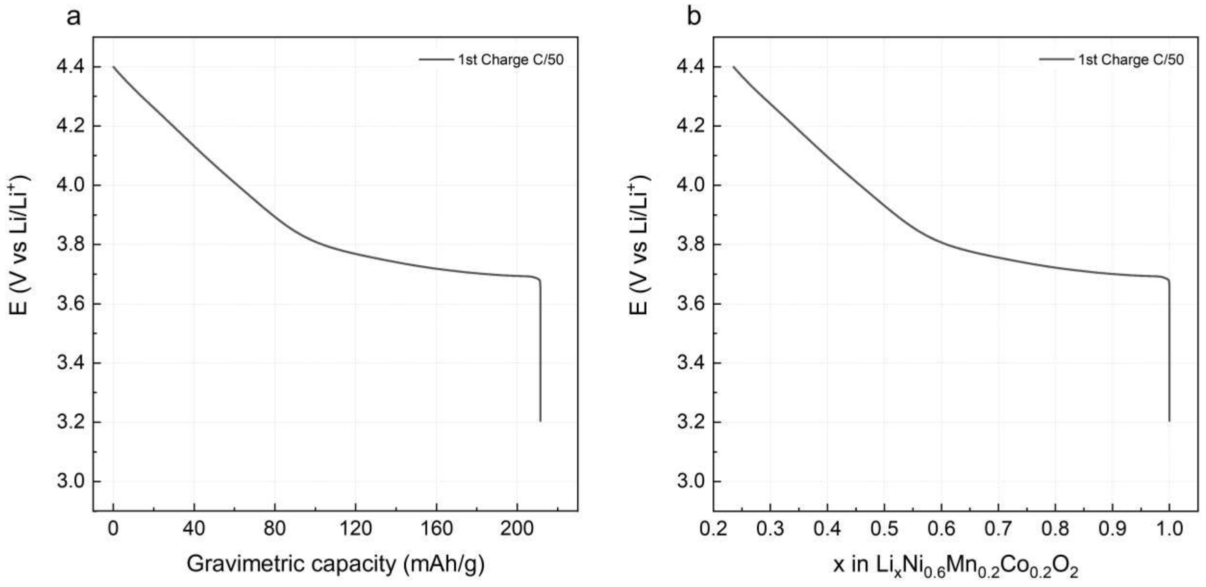

Figure 4. 6: First delithiation of a NMC622 vs Li/Li$^+$ half-cell with 1M LiPF$_6$ in EC:DEC at C/50 from OCV to V$_{high}$ = 4.4 V; a. Gravimetric scale (mAh.g^{-1}); b. Li content scale, scaled by assuming that the pristine electrode contains xLi = 1

In a second step, represented in red in Figure 4. 5, the cell undergoes several formation cycles at C/50 in order to circulate the cyclable Li between the anode and the cathode. Additionally, those cycles will be used during data analysis to determine the current bias of the channel tester. Regardless of the calibration of the tester, each channel presents an inherent bias that can induce a shift of the data along the x-axis. The current bias is computed by calculating how much correction to the current is needed to have two subsequent cycles, at the same C-rate, overlap at the high potential cut-off. Two formation cycles were needed for NMC622 but other cathode materials possibly require more. The first (red – full line) and second (red – dotted line) formation cycles are represented in Figure 4. 7 after a current correction of -0.39 µA has been applied.

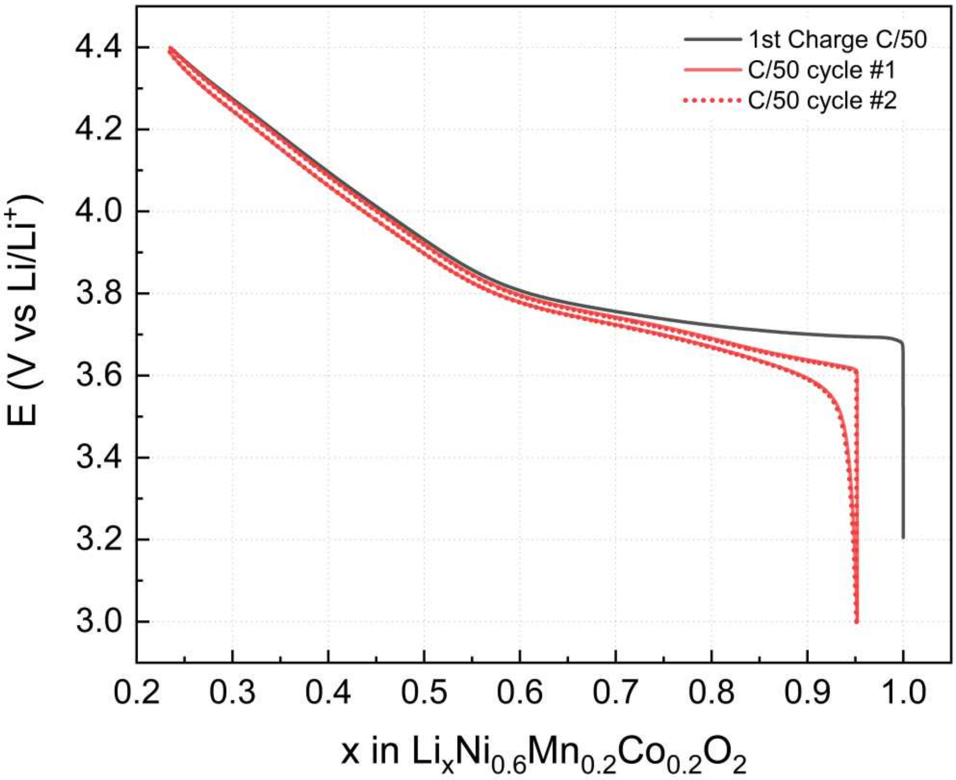

Figure 4. 7: Intercalation/deintercalation profile of the OCP determination procedure of the NMC622 cell up to the current bias determination step. First delithiation of the NMC622 cell at C/50 (black) and subsequent C/50 cycles between V_{high} *= 4.4 V and 3.0 V in order to extract the current bias inherent to the battery tester channel; First C/50 cycle (red - full line); Second C/50 cycle (red - dotted line). The data has been corrected with a current bias of* $I_{bias} = -0.39\ \mu A$

The OCP curve has been estimated in literature by using GITT, and often extracting the rest potential of each step by fitting the relaxation profile to diminish the measurement time.[106,108,134,135] In order to access the thermodynamic information faster, a pseudo-OCP method has been developed where the pseudo-OCP curve is determined by averaging the lithiation and delithiation curves at a slow C/25 rate.[66,136] We have demonstrated in the previous chapters that the NMC materials have several Li diffusion regimes. In a first regime, the polarization of the material on the lithiation and on the delithiation are symmetrical, as can be observed from literature with GITT measurements.[114,137,138] We call this regime the trust region. To obtain an accurate OCP curve in this region without compromising on the amount of data points collected or the measurement time by using a GITT method, we propose a new measurement based on the pseudo-OCP method. In the trust region, the average of the lithiation and delithiation curves provide an accurate measurement of the OCP curve. The polarization on the (de)lithiation increases with increasing C-rate and the capacity reached upon cycling decreases with increasing C-rate, hence the average of the lithiation and delithiation curves for various C-rates differ above a certain Li content, marking the end of the trust region. In order to determine the end of the trust region, we compare the average of the lithiation and delithiation curves of two different C-rates. In Figure 4. 8, a C/50 cycle (red) and a C/25 cycle (blue) are plotted, with the faster C/25 rate exhibiting a higher overpotential and accessing less capacity than the slower C/50 rate. For each C-rate, the lithiation and delithiation are averaged and compared in Figure 4. 8. The overlap of the two average curves, up to the first time they differ by more than 2 mV, is used to determine the potential at which the trust region ends. Because the OCP curve determined with this method is only in the trust region, the result is not a pseudo-OCP curve but a true OCP curve.

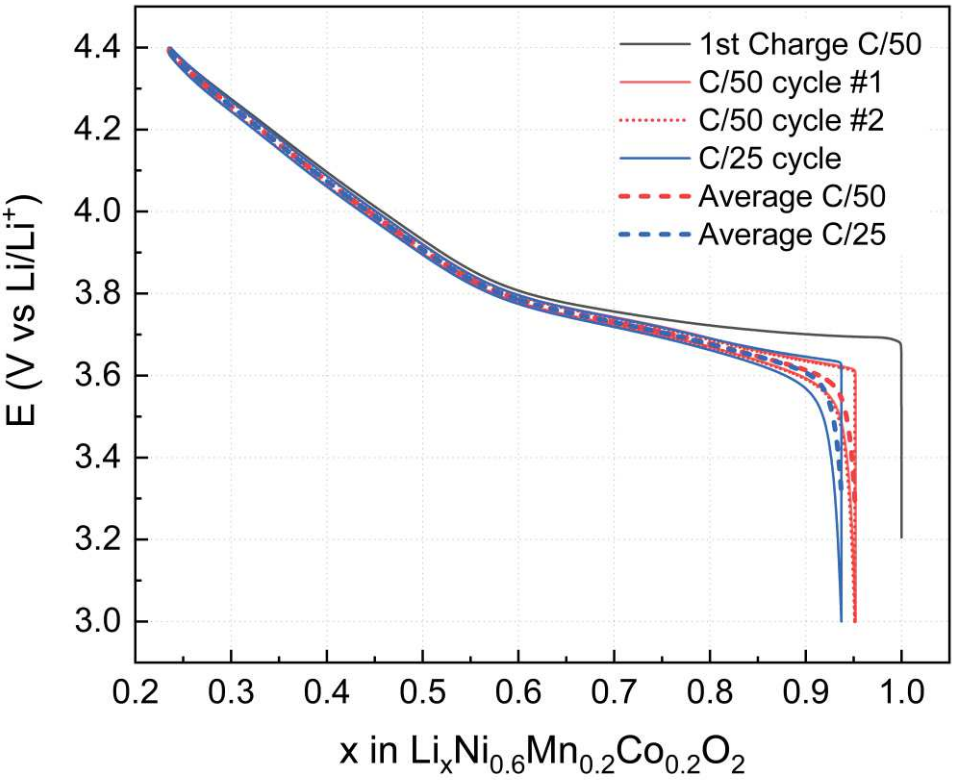

Figure 4. 8: Intercalation/deintercalation profile of the OCP determination procedure of the NMC622 cell up to the trust-voltage determination step; First delithiation of the NMC622 cell at C/50 (black) and C/50 cycles between V_{high} = 4.4 V and 3.0 V (red; first C/50 cycle - full line, second C/50 cycle - dotted line) followed by a C/25 cycle (blue - full line. The data has been corrected with a current bias of I_{bias} = -0.39 µA

The potential difference between the two averaged curves is represented in Figure 4. 9. and a threshold of 2 mV difference was chosen in order to determine the potential V_{trust}, marking the end of the trust region. The 2 mV difference between the average curves occurs at 3.68 V for NMC622 and is marked by a star in Figure 4. 9. From V_{high} to the potential V_{trust}, the Li diffusion regime is the same and the average of the C/50 lithiation and delithiation (equal to the average of the C/25 lithiation and delithiation in this region) can be used as the OCP curve, as shown in Figure 4. 10.

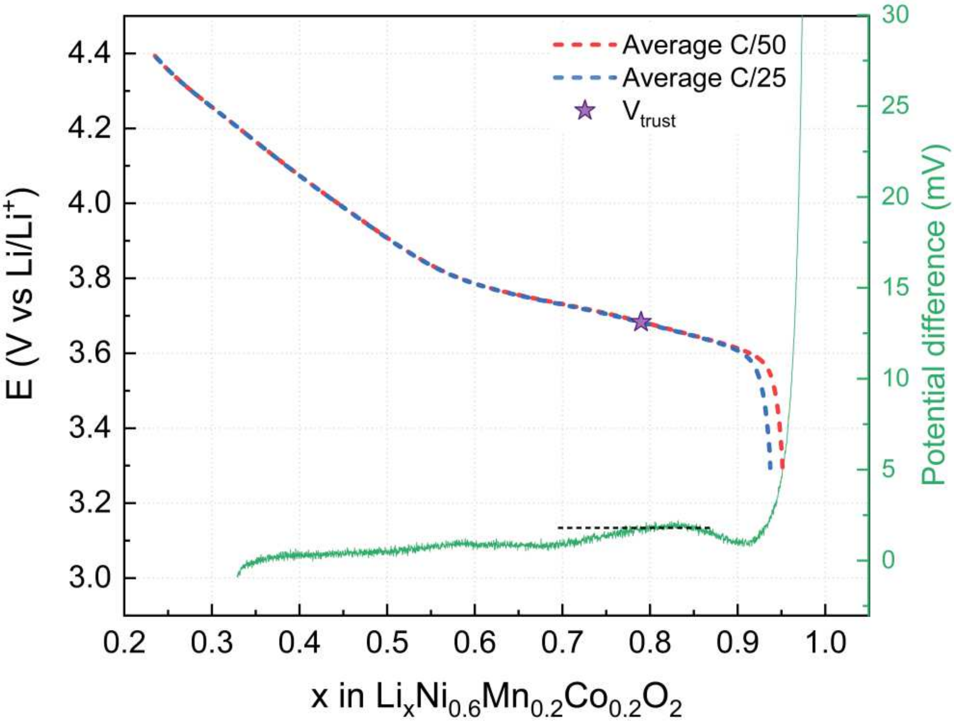

Figure 4. 9: Intercalation/deintercalation profile of the OCP determination procedure of the NMC622 cell up to the trust-voltage determination step; Average of the second C/50 cycle (red dashed line) and average of the C/25 cycle (blue dashed line) with their potential difference in mV (green) plotted on the right y-axis. The threshold of 2 mV difference, used to determine V_{trust} is marked by a dashed line on the potential difference curve and by a star (purple) on the average curve. The data has been corrected with a current bias of I_{bias} = -0.39 µA

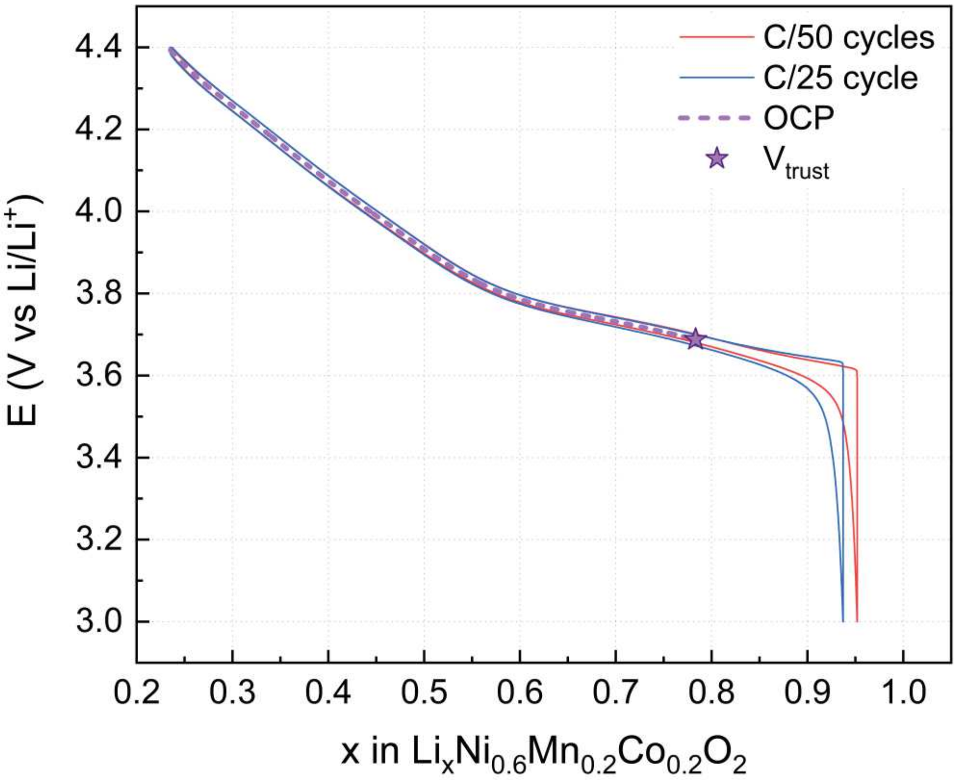

Figure 4. 10: OCP curve from V_{high} to V_{trust} extracted from the average of the C/50 and C/25 cycles (purple dashed line) with a marker at V_{trust} for the end of the trust region, C/50 cycle (red) and C/25 cycle (blue)

After the determination of V_{trust} and the OCP curve in the trust region, an intermediate C/50 cycle (red – dot/dash line in Figure 4. 5 and Figure 4. 11.a and b) is applied to bring back the NMC622 material close to the initial capacity reached after the first charge to V_{high}.

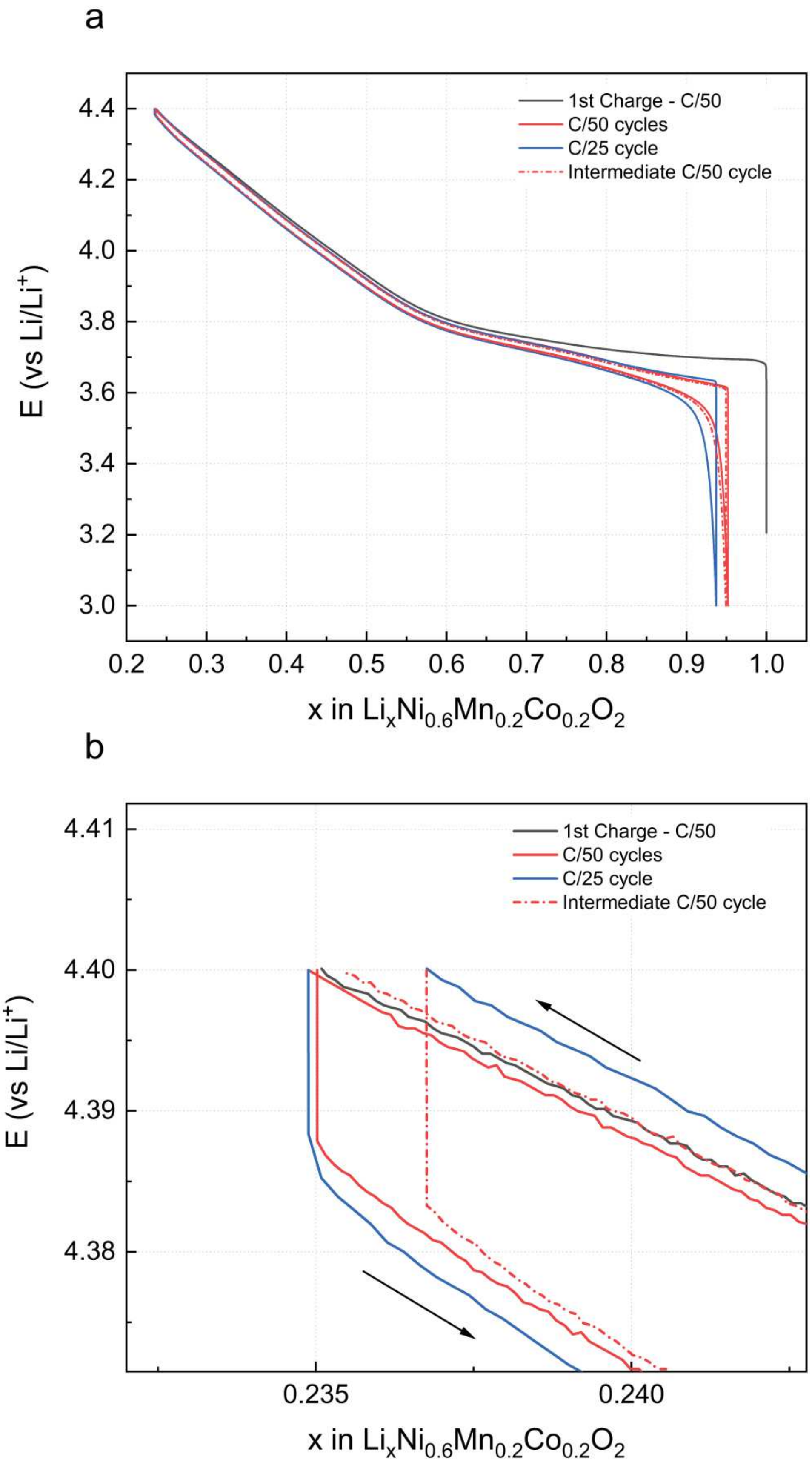
a
1st Charge - C/50
C/50 cycles
C/25 cycle
Intermediate C/50 cycle
E (vs Li/Li$^+$)
4.4
4.2
4.0
3.8
3.6
3.4
3.2
3.0
0.2
0.3
0.4
0.5
0.6
0.7
0.8
0.9
1.0
x in Li$_x$Ni$_{0.6}$Mn$_{0.2}$Co$_{0.2}$O$_2$
b
1st Charge - C/50
C/50 cycles
C/25 cycle
Intermediate C/50 cycle
E (vs Li/Li$^+$)
4.41
4.40
4.39
4.38
0.235
0.240
x in Li$_x$Ni$_{0.6}$Mn$_{0.2}$Co$_{0.2}$O$_2$

Figure 4. 11.a : Intercalation/deintercalation profile of the OCP determination procedure of the NMC622 cell up to the preparation for pseudo-GITT step; First delithiation of the NMC622 cell at C/50 (black), C/50 cycles (#1 and #2, red – full line), C/25 cycle (blue), and subsequent C/50 cycle (red – dot/dash line) in order to prepare for the pseudo-GITT step. The data has been corrected with a current bias of I_{bias} *= -0.39 µA; b. Zoom to the high potential cut-off*

In a final step presented in Figure 4. 12. a, we determine the OCP curve between V_{trust} and $xLi^{ini} = 1$. Because the capacity accessed in this region is dependent on the C-rate used, we cannot apply the pseudo-OCP method. In order to identify the equilibrium potential of the NMC622 material, we follow a pseudo-GITT method with several discharge pulses at C/50 followed by relaxation periods until the capacity accessed exceeds $xLi^{ini} = 1$ by a few mAh.g^{-1} by coulomb counting.

We have demonstrated in Chapter 1 that the capacity lost between the first cycle and the subsequent cycles in the classic potential window can be accessed by discharging the half-cell below 3.0 V vs Li/Li^{+}. We have shown in Chapter 2 that the extent of cycling influences the degradation of the material with irreversible loss of the layered structure happening when the half-cell is lithiated to 0.8 V vs Li/Li^{+}. By investigating the structure and oxidation state variations when cycling to xLi = 1 (OL1) and back to V_{high}, we have demonstrated that the material is capable of retaining the initial layered structure and cycle Li reversibly in the potential window of V_{high} to 1.6 V vs Li/Li^{+}.

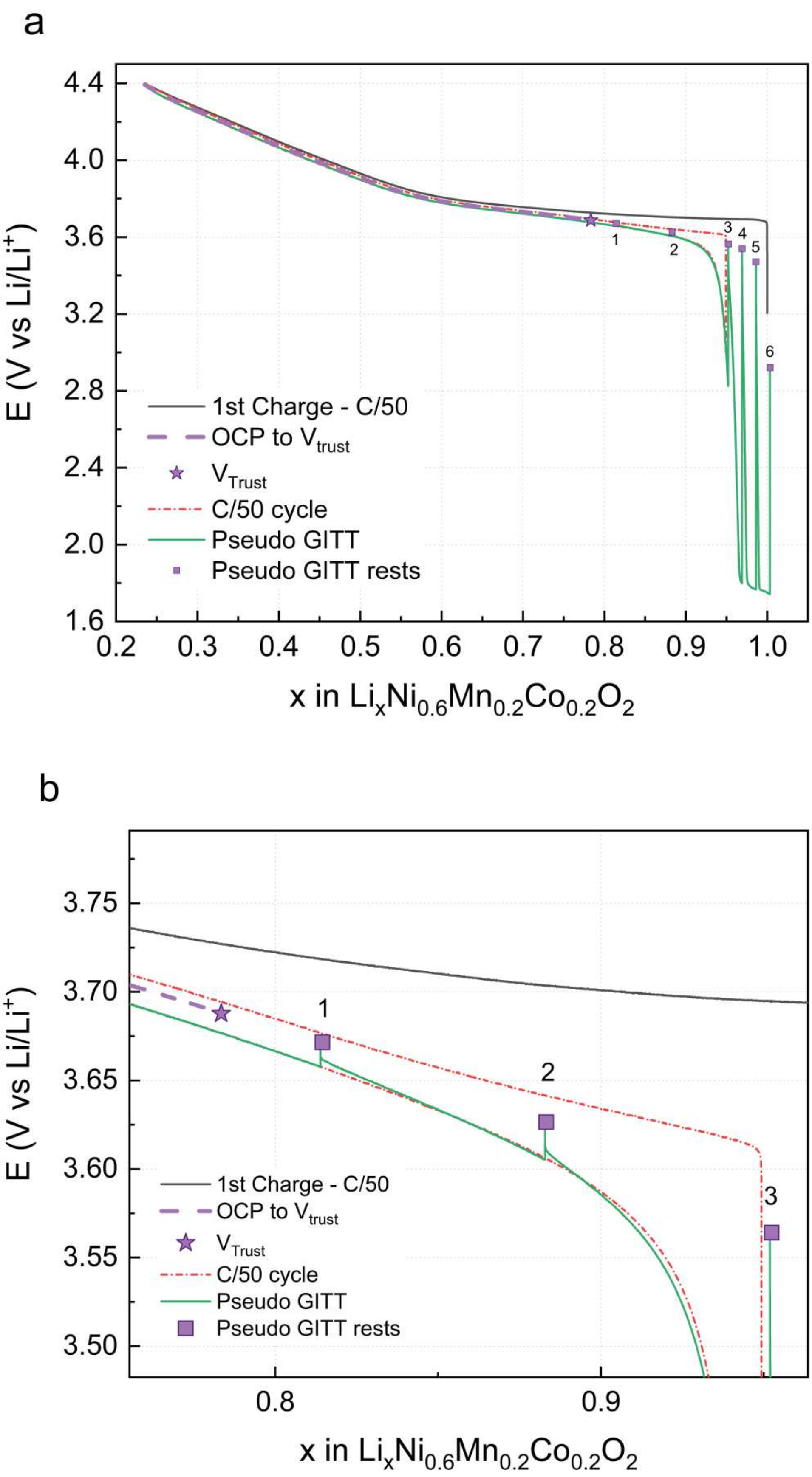
a
E (V vs Li/Li$^+$)
4.4
4.0
3.6
3.2
2.8
2.4
2.0
1.6
0.2
0.3
0.4
0.5
0.6
0.7
0.8
0.9
1.0
x in $Li_xNi_{0.6}Mn_{0.2}Co_{0.2}O_2$
1
2
3
4
5
6
1st Charge - C/50
OCP to V_{trust}
V_{Trust}
C/50 cycle
Pseudo GITT
Pseudo GITT rests
b
E (V vs Li/Li$^+$)
3.75
3.70
3.65
3.60
3.55
3.50
0.8
0.9
x in $Li_xNi_{0.6}Mn_{0.2}Co_{0.2}O_2$
1
2
3
1st Charge - C/50
OCP to V_{trust}
V_{Trust}
C/50 cycle
Pseudo GITT
Pseudo GITT rests

Figure 4. 12: a. Intercalation/deintercalation profile of the OCP determination procedure of the NMC622 cell up to the pseudo-GITT step; First delithiation of the NMC622 cell at C/50 (black), OCP curve from V_{high} to V_{trust} (purple – dashed line), subsequent C/50 cycle (red – dot/dash line) and pseudo-GITT step (green). The equilibrium potential of each pseudo-GITT step is marked by a square (purple); b. Zoom to first 3 rest points. The data has been corrected with a current bias of I_{bias} = -0.39 µA

The equilibrium potentials in the region below V_{trust} are identified in Figure 4. 12. a through several pseudo-GITT steps at C/50, by applying a discharge pulse followed by a rest period. In Figure 4. 12. b, pulses of 6% of the capacity of the first charge are applied from V_{trust} trust until the capacity of xLi^{ini} = 0.95 is reached (from coulombs counting based on the initial xLi^{ini} = 1 value). Shorter pulses of 1.7% of the capacity are applied above xLi^{ini} = 0.95 in order to obtain more data points. The capacity of the discharge pulse can be adjusted to increase the accuracy of the xLi = 1 position. The rest period needed to reach the true rest potential varies with the degree of lithiation. In the experiment presented in this study, the rest times vary between 48 hours and 120 hours. As seen in Figure 4. 13. a, the relaxation time at some Li concentrations should be reduced in the future to optimize the measurement without compromising on the data accuracy.

Several simultaneous mechanisms responsible for the potential variations upon current interruption are summarized in Table 4. 1. The Li (de)intercalation upon current interruption is impacted by the relaxation of gradients induced by the discharge in the electrolyte, in the solid electrode, and within the solid particles. Each gradient has a different time scale. The time constant of the relaxation of the gradient in the electrolyte, for the stack described in the experimental section and the diffusivity of 1M $LiPF_6$ in EC:DEC at 25ºC proposed by Lee et al,[139] is very fast with $\tau_{electrolyte} < 1\ s$. A second gradient, due to the difference in potential at the front of the electrode and at the back of the electrode, leads to Li redistribution of the Li within the solid matrix. The time scale of this gradient at the beginning of the tail region is estimated from the equations detailed in the appendix to be $\tau_{electrode}\ <\ 4s$. A third gradient appears within each particle, leading to a core-shell structure. Estimating the time scale of this relaxation process would not be correct with our GITT-type measurement as the diffusion coefficient in the electrode is extracted from similar relaxations pulses.[140] Nevertheless, from the comparison of the time constant previously estimated with the length of the relaxation profiles, it is clear that, in agreement with literature, the relaxation of the gradient within the particles is the rate-limiting step in the relaxation of the potential. All these changes occur without changing the net SOC of the electrode.

Table 4. 1: Relaxation processes upon current interruption

Relaxation process	Time scale
Concentration gradient in the electrolyte	$\tau_{electrolyte} = \frac{L^2}{\pi^2 . D_{Salt}^{Electrolyte}}$ $\tau_{electrolyte} < 1s$
Concentration gradient from the front to the back of the electrode	Li redistribution from the front of the electrode to the back of the electrode. Rapid equilibration due to current passing between the front and the back of the electrode. [115] $\tau_{electrode} = \frac{Fl^2}{\kappa . A}$ With A the slope of the OCP curve, in the tail region: $\tau_{electrode} < 4s$
Concentration gradient within individual particles	Core-shell model with Li diffusion from the surface to the core $\tau_{particle} = \frac{{R_p}^2}{D_{Lithium}^{Cathode}}$ Rate limiting step in the relaxation[126]

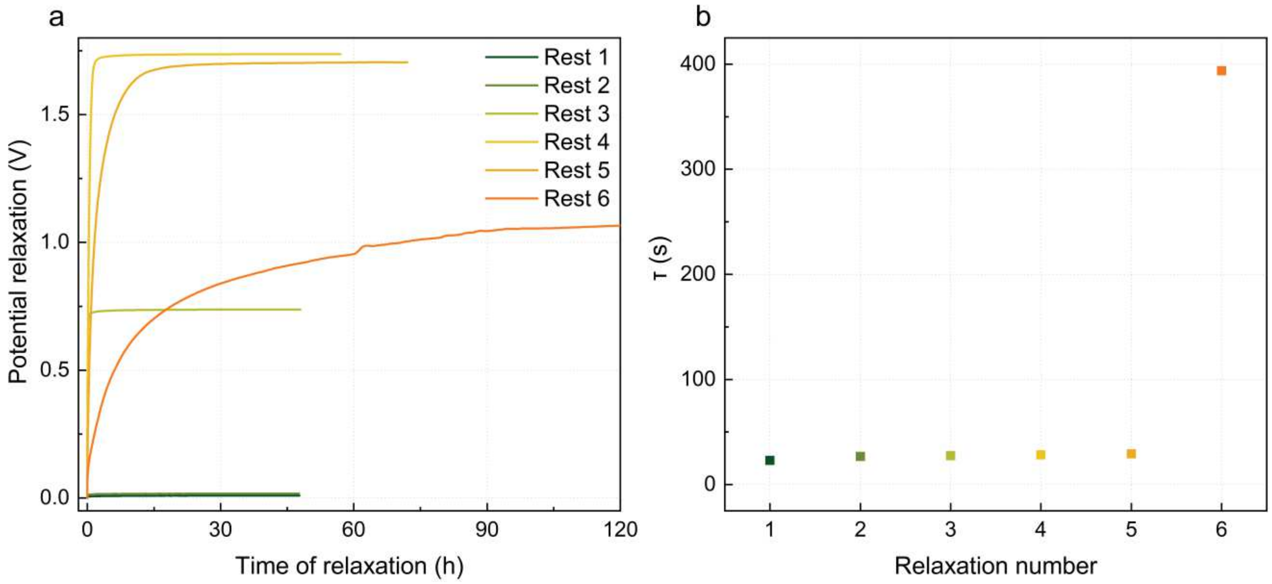

Figure 4. 13: a. Potential relaxation profiles of the pseudo GITT rests vs time; b. τ vs relaxation number with $V-V_{inf} = e^{-t/\tau}$

As a mean to compare the Li diffusion through the pseudo-GITT relaxation steps presented in Figure 4. 13. a, the time contribution τ for each relaxation profile is calculated based on equation [7] from the relaxation profiles (example in Figure SI. 9) and presented in Figure 4. 13. b. We see a linear increase for the rests 1 to 5 and a clear change in regime can be observed from the rest point 5 to the rest point 6. We interpret the change in relaxation time constant as a confirmation that the xLi = 1 mark has been passed, and we use the coulombs passed at rest 6 with the initial assumption of $xLi^{ini} = 1$ to validate the setting x-axis for the OCP curve. The resolution of the position xLi = 1 can be increased by adding more GITT rests around the $xLi^{ini} = 1$. The final OCP curve for the material NMC622 is extracted by fitting the curve between V_{trust} and the pseudo-GITT rests, leading to the curve presented in Figure 4. 14. a and b.

$$V - V_{inf} = e^{\frac{-t}{\tau}} \qquad [7]$$

for $t >> \tau$

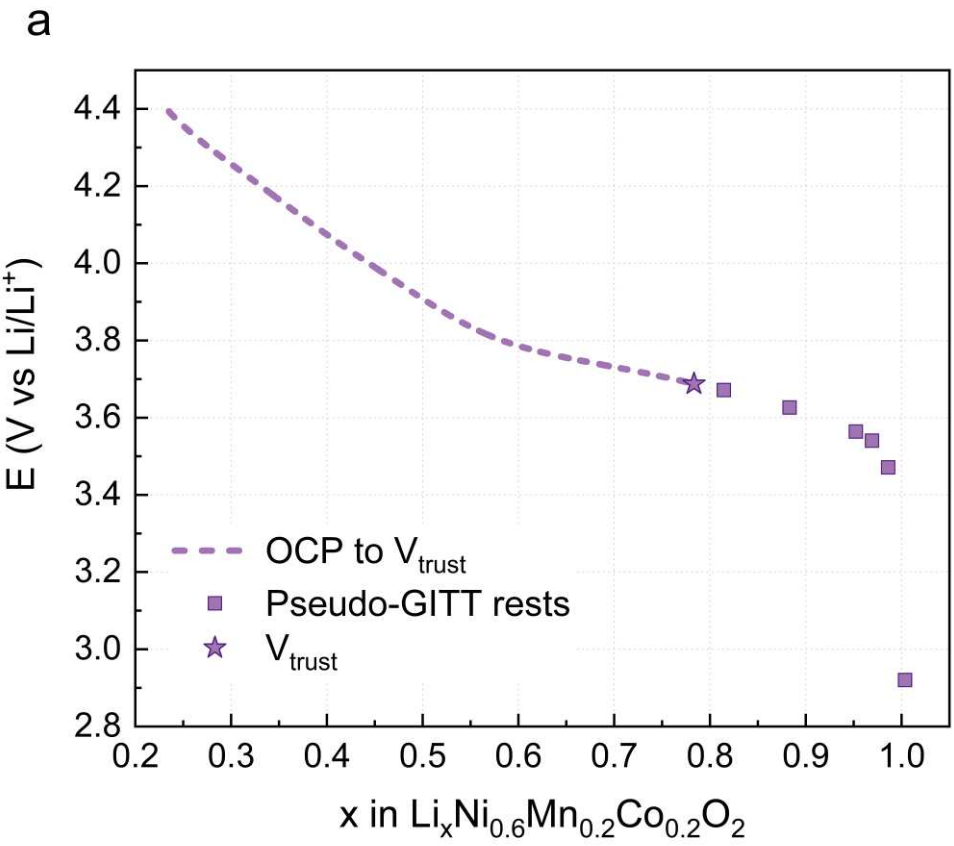
a
E (V vs Li/Li+)
4.4
4.2
4.0
3.8
3.6
3.4
3.2
3.0
2.8
0.2
0.3
0.4
0.5
0.6
0.7
0.8
0.9
1.0
x in LixNi0.6Mn0.2Co0.2O2
OCP to Vtrust
Pseudo-GITT rests
Vtrust

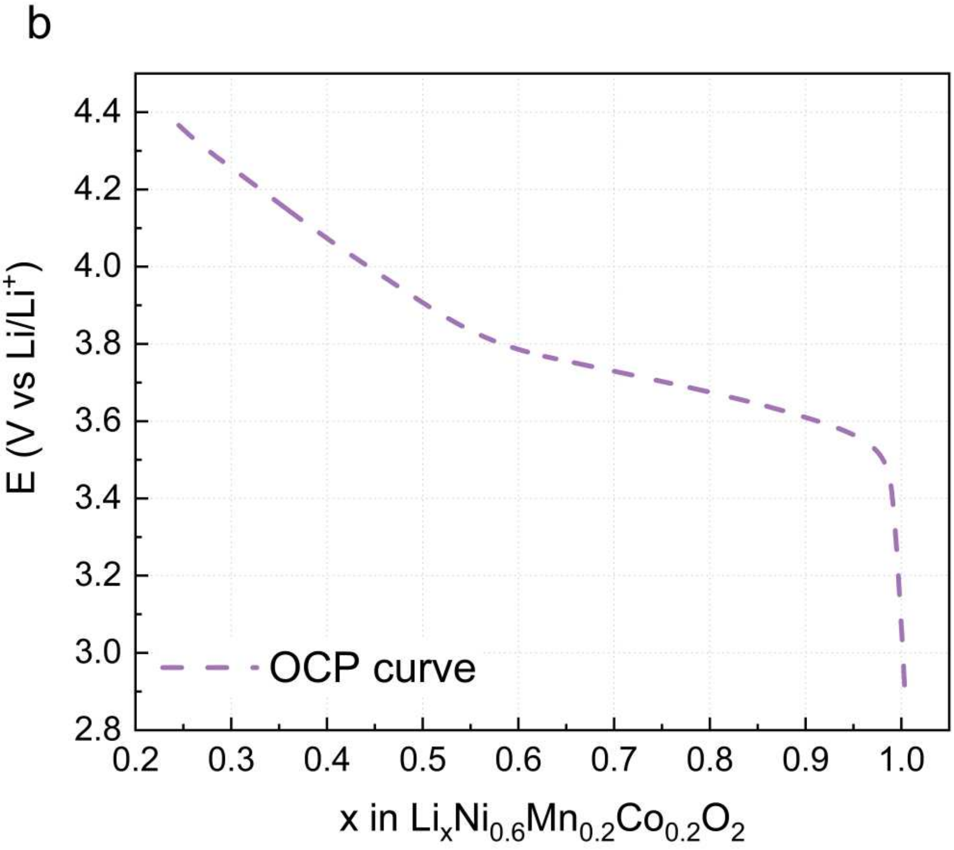
b
E (V vs Li/Li+)
4.4
4.2
4.0
3.8
3.6
3.4
3.2
3.0
2.8
0.2
0.3
0.4
0.5
0.6
0.7
0.8
0.9
1.0
x in LixNi0.6Mn0.2Co0.2O2
OCP curve

Figure 4. 14: a. OCP curve of NMC622 (purple –dashed) in the trust region and relaxation potential of the pseudo-GITT step; b. Final OCP curve of NMC622 (purple - dashed)

2. Comparison with literature and outcome of the method

The NMC622 OCP curve that we determined with our new method is compared with NMC622 C/20 half-cell data reported by Arumugam et al.[56] in Figure 4. 15. In a first step, the data is compared with our first cycle on a gravimetric scale in Figure 4. 15. a. A difference in the initial charge capacity is observed and is expected to come from different Li concentration in the pristine electrode, potentially due to storage conditions, different thickness or different particle size. The two profiles are in good agreement for the rest of the cycling. The two data sets are converted to a Li content scale by applying the same factor as described in step 1 of our OCP determination method. The average of the lithiation and delithiation curves, presented in Figure 4. 15. b, is compared with our OCP curve in Figure 4. 15. c, which highlights the additional information in the tail region brought by our new OCP curve characterization method.

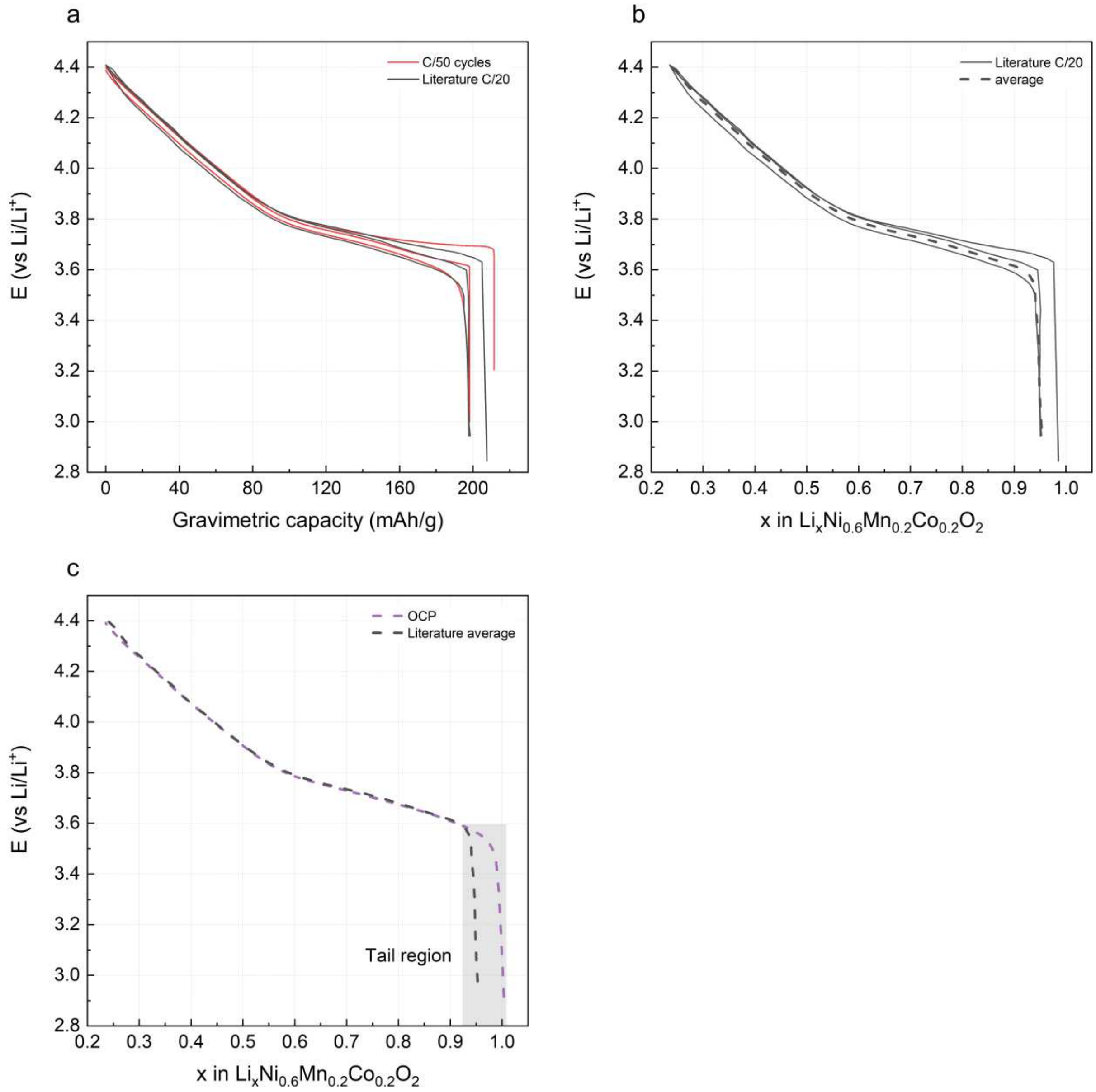

Figure 4. 15: Comparison of the NMC622 OCP curve with C/20 literature data[56]*; a. Comparison of the intercalation/deintercalation profile for the first charge to* V_{high} *and the subsequent cycle between* V_{high} *and 3.0 V of the previously presented NMC622 C/50 cycles (red) and the C/20 NMC622 data from Arumugam et al.*[56] *(black) on the gravimetric scale (mAh.g*$^{-1}$*); b. Average of the lithiation and delithiation at C/20 of the literature data (black – dot/dash); c. Comparison between the average of the C/20 cycles from literature (black – dotted) and our OCP curve (purple - dotted)*

Other NMC materials OCP are compared with literature data in Figure 4. 16. The GITT data on NMC111 obtained by Buchberger et al.[26] is compared with the NMC111 data obtained following our OCP characterization method in Figure 4. 16. a. The GITT data is in good agreement with our NMC111 OCP curve, with the addition of the tail region for the later. The NMC532 presented in Figure 4. 16. b from Weber et al.[62] was cycled at C/50 up to 4.5 V. A minimal shift of 5.5 mAh.g^{-1} was applied to the literature data to match our OCP curve, leading to a difference in profile between the literature data and our OCP at higher potential, possibly due to side reactions occurring at high potential. Our NMC811 OCP curve is compared with the data obtained by Li et al.[64] at C/20. A shift of 2 mAh.g^{-1} was applied to the data. The comparison of our OCP curve characterization method highlights the additional information brought in the tail region for each material. The initial Li content of the pristine NMC532 suggests a slight overlithiation of the material before cycling whereas the initial content of the pristine NMC811 suggests a lower Li content. These observations are in agreement with previous observations for these materials.[74]

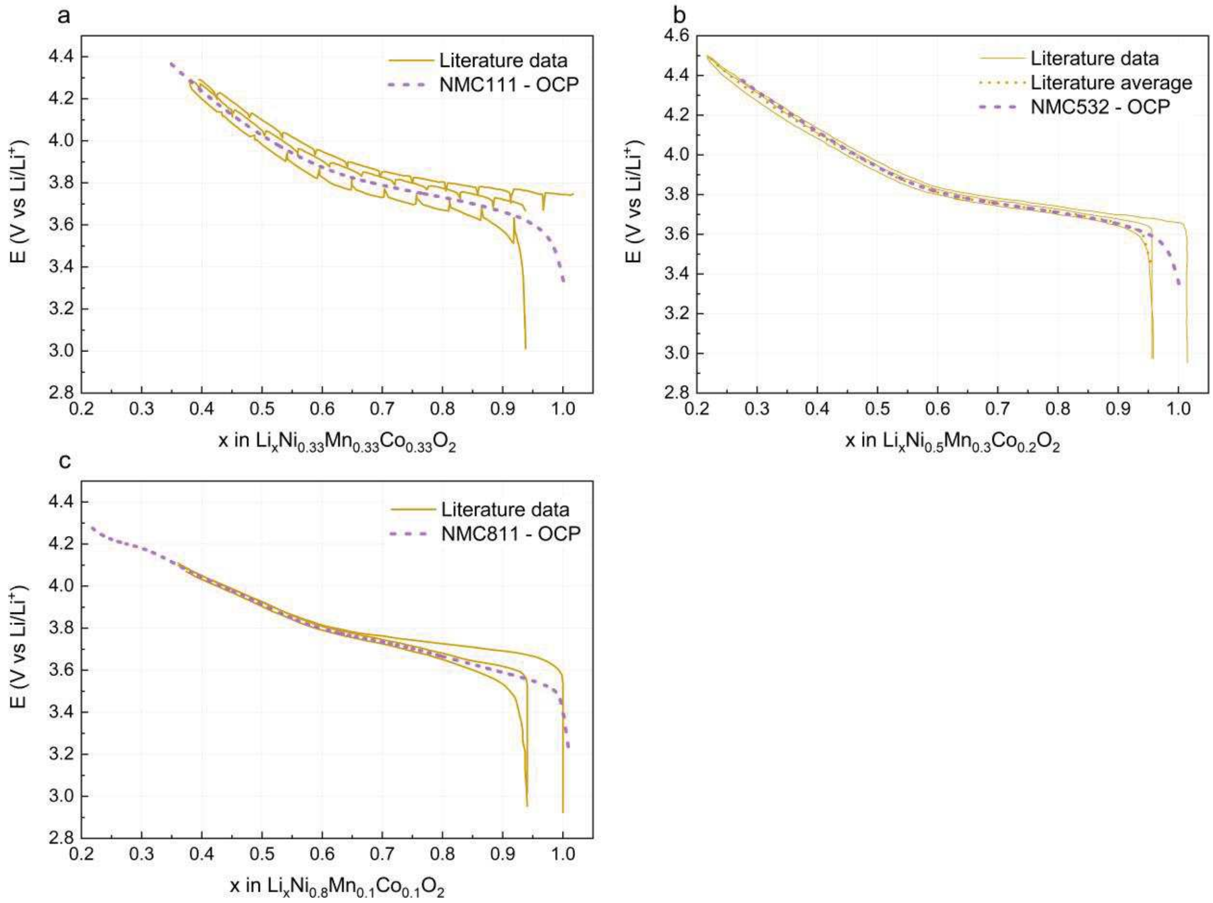

Figure 4. 16: a. Comparison of the NMC111 OCP curve with scaled GITT literature data from Buchberger et al.[26]; b. Comparison of the NMC532 OCP curve with scaled literature data from Weber et al.[62](C/50); c. Comparison of the NMC811 OCP curve with scaled literature data from Li et al.[64] (C/20)

Summary

The electrochemical and structural results obtained on the lithiation of NMC cathode materials at potentials below 3.0 V vs Li/Li^+ were used in order to develop a method to map the OCP of a cathode to its Li content. A current correction method was applied in order to correct for the inherent bias of the battery tester channels. Several cycles at different C-rates were used to identify a trust regime in which the average of the lithiation and the delithiation curves can be used as the OCP curve. Below the potential of this trust regime, GITT steps were used in order to identify the OCP at high lithiation degrees. The position of xLi = 1 was estimated by the potential profile of the relaxation of the GITT steps around the $xLi^{ini} = 1$ position. The capacity of the lithiation pulses can be tuned in order to determine the xLi = 1 position with more precision.

Aside from bringing information on the tail region of the OCP curve of cathode materials to the ABMS, our OCP characterization method allows for better comparison between research results from different laboratories. Additionally, the OCP curve can be used to link electrochemical studies to structural investigations of cathode materials with the use of a more precise x-axis scale. The thorough investigation of the structure and Li dynamics in NMC811 done by Marker et al.[13] is a great platform for how the use of an OCP database can allow different research groups to link results obtained by NMR or XRD to future investigation, by using the relationship between OCP and Li content established by our OCP characterization method.

Conclusion

Ni-based cathode materials were investigated in this thesis with the objective of providing parameters to the advanced battery management system. This work was divided in two sections. A first part was dedicated to a fundamental study of NMC cathode materials upon deep lithiation. This first section included an electrochemical study of various stoichiometry of NMC cathodes, a structural characterization of the electrodes at different lithiation degrees, with XRD and XAS, and a gas analysis of the stability of different electrolytes in an extended potential window. A second section was dedicated to the development of a method to electrochemically characterize the OCP curve vs Li content of cathodes, based on the fundamental understanding gained in the first section.

In chapter 1, NMC111, NMC442, NMC532, NMC622, and NMC811 were cycled in the extended potential window of 4.3-4.4 to 0.8 V vs Li/Li^+. A first lithiation plateau was observed upon recovery of the initial delithiation capacity, appearing at different potentials depending on the NMC stoichiometry. The apparition of this plateau below 2.0 V vs Li/Li^+ was linked to the formation of a Li-rich phase at the surface of the particles due to the slow Li diffusion in the monovacancy hopping regime reached at high lithiation degrees. The potential of this first lithiation plateau was linked to the proportion of trivalent Ni in the pristine material, with the highest potential observed for NMC811. A relative reversibility of the cycling between V_{high} and $xLi = 1$ (corresponding to the recovery of the initial capacity) was observed upon ~ 40 cycles.

Deep lithiation to reach twice the theoretical capacity ($xLi = 2$) was done by lowering the potential to ~ 0.8 V vs Li/Li^+ in order to form the Li-rich phase in the bulk of the material. This deep lithiation allowed to reach an extra ~ 315 $mAh.g^{-1}$ and lead to the apparition of a second lithiation plateau for the Ni-rich NMC materials. The capacity reached upon the first plateau was compared with the theoretical capacity resulting from the reduction of Ni to Ni^{2+} and it appeared that other TMs have to be reduced in order to reach the capacity accessed. The second plateau observed for Ni-rich NMCs was estimated to result from the reduction of Co and Mn and the total capacity reached upon deep lithiation to $xLi = 2$ was in good agreement with the reduction of all TMs to the valence state 2^+ with minimal side reactions expected.

The delithiation to V_{high} after deep lithiation to xLi = 2 exhibited a minimal capacity loss of ~ 1% of the total capacity for NMC111, NMC532, and NMC622, whereas NMC811 lost about 45 % of the lithiation capacity. This capacity loss was expected to result from structural degradation upon the lithiation in the range of xLi = 1 to xLi = 2. Surprisingly the NMC442 material gained capacity upon delithiation after lithiation to xLi = 2, which was attributed to significant Mn^{2+} dissolution towards the anode upon deep lithiation, leading to the formation of a Ni-rich structure for NMC442 allowing the material to reach more capacity upon delithiation. The hypotheses made from the electrochemical cycling and the theoretical calculations were investigated in a characterization study with XRD and XAS measurements.

Through a detailed XRD and XAS investigation, the lithiation to xLi = 1 was shown to result from the reduction of the bulk Ni, with minimal reduction of all TMs at the surface of the material, supporting the hypothesis of the formation of a Li-rich phase at the surface of the particles. The same XRD diffraction pattern was obtained for materials delithiated to V_{high} after lithiation to xLi = 1 and cathodes delithiated to V_{high}. In similarity, the valence of the TMs in the bulk and the surface of the material upon delithiation after lithiation to xLi = 1 returned to that of samples delithiated to V_{high}, supporting the good reversibility observed with electrochemistry.

The formation of the Li-rich 1T-Li_2MO_2 phase was observed with XRD at along the second lithiation plateau upon deep lithiation to xLi = 2. The NMC structure at xLi = 2 appeared to be a combination of the 1T-Li_2MO_2 phase and a disordered 3R-$LiMO_2$ phase, possibly indicating cation mixing and particle size reduction upon deep lithiation. No spinel phase was observed in the materials but further structural characterization is recommended. All TMs reduced towards the oxidation state 2^+ at xLi = 2, supporting the calculations made in the electrochemical section and indicating minimal side reactions. The investigation of the NMC structure upon delithiation to V_{high} after deep lithiation to xLi = 2 highlighted the partial loss of the layered structure. The investigation to the oxidation state of the TMs at V_{high} after lithiation to xLi = 2 showed a more reduced Ni compared to the samples delithiated to V_{high} even for the NMC materials exhibiting good reversibility, indicating a limited capacity for the NMC materials to withstand many cycles in this extended potential window.

The anticipated poor reversibility over several overlithiation cycles was confirmed with electrochemistry as all NMC cathodes lost capacity over 5 overlithiation cycles. The formation of a new Ni-rich NMC structure for NMC442 at xLi = 2 after Mn dissolution was confirmed by the capacity loss observed in the material over the 5 overlithiation cycles, in line with that of the other Ni-rich NMC materials studied.

To investigate the role of the electrolyte in the changes observed upon electrochemistry, several electrolytes were used to cycle NMC622 vs Li half-cells. A lower capacity was accessed upon the first delithiation to V_{high} with the electrolytes 1M $LiPF_6$ in EC:EMC:DMC, 1M $LiPF_6$ in EC:DEC:FEC, and 1M $LiClO_4$ in EC:DEC:FEC compared to the baseline electrolyte 1M $LiPF_6$ in EC:DEC. This difference was linked to a higher impedance in those cells, either due to a different charge-transfer resistance for 1M $LiPF_6$ in EC:EMC:DMC, or to the chemical formation of a passivation layer for the electrolytes with FEC. After a lithiation to xLi = 2, the cells cycled with the electrolytes containing FEC exhibited a higher capacity loss, indicative of a negative effect of the solvent.

The K-edge spectra of cathodes cycled with 1M $LiPF_6$ in EC:DEC:FEC were compared with that of cathodes cycled with 1M $LiPF_6$ in EC:DEC. The difference in capacity reached upon first delithiation was confirmed by a lower oxidation state of Ni at V_{high}. Additionally, even though the oxidation state of all TMs was similar in both samples lithiated to 3.0 V, the oxidation state of Ni appeared significantly more reduced in the sample lithiated to xLi = 1 in presence of FEC. The comparison of the capacity corresponding to the Ni valence change observed from 3.0 V to xLi = 1 for the sample with FEC with the actual capacity reached in this potential window revealed that a significant portion of this capacity was lost to side reactions.

The gases evolving in a NMC622 vs Li half-cell cycled with 1M $LiPF_6$ in EC:DEC were investigated with a custom gas analysis set-up. Ethylene gas evolution was observed at ~ 0.8 V vs Li/Li^+, indicative of the formation of a passivation layer on the cathode due to EC reduction. The oxidation of this layer was observed at high potential. No gases resulting from the NMC622 structural changes were observed. The different electrolytes were then investigated with cyclic voltammetry in a carbon paper vs Li half-cell. The evolution of ethylene gas at ~ 0.8 V vs Li/Li^+ was observed for all the electrolytes, with significantly more ethylene gas produced for the electrolytes without FEC. In presence of FEC, an evolution of carbon dioxide was observed at ~ 1.5 V vs Li/Li$^+$, sign of FEC reduction. The carbon dioxide produced was immediately consumed and potentially lead to Li_2CO_3 formation. The subsequent reduction of EC appeared hindered by the FEC reduction, leading to the formation of a different passivation layer. The better cycling capabilities observed upon cycling in the extended potential window of 4.4 V – 0.8 V vs Li/Li$^+$ for the cells without FEC appears linked to the formation of a better passivation layer upon EC reduction.

The fundamental study of NMC cathodes upon extreme lithiation to xLi = 2 highlighted irreversible structural changes in the cathode material as well as electrolyte reduction. An overlithiation to xLi = 1, or up to the first lithiation plateau however did not trigger irreversible structural changes in the cathode, and with an adequate electrolyte no gas evolution was observed. This observation of good reversibility over an extended potential window of 4.4 V to ~ 1.5 V vs Li/Li$^+$ was used to develop a new OCP characterization method.

The OCP curve is one of the key parameters needed in the advanced battery management system. It provides the equilibrium potential of a material as a function of the Li content. As the ABMS relies on the depth-resolved physical properties of the battery materials, a surface characterization of the electrodes is needed. Upon lithiation, the surface of the material can experience a higher lithiation degree that its bulk, leading to the need of an OCP curve outside of the classic potential window. Based on the understanding gained in the fundamental study of NMC cathodes, a new OCP curve determination method was developed. A trust region was determined by comparing the cycling profiles of different C-rates. The OCP in this trust region was obtained as the average of the lithiation and delithiation curves. The equilibrium potential of the material was reached outside of the trust region by using GITT steps up to the initial Li content of 1. The position of the xLi = 1 was set by comparing the relaxation constant τ of the GITT steps. This new OCP characterization method not only allows access to additional information in the tail region, it also sets the x-axis of the OCP curve, allowing for an easier comparison of data between research groups.

List of figures

List of tables

Appendix Chapter 1: Electrochemical overlithiation of NMC cathode materials

Table SI. 1 : Summary of coulomb counting for the determination of the Li content in NMC cathodes

Cathode	Capacity reached (mAh.g^{-1})	xLi
NMC111 cycled from 4.4 V to 1.38 V	279.52	1.00
NMC111 cycled from 4.4 V to 0.8 V	579.18	2.07
NMC442 cycled from 4.4 V to 1.13 V	278.67	1.00
NMC442 cycled from 4.4 V to 0.8 V	575.36	2.06
NMC532 cycled from 4.4 V to 1.58 V	277.59	1.00
NMC532 cycled from 4.4 V to 0.8 V	575.65	2.07
NMC622 cycled from 4.4 V to 1.60 V	276.51	1.00
NMC622 cycled from 4.4 V to 1.52 V	332.4	1.20
NMC622 cycled from 4.4 V to 1.03 V	369.2	1.33
NMC622 cycled from 4.4 V to 1.01 V	418.9	1.51
NMC622 cycled from 4.4 V to 0.8 V	463.3	1.68
NMC111 cycled from 4.4 V to 0.8 V	570.6	2.06
NMC811 cycled from 4.3 V to 1.79 V	275.51	1.00
NMC811 cycled from 4.3 V to 0.8 V	561.46	2.04

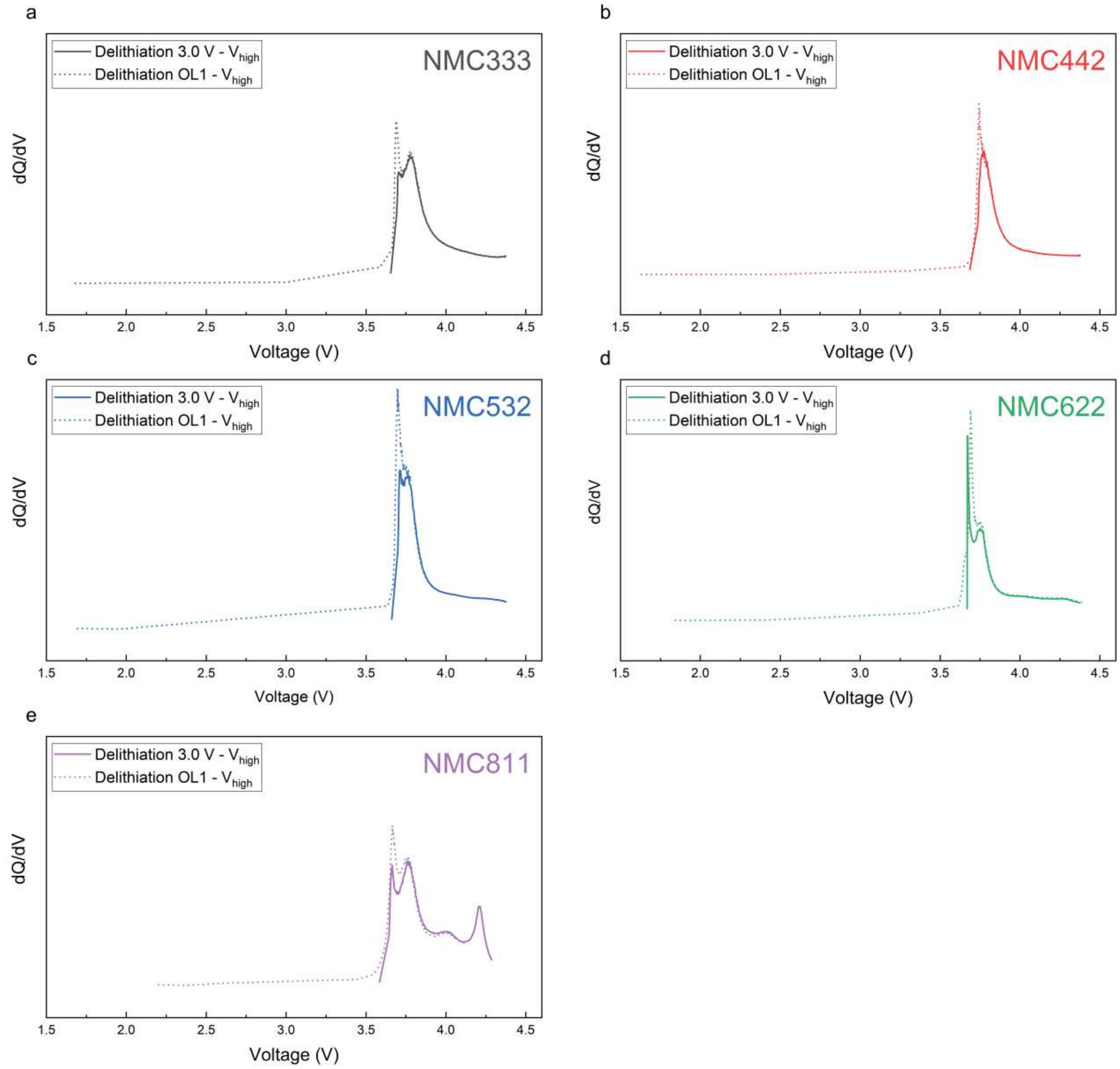

Figure SI. 2: Comparison of the delithiation from 3.0 V – V_{high} and delithiation from OL1 – V_{high} in a dQ/dV vs V plot for NMC111, NMC442, NMC532, NMC622, and NMC811. The potential of apparition of the peaks remains the same upon delithiation after a lithiation to OL1.

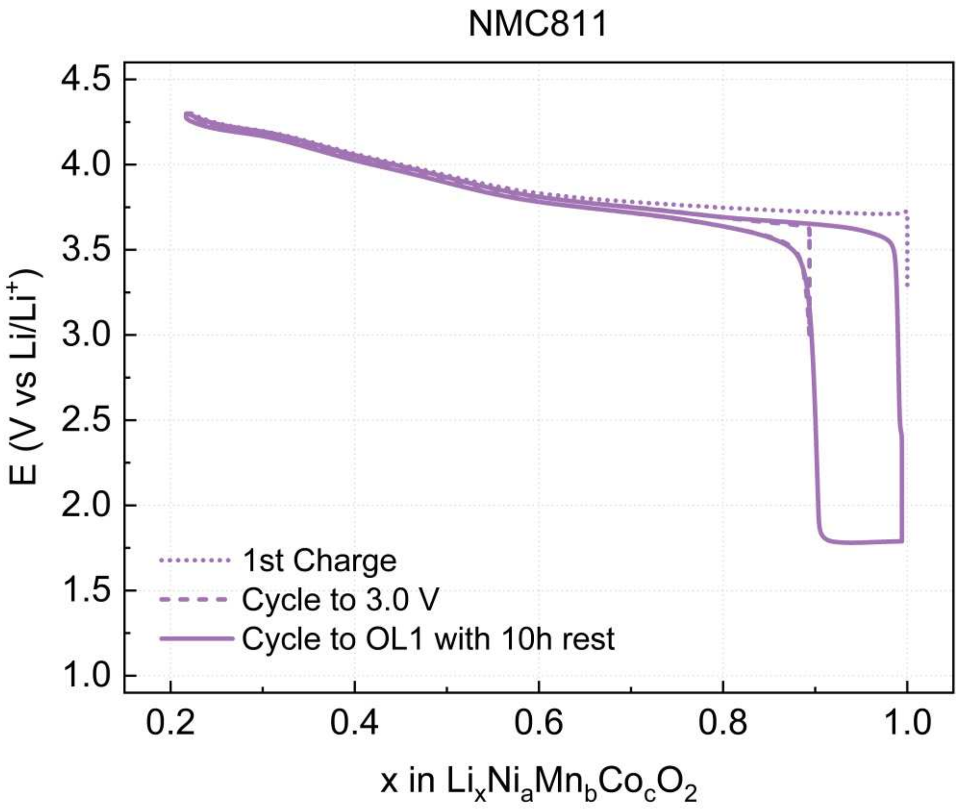

Figure SI. 3: Lithiation/delithiation profile of NMC811 to xLi = 1 with a rest of 10 hours after lithiation

Table SI. 4: Calculations for estimating the capacity associated with reduction of Ni, Co, and Mn ions in NMC532 from their pristine oxidation state (valence) to 2+

Element	Ni in NMC532	Mn in NMC532	Co in NMC532	Comment
Initial stoichiometry	0.5	0.3	0.2	$Li_1Ni_aMn_bCo_cO_2$
Initial valence	2.4	4	3	From Wu et al.[73]
Valence: reduction to 2^+	0.4	2	1	Difference between initial valence and 2^+
Capacity accessed upon reduction to 2^+	55.52	166.55	55.52	$mAh.g^{-1}$ associated with valence change

Table SI. 5: Calculations for estimating the capacity associated with reduction of Ni, Co, and Mn ions in NMC622 from their pristine oxidation state (valence) to 2^+

Element	Ni in NMC622	Mn in NMC622	Co in NMC622	Comment
Initial stoichiometry	0.6	0.2	0.2	$Li_1Ni_aMn_bCo_cO_2$
Initial valence	2.66	4	3	From Tian et al.[43]
Valence: reduction to 2^+	0.66	2	1	Difference between initial valence and 2^+
Capacity accessed upon reduction to 2^+	109.50	110.60	55.30	mAh.g^{-1} associated with valence change

Table SI. 6: Calculations for estimating the capacity associated with reduction of Ni, Co, and Mn ions in NMC811 from their pristine oxidation state (valence) to 2^+

Element	Ni in NMC811	Mn in NMC811	Co in NMC811	Comment
Initial stoichiometry	0.8	0.1	0.1	$Li_1Ni_aMn_bCo_cO_2$
Initial valence	2.875	4	3	From Gao et al.[46]
Valence: reduction to 2^+	0.875	2	1	Difference between initial valence and 2^+
Capacity accessed upon reduction to 2^+	192.86	55.10	27.55	mAh.g^{-1} associated with valence change

Appendix Chapter 2: Structural characterization of NMC materials upon deep lithiation

Table SI. 7: Oxidation state (valence) values of Ni, Co, and Mn TMs in NMC622, capacities that would be associated with the identified valence changes, and a comparison to the measured capacities via electrochemistry

xLi	Ni valence	Co valence	Mn valence	Capacity (mAhg^{-1})	Difference from electrochemistry
1.20	+2.54	+2.87	+3.94	314.2	7 %
1.33	+2.47	+2.84	+3.94	325.4	16 %
1.51	+2.30	+2.43	+3.02	427.8	3 %
1.68	+2.30	+2.35	+2.84	442.9	7 %
2.06	+1.91	+2.21	+2.57	529.1	15 %

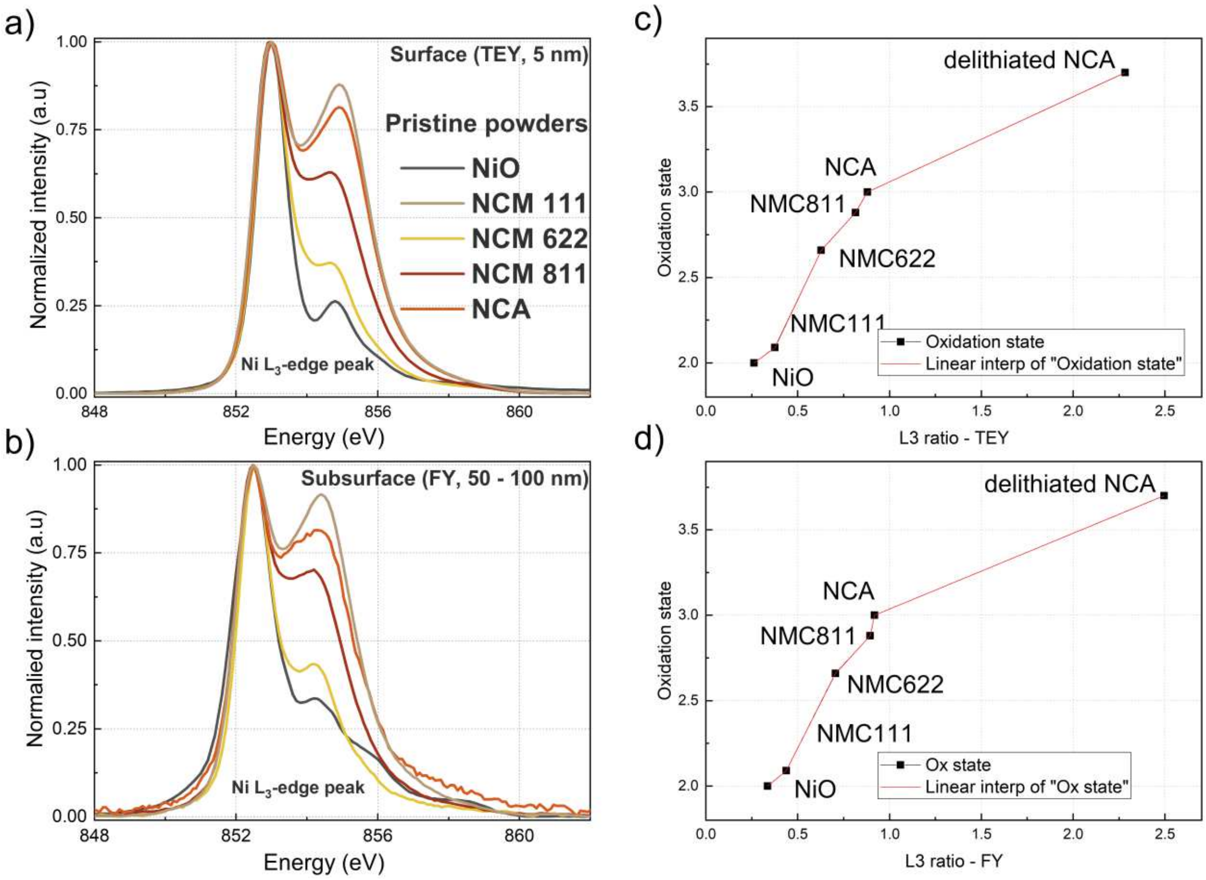

Figure SI. 8: L-edge spectra of standards (powder) a. TEY; b. FY; Oxidation state vs $L_{3,high}/L_{3,low}$ ratio and corresponding interpolation curve c. TEY; d. FY

Appendix Chapter 4: Open-circuit potential curve determination

Estimation of the relaxation of the Li concentration gradient from the top to the bottom of the electrode

Assumptions made: the electronic redistribution is extremely fast because the electronic conductivity is higher than the ionic conductivity, we ignore surface kinetics

Ohms law for the current passing through the electrolyte phase:

$$i_{ionic} = -\kappa \nabla \Phi$$

Potential in the material from the OCP curve:

$$\mathrm{U}_{in\ the\ material} = f\ (c_{Li})$$

From Taylor series with U_0 potential at a given point, A the slope of the OCP curve, c_{Li} the Li concentration

$$\mathrm{U}_{in\ the\ material} = \mathrm{U}_0 + A(c_{Li} - c_{Li}^0)$$

From the kinetics:

$$\left(\Phi_{metal} - \Phi_{eletrolyte} - \mathrm{U}_{in\ the\ material}\right) = 0$$

Material balance on Li ions in the cathode:

$$\frac{\partial c_{Li}}{\partial t} = -\frac{1}{F} \nabla \cdot \underline{i}$$

$$\frac{\partial c_{Li}}{\partial t} = \frac{\kappa}{F} \nabla^2 \Phi$$

$$\Phi_{metal} - \Phi_{eletrolyte} = \mathrm{U}_0 + A(c_{Li} - c_{Li}^0)$$

$$\frac{\partial \Phi}{\partial t} = A \frac{\partial c_{Li}}{\partial t}$$

$$\frac{\partial \Phi}{\partial t} = \frac{A\kappa}{F} \nabla^2 \Phi$$

$$\tau = \frac{Fl^2}{\kappa A}$$

With l thickness of the coating

$$l = 38\ \mu m;\ \kappa = 10\ mS.cm^{-1};$$

$$A = \frac{a}{[Li]}; with\ a\ slope\ of\ the\ OCP\ curve\ at\ a\ given\ point;$$

$$1 \leq a_{tail\ region} \leq 5$$

$$[Li] = 2.5.10^4\ mol.m^{-3}$$

$$calculated\ from\ the\ density\ of\ the\ active\ material\ of\ 2.37\ g.cm^{-3}$$

$$and\ the\ molar\ mass\ M_{NMC622} = 96.93\ g.mol^{-1}$$

Figure SI. 9: Example of fit of τ for GITT rest 4

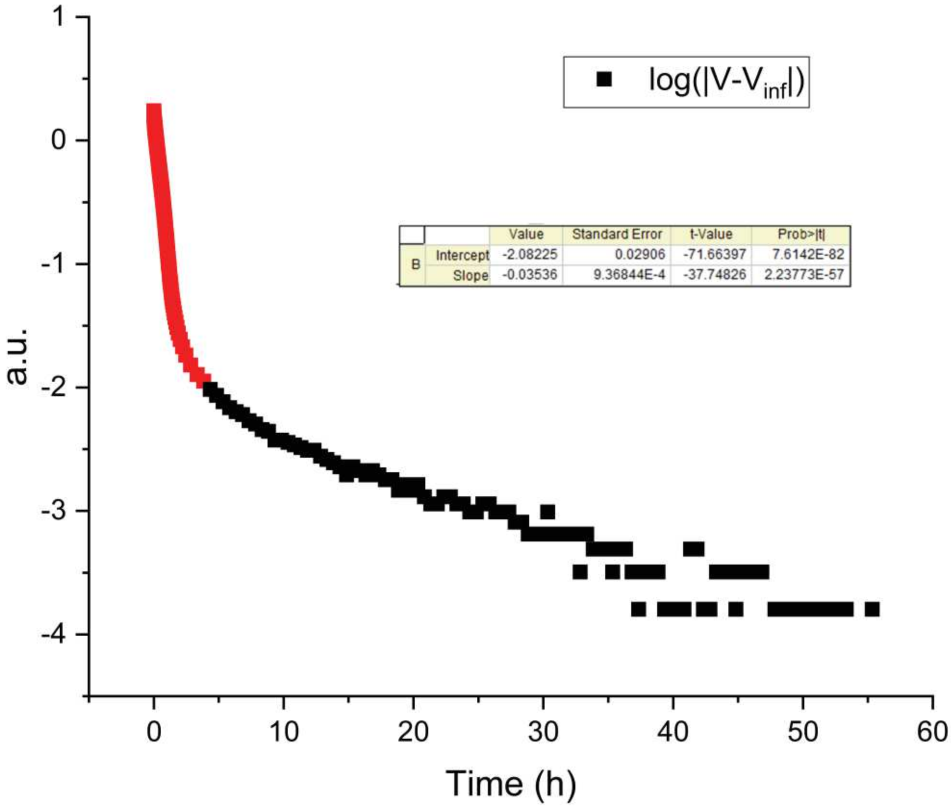

		Value	Standard Error	t-Value	Prob>|t|
B	Intercept	-2.08225	0.02906	-71.66397	7.6142E-82
	Slope	-0.03536	9.36844E-4	-37.74826	2.23773E-57

References

1 Z. Liu, P. Ciais, Z. Deng, R. Lei, S. J. Davis, S. Feng, B. Zheng, D. Cui, X. Dou, B. Zhu, R. Guo, P. Ke, T. Sun, C. Lu, P. He, Y. Wang, X. Yue, Y. Wang, Y. Lei, H. Zhou, Z. Cai, Y. Wu, R. Guo, T. Han, J. Xue, O. Boucher, E. Boucher, F. Chevallier, K. Tanaka, Y. Wei, H. Zhong, C. Kang, N. Zhang, B. Chen, F. Xi, M. Liu, F. M. Bréon, Y. Lu, Q. Zhang, D. Guan, P. Gong, D. M. Kammen, K. He and H. J. Schellnhuber, *Nat. Commun.*, 2020, **11**, 1–12.

2 A. Manthiram, *ACS Cent. Sci.*, 2017, **3**, 1063–1069.

3 N. A. Chaturvedi, R. Klein, J. Christensen, J. Ahmed and A. Kojic, *IEEE Control Syst. Mag.*, 2010, 49–68.

4 K. Mizushima, P. C. Jones, P. J. Wiseman and J. B. Goodenough, *Mater. Res. Bull.*, 1980, **15**, 783–789.

5 C. Daniel, D. Mohanty, J. Li and D. L. Wood, *AIP Conf. Proc.*, 2014, **1597**, 26–43.

6 M. D. Radin, S. Hy, M. Sina, C. Fang, H. Liu, J. Vinckeviciute, M. Zhang, M. S. Whittingham, Y. S. Meng and A. Van der Ven, *Adv. Energy Mater.*, 2017, 7.

7 S. M. Bak, Z. Shadike, R. Lin, X. Yu and X. Q. Yang, *NPG Asia Mater.*, 2018, **10**, 563–580.

8 N. Tsiouvaras, S. Meini, I. Buchberger and H. A. Gasteiger, *J. Electrochem. Soc.*, 2013, **160**, A471–A477.

9 S. Meini, S. Solchenbach, M. Piana and H. A. Gasteiger, *J. Electrochem. Soc.*, 2014, **161**, A1306–A1314.

10 M. Metzger, C. Marino, J. Sicklinger, D. Haering and H. A. Gasteiger, *J. Electrochem. Soc.*, 2015, **162**, A1123–A1134.

11 R. Jung, M. Metzger, F. Maglia, C. Stinner and H. A. Gasteiger, *J. Electrochem. Soc.*, 2017, **164**, A1361–A1377.

12 M. Wood, J. Li, R. E. Ruther, Z. Du, E. C. Self, H. M. Meyer, C. Daniel, I. Belharouak and D. L. Wood, *Energy Storage Mater.*, 2020, **24**, 188–197.

13 K. Märker, P. J. Reeves, C. Xu, K. J. Griffith and C. P. Grey, *Chem. Mater.*, 2019, **31**, 2545–2554.

14 X. Yu, Y. Lyu, L. Gu, H. Wu, S. M. Bak, Y. Zhou, K. Amine, S. N. Ehrlich, H. Li, K. W. Nam and X. Q. Yang, *Adv. Energy Mater.*, 2014, **4**, 1–11.

15 M. L. Baker, M. W. Mara, J. J. Yan, K. O. Hodgson, B. Hedman and E. I. Solomon, *Coord. Chem. Rev.*, 2017, **345**, 182–208.

16 A. Manceau, M. A. Marcus and S. Grangeon, *Am. Mineral.*, 2012, **97**, 816–827.

17 S. M. Webb, *Phys. Scr.*

18 R. Qiao, T. Chin, S. J. Harris, S. Yan and W. Yang, *Curr. Appl. Phys.*, 2013, **13**, 544–548.

19 J. Stohr, *NEXAFS Spectroscopy*, Berlin Heidelberg, 1992.

20 V. A. Solé, E. Papillon, M. Cotte, P. Walter and J. Susini, *Spectrochim. Acta - Part B At. Spectrosc.*, 2007, **62**, 63–68.

21 B. Zhang, M. Metzger, S. Solchenbach, M. Payne, S. Meini, H. A. Gasteiger, A. Garsuch and B. L. Lucht, *J. Phys. Chem. C*, 2015, **119**, 11337–11348.

22 R. Bernhard, M. Metzger and H. A. Gasteiger, *J. Electrochem. Soc.*, 2015, **162**, A1984–A1989.

23 M. Metzger, B. Strehle, S. Solchenbach and H. A. Gasteiger, *J. Electrochem. Soc.*, 2016, **163**, A1219–A1225.

24 M. Metzger, B. Strehle, S. Solchenbach and H. A. Gasteiger, *J. Electrochem. Soc.*, 2016, **163**, A798–A809.

25 S. Aryal, E. V. Timofeeva and C. U. Segre, *J. Electrochem. Soc.*, 2018, **165**, A71–A78.

26 I. Buchberger, S. Seidlmayer, A. Pokharel, M. Piana, J. Hattendorff, P. Kudejova, R. Gilles and H. A. Gasteiger, *J. Electrochem. Soc.*, 2015, **162**, A2737–A2746.

27 C. Usubelli, M. M. Besli, S. Kuppan, N. Jiang, M. Metzger, A. Dinia, J. Christensen and Y. Gorlin, *J. Electrochem. Soc.*, 2020, **167**, 080514.

28 E. J. Cairns and P. Albertus, *Annu. Rev. Chem. Biomol. Eng.*, 2010, **1**, 299–320.

29 P. Y. Liao, J. G. Duh and S. R. Sheen, *J. Power Sources*, 2005, **143**, 212–218.

30 H. Arai, S. Okada, Y. Sakurai and J. Yamaki, *Solid State Ionics*, 1997, **95**, 275–282.

31 W. Li, J. Reimers and J. Dahn, *Solid State Ionics*, 1993, **67**, 123–130.

32 J. Zheng, Y. Ye, T. Liu, Y. Xiao, C. Wang, F. Wang and F. Pan, *Acc. Chem. Res.*, 2019, **52**, 2201–2209.

33 D. Peramunage, *J. Electrochem. Soc.*, 1998, **145**, 1131.

34 S. Priyono, S. Hardiyani, N. Syarif, A. Subhan and A. Suhandi, *J. Phys. Conf. Ser.*, 2019, **1191**, 012022.

35 Y.-K. Sun, M. G. Kim, S.-H. Kang and K. Amine, *J. Mater. Chem.*, 2003, **13**, 319–322.

36 N. Nitta, F. Wu, J. T. Lee and G. Yushin, *Mater. Today*, 2015, **18**, 252–264.

37 N. Yabuuchi, Y. Makimura and T. Ohzuku, *J. Electrochem. Soc.*, 2007, **154**, A314.

38 I. Belharouak, Y. K. Sun, J. Liu and K. Amine, *J. Power Sources*, 2003, **123**, 247–252.

39 K. . Shaju, G. . Subba Rao and B. V. . Chowdari, *Electrochim. Acta*, 2002, **48**, 145–151.

40 R. V. Chebiam, F. Prado and A. Manthiram, *Chem. Mater.*, 2001, **13**, 2951–2957.

41 C. S. Yoon, K. J. Park, U. H. Kim, K. H. Kang, H. H. Ryu and Y. K. Sun, *Chem. Mater.*, 2017, **29**, 10436–10445.

42 Q. Wang, C. H. Shen, S. Y. Shen, Y. F. Xu, C. G. Shi, L. Huang, J. T. Li and S. G. Sun, *ACS Appl. Mater. Interfaces*, 2017, **9**, 24731–24742.

43 C. Tian, D. Nordlund, H. L. Xin, Y. Xu, Y. Liu, D. Sokaras, F. Lin and M. M. Doeff, *J. Electrochem. Soc.*, 2018, **165**, A696–A704.

44 S. T. Myung, F. Maglia, K. J. Park, C. S. Yoon, P. Lamp, S. J. Kim and Y. K. Sun, *ACS Energy Lett.*, 2017, **2**, 196–223.

45 N. Zhang, J. Li, H. Li, A. Liu, Q. Huang, L. Ma, Y. Li and J. R. Dahn, *Chem. Mater.*, 2018, **30**, 8852–8860.

46 S. Gao, Y. T. Cheng and M. Shirpour, *ACS Appl. Mater. Interfaces*, 2019, **11**, 982–989.

47 M. Dixit, B. Markovsky, F. Schipper, D. Aurbach and D. T. Major, *J. Phys. Chem. C*, 2017, **121**, 22628–22636.

48 M. D. Radin and A. Van Der Ven, *Chem. Mater.*, 2018, **30**, 607–618.

49 C. Shen, D. Xiong, L. D. Ellis, K. L. Gering, L. Huang and J. R. Dahn, *J. Electrochem. Soc.*, 2017, **164**, A3349–A3356.

50 H. J. Noh, S. Youn, C. S. Yoon and Y. K. Sun, *J. Power Sources*, 2013, **233**, 121–130.

51 C. Delmas, J. P. Pc, A. Rougier, A. Demourgues, F. Weill, A. Chadwick, M. Broussely, F. Perton, P. Biensan and P. Willmann, .

52 J. P. Peres, C. Delmas, A. Rougier, M. Broussely, F. Perton, P. Biensan and P. Willmann, *J. Phys. Chem. Solids*, 1996, **57**, 1057–1060.

53 J. R. Mueller-Neuhaus, R. A. Dunlap and J. R. Dahn, *J. Electrochem. Soc.*, 2000, **147**, 3598–3605.

54 S. H. Kang, W. S. Yoon, K. W. Nam, X. Q. Yang and D. P. Abraham, *J. Mater. Sci.*, 2008, **43**, 4701–4706.

55 Y. M. Todorov and K. Numata, *Electrochim. Acta*, 2004, **50**, 495–499.

56 R. S. Arumugam, L. Ma, J. Li, X. Xia, J. M. Paulsen and J. R. Dahn, *J. Electrochem. Soc.*, 2016, **163**, A2531–A2538.

57 Y. Ruan, X. Song, Y. Fu, C. Song and V. Battaglia, *J. Power Sources*, 2018, **400**, 539–

548.

58 J. Choi and a Manthiram, *Electrochem. Solid State Lett.*, 2005, **8**, C102–C105.

59 Y. Chen, Y. Zhang, F. Wang, Z. Wang and Q. Zhang, *J. Alloys Compd.*, 2014, **611**, 135–141.

60 J. R. Dahn, U. von Sacken and C. A. Michal, *Solid State Ionics*, 1990, **44**, 87–97.

61 S.-H. Kang, S.-H. Park, C. S. Johnson and K. Amine, *J. Electrochem. Soc.*, 2007, **154**, A268.

62 R. Weber, C. R. Fell, J. R. Dahn and S. Hy, *J. Electrochem. Soc.*, 2017, **164**, A2992–A2999.

63 J. Li, R. Petibon, S. Glazier, N. Sharma, W. K. Pang, V. K. Peterson and J. R. Dahn, *Electrochim. Acta*, 2015, **180**, 234–240.

64 J. Li, L. E. Downie, L. Ma, W. Qiu and J. R. Dahn, *J. Electrochem. Soc.*, 2015, **162**, A1401–A1408.

65 C. Liu, Z. G. Neale and G. Cao, *Mater. Today*, 2016, **19**, 109–123.

66 A. Barai, K. Uddin, M. Dubarry, L. Somerville, A. McGordon, P. Jennings and I. Bloom, *Prog. Energy Combust. Sci.*, 2019, **72**, 1–31.

67 C. S. Johnson, J. S. Kim, A. Jeremy Kropf, A. J. Kahaian, J. T. Vaughey and M. M. Thackeray, *Electrochem. commun.*, 2002, **4**, 492–498.

68 C. S. Johnson, J. S. Kim, A. J. Kropf, A. J. Kahaian, J. T. Vaughey, L. M. L. Fransson, K. Edström and M. M. Thackeray, *Chem. Mater.*, 2003, **15**, 2313–2322.

69 A. Van der Ven, G. Ceder, M. Asta and P. D. Tepesch, *Phys. Rev. B - Condens. Matter Mater. Phys.*, 2001, **64**, 1–17.

70 V. A. Voronov, A. O. Shvetsov, S. P. Gubin, A. V. Cheglakov, D. Y. Kornilov, A. S. Karaseva, E. S. Krasnova and S. V. Tkachev, *Inorg. Mater. Appl. Res.*, 2017, **8**, 229–237.

71 T. Li, X.-Z. Yuan, L. Zhang, D. Song, K. Shi and C. Bock, *Degradation Mechanisms and Mitigation Strategies of Nickel-Rich NMC-Based Lithium-Ion Batteries*, Springer Singapore, 2020, vol. 3.

72 J. R. Mueller-neuhaus, *Analysis*.

73 Z. Wu, S. Ji, J. Zheng, Z. Hu, S. Xiao, Y. Wei, Z. Zhuo, Y. Lin, W. Yang, K. Xu, K. Amine and F. Pan, *Nano Lett.*, 2015, **15**, 5590–5596.

74 Z. Wu, S. Ji, Z. Hu, J. Zheng, S. Xiao, Y. Lin, K. Xu, K. Amine and F. Pan, *ACS Appl. Mater. Interfaces*, 2016, **8**, 15361–15368.

75 C. Delmas, C. Fouassier and P. Hagenmuller, *Phys. B+C*, 1980, **99**, 81–85.

76 H. Ben Yahia, M. Shikano and H. Kobayashi, *Chem. Mater.*, 2013, **25**, 3687–3701.

77 C. Delmas, J.-J. Braconnier and P. Hagenmuller, *Mater. Res. Bull.*, 1982, **17**, 117–123.

78 S. H. Kang, D. P. Abraham, W. S. Yoon, K. W. Nam and X. Q. Yang, *Electrochim. Acta*, 2008, **54**, 684–689.

79 R. Robert and P. Novák, *Chem. Mater.*, 2018, **30**, 1907–1911.

80 N. Iwashita, *X-ray Powder Diffraction*, Tsinghua University Press Limited., 2016.

81 C. Tian, F. Lin and M. M. Doeff, *Acc. Chem. Res.*, 2018, **51**, 89–96.

82 M. M. Besli, A. K. Shukla, C. Wei, M. Metzger, J. Alvarado, J. Boell, D. Nordlund, G. Schneider, S. Hellstrom, C. Johnston, J. Christensen, M. M. Doeff, Y. Liu and S. Kuppan, *J. Mater. Chem. A*, 2019, **7**, 12593–12603.

83 F. Lin, I. M. Markus, D. Nordlund, T. C. Weng, M. D. Asta, H. L. Xin and M. M. Doeff, *Nat. Commun.*, 2014, **5**, 3529.

84 F. M. F. De Groot, M. Abbate, J. Van Elp, G. A. Sawatzky, Y. J. Ma, C. T. Chen and F. Sette, *J. Phys. Condens. Matter*, 1993, **5**, 2277–2288.

85 T. Hatsui, Y. Takata and N. Kosugi, *Chem. Phys. Lett.*, 1998, **284**, 320–324.

86 Y. Takata, T. Hatsui and N. Kosugi, *J. Electron Spectros. Relat. Phenomena*, 1999, **101–103**, 443–447.

87 H. Liu, J. Guo, Y. Yin, A. Augustsson, C. Dong, J. Nordgren, C. Chang, P. Alivisatos, G. Thornton, D. F. Ogletree, F. G. Requejo, F. De Groot and M. Salmeron, *Nano Lett.*, 2007, **7**, 1919–1922.

88 D. Asakura, E. Hosono, Y. Nanba, H. Zhou, J. Okabayashi, C. Ban, P. A. Glans, J. Guo, T. Mizokawa, G. Chen, A. J. Achkar, D. G. Hawthron, T. Z. Regier and H. Wadati, *AIP Adv.*, 2016, **6**, 1–8.

89 R. Fong, U. von Sacken and J. R. Dahn, *J. Electrochem. Soc.*, 1990, **137**, 2009–2013.

90 E. Peled, *J. Electrochem. Soc.*, 1979, **126**, 2047–2051.

91 K. Xu, *Chem. Rev.*, 2014, **114**, 11503–11618.

92 K. Xu, *Chem. Rev.*, 2004, **104**, 4303–4417.

93 T. Hou, G. Yang, N. N. Rajput, J. Self, S. W. Park, J. Nanda and K. A. Persson, *Nano Energy*, 2019, **64**, 103881.

94 M. Hekmatfar, I. Hasa, R. Eghbal, D. V. Carvalho, A. Moretti and S. Passerini, *Adv. Mater. Interfaces*, 2020, **7**, 1–13.

95 B. Strehle, S. Solchenbach, M. Metzger, K. U. Schwenke and H. A. Gasteiger, *J.*

Electrochem. Soc., 2017, **164**, A2513–A2526.

96 K. U. Schwenke, M. Metzger, T. Restle, M. Piana and H. A. Gasteiger, *J. Electrochem. Soc.*, 2015, **162**, A573–A584.

97 B. Strehle, K. Kleiner, R. Jung, F. Chesneau, M. Mendez, H. A. Gasteiger and M. Piana, *J. Electrochem. Soc.*, 2017, **164**, A400–A406.

98 R. Jung, P. Strobl, F. Maglia, C. Stinner and H. A. Gasteiger, *J. Electrochem. Soc.*, 2018, **165**, A2869–A2879.

99 M. Nie and B. L. Lucht, *J. Electrochem. Soc.*, 2014, **161**, A1001–A1006.

100 T. Hatsukade, A. Schiele, P. Hartmann, T. Brezesinski and J. Janek, *ACS Appl. Mater. Interfaces*, 2018, **10**, 38892–38899.

101 Y. Jin, N. J. H. Kneusels, L. E. Marbella, E. Castillo-Martínez, P. C. M. M. Magusin, R. S. Weatherup, E. Jónsson, T. Liu, S. Paul and C. P. Grey, *J. Am. Chem. Soc.*, 2018, **140**, 9854–9867.

102 N. A. Chaturvedi, R. Klein, J. Christensen, J. Ahmed and A. Kojic, *Proc. 2010 Am. Control Conf. ACC 2010*, 2010, 1997–2002.

103 R. Xiong, J. Cao, Q. Yu, H. He and F. Sun, *IEEE Access*, 2017, **6**, 1832–1843.

104 V. Pop, H. J. Bergveld, P. H. L. Notten, J. H. G. Op het Veld and P. P. L. Regtien, *Meas. J. Int. Meas. Confed.*, 2009, **42**, 1131–1138.

105 N. Watrin, B. Blunier and A. Miraoui, *2012 IEEE Transp. Electrif. Conf. Expo, ITEC 2012*, 2012, 1–6.

106 B. Rumberg, B. Epding, I. Stradtmann and A. Kwade, *J. Energy Storage*, 2019, **25**, 100890.

107 X. Qin, M. Gao, Z. He and Y. Liu, *IEEE Int. Conf. Ind. Informatics*, 2019, **2019-July**, 1706–1711.

108 V. Pop, H. J. Bergveld, D. Damilov, P. P. L. Regtien and P. H. L. Notten, *Battery Management Systems Accurate State-of-Charge Indication for Battery-Powered Applications*, 2008.

109 John Warner, *7 - Lithium-Ion Battery Packs for EVs*, Elsevier, 2014.

110 Y. S. Lee and M. W. Cheng, *IEEE Trans. Ind. Electron.*, 2005, **52**, 1297–1307.

111 J. Gao, S. Q. Shi and H. Li, *Chinese Phys. B*, 2015, **25**, 1–24.

112 K. W. Kimura, R. Wilhelm, M. M. Besli, S. Kim, C. Usubelli, J. C. Ziegler, R. Klein, J. Christensen and Y. Gorlin, *J. Electrochem. Soc.*, 2020, **167**, 040510.

113 L. Lavigne, J. Sabatier, J. M. Francisco, F. Guillemard and A. Noury, *J. Power Sources*,

2016, **324**, 694–703.

114 C.-H. Chen, F. Brosa Planella, K. O'Regan, D. Gastol, W. D. Widanage and E. Kendrick, *J. Electrochem. Soc.*, 2020, **167**, 080534.

115 T. F. Fuller, M. Doyle and J. Newman, 1994, **141**, 982–990.

116 A. Barai, G. H. Chouchelamane, Y. Guo, A. McGordon and P. Jennings, *J. Power Sources*, 2015, **280**, 74–80.

117 F. M. Kindermann, A. Noel, S. V. Erhard and A. Jossen, *Electrochim. Acta*, 2015, **185**, 107–116.

118 A. Nyman, T. G. Zavalis, R. Elger, M. Behm and G. Lindbergh, *J. Electrochem. Soc.*, 2010, **157**, A1236.

119 A. Barai, W. D. Widanage, J. Marco, A. Mcgordon and P. Jennings, *J. Power Sources*, 2015, **295**, 99–107.

120 I. Baccouche, S. Jemmali, B. Manai, N. Omar and N. Essoukri Ben Amara, *Energies*, 2017, **10**, 1–22.

121 A. Nikolian, J. Jaguemont, J. de Hoog, S. Goutam, N. Omar, P. Van Den Bossche and J. Van Mierlo, *Int. J. Electr. Power Energy Syst.*, 2018, **98**, 133–146.

122 Y. Zhang, C. Y. Wang and X. Tang, *J. Power Sources*, 2011, **196**, 1513–1520.

123 M. Kassem, J. Bernard, R. Revel, S. Pélissier, F. Duclaud and C. Delacourt, *J. Power Sources*, 2012, **208**, 296–305.

124 C. Truchot, M. Dubarry and B. Y. Liaw, *Appl. Energy*, 2014, **119**, 218–227.

125 J. Wang, J. Purewal, P. Liu, J. Hicks-Garner, S. Soukazian, E. Sherman, A. Sorenson, L. Vu, H. Tataria and M. W. Verbrugge, *J. Power Sources*, 2014, **269**, 937–948.

126 M. Dubarry, C. Truchot, M. Cugnet, B. Y. Liaw, K. Gering, S. Sazhin, D. Jamison and C. Michelbacher, *J. Power Sources*, 2011, **196**, 10328–10335.

127 Y. Xing, W. He, M. Pecht and K. L. Tsui, *Appl. Energy*, 2014, **113**, 106–115.

128 I. Bloom, L. Trahey, A. Abouimrane, I. Belharouak, X. Zhang, Q. Wu, W. Lu, D. P. Abraham, M. Bettge, J. W. Elam, X. Meng, A. K. Burrell, C. Ban, R. Tenent, J. Nanda and N. Dudney, *J. Power Sources*, 2014, **249**, 509–514.

129 M. Dubarry, C. Truchot, B. Y. Liaw, K. Gering, S. Sazhin, D. Jamison and C. Michelbacher, *J. Electrochem. Soc.*, 2013, **160**, A191–A199.

130 T. Huria, G. Ludovici and G. Lutzemberger, *J. Power Sources*, 2014, **249**, 92–102.

131 R. Jung, M. Metzger, F. Maglia, C. Stinner and H. A. Gasteiger, *J. Phys. Chem. Lett.*, 2017, **8**, 4820–4825.

132 J. Kasnatscheew, B. Streipert, S. Röser, R. Wagner, I. Cekic Laskovic and M. Winter, *Phys. Chem. Chem. Phys.*, 2017, **19**, 16078–16086.

133 J. Sicklinger, M. Metzger, H. Beyer, D. Pritzl and H. A. Gasteiger, *J. Electrochem. Soc.*, 2019, **166**, A2322–A2335.

134 C. Unterrieder, C. Zhang, M. Lunglmayr, R. Priewasser, S. Marsili and M. Huemer, *J. Power Sources*, 2015, **278**, 274–286.

135 C. R. Birkl, E. McTurk, M. R. Roberts, P. G. Bruce and D. A. Howey, *J. Electrochem. Soc.*, 2015, **162**, A2271–A2280.

136 V. J. Ovejas and A. Cuadras, *J. Power Sources*, 2019, **418**, 176–185.

137 A. Verma, K. Smith, S. Santhanagopalan, D. Abraham, K. P. Yao and P. P. Mukherjee, *J. Electrochem. Soc.*, 2017, **164**, A3380–A3392.

138 M. Rashid, T. S. Pathan, A. McGordon, E. Kendrick and W. D. Widanage, *J. Power Sources*, 2019, **440**, 227153.

139 S. I. Lee, U. H. Jung, Y. S. Kim, M. H. Kim, D. J. Ahn and H. S. Chun, *Korean J. Chem. Eng.*, 2002, **19**, 638–644.

140 A. Nickol, T. Schied, C. Heubner, M. Schneider, A. Michaelis, M. Bobeth and G. Cuniberti, *J. Electrochem. Soc.*, 2020, **167**, 090546.

UNIVERSITÉ DE STRASBOURG

École doctorale
Physique, chimie-physique
ED 182
Université de Strasbourg

Camille USUBELLI

Fundamental investigation of cathode materials upon deep lithiation for advanced battery management system parametrization

Résumé

Une étude des matériaux cathode à base de Ni a été réalisée dans une fenêtre de potentiel étendue de 4,4 V à ~0,8 V vs Li/Li+. Les différences observées par électrochimie sont interprétées avec les changements de structure du matériau et les changements de valence des métaux de transition. La lithiation à xLi = 1 s'avère entièrement réversible, tandis que les changements dus à la lithiation excessive à xLi = 2 déclenchent une perte de capacité irréversible.

L'identification d'une stabilité des matériaux NMC entre 4,4 V et xLi = 1 a été mise à profit pour développer une nouvelle méthode permettant de caractériser le potentiel « open-circuit » en fonction de la quantité de lithium (courbe OCP). Cette courbe OCP est un paramètre clé pour le système de gestion avancé des batteries, et cette nouvelle méthode permet d'accéder à des informations supplémentaires dans les régions riches en lithium ainsi qu'à un réglage plus précis de l'abscisse.

Mots clés :
Batteries lithium ion, cathode NMC, overlithiation, courbe OCP, système avancé de gestion des batteries

Résumé en anglais

A fundamental investigation of Ni-based layered cathode materials was done in an extended potential window of 4.4 V to ~0.8 V vs Li/Li$^+$. The differences in the lithiation profile observed with electrochemistry were linked to structural changes in the material and valence changes of the transition metals. The lithiation to xLi = 1 was shown to be fully reversible whereas the changes occurring in the structure of the materials upon deep lithiation to xLi = 2 triggered irreversible capacity loss.

The identification of an extended stable cycling window up to xLi = 1 for the NMC materials was leveraged to develop a new method to characterize the open-circuit potential as a function of the lithiation content (OCP curve). This OCP curve is a key parameter for the parametrization of the advanced battery management system, and this new method allows access to additional information in the tail region as well as a more precise setting of the x-axis.

Keywords:

Lithium ion battery, NMC cathode, overlithiation, OCP curve determination, advanced battery management system